THE UNIVERSITY
of EDINBURGH

Experimental Studies on Displacements of CO_2 in Sandstone Core Samples

THE UNIVERSITY *of* EDINBURGH

Ebraheam Saheb Azeaz Al-Zaidi

A Thesis Submitted for the Degree of Doctor of Philosophy
The University of Edinburgh
2018

Declaration

I declare that the research reported in this thesis has been conducted by myself, Ebraheam Saheb Azeaz Al-Zaidi, and the work presented in this thesis is my own, except where stated otherwise. Further, this thesis has not been submitted for the award of any other degree or professional qualification except as specified. Where other sources are quoted full references are given.

Ebraheam Al-Zaidi

2018

Thesis Supervisors

Prof. Xianfeng Fan, The University of Edinburgh, School of Engineering, Edinburgh, United Kingdom.

Dr. Ahn Hyungwoong, The University of Edinburgh, School of Engineering, Edinburgh, United Kingdom.

Abstract

CO_2 sequestration is a promising strategy to reduce the emissions of CO_2 concentration in the atmosphere, to enhance hydrocarbon production, and/or to extract geothermal heat. The target formations can be deep saline aquifers, abandoned or depleted hydrocarbon reservoirs, and/or coal bed seams or even deep oceanic waters. Thus, the potential formations for CO_2 sequestration and EOR (enhanced oil recovery) projects can vary broadly in pressure and temperature conditions from deep and cold where CO_2 can exist in a liquid state to shallow and warm where CO_2 can exist in a gaseous state, and to deep and hot where CO_2 can exist in a supercritical state.

The injection, transport and displacement of CO_2 in these formations involves the flow of CO_2 in subsurface rocks which already contain water and/or oil, i.e. multiphase flow occurs. Deepening our understanding about multiphase flow characteristics will help us building models that can predict multiphase flow behaviour, designing sequestration and EOR programmes, and selecting appropriate formations for CO_2 sequestration more accurately. However, multiphase flow in porous media is a complex process and mainly governed by the interfacial interactions between the injected CO_2, formation water, and formation rock in host formation (e.g. interfacial tension, wettability, capillarity, and mass transfer across the interface), and by the capillary , viscous, buoyant, gravity, diffusive, and inertial forces; some of these forces can be neglected based on the rock-fluid properties and the configuration of the model investigated. The most influential forces are the capillary ones as they are responsible for the entrapment of about 70% of the total oil in place, which is left behind primary and secondary production processes.

During CO_2 injection in subsurface formations, at early stages, most of the injected CO_2 (as a non-wetting phase) will displace the formation water/oil (as a wetting phase) in a drainage immiscible displacement. Later, the formation water/oil will push back the injected CO_2 in an imbibition displacement. Generally, the main concern for most of the CO_2 sequestration projects is the storage capacity and the security of the target formations, which directly influenced by the dynamic of CO_2 flow within these formations. Any change in the state of the injected CO_2 as well as the subsurface conditions (e.g. pressure, temperature, injection rate and its duration), properties of the injected and present fluids (e.g. brine composition and concentration, and viscosity and density), and properties of the rock formation (e.g. mineral composition, pore size distribution, porosity, permeability, and wettability) will have

a direct impact on the interfacial interactions, capillary forces and viscous forces, which, in turn, will have a direct influence on the injection, displacement, migration, storage capacity and integrity of CO_2. Nevertheless, despite their high importance, investigations have widely overlooked the impact of CO_2 the phase as well as the operational conditions on multiphase characteristics during CO_2 geo-sequestration and CO_2 enhanced oil recovery processes.

In this PhD project, unsteady-state drainage and imbibition investigations have been performed under a gaseous, liquid, or supercritical CO_2 condition to evaluate the significance of the effects that a number of important parameters (namely CO_2 phase, fluid pressure, temperature, salinity, and CO_2 injection rate) can have on the multiphase flow characteristics (such as differential pressure profile, production profile, displacement efficiency, and endpoint CO_2 effective (relative) permeability). The study sheds more light on the impact of capillary and viscous forces on multiphase flow characteristics and shows the conditions when capillary or viscous forces dominate the flow. Up to date, there has been no such experimental data presented in the literature on the potential effects of these parameters on the multiphase flow characteristics when CO_2 is injected into a gaseous, liquid, or supercritical state.

The first main part of this research deals with gaseous, liquid, and supercritical CO_2-water/brine drainage displacements. These displacements have been conducted by injecting CO_2 into a water or brine-saturated sandstone core sample under either a gaseous, liquid or supercritical state. The results reveal a moderate to considerable impact of the fluid pressure, temperature, salinity and injection rate on the differential pressure profile, production profile, displacement efficiency, and endpoint CO_2 effective (relative) permeability). The results show that the extent and the trend of the impact depend significantly on the state of the injected CO_2.

For gaseous CO_2-water drainage displacements, the results showed that the extent of the impact of the experimental temperature and CO_2 injection rate on multiphase flow characteristics, i.e. the differential pressure profile, production profile (i.e. cumulative produced volumes), endpoint relative permeability of CO_2 (K_{rCO2}) and residual water saturation (S_{wr}) is a function of the associated fluid pressure. This indicates that for formations where CO_2 can exist in a gaseous state, fluid pressure has more influence on multiphase flow characteristics in comparison to other parameters investigated.

Overall, the increase in fluid pressure (40-70 bar), temperature (29-45 °C), and CO_2 injection rate (0.1-2 ml/min) caused an increase in the differential pressure. The increase in differential pressure with increasing fluid pressure and injection rate indicate that viscous forces dominate the multi-phase flow. Nevertheless, increasing the differential pressure with temperature indicates that capillary forces dominate the multi-phase flow as viscous forces are expected to decrease with this increasing temperature. Capillary forces have a direct impact on the entry pressure and capillary number. Therefore, reducing the impact of capillary forces with increasing pressure and injection rate can ease the upward migration of CO_2 (thereby, affecting the storage capacity and integrity of the sequestered CO_2) and enhance displacement efficiency. On the other hand, increasing the impact of the capillary force with increasing temperature can result in a more secure storage of CO_2 and a reduction in the displacement efficiency. Nevertheless, the change in pressure and temperature can also have a direct impact on storage capacity and security of CO_2 due to their impact on density and hence on buoyancy forces. Thus, in order to decide the extent of change in storage capacity and security of CO_2 with the change in the above-investigated parameters, a qualitative study is required to determine the size of the change in both capillary forces and buoyancy forces.

The data showed a significant influence of the capillary forces on the pressure and production profiles. The capillary forces produced high oscillations in the pressure and production profiles while the increase in viscous forces impeded the appearance of these oscillations. The appearance and frequency of these oscillations depend on the fluid pressure, temperature, and CO_2 injection rate but to different extents. The appearance of the oscillations can increase CO_2 residual saturation due to the re-imbibition process accompanied with these oscillations, thereby increasing storage capacity and integrity of the injected CO_2. The differential pressure required to open the blocked flow channels during these oscillations can be useful in calculating the largest effective pore diameters and hence the sealing efficiency of the rock.

S_{wr} was in ranges of 0.38-0.42 while K_{rCO2} was found to be less than 0.25 under our experimental conditions. Increasing fluid pressure, temperature, and CO_2 injection rate

resulted in an increase in the K_{rCO2}, displacement efficiency (i.e. a reduction in the S_{wr}), and cumulative produced volumes.

For liquid CO_2-water drainage displacements, the increase in fluid pressure (60-70 bar), CO_2 injection rate (0.4-1ml/min) and salinity (1% NaCl, 5% NaCl, and 1% $CaCl_2$) generated an increase in the differential pressure; the highest increase occurred with increasing the injection rate and the lowest with increasing the salinity. On the other hand, on the whole, increasing temperature (20-29 °C) led to a reduction in the differential pressure apart from the gradual increase occurred at the end of flooding. The data indicate that viscous forces dominate multiphase flow when fluid pressure, temperature and injection rate increased; however, as salinity increased, capillary forces dominant dominate the multiphase flow. Increasing the differential pressure with the slight increase in salinity indicates that capillary forces dominate the multi-phase flow as no practical change in viscous forces are expected to occur with this slight adding of salts to water. Increasing the impact of capillary forces impact with salinity can lead to an increase in the storage capacity and integrity of the injected CO_2 but can cause a decrease in displacement efficiency. However, the reduction in CO_2 solubility with increasing salinity can lead to a reduction in the storage capacity and security of CO_2. Therefore, a quantitative study is required to determine the magnitude of change in CO_2 storage capacity and security with salinity as a result of increasing capillary forces but reducing solubility.

S_{wr} was in ranges of 0.3062- 0.384 while K_{rCO2} was in ranges of 0.112-0.203. The S_{wr} decreased with increasing fluid pressure and injection rate; the largest reduction occurred with the injection rate. The S_{wr} increased with increasing temperature and water salinity; the largest increase occurred with salinity. The K_{rCO2} decreased with increasing fluid pressure, temperature, injection rate and salinity; the highest reduction occurred with increasing temperature whiles the lowest occurred with increasing fluid pressure. The cumulative produced volumes decreased slightly with increasing fluid pressure and salinity but showed no noticeable change with increasing temperature and injection rate. The reduction in the cumulative produced volumes with pressure and salinity might indicate an increase in the amount of the stored liquid CO_2.

For supercritical CO_2-water displacements, the results revealed that the extent of the impact of each parameter (e.g. fluid pressure) on the differential pressure profile, cumulative produced volumes, S_{wr} and K_{rCO2} is a function of the associated parameters (e.g. temperature and injection rate).

Most importantly the data show that increasing pressure (74-90 bar) caused a considerable reduction in the differential pressure profile and a transformation of supercritical CO_2 behaviour to a liquid-like CO_2 behaviour; increasing temperature (33-55 °C), on the other hand, resulted in a significant increase in the differential pressure profile and a transformation of supercritical CO_2 behaviour to a gaseous-like CO_2 behaviour. Increasing the injection rate causes the transformation to a liquid-like CO_2 behaviour to occur at lower pressure. The change observed in the differential pressure reflects the change in the capillary forces and viscous forces. The results suggest that multiphase flow was dominated by capillary forces as fluid pressure and temperature increased and by viscous forces as CO_2 injection rate increased considerably. CO_2 transformation to a liquid-like CO_2 behaviour might enhance the displacement efficiency and upward migration of CO_2, thereby reducing the storage capacity and disturbing the integrity of the CO_2 sequestration projects.

S_{wr} was in ranges of 0.34 to 0.41 while K_{rCO2} was less than 0.37. The increase in the fluid pressure and injection rate (0.1-1 ml/min) caused a reduction in the S_{wr} and a rise in the K_{rCO2}. Increasing temperature caused an increase in the S_{wr}; but, it a caused decline in the K_{rCO2} at high fluid pressures (90 bar) and an increase at lower fluid pressures (75 bar). The cumulative produced volumes decreased with increasing fluid pressure and increased with increasing temperature and injection rate.

The second main section of this research deals with CO_2-oil displacements that were performed under gaseous, liquid, and supercritical conditions to investigate the impact of fluid pressure, temperature, and CO_2 injection rate as a function of the CO_2 phase on the differential pressure profile, displacement efficiency, and CO_2 endpoint effective and relative permeabilities. These displacements have been conducted by injecting CO_2 into an oil-saturated sandstone core sample under either a gaseous, liquid or supercritical state. The results reveal a considerable impact for the fluid pressure, temperature, and injection rate on the differential pressure profile, cumulative produced volumes, endpoint CO_2 relative

permeability and oil recovery; the trend and the size of the changes are dependent on the CO_2 state as well as the fluid pressure range in case of gaseous CO_2-oil displacement. In general, liquid CO_2-displacements gave the highest differential pressure magnitude. This indicates that a higher energy is required to produce oils from cold environments where CO_2 can exist in a liquid state, e.g. West Sak reservoir.

As fluid pressure increased, the differential pressure profile of subcritical CO_2 (gaseous and liquid)-oil displacements increased while that of supercritical CO_2-oil displacements decreased. The results indicate that viscous forces were dominant multiphase flow in subcritical CO_2 displacements while capillary forces were dominant the in supercritical CO_2 displacements. For reservoirs with supercritical CO_2 conditions, the reduction in the differential with increasing pressure means maintaining the reservoir pressure at its highest possible level would result in reducing the energy loss, for the displacement of oil towards producing wells, to its lowest level.

On the other hand, increasing temperature caused a reduction in the differential pressure of both subcritical and supercritical CO_2-oil displacements while increasing injection rates caused an increase in the differential pressure profiles of these displacements. Moreover, increasing temperature caused the appearance of the differential pressure oscillations in that of gaseous and supercritical displacements but not in that of liquid CO_2 displacements. With increasing temperature and CO_2 injection rates, the viscous forces became more dominant than capillary forces in both subcritical and supercritical CO_2 displacements. The appearance of oscillations with increasing temperature means that as temperature increases the residual trapping due to capillary forces increase. Consequently, a possible reduction in the reservoir temperature due to CO_2 injection would result in reducing the impact of capillary forces, thereby increasing displacement efficiency. The significant increase in the differential pressure with increasing injection rate means a considerable reduction in the formation energy can occur as injection rate increases in multiphase flow flooding. Thus, an optimization evaluation is required to determine the optimum injection rate that leads to the highest increase in displacement efficiency and the least reduction in the reservoir energy.

S_{wr} was in ranges of around 0.44 to 0.7; liquid CO_2 gave the lowest while low-fluid pressure gaseous CO_2 gave the highest. K_{rCO2} during these oil displacements was in ranges of about

0.015 to 0.657; supercritical CO_2 gave the highest while low-fluid pressure gaseous CO_2 gave the lowest.

The third main section of this research deals with water (brine)-CO_2 imbibition displacements that were performed under gaseous, liquid, and supercritical conditions to investigate the impact of fluid pressure, temperature, and salinity as a function of the CO_2 phase on the differential pressure profile, displacement efficiency, and endpoint effective and relative permeabilities. During these imbibition displacements, deionised water or brine solution (1 % wt. $CaCl_2$) was injected to displace CO_2 (as a gaseous, liquid, or supercritical state) from a Berea sandstone core sample. The results showed that the CO_2 phase governs the magnitude of the changes observed in the differential pressure profile, endpoint water relative permeability and endpoint water saturation due to the variation in the fluid pressure, temperature, and salinity.

Overall, the increase in the fluid pressure, and temperature as well as using of brine solution instead of deionised water caused a reduction in the differential pressure by around 4 to 36%. The magnitude of this reduction is dependent on the state of CO_2; the largest reduction in the maximum-differential pressure occurred in liquid CO_2 imbibition displacements. The reduction in the differential pressure with increasing pressure and temperature means as CO_2 travels upward and hence pressure and temperature are reduced, then more and more energy is required to displace CO_2 out of the system, which is preferable for a secure storage of CO_2. The reduction of differential pressure with increasing salinity suggests that if the salinity of formation fluids is dropped (due to injection of large amounts of low salinity brine), then more energy is required for the displacement of CO_2 out of the system, which is also preferable for CO_2 security.

Endpoint water relative permeability was in ranges of 0.174 to 0.711 while endpoint water (brine) saturation was in ranges of 0.55 to 0.94. The response of the endpoint water relative permeability and endpoint water saturation to increasing fluid pressure, experimental temperature, and salinity are dependent on the state of CO_2.

This study has not investigated the impact of gravity and buoyancy forces on the differential pressure profile and production profile while in reality their impact would be expected to be

taken into consideration. Moreover, the range of pressure and temperature investigated might be of more interest for shallow formations. The brines investigated are of low concentrations while formation waters, in reality, have much higher concentrations. However, despite these limitations, the findings of this study would still provide deep and detail insight into the impact of the parameters investigated on multiphase flow characteristics, therefore, on injection, migration, displacement, storage capacity and security of CO_2. The findings also shed more light on the impact of capillary and viscous forces on multiphase flow characteristics and showed the conditions when one of these forces are expected to dominate the flow.

Due to the complexity of real reservoirs, some of the above observations might not be noticed or detected on a field scale. However, one way of upscaling the pressure data is to use the Leverett's J-function which has been intensively used to convert all the capillary pressure (Pc) data, as a function of the invaded fluid saturation, to a universal curve. To have an idea about the expected impact of capillary and viscous forces on the pressure and production data of a target formation, the parameters that influence these forces of the target formation need to be known; these parameters include the interfacial tension, contact angle, permeability, porosity, and pore size distribution as well as viscosities and saturations of fluids.

Lay Summary

CO_2 capture and storage in subsurface formations can be a potential strategy to reduce the concentration of CO_2 in the atmosphere with the added benefits of enhancing oil recovery (EOR). The target formations for CO_2 sequestration and EOR can vary widely in pressure and temperature conditions from shallow and warm where CO_2 can exist in a gaseous state, to deep and cold where CO_2 can exist in a liquid state, and to deep and hot where CO_2 can exist in a supercritical state. The injection, displacement, and migration of CO_2 in these formations involve the flow of CO_2 in subsurface rocks which already contain water and/or oil, i.e. multiphase flow occurs. Multiphase flow in these formations is a complex process due to the involvement of many factors such as interfacial interactions (interfacial tension, wettability and mass transfer at CO_2-water/oil interface) and forces (capillary, viscous, gravity, buoyancy, and inertial). Of these forces, the capillary forces can result in the entrapment of substantial quantities of oils (about 70 % of original oil in place) in the reservoir. Thus, having a deep understanding of multiphase flow will help us building models that can predict CO_2 flow behaviour in these formations, designing sequestration programme and EOR projects, and selecting appropriate locations for CO_2 storage more accurately.

The movement of CO_2 in subsurface formations is governed by the resistivity of these formations to its flow. The resistivity to flow can have a direct influence on the injection, displacement, migration, storage capacity and integrity of CO_2. One way to measure the system resistivity to flow is by measuring the differential pressure across the core sample. Any change in CO_2 state, operational conditions (pressure, temperature, injection rate and its duration), fluid properties (e.g. concentration and composition of brine solution), and core sample properties (e.g. mineral composition, pore size distribution, permeability and porosity) can have a direct impact on resistivity to flow (i.e. differential pressure), displacement efficiency, and relative permeability due to their direct influence on the interfacial interactions and capillary and viscous forces. The displacement efficiency shows how much fluid (e.g. water/brine or oil) can be displaced out of the core sample upon the injection of another fluid (e.g. CO_2). Relative permeability is a measure of how easy is to displace a fluid, which exists simultaneously with another fluid, out of the core sample.

As CO_2 is injected, generally, at first it displaces formation fluids (water or oil) in a process called drainage. Then, the formation fluids will push back the injected CO_2 in a process called imbibition. In this study, we explored the impact of the CO_2 phase, pressure, temperature,

injection rate, and salinity on the differential pressure, production profile, displacement efficiency and endpoint relative permeability of drainage and imbibition displacements. The drainage displacements were conducted by injecting CO_2 (as a gaseous, liquid, and supercritical state) to displace water/brine solution/or oil out of the saturated sandstone core sample. Then, imbibition displacements were performed by injecting water or brine solution to displace CO_2 (as a gaseous, liquid, or supercritical state) exist in the core sample out of it. Performing these displacements under gaseous, liquid, and supercritical state enables us to see the difference that can occur in the differential pressure, displacement efficiency, and endpoint relative permeability when the state of CO_2 is changed.

Our investigations have shown that changing the CO_2 state and the above-investigated conditions can have a moderate to significant impact on the differential pressure, production profile, displacement efficiency and endpoint relative permeability. It should be noted that in what is follow, only the main observations and their implications are introduced.

For drainage CO_2-water/brine experiments conducted under either a gaseous, liquid or supercritical state, the data shows that displacements performed by injecting gaseous CO_2 were characterized by the highest differential pressure, followed by supercritical displacements and then by liquid displacements. This means that as CO_2 phase transforms from a supercritical or liquid state to a gaseous state due to pressure and temperature change, the resistivity of CO_2 to flow become higher, which can enhance the security of CO_2.

The data shows that the trend (i.e. increase or decrease), and magnitude of change in the differential pressure due to the change in pressure, temperature, and injection rate as well as salinity in case of liquid displacement are significantly dependent on the state of the injected CO_2. As pressure, temperature, and injection rate increased, the differential pressure of gaseous CO_2 displacements increased. However, for liquid displacements, the differential pressure increased with increasing pressure, injection rate, and salinity but reduced with increasing temperature. For supercritical displacements, the differential pressure decreased with increasing pressure but increased with increasing temperature and injection rate. Moreover, the differential pressure profile of supercritical CO_2 displacements transformed to the likeness of that of liquid CO_2 displacements as pressure increased and to that of gaseous displacements as temperature increased.

The change observed in the differential pressure reflects the change in the capillary forces and viscous forces. For illustration, the reduction in the differential pressure of supercritical

CO_2 displacements with increasing pressure can be attributed to the reduction in capillary forces as viscous forces are expected to increase with increasing pressure. Similarly, increasing the differential pressure of supercritical displacement with increasing temperature can be associated with increasing capillary forces as viscous forces are expected to decrease with increasing temperature. This means that capillary forces dominate the multiphase flow characteristics of supercritical CO_2 displacements as pressure and temperature changed. Decreasing the capillary forces with increasing pressure can ease the upward migration of CO_2 out of the system, hence reducing the security and storage capacity of CO_2. Nevertheless, the decrease in buoyancy forces, due to the reduction in the density difference between CO_2 and formation fluid decrease, with increasing pressure can reduce CO_2 upward migration, and hence increasing security storage of CO_2 as well as increasing storage capacity due to increasing density. In summary, in order to evaluate the impact of CO_2 state, pressure, temperature, and injection rate as well as salinity on the storage capacity and security of CO_2, a quantitative study is required to determine the magnitude of change in capillary forces, viscous forces and buoyancy forces with the parameters investigated.

The differential pressures of gaseous CO_2 displacements were characterized by cyclic oscillations, the frequency and magnitude of these oscillations are dependent on the operational conditions. On the other hand, the differential pressures of liquid displacements showed no oscillations. For supercritical displacements, these oscillations appeared under high temperature and low-pressure conditions. The appearance of these oscillations can increase CO_2 residual saturation due to the re-imbibition process accompanied with these oscillations, thereby increasing the storage capacity and integrity of a CO_2 project. The differential pressure required to open the blocked flow channels during these oscillations can be useful in calculating the largest effective pore diameters and hence the sealing efficiency of the rock. Since these oscillations occurred mainly at gaseous state, thus CO_2 transformation from a supercritical or a liquid state to a gaseous state might result in an increase in residual trapping.

The data shows that liquid CO_2 displacements were characterized by the highest displacement efficiency (from 0.616 to 0.694), followed by supercritical CO_2 displacements (0.59-0.66) and then by gaseous CO_2 displacements (0.58-0.68). The endpoint relative permeability of CO_2 was less than 0.25 for gaseous CO_2 displacements, in ranges of 0.112-0.203 for liquid CO_2 displacements, and was less than 0.37 for supercritical CO_2

displacements. The result showed an increase in the displacement efficiency of gaseous CO_2 displacements as pressure, temperature, and injection rate increased. For the injection of liquid and supercritical CO_2, the displacement efficiency increased with increasing pressure and injection rate and decreased with increasing temperature and salinity. As fluid pressure, temperature, and CO_2 injection rate increased, the endpoint relative permeability of gaseous CO_2 increased while that of liquid displacement decreased. For supercritical CO_2 displacements, increasing fluid pressure and CO_2 injection rate caused an increase in the endpoint relative permeability. However, with increasing temperature, the endpoint relative permeability showed a declining trend at high fluid pressures (90 bar) but an increasing trend at low fluid pressures (75 bar).

For CO_2-oil displacements, i.e. CO_2 is injected into oil-saturated sandstone core sample, the data show that increasing fluid pressure caused an increase in the differential pressure profile of subcritical (gaseous and liquid) CO_2 displacements but a reduction in that of supercritical CO_2 displacements. The increase in fluid pressure is expected to cause an increase in the viscous forces and a decrease in the capillary forces. Thus, the change observed in the differential pressure indicates that viscous forces dominate the multiphase flow during subcritical displacements while capillary forces dominate the flow during supercritical displacements. Therefore, for reservoirs with supercritical CO_2 conditions, since the differential pressure decreases with increasing pressure, this suggests that maintaining the reservoir pressure at its highest possible level would result in reducing the energy loss, for the displacement of oil to producing wells, to its lowest level.

The data also show that the differential pressure decreased with increasing temperature for the displacements conducted under gaseous, liquid, and supercritical CO_2 displacements while increasing injection caused an increase in the differential pressure for all CO_2 phases. Increasing the temperature resulted also in the appearance of oscillations in the differential pressure. The appearance of oscillations with increasing temperature means that the residual trapping due to capillary forces increases with increasing temperature; consequently, a possible reduction in the reservoir temperature due to CO_2 injection would result in reducing the impact of capillary forces, thereby reducing residual trapping and increasing displacement efficiency.

The displacement efficiency was in ranges of around 0.3 to 0.56; liquid CO_2 gave the highest while low-fluid pressure gaseous CO_2 gave the lowest. The endpoint CO_2 relative permeability

(K_{rCO2}) was in ranges of about 0.015 to 0.657; supercritical CO_2 gave the highest and low-pressure gaseous CO_2 gave the lowest. The magnitude of change with varying the operational conditions depends on the state of the injected CO_2.

During water (brine)-gaseous, liquid, and CO_2 imbibition displacements, the response of differential pressure, endpoint permeability and displacement efficiency to the change in the parameters investigated depends significantly on the state of CO_2. The endpoint relative permeability (K_{ew}) was in ranges of 0.174 to 0.711 while the endpoint water saturation (S_{ew}) was in ranges of 0.55 to 0.94, depending on the state of CO_2 as well as pressure, temperature and salinity.

The data shows that the increase in pressure, temperature, and injection rate as well using brine solution (1 % $CaCl_2$) instead of deionized water caused a reduction in the differential pressure for the displacements conducted under gaseous, liquid, and supercritical displacements. The highest change in the differential pressure occurred as liquid CO_2 displaced out of the system. The reduction in the differential pressure with increasing pressure and temperature means as CO_2 travels upward, more and more energy is required for the displacement of CO_2 out of the system, which is preferable for the security of CO_2 storage. The reduction of differential pressure with salinity indicates more difficult displacement of CO_2 as the salinity of formation fluids reduces due to injection of large quantities of low salinity brine, which is also for a secure storage of CO_2.

Acknowledgements

I thank Allah, the One true God the Almighty, for his mercy and grace that saw me through the challenges of this journey and all my life. I give Him all the glory, honour, and adoration for the successful completion of this programme.

I would like to express my deepest gratitude to my supervisor, Prof. Xianfeng Fan, for his tremendous help in my research, unwavering and untiring support that have made this work successful. His constructive criticisms, invaluable advice, guidance, patience and encouragement have added so much value to this work and contributed immensely to my personal development and scientific maturity, my great gratitude goes also to my second supervisor, Ahn Hyungwoong. I would like also to deeply thank Dr Katriona Edlmann, Dr Francis Bougie, Julien Mouli-Castillo, and Changyou Xia for their valuable comments and help with my published papers. I would also like to thank the reviewers and editors from the journals that we have published in them. Their constructive and helpful suggestions improved my work and finally led to the publication of the content of some of my work.

I would also like to express my appreciation for the electric and mechanical technical support for my experimental apparatus by Kevin Tierney, Douglas Carmichael, Gilfether Grant, Steve Gourlay, and others.

I would also like to acknowledge the support of the Higher Committee for Education development in Iraq and the Ministry of Oil in Iraq. They sponsored me and my family through my PhD study. Without their financial support, it would have been impossible for me to complete this PhD project.

Lastly, I express my sincerest appreciations to my dear Mother, deceased father, deceased brothers (Ammar and Ismail), brother Abdullah, My cousin Ahmed, my sisters, my wife and my kids for their great favour upon me. Also, I would like to thank all my relatives and all my friends in my home country and all my friends and colleagues of the University of Edinburgh and Edinburgh City for their invaluable support.

Publications

1. **Al-Zaidi**, **E.**, & Fan, X. (**2018**). Effect of Aqueous Electrolyte Concentration and Valency on Contact Angle on Flat Glass Surfaces and Inside Capillary Glass Tubes. Colloids and Surfaces A: Physicochemical and Engineering Aspects, 543, 1-8.

2. **Al-Zaidi**, **E.**, Nash, J., & Fan, X. (**2018**). Effect of CO_2 phase on its Water Displacements in a Sandstone Core Sample. IJGGC, 71, 227-238.

3. **Al-Zaidi**, **E.**, Fan, X., & Edlmann, K. (**2018**). The Effect of CO_2 Phase on Oil Displacement in a Sandstone Core Sample. Fluids, 3 (1), 23.

4. **Al-Zaidi**, **E.**, Edlmann, K., & Fan, X. Gaseous CO_2 Behaviour during Water Displacements in a Sandstone Core Sample. IJGGC (submitted).

5. **Al-Zaidi**, **E.**, & Fan, X. Liquid CO_2 Behaviour during Water Displacements in a Sandstone Core Sample. JNGSE (submitted).

6. **Al-Zaidi**, **E.**, Fan, X., & Edlmann, K. Supercritical CO_2 Behaviour during Water Displacements in a Sandstone Core Sample. IJGGC (submitted).

Contents

List of Figures

List of Tables

1 Chapter 1: Introduction

1.1 Project Background, Motivation and Objectives

CO_2 capture and storage (CCS) is considered as a potential strategy to tackle the increasing concentrations of anthropogenic CO_2 emissions into the atmosphere due to human activities such as the burning of fossil fuel and land clearing of forests and vegetation [1, 2]. The captured CO_2 can be stored in deep saline aquifers, abandoned or depleted oil and gas reservoirs [3], or unmineable coal beds [4, 5]. The injected CO_2 can also be utilized as a working fluid to enhance oil recovery (EOR) from oil and gas reservoirs, enhance methane production from coal beds, or extract geothermal heat from subsurface formations [4, 6].

Enhanced oil recovery (EOR) techniques are used because of the small amounts of oil produced during primary and secondary oil recoveries, which are around one-third of the original oil in place [7], the growing world energy demand, the decline in the exploration of new oil reservoirs, and the maturity of oil fields that produce most of the hydrocarbons [8]. Generally, EOR techniques are categorized into three main methods: thermal, chemical, and gas recovery methods. Thermal recovery methods have their limitations; they are not suitable for heavy oil reservoirs if the formations are thin (<10 m) or too deep (>1000 m) due to heat loss to surrounding formations [9]; they are also not suitable for reservoirs with low permeability and low oil saturation [10]. Chemical flooding methods are a good candidate, but they are generally not implemented because of their high cost.

Recently, application of CO_2 for CO_2 enhanced oil recovery (CO_2-EOR) has gained much momentum as it can be used to enhance oil recovery with the added benefit of reducing CO_2 emissions into the atmosphere [11] via CO_2 sequestration processes [12]. It is estimated that about 80% of oil reservoirs around the world are good candidates for CO_2-EOR processes [13]. The injection of CO_2 can increase oil recovery, firstly, by displacing oil that is left behind during water displacement. Moreover, it can enhance oil recovery gradually over years through a number of different mechanisms, including oil swelling, viscosity reduction, capillary impact reduction via CO_2–oil interfacial tension (IFT) reduction [14], oil extraction [9, 15-17], permeability alteration [18], mass transfer through diffusion and dispersion, and miscibility [19]. Oil viscosity can drop significantly by about 90% of its original value upon

mixing with the injected CO_2 [20, 21], leading to a high increase in oil mobility. Oil swelling due to CO_2 dissolution can enhance oil recovery by expelling oil out of the matrix and increasing oil volume above the residual saturation, leading more oil to flow. Reduction in residual oil saturation can also be achieved by oil extraction upon exposing the oil to a sufficient flow of CO_2-rich gas [14]. However, the evaporation of light components of the oil into CO_2 may cause oil to increase in density [14]. It is worth mentioning that the extraction mechanism is inversely related to oil density. Thus, heavy crude oils are less influenced by this mechanism in comparison to light crude oils [9]. The contribution of each aforementioned mechanism to oil recovery is controlled by pressure, temperature, and CO_2 solubility.

The injected CO_2 can displace oils through miscible, near miscible, and immiscible CO_2 flooding depending on the pressure and temperature conditions and oil and reservoir characteristics [22]. Miscible CO_2 processes are the most attractive scenario for oil recovery due to their high displacement efficiency [9]. The dissolution of CO_2 in the oil phase can substantially improve oil recovery [9] by avoiding the adverse effect of gas–oil interfacial tension, i.e., eliminating trapping forces [9, 21]. However, miscible displacements can only be achieved when the reservoir pressure is higher than the minimum miscibility pressure (MMP), which is not the case for the mature oil fields (due to the depletion of formation energy) and low permeability formations (due to the high-differential pressure drop between injecting and producing wells) [22]. The MMP depends on CO_2 purity, temperature, and oil composition [23]; the MMP decreases when the reservoir pressure increases but increases as the reservoir temperature increases [20]; Yellig and Metcalf observed that increasing CO_2 temperature by 1 °F (≈0.56 °C) over a temperature range from 95 to 192 °F (35–89 °C) caused the MMP to increase by approximately 15 psi (1 bar) [20]. Near miscible flooding refers to the process of not having a full miscibility and occurs when CO_2 is injected at a pressure slightly below the MMP [22, 24]. The main displacement mechanisms are oil swelling, oil viscosity reduction, oil extraction, and IFT reduction that leads to favourable conditions [24, 25]. On the other hand, immiscible CO_2 flooding is a promising and a field-proven method [26] that occurs when reservoir pressure is less than the MMP. Maximum oil recovery can be achieved with this method when the injected CO_2 is enough to saturate the oil and water. The key factor that governs the success of the CO_2 immiscible displacement is the availability of enough resources of CO_2 at low cost [26]. This technique can be used (a) for low-pressure

reservoirs (≤1000 m depth) and thin and heavy oil reservoirs (10–25° API and >3000 m depth [27]) where thermal recovery processes are generally unsuitable [10, 27], (b) with moderately viscous oils [15], and (c) for some shallow-light oil reservoirs where the pressure needed for miscibility cannot be achieved [26]. This technique can also be deployed with gravity-assisted injection into the top of a reservoir [28].

The injection, transport and displacement of CO_2 in subsurface formations involves the flow of CO_2 in subsurface rocks which already contain water and/or oil, i.e. multiphase flow occurs. Multiphase flow is a complex process and governed mainly by the interfacial interactions (e.g. interfacial tension, wettability, capillarity, and interfacial mass transfer [29]) and capillary, viscous, buoyancy, gravitational, diffusive, and inertial forces [27]). Some of these forces can be neglected based on the rock-fluid properties and the configuration of the experimental model [27]. Multiphase flow in geological formation is greatly influenced by the capillary forces [30], especially in low permeability rocks and fractured reservoirs [31]. Capillary forces are responsible for the entrapment of around 70% of oil in place that is left behind the primary and secondary recovery. The capillary forces arise from the presence of the interface between immiscible fluids [32]. The capillary forces are controlled by interfacial tension, system wettability, and effective pore diameter [32-35].

The target formations for CO_2 sequestration and EOR projects can vary widely in pressure and temperature conditions causing the injected CO_2 to exist in a gaseous, liquid or supercritical state [36-41], as shown in Figure 1-1. The change in CO_2 phase, operational conditions (pressure, temperature, injection rate and in its duration), properties of injected and host formation fluids (e.g. brine composition and concentration, density, viscosity), and properties of the target formation (e.g. mineral composition, pore size distribution, porosity, permeability, and wettability) [42-45] will have a direct impact on the interfacial interactions [5, 36, 46-49], capillary forces, and viscous forces [50]. The interfacial interactions and capillary and viscous forces, in turn, are likely to have an impact on multiphase flow characteristics such as entry pressure, differential pressure across the core sample, relative permeability, and displacement rate and efficiency. Consequently, they will have a direct influence on the injection, displacement, migration, storage capacity and security of CO_2 during sequestration [36, 51-53] and enhanced hydrocarbon recovery processes [54, 55]. The injectivity and performance of CO_2 flood are highly influenced by underground conditions of

pressure and temperature as well properties of the rock and fluids in host formations [9, 15, 56, 57]. The CO_2 injectivity can help in determining the amount, pace, and period of CO_2 injection in subsurface formations [58].

We do not exactly know the impact of the individual parameter such as CO_2 state, pressure, temperature, salinity and injection rate on multiphase flow characteristics (e.g. differential pressure, displacement efficiency as well endpoint relative and effective permeabilities) nor do we know their relative importance. Thus, gaining a proper understanding of the impact of these parameters on multiphase flow characteristics could help us building models that can predict multiphase flow behaviour, selecting appropriate locations for CO_2 sequestration, and designing CO_2 sequestration and enhanced oil recovery projects more accurately. Up to date, there has been no such experimental data presented in the literature on the potential effects of these parameters on the multiphase flow characteristics when CO_2 is injected into a gaseous, liquid, or supercritical state.

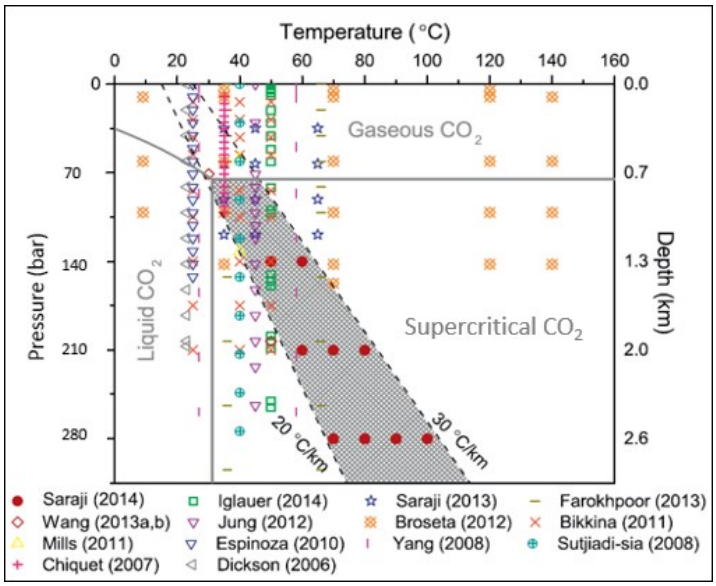

Figure 1-1: The pressure and temperature ranges at which saline aquifers are found underground [38]

As CO_2 is injected in subsurface formations, at first, the bulk of the injected CO_2 (as a non-wetting fluid) will displace reservoir fluids (as a wetting fluid) in a process called drainage [59, 60]. Later, the reservoir fluid will push back the injected CO_2 in a process called imbibition. In this PhD project, dynamic drainage and imbibition displacements were conducted under gaseous, liquid, and supercritical CO_2 conditions to: (**a**) investigate the impact of the CO_2 phase, fluid pressure, temperature, salinity, and CO_2 injection rate on multiphase flow

characteristics, especially focusing on the differential pressure profile, endpoint effective and relative permeabilities and displacement efficiency, (**b**) highlight the impact of capillary and viscous forces on multiphase flow characteristics and show the conditions when capillary or viscous forces dominate the flow. During the drainage experiments, pure gaseous, liquid, or supercritical CO_2 was injected to flood a deionised water, brine (e.g. 1% NaCl, 5% NaCl, or 1% $CaCl_2$), or crude oil saturated sandstone core sample. During the imbibition displacements, deionised water or brine solution (1% $CaCl_2$) was injected to displace CO_2 (as a gaseous, liquid, or supercritical state) from a sandstone core sample.

It should be noted that the differential pressure profile reflects the resistance of the porous medium to the flux of fluids inside it. Therefore, it can be used as an indicator to determine the best locations for exploration (by determining the volume and position of the hydrocarbons trapped) and the zone of drilling hazard (by determining the overpressured formation). In the design of enhanced oil recovery and geological storage, the resistance to flow governs the limit on both the injection pressure and storage capacity of the subsurface formation to avoid an upward migration of the injected fluid into the overlying formations. The differential pressure data can be useful also in determining the capillary entry pressure, capillary breakthrough pressure, capillary-saturation curves, the absolute, effective and relative permeability. The differential pressure can give an indication about the wettability of the system and whether miscible flooding is applicable for a specific reservoir. This is because miscible displacements can only be achieved when the reservoir pressure is higher than the minimum miscibility pressure (MMP). If the differential pressure due to the fluid displacement between injecting and producing wells causes the reservoir pressure to drop below the MMP (especially in low permeability formations), then miscible displacement flooding cannot be achieved [22].

1.2 Thesis Structure

This thesis consists of nine chapters and three Appendices. Chapter 1 provides an introduction to the project background, motivation and objectives. Chapter 2 describes the theoretical background information and literature reviews related to this PhD project. It explains the concepts of wetting, trapping of fluids, permeability, and enhanced oil recovery. Chapter 3 deals with the materials and the experimental methodologies used. Chapter 4 to Chapter 8 form the main body of this thesis and present the results of both drainage and

imbibition displacements. Both drainage and imbibition displacements were investigated to resemble the processes occurred during CO_2 geo-sequestration and CO_2 enhanced oil recovery processes, as stated above.

Chapter 4, Chapter 5 and Chapter 6 presents the experimental results for gaseous CO_2-water displacements, liquid CO_2-water displacements, and supercritical CO_2-water drainage displacements in a sandstone core sample, respectively. During these studies, the effect of fluid pressure, temperature, and CO_2 injection rate on the differential pressure profile, production behaviour, endpoint CO_2 relative and effective permeabilities, and displacement efficiency are thoroughly investigated for each phase. For liquid CO_2-water displacements, the effect of salinity (brine concentration and valency) is also investigated. Conducting these displacements under different states of CO_2 helps in investigating the impact of CO_2 phase on pressure and production data. These studies show the impact of capillary or viscous forces on multiphase flow characteristics and show the conditions when capillary or viscous forces dominate the flow. The results show a moderate to a significant impact of the parameters investigated on the pressure and production profiles. Capillary or viscous forces played a slight to substantial impact on multiphase flow characteristics depending on the state of the injected CO_2 and the parameters investigated.

Chapter 7 presents the experimental results for gaseous, liquid, and supercritical CO_2-oil drainage displacements. During these displacements, the impact of fluid pressure, temperature, and CO_2 injection rate on the differential pressure profile, endpoint CO_2 effective and relative permeabilities, and residual oil saturation are investigated as a function of the CO_2 state. The results reveal a moderate to a significant impact of the CO_2 phase and the parameters investigated on the pressure and production behaviours.

Chapter 8 presents the experimental results for water- gaseous, liquid, and supercritical CO_2 imbibition displacements. During these displacements, the impact of fluid pressure, temperature, and salinity on the differential pressure profile, endpoint water relative permeability, and endpoint water saturation (i.e. residual CO_2 saturation) are investigated as a function of the CO_2 state. The results reveal a moderate to a significant impact of the CO_2 phase and the parameters investigated on the differential pressure profile and the endpoint relative permeability and endpoint saturation.

Chapter 9 shows the main findings, highlights the importance of the study, and includes some recommendations for future studies.

Appendix A investigates static contact angles of various common salts measured on flat glass surfaces and inside glass capillaries and indicates that contact angles on flat glass surfaces in an open space are different from those measured in micro-glass pores. This study is moved out of the main body of this thesis on the suggestion of the examiners. Appendix B provides background information about topics related to this project such as fluid spreading, equations and methods used to calculate contact angle, surface tension, conventional EOR techniques, fundamentals of displacements. Appendix B also provides a literature review about the impact of salinity on wettability. Appendix C provides information about the description of the core sample that used in Chapters 4-6 and 8.

1.3 Reference

1. Kazemifar F, Blois G, Kyritsis DC, Christensen KT. Quantifying the flow dynamics of supercritical CO_2–water displacement in a 2D porous micromodel using fluorescent microscopy and microscopic PIV. Advances in Water Resources. 2015.

2. Hangx S, van der Linden A, Marcelis F, Bauer A. The effect of CO_2 on the mechanical properties of the captain sandstone: geological storage of CO_2 at the Goldeneye field (UK). IJGGC. 2013;19:609-19.

3. Li Z, Dong M, Li S, Huang S. CO_2 sequestration in depleted oil and gas reservoirs—caprock characterization and storage capacity. Energy Conversion and Management. 2006;47(11):1372-82.

4. Kaveh NS, Wolf K, Ashrafizadeh S, Rudolph E. Effect of coal petrology and pressure on wetting properties of wet coal for CO_2 and flue gas storage.IJGGC. 2012;11:S91-S101.

5. Plug W-J, Bruining J. Capillary pressure for the sand–CO_2–water system under various pressure conditions. Application to CO_2 sequestration. Advances in Water Resources. 2007;30(11):2339-53.

6. Tutolo BM, Luhmann AJ, Kong X-Z, Saar MO, Seyfried WE. CO_2 sequestration in feldspar-rich sandstone: coupled evolution of fluid chemistry, mineral reaction rates, and hydrogeochemical properties. Geochimica et Cosmochimica Acta. 2015;160:132-54.

7. Bondor P. Applications of carbon dioxide in enhanced oil recovery. Energy Conversion and Management. 1992;33(5):579-86.

8. Alvarado V, Manrique E. Enhanced oil recovery: an update review. Energies. 2010;3(9):1529-75.

9. Emadi A, Sohrabi M, Farzaneh SA, Ireland S, editors. Experimental investigation of liquid-CO_2 and CO_2-emulsion application for enhanced heavy oil recovery. EAGE Annual Conference & Exhibition incorporating SPE Europec; London, UK, 10–13 June 2013: SPE: Houston, TX, USA, 2013.

10. Srivastava R, Huang S, Dyer S, Mourits F, editors. Heavy oil recovery by subcritical carbon dioxide flooding. SPE Latin America/Caribbean Petroleum Engineering Conference; Buenos Aires, Argentina, 27–29 April 1994: SPE: Houston, TX, USA, 1994.

11. Tahmasebi P, Sahimi M, Kohanpur AH, Valocchi A. Pore-scale simulation of flow of CO_2 and brine in reconstructed and actual 3D rock cores. JPSE. 2017;155:21-33.

12. Liu Y, Teng Y, Jiang L, Zhao J, Zhang Y, Wang D, et al. Displacement front behavior of near miscible CO_2 flooding in decane saturated synthetic sandstone cores revealed by magnetic resonance imaging. Magnetic resonance imaging. 2017;37:171-8.

13. Vega B, Kovscek AR. Carbon dioxide (CO_2) sequestration in oil and gas reservoirs and use for enhanced oil recovery (EOR). Developments and Innovation in Carbon Dioxide (CO_2) Capture and Storage Technology. 2: Woodhead Publishing: Sawston, UK; 2010. p. 104-26.

14. Moortgat JB, Firoozabadi A, Li Z, Espósito RO. CO_2 injection in vertical and horizontal cores: measurements and numerical simulation. SPE Journal. 2013;18(02):331-44.

15. Klins MA, Ali SMF. Heavy oil production by carbon dioxide injection. PETSOC-82-05-06. 1982.

16. Todd M, Grand G. Enhanced oil recovery using carbon dioxide. Energy conversion and management. 1993;34(9):1157-64.

17. Huang ET, Tracht JH, editors. The displacement of residual oil by carbon dioxide. SPE Improved Oil Recovery Symposium; Tulsa, Oklahoma, 22–24 April 1974: SPE: Houston, TX, USA, 1974.

18. Spivak A, Garrison WH, Nguyen JP. Review of an immiscible CO_2 project, tar zone, fault block V, Wilmington field, California. SPE reservoir engineering. 1990;5(02):155-62.

19. Hao H, Hou J, Zhao F, Song Z, Hou L, Wang Z. Gas channeling control during CO_2 immiscible flooding in 3D radial flow model with complex fractures and heterogeneity. JPSE. 2016;146 (Supplement C):890-901.

20. Yellig W, Metcalfe R. Determination and prediction of CO_2 minimum miscibility pressures (includes associated paper 8876). JPT. 1980;32(01):160-8.

21. Tran TQMD, Neogi P, Bai B. Stability of CO_2 Displacement of an Immiscible Heavy Oil in a Reservoir. SPE Journal. 2017;22.

22. Behrenbruch P, Huu MTD, Hoang TG, Bui KD, editors. Modelling of drainage capillary pressure: A Comparative study of various analytical capillary pressure formulations in matching laboratory results. In Proceedings of the SPE Asia Pacific Oil & Gas Conference and Exhibition; Perth, Australia, 25–27 October 2016: SPE: Houston, TX, USA, 2016.

23. Stalkup F. Carbon dioxide miscible flooding: past, present, and outlook for the future. JPT. 1978;30(08):1,102-1,12.

24. Bui LH. Near miscible CO_2 application to improve oil recovery [PhD. Thesis]: University of Kansas, Lawrence, KS, USA; 2010.

25. Shyeh-Yung J, editor. Mechanisms of miscible oil recovery: effects of pressure on miscible and near-miscible displacements of oil by carbon dioxide. SPE Annual Technical Conference and Exhibition; Dallas, TX, USA, 6–9 October 1991: SPE: Houston, TX, USA, 1991.

26. Khatib AK, Earlougher RC, Kantar K. CO_2 Injection As An Immiscible Application For Enhanced Recovery In Heavy Oil Reservoirs. 1981/1/1/. SPE California Regional Meeting, 25-27 March, Bakersfield, California 1981.

27. Rojas G, Ali S. Dynamics of subcritical CO_2/brine floods for heavy-oil recovery. SPE Reservoir Engineering. 1988;3(01):35-44.

28. Hatchell D, Benson S. Examining the Potential of Immiscible CO_2 for Gravity-assisted Enhanced Oil Recovery and Storage. Energy Procedia. 2017;114:6980-8.

29. Chalbaud C, Robin M, Lombard J, Martin F, Egermann P, Bertin H. Interfacial tension measurements and wettability evaluation for geological CO_2 storage. Advances in Water Resources. 2009;32(1):98-109.

30. Roof J. Snap-off of oil droplets in water-wet pores. SPE. 1970;10(01):85-90.

31. Schembre JM, Kovscek AR. A technique for measuring two-phase relative permeability in porous media via X-ray CT measurements. JPSE. 2003;39(1-2):159-74.

32. Bikkina P, Wan J, Kim Y, Kneafsey TJ, Tokunaga TK. Influence of wettability and permeability heterogeneity on miscible CO_2 flooding efficiency. Fuel. 2016;166:219-26.

33. Alkan H, Cinar Y, Ülker E. Impact of capillary pressure, salinity and in situ conditions on CO_2 injection into saline aquifers. Transport in porous media. 2010;84(3):799-819.

34. Chatzis I, Morrow NR. Correlation of capillary number relationships for sandstone. SPE. 1984;24(05):555-62.

35. Fulcher Jr RA, Ertekin T, Stahl C. Effect of capillary number and its constituents on two-phase relative permeability curves. JPT. 1985;37(02):249-60.

36. Espinoza DN, Santamarina JC. Water-CO_2-mineral systems: Interfacial tension, contact angle, and diffusion—Implications to CO_2 geological storage. Water resources research. 2010;46(7).

37. Bachu S. Sequestration of CO_2 in geological media: criteria and approach for site selection in response to climate change. Energy conversion and management. 2000;41(9):953-70.

38. Saraji S, Piri M, Goual L. The effects of SO_2 contamination, brine salinity, pressure, and temperature on dynamic contact angles and interfacial tension of supercritical CO_2/brine/quartz systems. IJGGC. 2014;28:147-55.

39. Sohrabi M, Jamiolahmady M, Al Quraini A, editors. Heavy Oil Recovery by Liquid CO_2/Water Injection. EUROPEC/EAGE Conference and Exhibition; London, UK 11–14 June 2007: SPE: Houston, TX, USA, 2007.

40. Nourpour Aghbash V, Ahmadi M, editors. Evaluation of CO_2-EOR and Sequestration in Alaska West Sak Reservoir Using Four-Phase Simulation Model. SPE Western Regional Meeting; Bakersfield, CA, USA, 21–23 March 2012: SPE: Houston, TX, USA, 2012.

41. Frailey SM, Grube JP, Seyler B, Finley RJ, editors. Investigation of liquid CO_2 sequestration and EOR in low temperature oil reservoirs in the Illinois basin. SPE/DOE Symposium on Improved Oil Recovery; Tulsa, OK, USA, 17–21 April 2004: SPE: Houston, TX, USA, 2004.

42. Chalbaud C, Robin M, Lombard J, Martin F, Egermann P, Bertin H. Interfacial tension measurements and wettability evaluation for geological CO_2 storage. Advances in Water Resources. 2009;32(1):98-109.

43. Sakurovs R, Lavrencic S. Contact angles in CO_2-water-coal systems at elevated pressures. Int J Coal Geo. 2011;87(1):26-32.

44. Pentland C, El-Maghraby R, Georgiadis A, Iglauer S, Blunt M. Immiscible displacements and capillary trapping in CO_2 storage. Energy Procedia. 2011;4:4969-76.

45. Wang S, Edwards IM, Clarens AF. Wettability phenomena at the CO_2-brine-mineral interface: implications for geologic carbon sequestration. Environ Sci Technol. 2013;47(1):234-41.

46. Yang D, Gu Y, Tontiwachwuthikul P. Wettability determination of the reservoir brine−reservoir rock system with dissolution of CO_2 at high pressures and elevated temperatures. Energy & Fuels. 2007;22(1):504-9.

47. Liu N, Ghorpade SV, Harris L, Li L, Grigg RB, Lee RL, editors. The effect of pressure and temperature on brine-CO_2 relative permeability and IFT at reservoir conditions. In Proceedings of the SPE Eastern Regional Meeting; Morgantown, WV, USA, 13–15 October 2010: SPE: Houston, TX, USA, 2010.

48. Arif M, Jones F, Barifcani A, Iglauer S. Electrochemical investigation of the effect of temperature, salinity and salt type on brine/mineral interfacial properties. IJGGC. 2017;59:136-47.

49. Al-Aulaqi T, Fisher Q, Grattoni C, Al-Hinai SM, editors. Wettability alteration by brine salinity and temperature in reservoir cores. SPE Saudi Arabia Section Technical Symposium and Exhibition; 2013.

50. Bachu S, Bennion DB. Interfacial tension between CO_2, freshwater, and brine in the range of pressure from (2 to 27) MPa, temperature from (20 to 125)° C, and water salinity from (0 to 334 000) mg· L− 1. Journal of Chemical & Engineering Data. 2008;54(3):765-75.

51. Saraji S, Goual L, Piri M, Plancher H. Wettability of supercritical carbon dioxide/water/quartz systems: simultaneous measurement of contact angle and interfacial tension at reservoir conditions. Langmuir: the ACS journal of surfaces and colloids. 2013;29(23):6856-66.

52. Wang D, Dong B, Breen S, Zhao M, Qiao J, Liu Y, et al. Review: Approaches to research on CO_2/brine two-phase migration in saline aquifers. Hydrogeology Journal. 2015;23(1):1-18.

53. Levine JS, Matter JM, Goldberg DS, Lackner KS, Supp MG, Ramakrishnan T. Two phase brine-CO_2 flow experiments in synthetic and natural media. Energy Procedia. 2011;4:4347-53.

54. Gozalpour F, Ren S, Tohidi B. CO_2 EOR and storage in oil reservoir. Oil & gas science and technology. 2005;60(3):537-46.

55. Qi R, Laforce T, Blunt M. Carbon Dioxide (CO_2) injection design to maximize underground reservoir storage and enhanced oil recovery (EOR). Developments and innovation in carbon dioxide (CO_2) capture and storage technology (ED MM Maroto-Valer), Woodhead Publishing Series in Energy, Oxford. 2010:169-84.

56. Kang S, Gao C, Zhang S. Scientific research and field application of CO_2 immiscible flooding in heavy oil recovery. In Proceedings of the SPE Enhanced Oil Recovery Conference; 2013/7/2/; Kuala Lumpur, Malaysia, 2–4 July 2013. SPE: SPE: Houston, TX, USA, 2013.; 2013.

57. Müller N. Supercritical CO_2-brine relative permeability experiments in reservoir rocks—Literature review and recommendations. Transport in porous media. 2011;87(2):367-83.

58. Mijic A, LaForce TC, Muggeridge AH. CO_2 injectivity in saline aquifers: The impact of non-Darcy flow, phase miscibility, and gas compressibility. Water Resources Research. 2014;50(5):4163-85.

59. Herring AL, Andersson L, Newell D, Carey J, Wildenschild D. Pore-scale observations of supercritical CO_2 drainage in Bentheimer sandstone by synchrotron x-ray imaging. IJGGC. 2014;25:93-101.

60. Basbug B, Gumrah F, Oz B, editors. Simulating the effects of deep saline aquifer properties on CO_2 sequestration. Canadian International Petroleum Conference; 2005: Petroleum Society of Canada.

2 Chapter 2: Theoretical Background and Literature Reviews

2.1 Wettability

Wetting process refers to the tendency of a liquid to spread on or adhere to a solid surface due to the interactions between the liquid and solid surface [1]. On the other hand, the de-wetting process refers to the instability or rupture of a thin liquid film on a solid surface that leads to dry spots/ formations on the substrate.

The liquid wetting and de-wetting of solid surfaces are ubiquitous phenomena that can exist in every aspect of our life [2]. An obvious example of the wetting phenomenon is the lotus effects, as shown in Figure 2-1. The wetting phenomenon is of key importance in many industrial applications and engineering fields that include: physical chemistry of surfaces and interfaces, material science, physics of fluids and thermodynamic, deposition of pesticides on plants leaves, cooling of industrial reactors, industry of ceramic and detergency, ink-jet and 3D printing, coating of porous materials, brazing, soldering, tissue engineering, cleaning and surface coating, microelectronics, optical and optoelectronic technology, and oil recovery [2-8].

Figure 2-1: Water on a lotus leaf surface [9]

To determine the wettability of a fluid-liquid-solid system, many qualitative and quantitative methods have been proposed in the literature [10, 11]. Of these quantitative techniques are

the Amott test, the USBM, and contact angle methods [10, 12, 13]. The Amott test and the USBM methods are used to evaluate the average wettability of a reservoir rock while the contact angle is used to determine the wettability of a specific solid substrate [10].

The contact angle refers to the angle formed between a liquid drop/bubble surface and a solid/liquid interface which measured through the dense phase [2, 14]. On a macroscopic scale, the contact angle is essential in determining the wetting behaviour of a material system in a laboratory situation and then forecasting the wetting behaviour and fluid body shape in another system [15]. On a microscopic scale, it is essential in searching into the physics and chemistry of the microscopic area close to the wetting line [15]. Due to its simplicity and being less time consuming, the contact angle measurement is still the most reliable technique despite some intrinsic problems, e.g. its high sensitivity to contamination [16, 17]. In general, when the contact angle is less than 90°, the surface is regarded as hydrophilic, however, if it is greater than 90°, then the surface is regarded as hydrophobic, as shown in Figure 2-2. However, according to Anderson when the contact angle is 0°-75°, 75°-115°, 115°-180°, the solid surface is considered to be water-wet, intermediate-wet, or oil-wet, respectively [18], more information can be seen in Appendix B- Section B.1, Section B.2 and B.3.

The wettability of the porous medium plays an important role in determining the imbibition and the distribution of the wetting and non-wetting phases inside the porous media [19]. The wettability determines the distribution of the wetting and non-wetting phases fluids within the porous medium because of its impact on the amount of fluid displaced and the way of displacement [20]. The non-wetting phase (e.g. CO_2) will occupy the centre of larger pores while the wetting phase (e.g. water) will form a thin layer around the surfaces of the larger pores. Nevertheless, the smaller pores will only be filled with the wetting phase [20].

The change in contact angle (i.e. wettability) can have a direct impact on capillary forces and entry pressure, which, in turn, can have a direct influence on the injection, displacement, migration, storage capacity and security of CO_2. Any change in the state of CO_2 [21, 22], pressure, temperature, and salinity might have a direct impact on contact angle. As the CO_2 phase transforms from a liquid to a gaseous phase, the contact angle can increase [21]. Increasing pressure [23] and salinity [24] can cause an increase in contact angle while increasing temperature [25] can cause a reduction in contact angle.

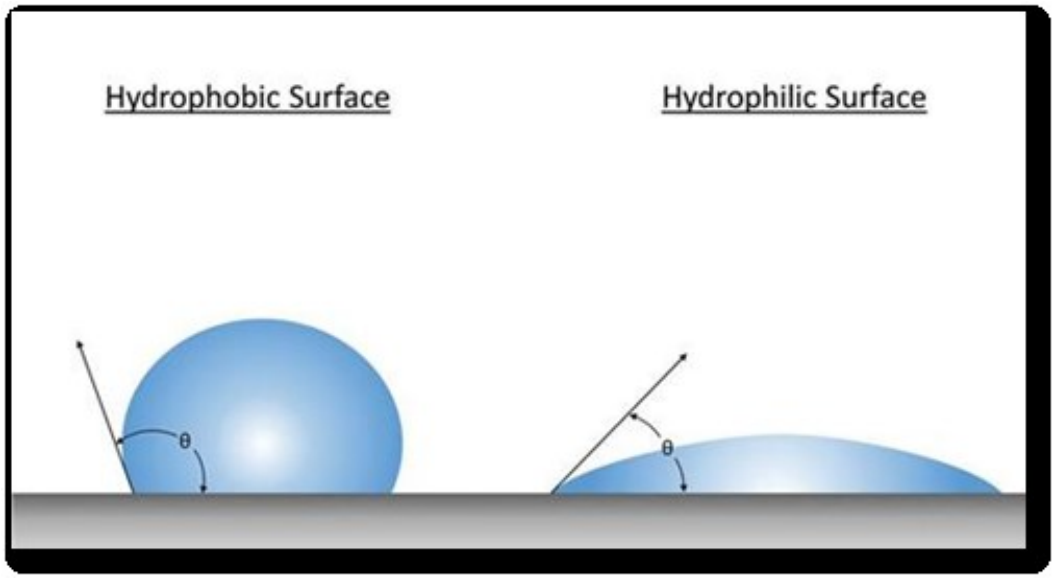

Figure 2-2: Hydrophobic and Hydrophilic surface [26].

2.2 Trapping of Fluids

2.2.1 Oil and Gas Reservoir Rocks

A natural reservoir is a subsurface trap where fluids of oil, gas, and formation water can accumulate and fill the pores, vugs, and fractures of the reservoir rocks in varying proportions. Usually, these subsurface formations are overlaid by a layer of sealing rocks to trap fluids in place, as shown in Figure 2-3.

After their formation in the source rock, oil and gas migrate through interconnected water-filled pores to the reservoir in significant amounts. In order for the migration of these fluids to occur, the buoyant forces acting on an oil globule must overcome the capillary and viscous forces that oppose the flow of the oil globule or the gas bubble (e.g. CO_2) from a pore rock through an adjacent pore throat [27-31]. The buoyant forces arise due to the density contrast between fluids in place, e.g. oil and water, and increase as the density contrast between fluids in place increases and that is why the buoyant forces of gas (e.g. CO_2) are much higher than that of oil [30]. When the resistive forces (capillary and viscous forces) become larger than buoyant forces, they prevent the continued upward flow of fluids (e.g. CO_2 or oil) through pore throats, trapping them inside the pore space regardless of the presence of stratigraphic and/or structural traps [29]. The magnitude of the capillary forces is determined by the radius of the pore throats of the rock, hydrocarbon-water interfacial tension, and wettability [31].

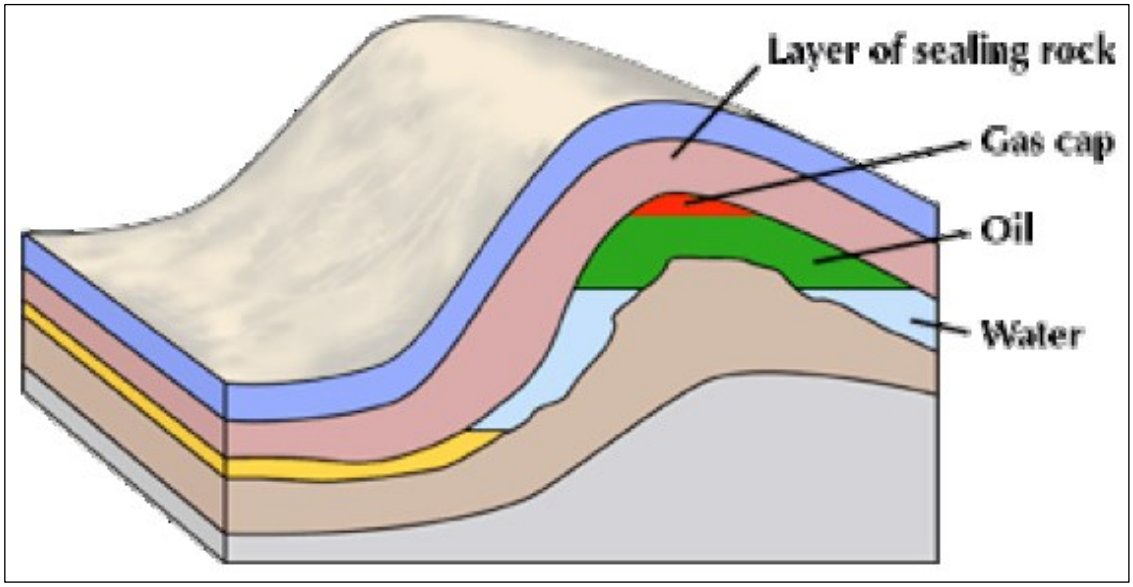

Figure 2-3: An example of a petroleum reservoir containing Oil, Gas and Water [32]

The two major mechanisms that govern migration through seal rocks are molecular diffusion and pressure-driven volume flow (Darcy flow) [33]. Molecular diffusion is an abundant and slow process that occurs when a molecule, e.g. hydrocarbon or CO_2, diffuses through a water-saturated pore space of the seal rock. The Darcy flow, on the other hand, occurs when the differential pressure across the seal rock is larger than the sealing capacity of the caprock. The Darcy flow is controlled by the geologic and hydrodynamic conditions of the system (which includes the reservoir, seal rock, and overburden formations) and the properties of the fluids in both reservoir and seal rock [34].

Once the differential pressure between the nonwetting and wetting phase becomes sufficiently high to overcome the capillary pressure at the pore throat, as shown in Figure 2-4, the nonwetting phase will advance along the channel. The displacement will last until reaching the next smaller pore throats of higher capillary pressure. When the differential pressure across the seal rock exceeds the capillary pressure of series of interconnected pore throats of arbitrarily large sizes, a continuous filament of nonwetting phase will occur, leading to the occurrence of the slow Darcy flow. The magnitude of the differential pressure is governed by the highest capillary pressure of interconnected series of pore throats which are first flooded by the nonwetting phase. The capillary pressure depends on the interfacial tension between the wetting and the non-wetting phase, wetting status of the surface, and properties of the core sample.

The Young's Laplace equation is used to correlate these parameters to the capillary pressure as follows:

$$\Delta P = P_n - P_w = 4\,\frac{\sigma_{CO_2-water}\,COS\theta}{d} \qquad (2\text{-}1)$$

where ΔP is the differential pressure across the seal rock, i.e. the capillary breakthrough pressure, P_n the pressure in the nonwetting phase, P_w the pressure in the wetting phase, $\sigma_{CO2\text{-}water}$ the CO_2-water interfacial tension, Θ the contact angle through the dense phase, and d the effective pore radius [12].

The differential pressure can be used to assess the sealing capacity of a seal rock of a hydrocarbon trap [33, 34]. Moreover, it can be used in many processes such as oil and gas evaluation in prior to exploitation, basin analysis, hydrocarbon secondary migration assessment, as well as in the selection of geological sites to store natural gas, CO_2 or industrial waste gases [35]. The change in CO_2 state as well as pressure, and temperature is most likely to have a direct influence on fluids migration and differential pressure due to their impact on both buoyant forces, and resistive forces (capillary and viscous forces).

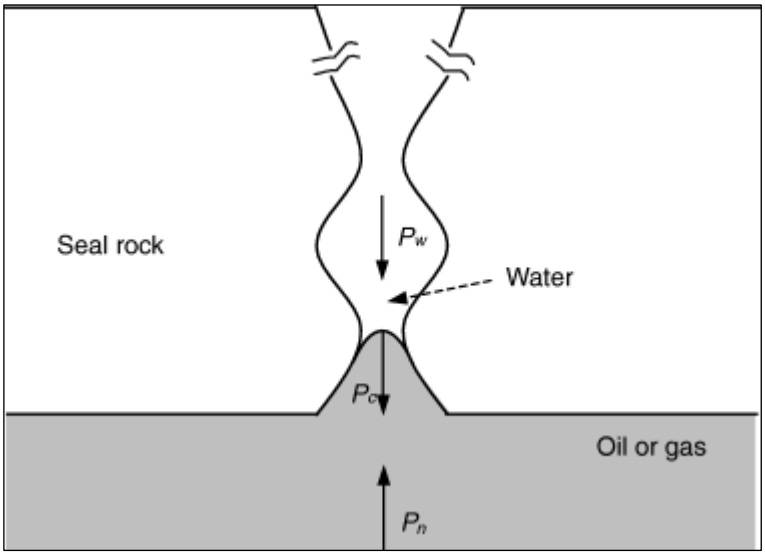

Figure 2-4: Schematic of capillary sealing mechanism in a pore throat of seal rock [34]

2.2.2 Carbon Capture and Storage (CCS)

As shown in Figure 2-5, CCS refers to the capture and separation, compression, transport, and injection of CO_2 into geological formations to be trapped for thousands of years [36-38]. CCS is regarded as one of the promising techniques to mitigate the increasing emissions of anthropogenic CO_2 in the atmosphere to acceptable levels. Human activities, such as fossil

fuel burning, land clearing of forests and vegetation [39, 40], caused the concentration of CO_2 in the atmosphere to increase from around 396 ppm at 2014 to 407.54 ppm in January 2018, as shown in Figure 2-6. The increasing concentration of CO_2 in the atmosphere has been closely associated with the rise in the earth temperature, i.e. global warming phenomenon [41]. Studies estimate that earth temperature will increase by 1-6 °C by 2070 in Australia, by 2-3.5 °C by 2080 in the UK, and by 1.4-5.8 °C by 2100 globally [42, 43], as shown in Figure 2-7.

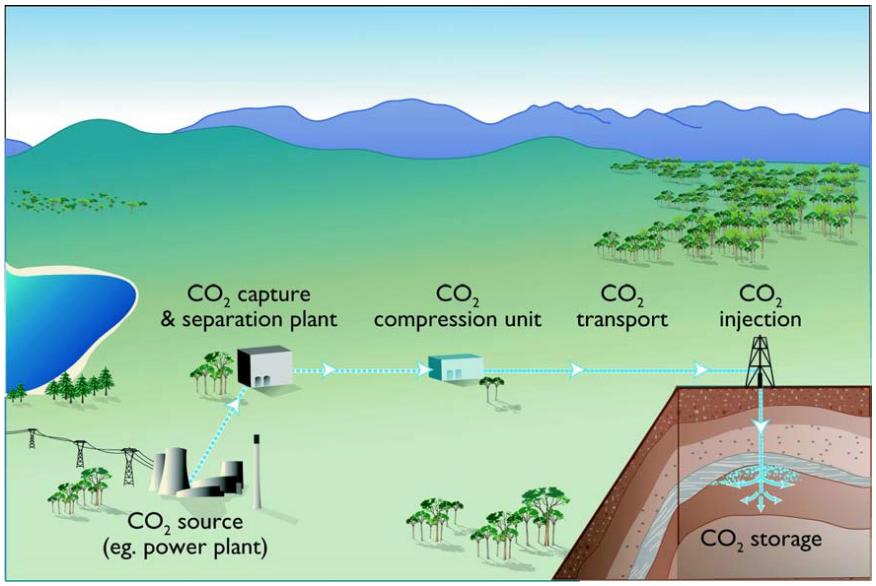

Figure 2-5: A schematic of CO_2 Capture and Storage (CCS) [36]

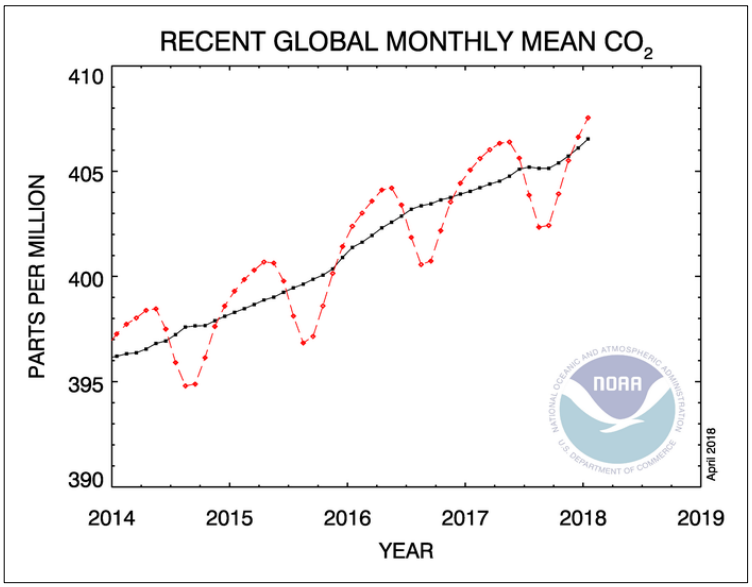

Figure 2-6: Global Carbon Dioxide Concentration Trends [44]

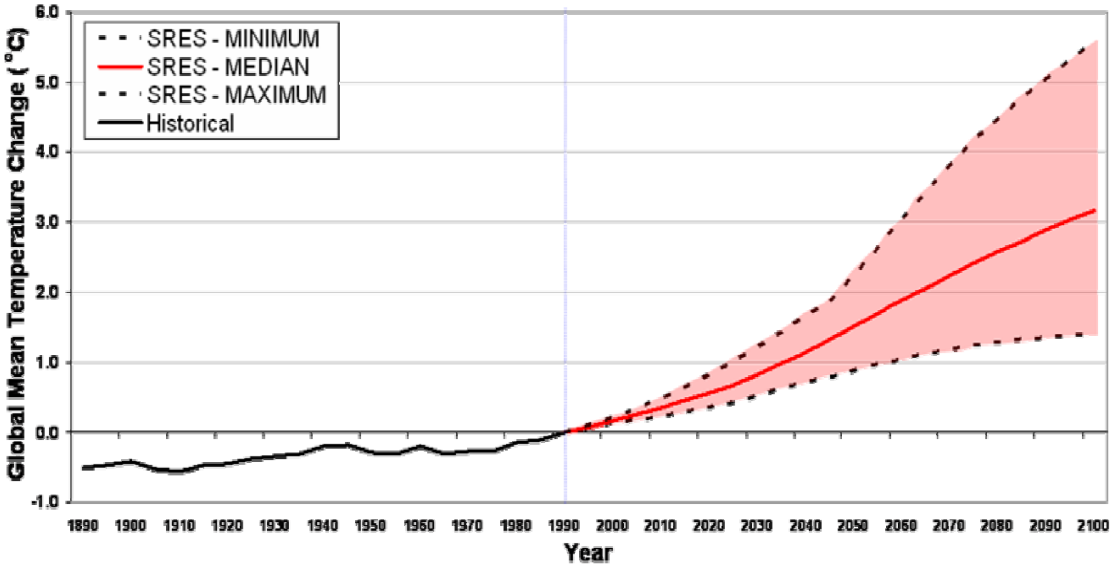

Figure 2-7: A schematic of projected changes in world temperature [42]

To reduce CO_2 concentration to pre-industrial era levels, scientists have proposed several measures that include: (I) improving the efficiency of fossil energy usage, (II) developing intensive fuels of less carbon content, (III) increasing reliance on renewable energy resources (e.g. wind, solar, and nuclear energy resources), and (IV) implementing CCS processes [36, 43, 45]. The development and wide implementation of the three first measures need a rather long time. Hence, the CCS is the most practical measure on a short to medium time scale [45]. Currently, several CO_2 storage projects, either at full or laboratory scale, are underway in: Norway (Sleipner and Snøhvit), USA (Cranfield, Entrada, La Berge), Germany (Ketzin), the Netherlands (K12-B), Algeria (In Salah), and Australia (Otway) [46].

The main potential targets for underground storage of CO_2 are deep saline aquifers, depleted or abandoned oil and gas reservoirs [47-49], and unmineable coal bed seams, as shown in Figure 2-8. Deep saline aquifers are porous formations saturated with high salinity brines [39]. These formations spread widely through the world and provide the largest potential storage capacity of 400-10,000 Gigatonnes (GT) [50], which accounts for around 90% of total potential storage capacity, as shown in Figure 2-9. The capacity of the abandoned oil and gas formations are estimated to be around 900 Gt [51], which accounts for about 9% of the potential storage capacity. Deep coal beds can store the injected CO_2 in very tiny pores within the coal, called microspores, leading to enhancement of methane production in a process called enhanced coal bed methane (ECBM). Although the abandoned hydrocarbons formations have lower storage capacity than saline aquifers, they are most likely to be used

as the first option for CO_2 storage. This is due to the additional economic benefits of using CO_2 to enhance oil and gas recovery [12, 48, 52], the availability of characterization data, and the existence of underground and surface infrastructures [52].

In general, the main concerns for a CO_2 storage project are the formation capacity, CO_2 security, and CO_2 injectivity [52]. The formation storage capacity is controlled by the volume of the formation and its effective porosity as well as the dynamic of CO_2 flow within the target formation, i.e. the displacement sweep efficiency at macroscopic and pore-scale levels [52], for more information about fundamentals of displacement efficiency see Appendix B- Section B.7. The investigation of the CO_2 flow dynamic is of significant importance for groundwater hydrology and remediation in addition to reservoir engineering [53], too. The main concern for CO_2 storage in oil and gas reservoirs is the existence of improperly sealed oil and gas wells that may provide an escape route for CO_2. Changing CO_2 state as well as pressure, temperature, and salinity and injection rate are most likely to have an impact on storage capacity and security as well as injectivity of CO_2.

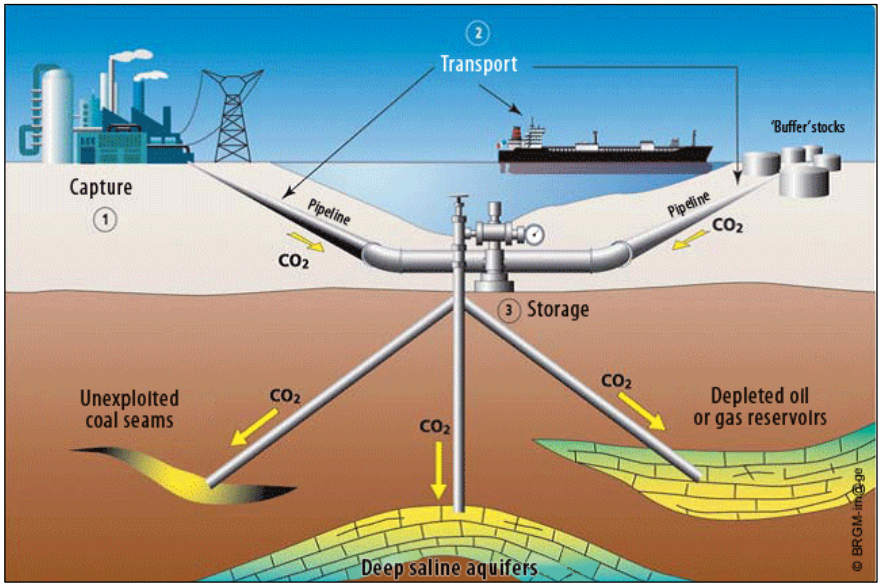

Figure 2-8: A schematic of CO_2 capture and transport, via ships and pipelines, from factories to the target formations such as unexploited coal seams, deep saline aquifers, and depleted oil or natural gas fields [54]

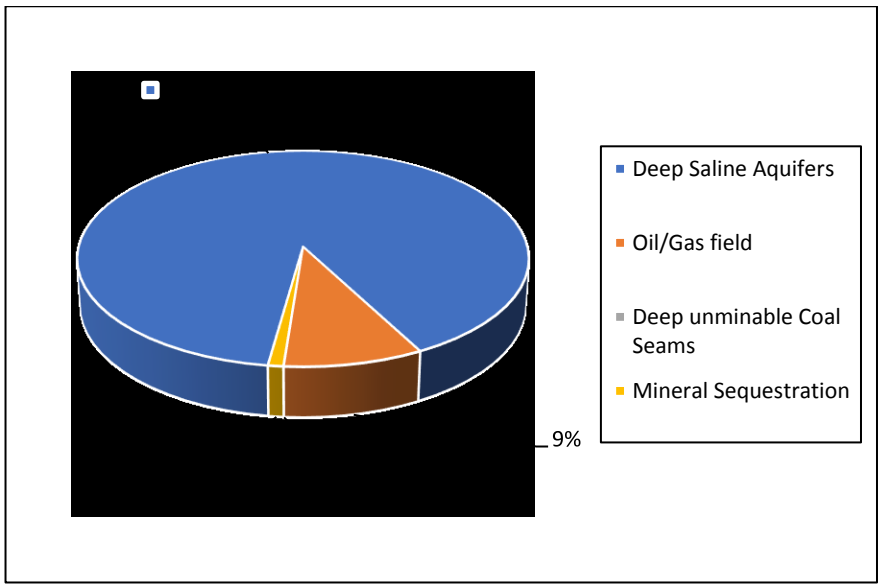

Figure 2-9: Relative order-of-magnitude potential of the various storage methods for the world [43]

2.2.2.1 CO_2 Trapping Mechanism

As shown in Figure 2-10, CO_2 can be trapped in one or more of the following trapping mechanisms which are: physical (e.g. structural/ stratigraphic and/or local capillary trapping), residual, solubility, and geochemical (i.e. mineral) trapping [45]. Each of these mechanisms has a role in the way CO_2 stays trapped in subsurface formations. Moving from structural to mineral trapping, the storage capacity of CO_2 will decrease while the security of CO_2 will increase.

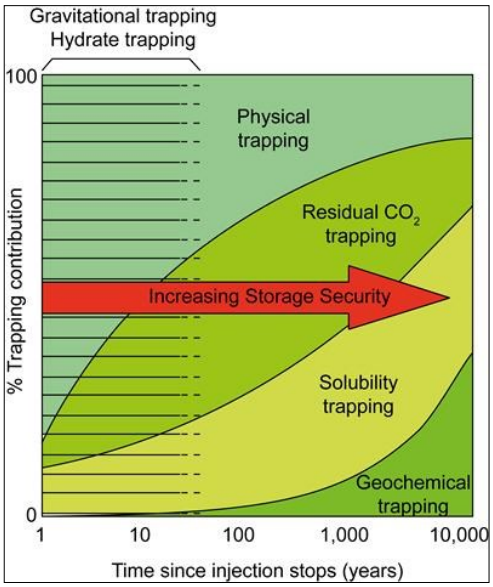

Figure 2-10: CO_2 trapping method performance [55]

2.2.2.1.1 Structural/Stratigraphic Trapping

Structural and stratigraphic trapping refers to the physical trapping of CO_2 and deals with the largest volume of the injected free-phase CO_2 [56]. CO_2 is trapped by extremely low porosity and permeability caprocks (i.e. seal formations), which are composed of very fine grains (e.g. shale rock or salt beds) and saturated with brine [47]. The seal formations such as the caprock, fractures, and faults within and above the storage zone act as a barrier of a high capillary entry pressure that prevents CO_2 from migration into the atmosphere due to buoyancy effect [36, 57, 58], as shown in Figure 2-11.

The integrity and capacity of the seal formations are driven by the capillary breakthrough pressure that depends on the interfacial tension, wettability, and reservoirs properties. Thus, storing CO_2 in the depleted oil and gas reservoirs instead of the original hydrocarbon will significantly reduce the sealing capacity of these reservoirs. This is due to the much lower interfacial tension of CO_2 and water system in comparison to that of oil and water system. The result is much lower capillary pressure of the CO_2 and water system compared to that of oil and water system, therefore less sealing capacity [38, 59].

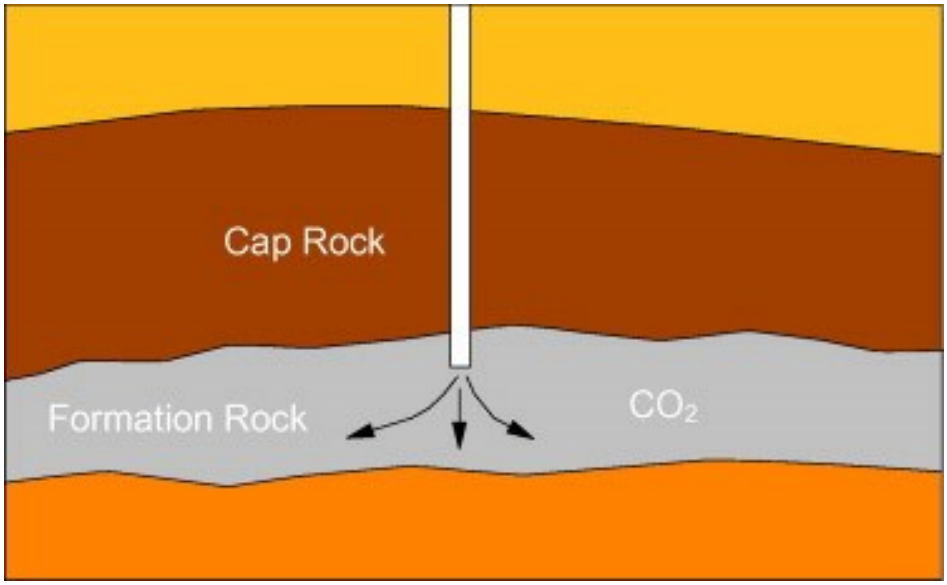

Figure 2-11: A schematic of the structural and stratigraphic trapping mechanism [60]

2.2.2.1.2 Local Capillary Trapping

Local capillary trapping refers to the amount of CO_2 trapped by the heterogeneity of capillary pressure. It occurs when the buoyancy-driven migration of CO_2 plume is prevented by local dense formations that span on a length scale of 0.01 to 10 m. These high dense formations

act as a local barrier by having a local capillary entry pressure larger than the average pressure [61, 62]. This trapping mechanism can ensure a secure CO_2 storage, even a failure of structural trapping was to occur.

2.2.2.1.3 Residual Trapping

During residual trapping, CO_2 can be trapped in pore spaces as disconnected bubbles [63]. This process occurs when the injected CO_2 forms a plume close to the injection wells. Later, due to the buoyancy effect, this plume will ascend to upper sections of the storage formation, leading to the displacement of fluids in a process called drainage. However, once the injection process comes to end, the displaced fluids will push back the injected CO_2 in a process called imbibition. As a result, some portions of the injected CO_2 at the trailing end of the ascending plum will be trapped in pore spaces as disconnected bubbles [63], as shown in Figure 2-12. The snap-off phenomenon, which depends on the capillary forces [36, 64] and relative permeability hysteresis [47, 62, 65], has a high impact on residual trapping.

During residual trapping, the immobilized CO_2 will be securely trapped in storage formations, even leakage events were to occur [66]. Nonetheless, the capacity of this mechanism is controlled by the effective porosity times the residual nonwetting saturation, which depends on the initial non-wetting saturation and the wettability of the porous medium as well as capillary forces and buoyancy forces. Simulation studies suggested that capillary forces may have an impact on the plume shape and velocity. When capillary forces are weak, CO_2 will form a fairly compact and fast migrated plume, over which saturation changes. Contrariwise, when capillary forces are strong, CO_2 will form a wide range and slowly migrated plume [67-70].

Residual trapping is the fastest trapping mechanism that can occur over time scales of days to months in core scale experiments [36, 66]. Within 10's of years, it is expected to store considerable amounts of CO_2. Laboratory investigations for sandstone formations demonstrate that between 13-92% of the injected CO_2 can be residually trapped. The main difference between the residual and local capillary trapping is that CO_2 trapped as a discontinues phase in the former case and as a free phase in the latter case [62].

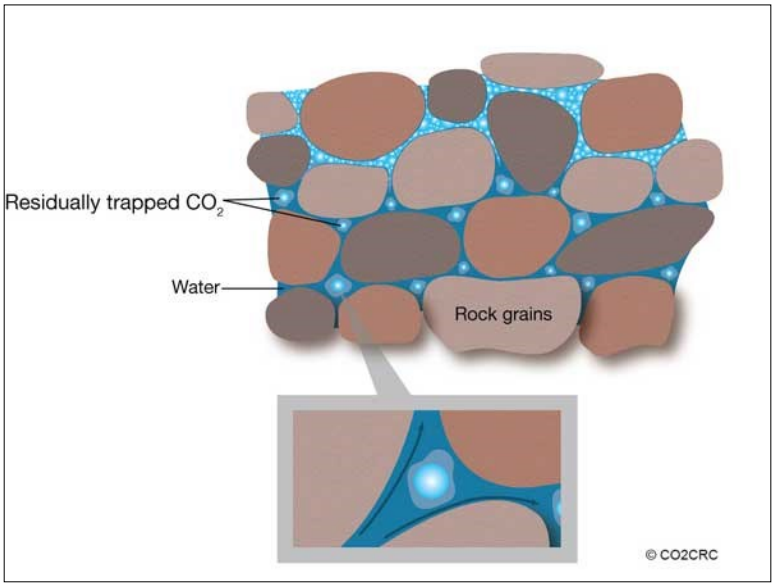

Figure 2-12: Residual trapping of CO_2 [71]

2.2.2.1.4 *Solubility Trapping*

Solubility trapping refers to the amount of CO_2 dissolved in oil or formation water [45, 64]. The dissolved CO_2 will increase the density of formation water [62, 66], by an order of magnitude of 0.1 to 1% [56], causing the CO_2 saturated formation water to sink. Consequently, the dissolved CO_2 will migrate with formation water during the flow of groundwater [62, 66]. Typically, the velocity of regional formation water is extremely slow (< 0.1 m/year) [72], extending the residence time from tens of thousands to millions of years [72].

Due to their impact on CO_2 solubility, the capacity of this technique is controlled by the prevailing conditions of pressure, temperature, and formation water salinity as well as capillary forces. Increasing pressure causes an increase in CO_2 solubility while increasing temperature and brine concentration cause a reduction in solubility. The capillary forces coerce the CO_2 plumes to move horizontally and hence increasing the area of contact between the CO_2 and formation water. As the contact area increases, the CO_2 dissolution increases.

2.2.2.1.5 *Mineral Trapping*

Mineral trapping refers to the CO_2 trapped in the form of carbonates mineral. Once it dissolved in formation water, CO_2 can form a carbonic acid (a weak acid) in the reaction [73].

$$CO_2 + H_2O \leftrightarrow H_2CO_3 \leftrightarrow HCO_3^- + H^+ \leftrightarrow CO_3^{2-} + 2H^+ \quad (2\text{-}2)$$

The carbonic acid then reacts with Mg^{+2} and Ca^{+2}, leading to the precipitation of the carbonate minerals [64]. One mineral which can be formed through these reactions is calcite (calcium carbonate) [73]:

$$CaAl_2Si_2O_8 + H_2O + CO_2 \rightarrow CaCO_3 + Al_2Si_2O_5(OH)_4 \quad (2\text{-}3)$$

Anorthite calcite kaolinite

The reaction process is very slow; yet, it is the most secure trapping mechanism of CO_2. It is expected that 90% of the injected CO_2 ultimately stored in this technique. However, this way of trapping is not expected to increase the capacity.

In summary, investigating multiphase flow characteristics as a function of the CO_2 phase, pressure, temperature and salinity is of practical importance. This is due to the potential effect of the parameters investigated on the integrity and capacity of CO_2 because of their direct impact on the capillary breakthrough pressure of seal formations as well as their impact on residual and solubility trapping.

2.3 Permeability Concept

Permeability is a measuring tool of the conductivity of a certain porous medium to a particular Newtonian fluid [74, 75]. Practically, the measuring unit for permeability is Darcy. A porous medium has a permeability of 1 Darcy if a fluid of 1 cp viscosity is produced at a flowrate of 1 cm^3/ sec when a differential pressure of 1 Atmosphere is applied to a cube of 1 cm sides in length. The Darcy equation below is used to define the permeability of a sufficiently slow, unidirectional, and steady flow.

$$Q = -\left(\frac{kA}{\mu}\right)\left(\frac{\Delta\mathcal{P}}{L}\right) \quad (2\text{-}4)$$

where Q is the volumetric flow rate "discharge", A the normal cross-sectional area of the sample, L the length of the sample in the macroscopic flow direction, $\mathcal{P}$ the "piezometric pressure", and μ the viscosity of the fluid. The following equation is used to define the piezometric pressure $\mathcal{P}$ as follows:

$$\mathcal{P} = P + \rho g z \quad (2\text{-}5)$$

where *z* is the distance measured vertically upward from an arbitrarily chosen datum level, *P* the hydrostatic pressure, *ρ* fluid density, and *g* the acceleration due to gravity [74].

Theoretically, a single steady state flow rate is enough to calculate the permeability of the porous medium. However, this can lead to a considerable error. Thus, it is advisable and customary that the core sample permeability is obtained by performing a range of low flowrates, plotting these flowrates against the corresponding differential pressure, and fitting a straight line to the data points. If the system is obeying Darcy's law then a straight line must pass through the data; however, if it is not, then Darcy's law is not applicable [74].

Practically, permeability is divided into absolute, effective and relative permeability. Absolute permeability is a medium property and can be obtained when only one fluid passes the porous medium. However, in reality, more than one immiscible fluid (e.g. gas, water, and oil) moves simultaneously in porous media. Therefore, only a fraction of the original pore space will be occupied by each fluid [76, 77]. Owing to the fact that the ability of each fluid to move is reduced by the existence of the other fluid, the total permeability is less than one, and thus the so-called relative permeability function (K_r) has been presented [76]. Relative permeability denotes the ratio of the effective permeability of a given phase to the absolute permeability of the porous media. The relative permeability to oil, gas and water is presented as follows:

$$K_{r\,o,g,w} = \frac{K_{e\,o,g,w}}{K} \tag{2-6}$$

where K_r, K_e, and K refers to the relative, effective, and absolute permeability respectively. The subscript *o, g, w* denotes the oil, gas, and water phases, respectively.

2.3.1 Methods for Measuring Permeability

Technically, relative permeability is measured by steady-state flow and/or unsteady state flow techniques [77]. During the steady-state techniques, more than one fluid is injected simultaneously at a constant flow rate until a constant pressure drop and saturation equilibrium are achieved. The constant pressure drop is reached when the wetting phase becomes immobile [76]. During the unsteady state techniques, one fluid is injected at a constant rate/pressure to displace the fluid in place. The outlet fluid composition and flowrate are measured and used to determine the relative permeability. The main difference

between the steady state and unsteady techniques is that saturation equilibrium is not achieved during the latter.

The main advantage of the unsteady state technique is its substantial speed [77]. However, the main drawbacks of this technique are: the restriction of saturation range to only one endpoint data every time, the influence of the capillary end effect on the recovery and pressure response data, the impact of injection rate and the length of the core on the measurements due to their direct influence on the capillary end effect [77]. On the other hand, the steady state method is designed to overcome these problems but also has its own disadvantages, which are: (a) the possibility that the fluid distribution is not a representative of the displacement process, and (b) the experimental restrictions imposed by the need to measure the saturation [77].

2.3.2 Factors Affecting Relative Permeability

Relative permeability depends on many factors such as rock structure, fluid properties (e.g. viscosity ratio or interfacial tension), saturation history and wettability [77, 78], and pressure and temperature conditions [78].

Increasing the saturation of certain fluid results in increasing its readiness to flow, thereby increasing its relative permeability. For instance, the increase in the non-wetting phase saturation on the expense of the wetting phase saturation will lead to a sharp increase in the non-wetting phase relative permeability (i.e. a sharp reduction in the wetting phase relative permeability), attaining almost unity at the residual water saturation [76].

Wettability of the porous medium has a high impact on relative permeability [78]. As shown in Figure 2-13, alteration of the wettability, e.g. from a water-wet status to an oil-wet status, can have a direct influence on the shape and the endpoints of the relative permeability curves. It can cause an increase or decrease in the relative permeability of the wetting or the non-wetting fluid. For illustration, altering a reservoir wettability towards a more water-wetting status by low salinity water injection can cause a reduction in the relative permeability of the water and an increase in that of oil. On the other hand, increasing the oil-wetness of the porous medium can cause the relative permeability of oil to decrease while that of water to increase [78].

The change in pressure and temperature can affect the relative permeability, too. For instance, Liu et al. observed a high increase in the endpoint relative permeability of CO_2 and

a high reduction in the endpoint brine saturation with increasing pressure. However, they observed that increasing temperature caused no major influence on the endpoint relative permeability of a brine-CO_2 system [67]. On the other hand, Al- Aulaqi et al. noticed a reduction in the relative permeability of the water wetting fluid with the increase in temperature [79]. Al- Aulaqi et al. attributed the reduction in the relative permeability to the increase in the aggregation of crude oil components on rock surface as temperature increased. The oil aggregation caused a water flow restriction when the mechanical forces initiated by viscous flooding were countered by the capillary forces originated from the adhesion of crude oil onto rock surface [79].

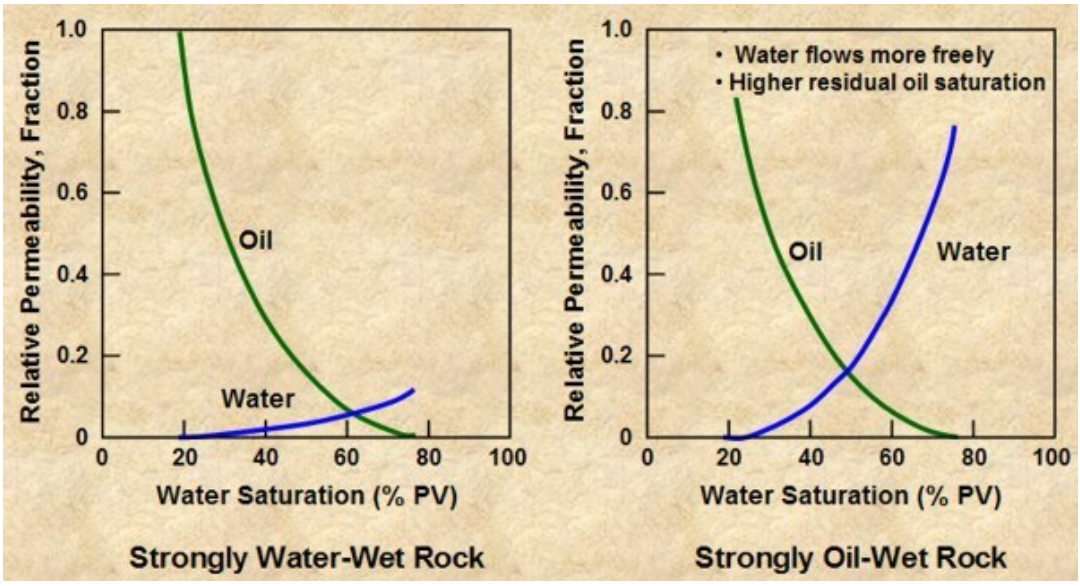

Figure 2-13: Relative permeability curves in water and oil wet reservoirs [80]

In this study, unsteady state techniques were used to explore the endpoint effective (relative) permeability of CO_2-water/brine/oil-sandstone system during drainage displacements and these of water/brine-CO_2 sandstone system during imbibition displacement. The drainage and imbibition displacement were conducted under gaseous, liquid, supercritical CO_2 conditions to study the impact of pressure, temperature, salinity and injection rate on endpoint relative and effective permeabilities as a function of the CO_2 phase.

2.4 Oil Recovery Mechanisms

In order to enhance oil recovery, one of the following techniques are commonly applied: (I) increase the capillary number by reducing the interfacial tension and/or altering wettability,

and hence mobilizing residual oil saturation; (II) decrease the mobility ratio by increasing the injected water viscosity via polymer addition; (III) reduce the permeability of heterogeneous formations such as high permeability zones or streaks, thereby increasing their sweeping efficiency of the.

Typically, oil recovery can be achieved through three main processes: primary, secondary and tertiary or enhanced oil recovery (EOR), as shown in Figure 2-14. Both primary and secondary processes can produce between 10-40% of the original oil in place (OOIP) [81]. Primary recovery alone can achieve between 5 to 20% of the OOIP, sometimes even higher [82]. Secondary recovery can cause an additional oil production by around 10 to 20% of OOIP [82].

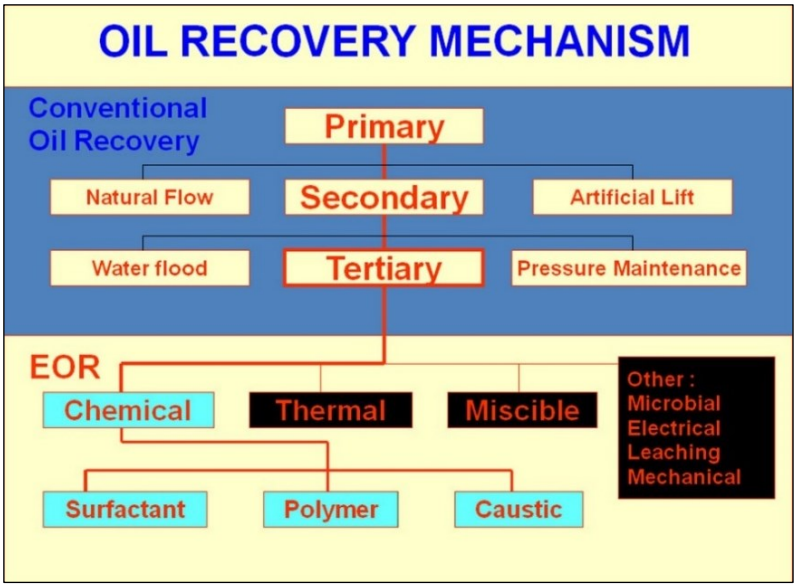

Figure 2-14: Oil Recovery Mechanism [81]

Primary recovery refers to the initial production of oil from porous media under the natural energy of the reservoir (i.e. reservoir pressure) [82, 83] or by an assisted flow, such as an artificial lift or the use of pumping devices. The natural energy can be derived from the swelling of the reservoir fluids, gas growth from gas originally dissolved in the crude oil, expansion of the gas originally present in the reservoir, or from the influx of the water from nearby aquifers communicating to the oil reservoir [82].

After the depletion of the natural energy during primary recovery, the secondary recovery process may be initiated to maintain the natural energy with an external source such as natural gas or water flooding [82, 83]. During gas flooding, the gas is injected into a gas cap

(i.e. a free gas zone) to maintain the reservoir pressure and enhance the production by way of a gravity drainage [83].

2.4.1 Enhanced Oil Recovery (EOR)

EOR techniques refer to the operations that include the displacement of in-situ oleic phase by continuous injection of different kinds of materials to preferably change the chemical and physical properties of the formation fluids (e.g. oil and water) and reservoir rocks [84, 85], and hence changing the spreading, adhesion, and wettability [86]. The displacing fluid may be immiscible (e.g. water) or miscible (e.g. solvent injection) [84].

EOR processes are of crucial importance to address the growing global demand for the hydrocarbon energy, maturity of the present oil resources [85, 87], and complexity of oil production processes for most of the unconventional oil reservoirs such as heavy crude oil reservoirs, shale reservoirs, and tight reservoirs. According to the International Energy Outlook 2016 (IEO2016), issued by the U.S. Energy Information Administration's, the consumption of world energy will increase by 48% between 2012 and 2040, as shown in Figure 2-15, and the fossil fuels will still account for more than three-quarters of the world energy consumption until 2040 [88]. EOR techniques target the considerable amounts of the oil (about 60-70% of the original oil reserves) that is left behind primary and secondary recovery stages (conventional techniques) [82, 83, 89-91]. EOR techniques can produce between 8-16% of OOIP, based on estimations form laboratories studies and numerical simulations [92].

Traditionally, conventional EOR techniques consist of waterflooding, thermal flooding (e.g. steam and combustion), electric flooding, gas flooding (miscible and immiscible flooding), and chemical flooding (surfactant and polymer flooding) [93]. The most used methods for the enhancement of oil production are: water flooding, thermal flooding, and chemical flooding processes. EOR processes, such as thermal flooding for heavy oil reservoirs, can be applied in the first stage when the natural reservoir energy becomes insufficient to displace oil into producing wells. Moreover, EOR processes, such as CO_2 flooding, can be deployed in the second stage to enhance oil flow and cause desirable recovery conditions. However, EOR processes are utilized mostly in the third stage when oil reservoirs start high water cut and low oil production rate [85].

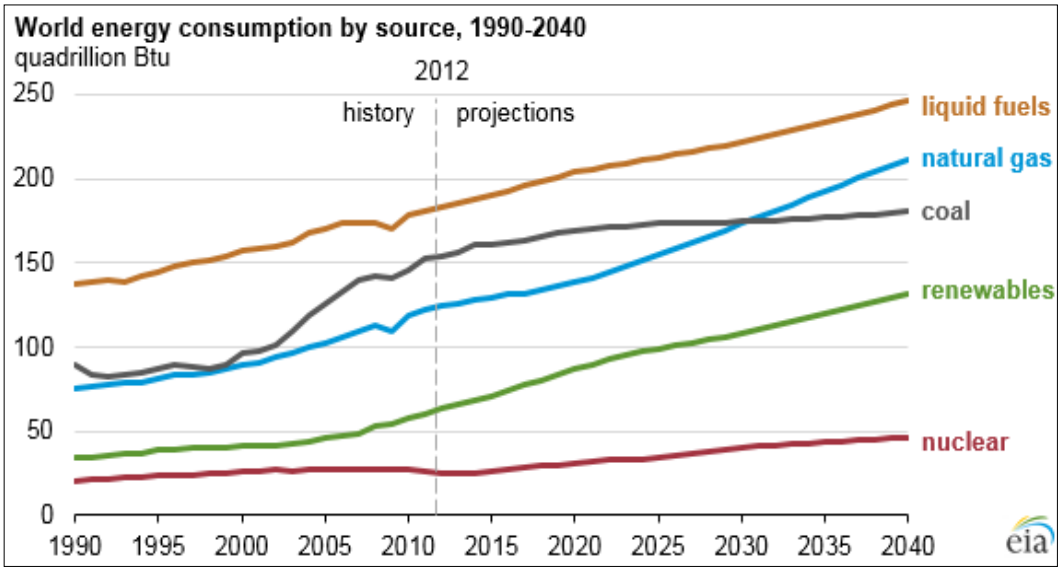

Figure 2-15: World energy consumption by source 1990-2040 [88]

2.4.1.1 CO_2-EOR

CO_2-EOR processes have been in practice since the early 1970's and with more than 80 projects worldwide they produce a total of over 170,000 barrel/day [48, 94, 95]. In the USA, CO_2-EOR techniques are responsible for more than 5% of the total oil production [96, 97]. Recently, CO_2-EOR techniques have gained much attention as a way of reducing CO_2 emissions in the atmosphere to accepted levels [58, 98] with the added benefits of enhancing oil recovery, mainly in light and medium gravity oil reservoirs [92, 95, 99].

Generally, CO_2-EOR processes are more preferable for light and low viscosity crude oils [82]. This is because low viscosity oils and light crude oils have a high percentage of light components that enhance the miscibility of the displacement [82]. The miscibility, in turn, will enhance the displacement efficiency by lowering CO_2-oil interfacial tension and hence alleviating capillary forces impact. Miscibility occurs because of CO_2 dissolving into crude oil upon contact between CO_2 and oil. The dissolved CO_2, in turn, will enhance the transfer of light components from the crude oil into carbon dioxide, leading to a more hydrocarbon-rich mixture instead of the original CO_2 [82].

The dissolved CO_2 can also enhance oil displacement by swelling oil and reducing its viscosity. Sehbi et al. noticed that using CO_2 instead of water to displace oil results in reducing the displacing fluid viscosity by 93% and the IFT by 99.6%. As a result, it caused a reduction in residual oil saturation by 34% [100].

Typically, CO_2 can displace oil through immiscible and/or miscible processes. CO_2 miscibility is governed by the reservoir conditions, constituents of the crude oils, and amount and type of the injected gas. The injected gas can be flue gas, nitrogen or hydrocarbon, CO_2 or gasses mixed with CO_2 such as methane (CH_4) and nitrogen (N_2) [101].

2.4.1.1.1 Immiscible CO_2-EOR Displacements

Immiscible displacements occur when reservoir conditions of pressure and temperature are not sufficient to extract enough components form the oil to the oil-enriched CO_2 phase to become miscible with the oil [102], i.e. they occur when the reservoir pressure is below the minimum miscible pressure (MMP) [48]. The magnitude of the MMP depends mainly on reservoir temperature and oil composition.

Immiscible CO_2-EOR flooding can produce about 5-10% of OOIP [101]. These immiscible CO_2 displacements are used with reservoirs that are characterized by high viscous oils and high oil saturation (≥ 20%), normally about 55%. High viscous oils normally have a viscosity as high as 100-1000 cp, API as low as 22°, and density as high as 0.922 g/ml [101]. However, these immiscible displacements can be influenced by many factors that include the CO_2 slug size, number of slugs, injection rates of water and CO_2 for WAG (water alternating gas) injection, WAG ratio and WAG cycle, reservoir operating pressure, extent of phase equilibrium, and other factors associated with rock-fluid interactions [103], more information can be found in Appendix B- Section B.5 and B.5.

Due to the high-density contrast between the displacing fluid (CO_2) and the displaced one (e.g. heavy crude oil), immiscible CO_2-oil displacements are characterized by a high mobility ratio which can reduce oil recovery. Thus, enhancement of oil recovery due to CO_2 injection is mainly attributed to CO_2 solubility and component exchange between oil and CO_2 that can promote several main mechanisms such as oil swelling, viscosity reduction, extraction of oil, interfacial tension reduction, injectivity increase and solution gas drive, for more information see Appendix B- Section B.6.

2.4.1.1.2 Miscible CO_2-EOR Displacement

If the reservoir pressure is higher than the minimum miscibility pressure (MMP), then the injected CO_2 and the present oils will mix together forming a single-phase fluid (i.e. miscible

displacement will develop) [48, 82]. That is, CO_2 miscibility develops when the injected CO_2 becomes able to extract the light and intermediate components from the oil, forming a compositional transition zone that is able to miscibly displace oil in front of it and is able to be miscibly displaced by CO_2 behind it.

The concomitant reduction in the CO_2-oil interfacial tension due to miscibility can sustainability reduce the residual oil saturation by alleviating the impact of trapping forces (i.e. capillary forces), leading to much higher oil production than immiscible displacements [82, 101]. Theoretically, the concomitant reduction in the interfacial tension means no oil can be trapped as a residual phase due to capillary forces [102]. However, the extraction of oil components by CO_2, which leads to the forming of an oil bank, is opposed by the dispersion, which leads to the breakdown of the oil bank. The result is about 5-10% of oil saturation will be trapped as a residual oil phase [102].

Compared to immiscible flooding, CO_2 miscible injection is preferable for low permeability reservoir where water injectivity is low [104] and for low viscosity oils. Miscible CO_2 flooding is most likely to be used with oils having a viscosity in the range of 10 cp with an average of 1.5 cp, API larger than 30° with an average of about 36°, and density of about 0.8769 g/ml with an average of 0.845 g/l [101].

Miscible CO_2 flooding can produce between 5-20% of OOIP [48, 101]. For instance, CO_2 miscible flooding in the Permian Basin of West Texas increased oil recovery by over 8% [48]. The performance of the miscible displacements depends on many factors that include the formation temperature, oil contents, amount and identity of gasses mixed with the CO_2 (e.g. CH_4 and N_2), and mobility ratio [82, 101]. The main restriction for this technique is that miscible fluid will not contact all the oil in place. This depends on the rock characteristics and the fluid flow properties such as relative permeability and viscosity of the displacing and displaced fluids.

2.4.1.1.3 Factors Affecting CO_2-EOR

CO_2-EOR are influenced by many factors that include: (a) displacement efficiency which is largely affected by CO_2 fingering and capillary forces, (b) oil prices, (c) the capital cost of pipelines and recycling and compression facilities, (d) technology, and (e) the availability of CO_2 supply since most CO_2 suppliers are running at full scale [67, 94, 97].

The availability of relatively cheap, pure, and abundant supply of CO_2 is an essential factor that governs the widespread of the CO_2-EOR techniques [94]. The resources of CO_2 that are used in EOR processes can be divided into natural and human activities-related one, i.e. anthropogenic CO_2. The natural resources are responsible collectively for the production of more than 18 $MtCO_2$/year (980 MMcfd)[2] [95]. Most of the CO_2-EOR projects are in the USA due to the availability of low-cost natural CO_2 reservoirs that include the huge McElmo Dome, St. Johns Dome, and Jackson Dome natural CO_2 reservoirs in Colorado, Arizona, and Mississippi, respectively. However, due to the high cost of CO_2, less CO_2-EOR projects are available outside the United States. The largest CO_2-EOR project outside the USA is the Weyburn in southeastern Saskatchewan of Canada which uses around 1$MtCO_2$/year [48, 95]. However, in order to tackle the global warming problem, the anthropogenic CO_2 should be used in the EOR-CO_2 processes. The anthropogenic CO_2 comes from large-scale industrial applications such as power plants, steel industry, refineries, and petrochemical plants, etc. [95, 96, 105].

2.4.1.1.4 CO_2 Fingering

CO_2 is considered an ideal displacing fluid to improve microscopic sweep efficiency [96, 97]. Despite that, the overall sweep efficiency of CO_2 is quite poor, as shown in Figure 2-16, which is mainly due to the phenomena of CO_2 fingering. CO_2 fingering causes an early breakthrough and the bypass of the largest portion of the injected CO_2. CO_2 fingering occurs as a result of the growth of perturbations, in the CO_2-oil/water interface, with time [106], causing uneven front between the displacing and displaced fluids and hence affecting the stability of flow. After the inception of CO_2 fingering, the growth of fewer principal fingers will continue with the loss of small fingers due to the process of depression by the lateral pressure gradient both before and after the advancing front [107].

CO_2 fingering phenomenon is largely influenced by capillary, gravitational and viscous forces as well as mobility ratio. The existence of highly heterogeneous formations (e.g. highly permeable streaks or fractures) will enhance CO_2 fingering [82, 108]. The mobility ratio has an impact on the injection rate and pressure increase during CO_2 injection as well as on the distance the injected CO_2 and the replaced fluid (brine) can travel inside the formation [109]. Improving mobility control can have a positive impact on the sweep efficiency and

optimization of CO_2 storage [110]. Improving the mobility ratio can be achieved by: (I) reducing CO_2 relative permeability through WAG techniques, (II) increasing CO_2 viscosity through the addition of direct CO_2 thickeners such as fluoroacrylate-styrene copolymer polyFAst and silicone oil-toluene solutions (which are economically unviable), and (III) introducing CO_2-in brine foams [101]. In 1958, Bond and Holbrook recommended the use of foams for mobility control [111].

Capillary number (*Ca*) and viscosity ratio (*M*) can have a direct impact on CO_2 fingering by determining the type of flow regime. Increasing *Ca* reduces residual oil saturation as shown in Figure 2-17, thereby increasing ultimate oil recovery. Ca refers to the ratio of the viscous forces to capillary forces [112]; when the capillary number is in range of 10^{-4} to 10^{-5}, the capillary forces and viscous forces become equivalent [70]. *M* refers to the ratio of the viscosity of the displacing fluid to the viscosity of the displaced fluid. Increasing the contrast between the viscosity of the displacing and displaced fluid will result in a more unstable configuration front. The following formulas are used to define them:

$$Ca = \frac{\mu_2 V_2}{\sigma \, COS \, \theta} \tag{2-7}$$

$$M = \frac{\mu_2}{\mu_1} \tag{2-8}$$

where μ is the dynamic viscosity, σ the interfacial tension between the displaced and the displacing phases, *1* the subscript of the displaced phase, *2* the subscript of the displacing phase, Θ the contact angle between the two fluids and the surface, and V_2 the bulk velocity of the displacing fluid. The flowing equation is used to define the bulk velocity.

$$V_{bulk} = \frac{Q}{A \, \emptyset} \tag{2-9}$$

where *Q* is the volumetric injection rate, *A* the area of the frontal face of the core sample, and ϕ the core sample porosity [39].

Depending on *Ca* and *M*, flow regimes can be categorized into a stable flow, viscous fingering, and capillary fingering [39], as shown in Figure 2-18. Stable flow (large *Ca*, large *M)* takes place when the viscosity of the invading fluid is higher than the viscosity of the resident fluid. In this case, the dynamic interface between the invading and resident fluids will be nearly flat and transverse to the bulk flow with negligible distortions at the scale of some pores. Viscous fingering (large *Ca,* small *M)*, on the other hand, occurs when the displacing fluid is less

viscous than the displaced fluid [83, 113, 114]. The moving interface will be unstable and leads to the development of viscous fingering. In capillary fingering (Small *Ca,* all *M)*, the capillary forces (at the interface) dominate the flow. In capillary fingering, fluid can flow in any direction even perpendicular to the flow direction or enter new pores reversely, causing the entrapment of the wetting fluid [114].

Any change in underground conditions (pressure, temperature, and brine salinity [110]), CO_2 state, displacement velocity, fluid properties (e.g. density, viscosity, and interfacial tension), and system properties (geometry, permeability, and wettability) [27, 106, 107] will have a direct impact on the mobility ratio, capillary number, and capillary, gravity, and viscous forces, therefore on CO_2 fingering.

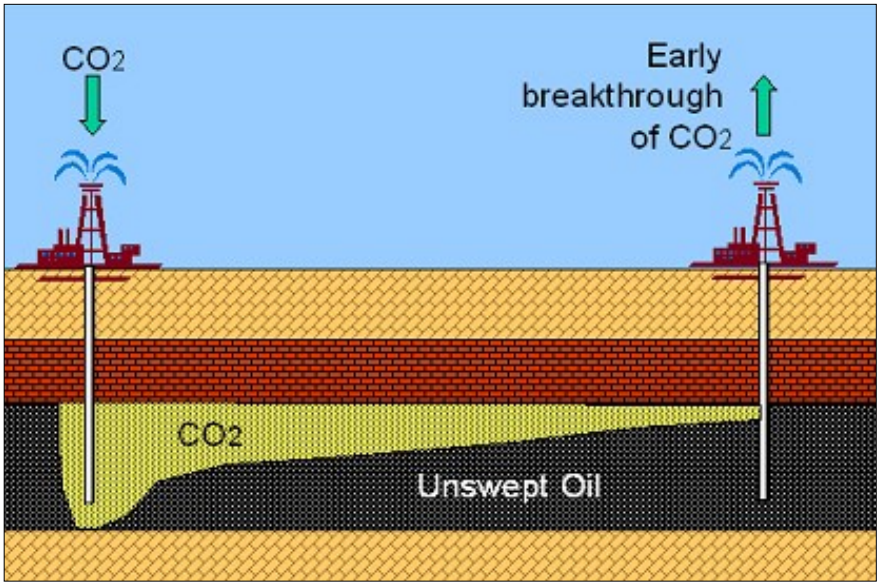

Figure 2-16: CO_2 sweep [115]

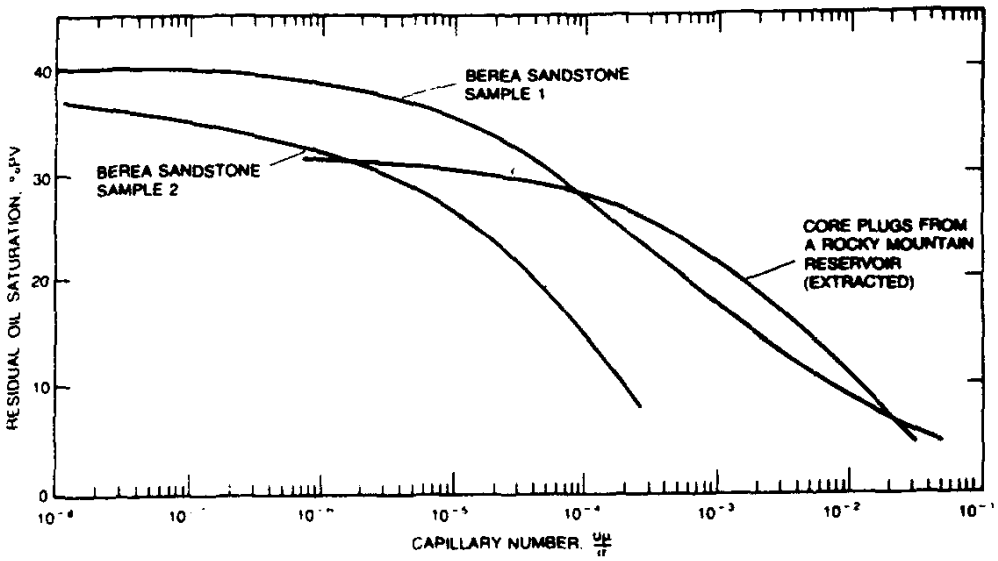

Figure 2-17: Oil saturation against the capillary number [82]

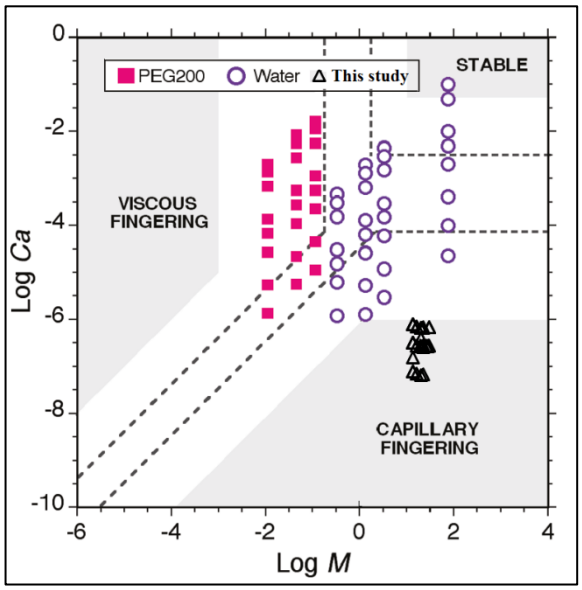

Figure 2-18: Stability diagram showing three flow regimes and the locations of the PEG200, water displacement, and the data of this study [114]

2.5 Immiscible Displacements Processes

Immiscible displacements are composed of two main processes: drainage and imbibition. These processes are largely governed by capillary forces that depend on the interfacial tension, contact angle, and pore diameter and geometry.

2.5.1 Drainage displacement

Drainage displacement refers to the process of displacing a wetting fluid (e.g. water) by a nonwetting fluid (e.g. CO_2) [116], as shown in Figure 2-19. Since it does not wet the core sample, the displacing fluid will invade the or enter a pore throat of inscribed r with contact angle Θ between the phases when a critical capillary pressure Pc value (i.e. a sufficient external pressure) is achieved [117], which occurs when the pressure of the non-wetting phase exceeds the pressure of the wetting phase. During drainage displacement, the non-wetting phase may only occupy pores and throats adjacent to pores already occupied with the nonwetting fluid. At every stage in this drainage process, the displacement of the wetting phase by the nonwetting phase occurs firstly through the pore or throats (large) that characterized by the lowest capillary pressure [118]. Nevertheless, in order for the flow of the nonwetting phase to occur, interconnected channels and intersections filled with this phase need to be present between the displaced meniscus and the existing end of the porous media. If the continuity is not achieved, the nonwetting fluid is trapped and the meniscus cannot advance [116].

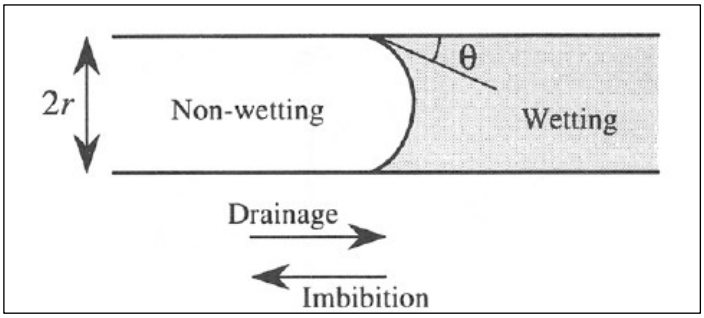

Figure 2-19: Piston-like displacement in a pore of radius r with contact angle Θ between the phases [118]

2.5.1.1 Previous Work on CO_2-Water (Brine) Drainage Displacements

Investigation of multiphase flow characteristics of CO_2-brine (water) displacements is of an essential importance for evaluating the capacity storage and the long-term fate of CO_2 in saline aquifers, fluid migration, injectivity in geologic formations [62, 119], and CO_2 EOR processes [48, 120]. The multiphase flow characterization of CO_2-water (brine) systems involves laboratory experiments [121], computational modelling [121-123], and field scale projects [62]. As CO_2 is injected into potential formation it can be either in the gaseous, liquid or supercritical state [19, 124-128]. Literature shows a scarce research has been allocated to multiphase flow characteristics of gaseous (G) [129-131] and liquid (L) CO_2-water

displacements [119, 132-135] compared to that allocated to supercritical (Sc) CO_2-brine (water) displacements [37, 132, 133, 136-148].

Literature shows that researchers have investigated different aspects of multiphase flow characteristics when gaseous CO_2 injection into water (brine) saturated porous systems. Islam et al. conducted GCO_2-water experiments at 1 bar and 25 °C using a vertical Hele-Shaw cell filled with micro-beads to investigate the crossover zone from capillary to viscous to fracture fingering. They found that all the three fingering patterns can occur in the cell but at different heights [129]. Jiang et al. performed both immiscible and miscible drainage GCO_2-water displacements inside a packed bed filled with quartz glass beads to have a better understanding of the two-phase flow characteristics inside porous media. The experiments were conducted at CO_2 injection rates ranging from 0.01 to 3 ml/min, pressure of 60 bar and temperature of 24.85 °C. They observed that: (I) at low CO_2 injection rates, the CO_2 dissolution increases; (II) the increase in glass beads diameter (i.e. higher permeability) leads to a decrease in the capillary forces [130]. Yu et al. conducted immiscible drainage GCO_2-water displacements at 60 bar and 24.85 °C inside a packed bed of glass beads (0.2 mm diameter) to study the impact of the capillary number on displacement efficiency. They noticed that the increase in capillary number, when it is between 10^{-11} to 10^{-10}, results in a sharp reduction in the residual water saturation due to increasing the impact of the viscous forces [131].

In summary, the existing GCO_2-water experiments were designed to investigate the crossover zone of fingering patterns, impact of CO_2 injection rates and permeability on two-phase flow characteristics, and impact of the capillary number on displacement efficiency [129-131]. However, the literature shows no detailed investigated have been conducted to explore the impact of pressure, temperature, and injection rate on the differential pressure, displacement efficiency, and endpoint effective and relative permeabilities when gaseous CO_2 is injected to displace water from a sandstone core sample.

On the other hand, researchers investigated the multiphase characteristics of liquid (L) CO_2-water/brine displacements in various core sample such as synthetic P3C alumina and Berea sandstone core sample, packed bed filled with glass beads, Rothbach sandstone core sample, and Triassic sandstone core sample [119, 132, 133, 135]. Levine et al. examined the flow-

properties of LCO_2-water/brine (1%, and 5% NaCl)-displacements in synthetic (synthetic P3C alumina) ceramic (CoorsTek^{TM}) and natural porous media (Berea sandstone core sample) at 100 bar and 20 °C by measuring the differential pressure against various flowrates. They noticed that drainage endpoint relative permeability of LCO_2 is between 0.34 and 0.44 [119]. Song et al. investigated the multiphase properties of LCO_2-water displacements, under immiscible conditions of 60 bar and 21.85 °C, in a packed bed filled with glass beads. They noticed that: (I) in general, the efficiency of water displacement is dependent on the permeability, displacement pattern, and CO_2 injection rate, (II) low permeability formations leads to an increase in the residual water saturation, and (III) CO_2 fingering or channelling phenomena occur even in liquid CO_2 displacements [132]. Alemu et al. injected liquid CO_2 into a brine-saturated Rothbach sandstone core sample at 100 bar and 20 °C to improve the then current understanding of CO_2 and brine behaviour. After 20 pore volume of CO_2 injection, the endpoint residual CO_2 saturation was 0.53; the amount and distribution of fluids in the core was dependent on the core sample properties [133]. Manceau et al. investigated the two-phase properties of LCO_2-water system with the emphasis on the impact of potential mineral changes. In these experiments, liquid CO_2 was injected into a water-saturated Triassic sandstone core sample at 90 bar and 28 °C; the Triassic core sample contains small amounts of carbonate minerals. They observed that liquid CO_2 injection caused a mineral dissolution, an increase in porosity and permeability, and a reduction in the capillary pressure. The change in permeability was linked to wettability alteration due to the dissolution of the less-wetting minerals [135].

Zhang et al. investigated the impact of pore-scale heterogeneity on the two-phase characteristics of LCO_2-water displacement. During these displacements, LCO_2 was injected into a dual permeability pore network model at 90 bar and 22 ± 1 °C. They noticed that at low injection rate: (a) the displacement is unstable, and (b) LCO_2 displaces water only from high permeability zones. However, as the CO_2 injection rate increased, (a) the displacement mechanism shifted from the capillary to viscous fingering, and (b) the liquid CO_2 displaced water from the lower permeability zones, too [134].

In summary, researchers have conducted liquid (L) CO_2-water displacements to explore multiphase flow characteristics in different porous media by measuring endpoint relative permeability [119], displacement efficiency and CO_2 fingering [132], endpoint residual CO_2

saturation [133], mineral dissolution, porosity and permeability, and capillary pressure [135], and pore-scale heterogeneity [134]. However, despite their high importance, these investigations overlooked the impact of pressure, temperature, salinity and injection rate on the differential pressure profile, production profile, displacement efficiency, and endpoint effective and relative permeabilities when liquid CO_2 is injected into a water/brine-saturated sandstone core sample.

Literature shows that many experimental investigations have been allocated to supercritical (Sc) CO_2-water displacements in comparison to that conducted on gaseous and liquid CO_2-water displacements. Saeedi et al. performed drainage $ScCO_2$-brine (20000 ppm NaCl) core floodings using a group of sandstone core samples at a pressure of 177.9 bar and a constant temperature of 83 °C to investigate fluid flow characteristics, focusing on the impact of cyclic CO_2-brine flooding. They found: (a) a high endpoint residual brine saturation, which was associated with the high mobility ratio and low interfacial tension, and (b) a strong influence of the CO_2 flowrate on the endpoint residual brine saturation. They observed also that cyclic CO_2-brine flooding can lead to: (a) a moderate to strong impact on the differential pressure and a result on the endpoint relative permeability, (b) a decrease in injectivity, and (c) an irreversible plastic deformation in the storage medium due to dissolution of some minerals present in the cement bounding the rock grains together [37].

Berg et al. conducted unsteady state drainage displacements on a homogenous Berea sandstone core sample to study the displacement process and mass transfer between CO_2 and brine. The experiments were conducted at 100 bar and 45 °C by using saturated and unsaturated CO_2 as well as decane to displace the brine-saturated core sample. They noticed a difference between the relative permeabilities of the CO_2-brine system and decane-brine system. They attributed that to the difference in wettability since the CO_2-brine system is more water-wet than the decane-brine system. They observed also that water dissolving in CO_2 leads to an evaporation near the inlet face while CO_2 dissolving in water leads to diminishing the displacement of brine by CO_2 [136].

Chang et al, Ott et al. and Cao et al. investigated $ScCO_2$-water/brine primary drainage displacements in low-permeability sandstone formations [138], dual-porosity limestone [146], and high-pressure micro model [147] under different pressure and temperature conditions. Chang et al. performed drainage $ScCO_2$-deionised water (DIW) displacements at

pressures larger than 80 bar and a constant temperature of 40 °C to investigate the operation of CO_2 injection into low-permeability sandstone formations. They used two low permeability sandstone core samples from the Shenhua Group CCS site in the Erdos Basin in China. For both core plugs, the residual water saturation at the end of the experiments was around 0.52. This high residual saturation was related to the high CO_2-water viscosity contrast and the non-uniformity of displacements, which was linked to the impact of sub-core heterogeneity. The estimated relative permeability varied from 0.13 to 0.23 [138]. Ott et al. investigated $ScCO_2$-brine primary drainage displacements in a dual-porosity limestone. These displacements were conducted at 100 bar and 50 °C into a brine-saturated Estaillades limestone core sample, which represents heterogeneous and dual-porosity carbonate rocks. The results showed lower fluid-phase mobilities, i.e. lower relative permeability, in larger-scale heterogeneity formations [146]. Cao et al. conducted experimental and numerical investigations on the pore-scale displacement phenomenon during the injection of $ScCO_2$ into brine saturated reservoirs. They performed drainage $ScCO_2$-brine (0-5 M NaCl) displacements in a high-pressure micromodel at a pressure of 80 bar and temperature of 45 °C. They found no change in the distribution of $ScCO_2$ and brine when $ScCO_2$ percolations through the porous medium are achieved. They observed also that: (I) increasing CO_2 injection rate and capillary number enhance brine displacement; (II) brine salinity hinders the displacement through the alteration of interfacial contact properties and displacement patterns; (III) a better injection efficiency and capillary trapping capacity can be obtained in reservoirs with more widely-distributed pore sizes [147].

Herring et al. investigated the volume and topology of supercritical CO_2 on a pore scale. They performed drainage $ScCO_2$-brine displacements on a Bentheimer sandstone core under pressure and temperature conditions of 83 bar and 37.5 °C, respectively. They noticed that after the normalization with the interfacial tension, the capillary pressure-saturation curves of $ScCO_2$-brine and ambient-brine curves are overlaid. Due to their use of a hydrophilic membrane at the brine outlet, they obtained a low endpoint drainage brine saturation of around 9%. The noticed that capillary fingering invasion of $ScCO_2$ occurs when the mobility ratio (M) is 0.03 and the capillary number is $10^{-8.6}$ [141].

Wang et al. investigated the impact of many parameters on the CO_2 plume transport and displacement efficiency. The parameters investigated were: the capillary pressure, injection rate, and heterogeneity and anisotropy of permeability. They conducted drainage $ScCO_2$-

water displacements in a packed bed of glass beads under a pressure of 80 bar and a temperature of 40 °C. They observed that: (I) both heterogeneity and anisotropy of permeability can improve the CO_2 displacement efficiency, (II) the capillary pressure can reduce the displacement efficiency by inhibiting pore water movement, (III) a direct relationship between the final average CO_2 saturation and CO_2 injection rate; increasing injection rate enhanced the final CO_2 saturation [142].

Pentland et al. conducted drainage $ScCO_2$-brine immiscible displacements on a Berea core sample to study the immiscible displacement and capillary trapping by measuring the residual non-wetting saturation and the contact angle of the $ScCO_2$. The displacement conditions were performed at 90 bar and 69.85 °C using equilibrated supercritical CO_2 and brine with different salinities, 1 wt. % KCl and 5 wt. % NaCl. They obtained a residual saturation of around 0.37. They suggested that $ScCO_2$ is a non-wetting phase in the presence of water. They argued that if the CO_2 had wet the core sample, then residual saturation obtained would be much less as CO_2 would be displaced through a continues layer of water [143].

Perrin and Benson, Shi et al., and Okabe et al. investigated the impact of sub core-scale heterogeneity on $ScCO_2$ core flooding with steady and unsteady state CO_2-brine displacements [144, 145, 149]. Perrin and Benson conducted steady state CO_2-brine displacements at 124.1 bar and 50 °C using two reservoir core samples (form CO_2CRC-Otway project, Victoria, South-West Australia) with different permeability and porosity properties. They noticed that sub-core scale heterogeneity has a significant impact on both sweep efficiency and spatial distribution of CO_2. They obtained a good correlation between the core sample porosity distribution and saturation distribution; they noticed that high and low porosity regions result in high and low CO_2 saturations, respectively [144]. Shi et al. performed experimental and numerical investigations of $ScCO_2$-brine drainage displacements in a heterogeneous Tako sandstone under a pressure of 100 bar and a temperature of 40 °C. They noticed that: (I) sub-core porosity heterogeneity has a high impact on CO_2 migration, (II) the increase in CO_2 injection reduces the impact of porosity heterogeneity on the mean CO_2 saturation profiles along the core, and (III) the numerical simulation has shown that the immiscible displacement could not be adequately described by a single capillary pressure model or a 3D model [145]. Okabe et al. conducted $ScCO_2$-brine (15 wt. % NaCl) core-flood experiments on a carbonate core sample from the Middle East at

a pressure of around 97.9 bar and an experimental temperature of 40 °C. The data revealed a strong influence of the core-heterogeneity on the CO_2 saturation [149].

Ott et al. investigated the formation dry out issue due to the injection of dry or under saturated $ScCO_2$ into sandstone formations. The drainage displacements were conducted in a Berea sandstone sample using dry $ScCO_2$ and synthetic brine (20 wt. % and 2 wt. % CsCl) at 100 bar and 45 °C. They observed that because of the capillary driven back-flow, the local salt accumulation was higher than the amount of salt initially dissolved in the same brine volume. The results showed an increase in the effective CO_2 permeability despite the significant reduction in the absolute CO_2 permeability owing to the high local salt accumulation [148].

Other researchers have conducted $ScCO_2$-brine displacements to study the CO_2-brine rock interactions under different pressure and temperature conditions [150-153]. Rosenbauer et al. investigated the $ScCO_2$-brine-rock reactions, using plagioclase-rich arkosic sandstone and limestone core samples, under pressures of 100-600 bar and temperature of 25-120 °C. They noticed:(I) compositional, mineralogical, and porosity changes within the limestone core sample, and (II) dependency between the reactions and the initial brine composition, especially the content of the dissolved sulfate [150]. Zhao et al. studied the $ScCO_2$-brine-rock interactions using a sample from Xinghe reservoir- the centre of Ordos Basin. In this study, four experiments were performed for 120 hours at a reaction pressure of 150, 200, 250, and 200 bar and a reaction temperature of 50, 50, 50, 100 °C, in sequence. The data revealed that the strongest mineral corrosion occurred in carbonate minerals, and followed by feldspar; quartz, on the other hand, showed the weakest corrosion. The increase in pressure and temperature intensified the rock corrosion and precipitation, decreased the permeability gradually, and increased the displacement pressure [151]. Wang et al. investigated the reactions between caprocks powder from the Qinshui Basin in China with $ScCO_2$ and brine as well as CO_2-free brine at 150 bar and 160 °C. They observed a change in the mineral compositions via dissolution of silicate minerals in lithic sandstone tests and a precipitation of carbonate minerals in calcareous mudstone experiments [152]. Shiraki and Dunn investigated the $ScCO_2$-brine-rock interactions in a sandstone rock sample, from Tensleep reservoirs in northern Wyoming-USA, under representative reservoir conditions (166 bar and 80 °C). The brines used were (Ca, Mg, Na) SO_4-NaCl with different salinities. They observed a

dissolution of dolomite, an alteration of feldspar to kaolinite, and a precipitation or dissolution of anhydrite [153].

In summary, literature shows that researchers have performed ScCO_2-brine (water) displacements to study fluid flow characteristics with the emphasis on the effect of cyclic CO_2-brine flooding [37], displacement process and mass transfer between CO_2 and brine [136], operation of CO_2 injection into low-permeability sandstone formations, dual-porosity limestone, and high pressure micro model [138, 146, 147], volume and topology of supercritical CO_2 on a pore-scale [141], CO_2 transport and displacement efficiency [142], immiscible displacement and capillary trapping [143], impact of core-heterogeneity on supercritical CO_2 core flooding [144, 145, 149], formation dry out issue [148], and CO_2-brine rock interactions [150-153]. Nevertheless, no detailed ScCO_2-water experiments have been conducted to explore the differential pressure profile, displacement efficiency, production profile, and endpoint effective and relative permeabilities as a function of pressure, temperature, and injection rate.

It can be seen from the literature that very few researchers have conducted CO_2-water (brine) drainage displacements under both supercritical and liquid phase conditions [119, 132, 154]. Levine et al. [119] examined the flow-properties by conducting liquid CO_2-water (1%, and 5% NaCl) core floodings in a Berea sandstone core sample at 100 bar and 20 °C, and supercritical CO_2-water (5% NaCl) displacements in a P3C alumina ceramic core sample at 100 bar and 50 °C. They noticed that drainage endpoint relative permeability of CO_2 displacing brine ranged between 0.34 and 0.44 [119]. Song et al. examined the multiphase properties of CO_2-water coreflooding in a packed bed filled with glass beads by performing immiscible liquid CO_2-water displacements at 60 bar and 21.85 °C, and miscible supercritical CO_2-water displacements at 80 bar and 39.85 °C. It should be noted that these liquid CO_2-immiscible displacements were stated above but mentioned here for comparison. They noticed from the supercritical CO_2-miscible displacements (observations of the liquid CO_2-water displacements are presented above) that: (I) miscible displacement is more efficient than immiscible displacement; (II) increasing CO_2 flowrate results in high residual water saturation and more uniform CO_2 front and CO_2 distribution [132]. Pini et al. performed both liquid and supercritical CO_2-water displacements on two sandstone core samples (a Barea core sample and a Middle Eastern core sample) at a pressure of 90 bar and temperatures of 25 and 50 °C by exploring the sub-core scale capillary heterogeneity and operational

conditions impact on contact angle. The data showed a key role for the sub-core scale capillary heterogeneity on the saturation distribution during multiphase flow processes. The data showed also that for the pressures ranging from 200 to 400 bar, the contact angle at 25 °C was higher than that at 50 °C. This was linked to the higher solubility of CO_2 into water phase at 25 °C, which results in rising water acidity and reducing the hydrophilic characteristics of the solid surface [154].

Other researchers have investigated the injection of CO_2 inside water (brine) saturated core samples under supercritical and gaseous conditions [52, 155]. Riazi et al. investigated the mechanism of CO_2 injection into hydrocarbon reservoirs and water-bearing formations. The experiments were conducted in a high-pressure transparent porous medium. They performed gaseous and supercritical displacements under different pressures (41.37 and 137.9 bar) and a constant temperature (37.77 °C). They observed that: (I) in comparison to $ScCO_2$ displacement, the breakthrough time of gaseous CO_2 happened faster, adversely affecting the CO_2 displacement performance, and (II) the micromodel test simulating CO_2 injection showed a faster CO_2 breakthrough into depleted oil reservoirs than aquifers, thereby less sequestration capacity was expected [52]. Perrin et al. examined the impact of pressure depressurization, from 124 to 69 bar, on the formation of exsolved CO_2 by conducting $ScCO_2$-water displacements at 124.11 bar and 50 °C as well as performing GCO_2-water displacement at 60.6 and 68.95 bar and 50 °C. They noticed that the initial reduction of pressure formed a separated phase of exsolved CO_2, which was fairly uniformly distributed along the core sample [155].

In conclusion, based on the aforementioned literature review, there has been no detailed study which was conducted under gaseous, liquid, and supercritical conditions simultaneously to investigate the CO_2 phase impact on the multiphase flow characteristics.

2.5.1.2 Previous Work on CO_2-Oil Drainage Displacements

Since CO_2 has been in use for several decades, extensive laboratory studies [156, 157], numerical simulations, and field applications of CO_2 flooding have been conducted in various light, medium, [158] and heavy oil reservoirs [159].

However, the literature review revealed that CO_2–oil displacements were conducted either under gaseous, liquid, or supercritical CO_2 conditions except for a few experiments that were

performed under more than one CO_2 state. Sankur [160] performed reservoir condition-gaseous displacements of oil by CO_2 and refinery gas for the Wilmington Tar zone CO_2 injection project. Their results showed that the injection of CO_2 enhances the recovery to a greater extent than the injection of the refinery gas for continuous or low water alternating gas (WAG). Moradi [161] conducted a numerical simulation to investigate the impact of liquid CO_2 injection on oil recovery. Liquid CO_2 injection yielded 14.79% oil recovery, which was higher than water flooding and natural depletion by around 3.9% and 8.59%, respectively. Arshad [162] performed supercritical CO_2 displacements to study the performance of CO_2 miscible flooding in tight oil reservoirs. The average oil recovery ranged from 87 to 96%. Chung [163] performed supercritical CO_2 core flooding experiments to examine the technical feasibility of the use of CO_2 flooding to enhance the recovery of viscous oil under immiscible displacements conditions. They found that CO_2 injection resulted in a higher recovery (66% of original oil in place (OOIP)) in comparison to waterflooding (44% of OOIP). In addition, the CO_2-alternate-brine injection significantly delayed the breakthrough of gas, produced slightly more oil and was more efficient in CO_2 utilization than continuous injection [163]. Huang [164] performed continuous immiscible supercritical CO_2 flooding, at 90 °F (32.2 °C) and 1250 psi (86.2 bar), into Texas oil (36° API) saturated watered-out cores to determine the oil recovery efficiency and improve the understanding of oil recovery mechanisms, especially in relation to phase behaviour. The data showed an oil recovery of 69% and 66% of residual oil from a 6 ft Berea and 20 ft sand-packed core sample, respectively. They attributed the oil recovery mainly to the CO_2 swelling and CO_2 extraction of oil.

For the experiments that were conducted under more than one CO_2 state, Wang [158] carried out both gaseous and liquid CO_2 oil recovery displacements under immiscible and miscible conditions to examine oil recovery and permeability reduction in a tight sandstone reservoir. They noticed that during immiscible flooding, the oil recovery was higher when the fluid pressure was between the onset pressure of asphaltene precipitation and the MMP; nonetheless, the reduction of oil effective permeability was greater at higher fluid pressure. Cao [165] conducted both immiscible and miscible CO_2 floodings into light crude oil saturated tight sandstone core plugs at gaseous and supercritical CO_2 conditions. The oil recovery increased monotonically as pressure increased during the immiscible flooding. Liu [166] conducted gaseous and supercritical near-miscible CO_2 floodings to examine the displacement front characteristics. The supercritical CO_2 displacements gave higher oil

recovery in comparison to gaseous displacements. Lashkarbolooki [167] and Bayat [168] investigated the efficiency of recovery during the injection of supercritical CO_2 and supercritical N_2 into a live crude oil. The core-flood experiments showed that supercritical CO_2 injection could result in a higher recovery (15.8% of OOIP) compared with supercritical N_2 injection (8.7% of OOIP).

In summary, the literature review shows no detailed displacements that were conducted to investigate the impact of fluid pressure, temperature, injection rate on the differential pressure, displacement efficiency, and endpoint effective and relative permeabilities as a function of the CO_2 state.

2.5.2 Imbibition displacement

Imbibition is the opposite of a drainage process [116]. It occurs when a wetting phase (e.g. water) dislodges a nonwetting phase (e.g. CO_2). Since it wets the invaded porous medium, the displacing fluid will imbibe spontaneously [117, 118], moving along the corners and roughness. During an imbibition process, the wetting phase enters the smaller pores and throat (with the highest threshold capillary pressure) more easily than larger pores [118]. The wetting phase exists through porous medium in the form of connected thin films or layers. This helps the wetting phase to enter even inside the smallest pores within the porous medium and displace the non-wetting phase. Generally, imbibition can occur either spontaneously or under an external force.

The primary (i.e. spontaneous) imbibition will happen when the pressures at both ends of a water-wet capillary pore are the same [169]. The main driving mechanism for spontaneous imbibition is the capillary forces [170, 171], which depend on the interfacial tension, pore size distribution, and wetting status [169]. Due to its direct impact influence on capillary forces, the wetting status of the reservoir will significantly affect the oil recovery by spontaneous imbibition. In a mixed or oil-wet reservoir, the capillary forces are weak or work in an opposite direction to the viscous forces [35] and, therefore, the water needs to be forced into the sample to displace oil [172]. Changing system's wettability to an effective water wetting status will result in reversing the direction of capillary forces, leading to a strong spontaneous imbibition of the wetting phase into the small pores of the oil matrix [75], thereby expelling oil out of it [169, 173]. Surfactants are commonly added to the injected water to reduce the oil-water interfacial tension and change the wettability of the

rock surface to a more water wet, thereby enhancing water imbibition into the oil containing matrix, and hence increasing oil recovery [35, 169, 171]. If the contact angle between the aqueous phases and pore space is less than 90°, the spontaneous imbibition will start, otherwise, a forced imbibition is required [169].

The forced imbibition occurs when there is a difference between the pressures at both ends of the capillary. Thus, for the wetting phase to displace the nonwetting phase from the capillary tube or a porous medium, an external force (differential pressure) needs to be applied. The forced imbibition is much faster than the spontaneous imbibition, especially when the external differential pressure is sufficiently high to overcome the capillary entry pressure of the core sample [169]. Nevertheless, even if the applied differential pressure is less than the entry pressure, the penetration of the meniscus inside the porous medium is possible by means of contact angle alteration, e.g. using surfactants [35, 169]. Normally, oil displacement by water injection or surfactant solutions occurs under external differential pressure, i.e. forced imbibition [35, 169, 171].

2.5.2.1 Mechanisms of Imbibition processes during Immiscible Displacement

The two main mechanisms that govern the displacement of immiscible fluids in an imbibition process are snap-off or choke off and piston-like mode.

2.5.2.1.1 Snap-off or Choke off

Snap-off occurs when fluid interface ruptures because of the reduction in the capillary pressure. The capillary reduction causes an increase in the radius of the curvature of the interface up to the point of instability [118, 174], as shown in Figure 2-20. When instability is reached, the meniscus no longer touches the wall and hence fluid interface rupture occurs. However, prior to its rupture, the fluid-fluid interface is stable and can advance and retreat in response to any decrease or increase in the capillary pressure [174]. During an imbibition displacement, the wetting phase forms an interface of a collar shape in pore throats. These collars have elements of negative and positive curvatures, i.e. the radii of curvature lay on both sides of an interface in selloidal or saddle-shaped, as shown in Figure 2-21. In addition to the selloidal shaped interface, a convex interface (only positive elements) can occur, as shown in Figure 2-22 [174].

The sudden invasion of a pore throat due to the snap off phenomenon results in the discontinuity of the non-wetting phase. If the non-wetting phase is isolated in the pore body and surrounded completely by the wetting phase, then its further displacement becomes not possible. These trapped or isolated blobs are associated with the residual saturation. The pore geometry and topology have a large influence on the shapes of the non-wetting phase blobs forming residual saturations. The size of these blobs, which can range over several orders of magnitudes, govern the magnitude of the capillary forces required for their displacement while the volume and surface of the blobs affect the mass transfer characteristics.

The pore geometry determines the position and shape of the thin wetting films that are formed during an imbibition process. The pore geometry can be composed of smooth circular capillaries and/or rectangular capillaries, as shown in Figure 2-23. For the former one, the wetting fluid forms a circular thin film that separates the non-wetting phase from the solid surface over the entire surface. For the latter one, the wetting fluid occupies the corners of the rectangular in addition to the thin films elsewhere. As suggested by Yu, a cross-section model is more realistic than a cylindrical tube one as sediments rock typically are formed of irregular surfaces [175]. For a throat of square cross-section and inscribed, *r*, the capillary pressure, *Pc,* at which the snap off phenomenon occurs is as follows [118]:

$$P_c = \frac{\sigma(cos\theta - sin\theta)}{r} \quad (2\text{-}10)$$

The amount of the non-wetting phase trapped due to the snap-off is determined by the aspect ratio (pore-to-throat effective diameter ratio) of the pore channels, interfacial tension of the fluids exist in the pores [37] and wettability of the system [176]. The reduction in the interfacial area within a pore causes the interface to become semi-rigid, thereby inhibiting the trapping of fluid by snap-off [177]. Decreasing the interfacial tension causes a significant reduction in the snap-off trapping mechanism, leading to a lower level of residual trapped CO_2 [37]. Increasing the water-wetness of the systems enhances the fluid snap-off and leads to a high residual saturation of the non-wetting phase [176]. Changing the pressure, temperature, salinity, CO_2 state, fluid and core sample properties will have a direct impact on the amount of fluids trapped due to the snap-off phenomenon.

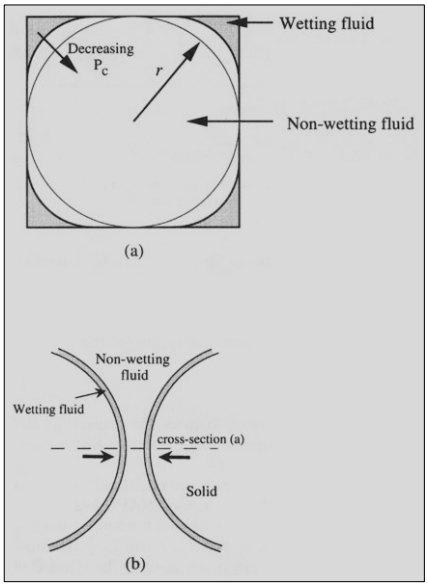

Figure 2-20: A schematic of snap-off in a throat with a square cross-section. (a) The cross-section of the throat, where r is the maximum inscribed radius of the square. During imbibition, the capillary pressure decreases, increasing the interfacial radius of curvature. The wetting fluid swells in the corners of the throat until the entire throat fills with the wetting fluid. Snap-off occurs in the smallest constriction in the throat, denoted by the arrows in (b) [174].

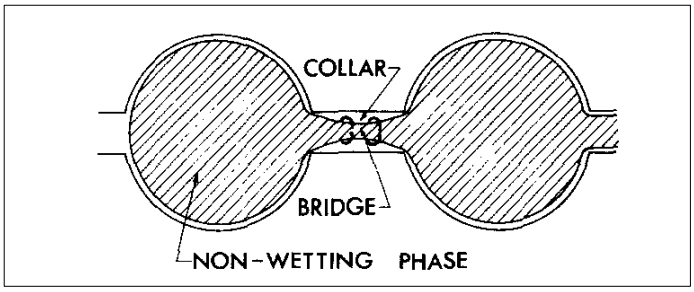

Figure 2-21: Two pores with connecting throat to illustrate nonwetting phase bridge (shaded) and wetting phase collar (plain) in throat. Interface is selloidal. The thickness of the continuous wetting film is greatly exaggerated [174].

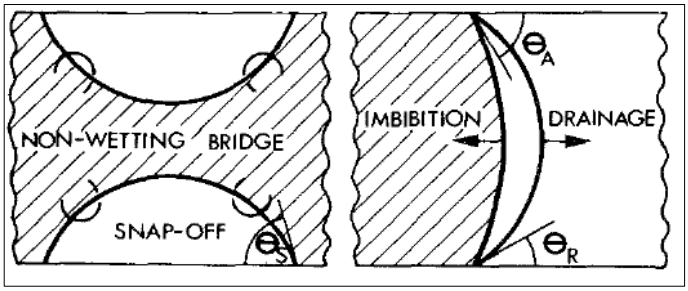

Figure 2-22: Selloidal interface (left) and convex interfaces (right) in cylindrical tube with horizontal axis. Two convex interfaces indicate the advancing and retreading positions with contact angle hysteresis (ΘA > ΘR) (Piston-type motion) [174]

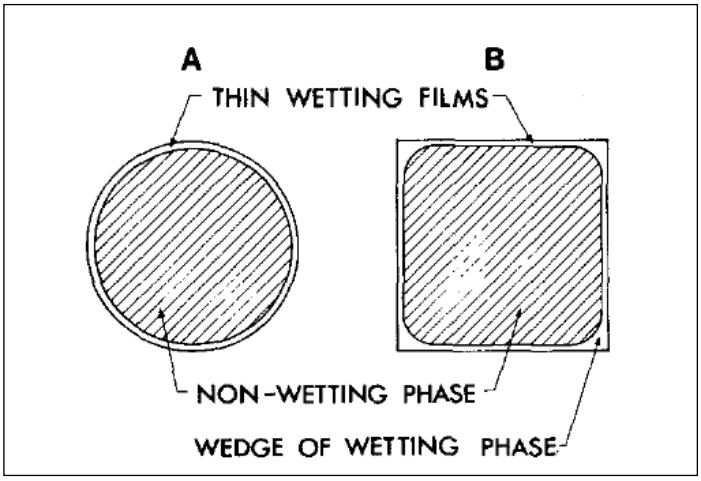

Figure 2-23: Conduits of circular and square cross-section to illustrate positions of thin films and wedges of wetting phase [175]

2.5.2.1.2 Piston-like Motion

Piston-like invasion refers to the advance or retreat of a convex interface in a pore body or throat [178] in a piston-like movement, as shown in Figure 2-19. For this process to happen, a complete filling of the nearby pore body or throat with the wetting phase is needed. The critical pressure for piston-like invasion is governed by the number of adjacent throats that completely filled with the wetting phase [118].

At high flowrates and low aspect ratio systems, the piston-like effects dominant the two-phase flow in imbibition displacements while at low flowrates and high aspect ratio systems the thin films or the interfacial displacements effects govern the two-phase flow. Thus, the viscous forces prevail at high flowrates while the capillary forces dominant at low flowrates. Dong et al. observed that increasing the flowrate changes the oil-water interface from a very gradual one to a piston-like front. However, increasing the oil-water viscosity ratio from 0.2 to 0.5 at very low flowrate changes the oil-water interface profile from a near piston-like front to a very gradual one [35, 179]. Due to the direct impact of the CO_2 phase, pressure, temperature, injection rate, and salinity on capillary and viscous forces, they, in turn, will have a direct impact on the piston-like motion.

2.5.2.2 Previous Work on Water-CO_2 Imbibition Displacements

Despite its widespread and high practical importance, the literature shows only scare experimental research that has been done on water-CO_2 imbibition displacements. Saeedi et al. performed unsteady-state imbibition CO_2-brine (20,000 ppm NaCl) displacements in a

group of sandstone core samples at supercritical CO_2 conditions of 177.9 bar and 83 °C. They obtained a low residual CO_2 saturation which was attributed to the low interfacial tension (IFT) of the supercritical CO_2-water system. They suggested that the low IFT may result in reducing the impact of the snap-off mechanism as a main trapping mechanism during CO_2 geo-sequestration. They noticed also that high permeability formation would be less preferable for CO_2 storage process despite allowing high CO_2 injectivity. This is because high permeability formation can cause extremely low levels of CO_2 entrapment in the form of residual saturation [37].

Berg et al. conducted unsteady-state imbibition displacements in a homogenous Berea sandstone core sample under supercritical conditions of 100 bar and 45 °C. The displacements were conducted by injecting unsaturated brine into a rock filled with mutually saturated CO_2 and brine at near-residual CO_2 saturation. They observed: (a) a dissolution of the trapped CO_2 during the displacement of the CO_2-saturated brine by the unsaturated brine, and (b) a transition from residual trapping to solubility trapping [136]. Chang et al. performed unsteady-state imbibition supercritical CO_2-water displacements at pressures larger than 80 bar and a constant temperature of 40 °C. They used two low permeability sandstone core samples from the Shenhua Group CCS site in the Erdos Basin in China. They observed a non-equilibrium CO_2 dissolution during water-flood displacements. This non-equilibrium CO_2 dissolution was attributed to the impact of sub-core heterogeneity, which caused a non-uniform distribution of water and CO_2. They observed also that CO_2 dissolution enhanced displacement by mobilizing additional free-phase CO_2 and increasing relative permeability. The amount of the dissolved CO_2 was 6-7% of the total mass of CO_2 initially present in the cores before the experiments. The estimated endpoint CO_2 saturation ranged from 0.1 to 0.17. Increasing the water injection rate displaced more free-phase CO_2 out of the cores [138].

Alemu et al. performed unsteady-state imbibition displacements in a Rothbach sandstone core sample under liquid CO_2 conditions of 100 bar and 20 °C. After injecting 10 pore volumes of water to displace the liquid CO_2, the water saturation reached 100% [133]. Shi et al. conducted unsteady-state imbibition supercritical CO_2-brine displacements and numerical simulation. The displacements were conducted in a heterogeneous Tako sandstone under pressure and temperature conditions of 100 bar and 40 °C. They noticed a high impact of the sub-core porosity heterogeneity on the CO_2 migration pattern at low injection rate (0.1

ml/min). Increasing the injection rate to 3 ml/min diminished the impact of the porosity heterogeneity on the mean CO_2 saturation profiles [145].

In summary, the literature review shows that water/brine-CO_2 imbibition displacements were conducted to investigate the fluid flow characteristics [37], displacement process and mass transfer between CO_2 and brine [136], operation of CO_2 injection into low-permeability sandstone formations [138], endpoint residual CO_2 saturation [133], and impact of sub-core heterogeneity on supercritical CO_2 core flooding [145]. It can be seen from this literature that of these five reported imbibition displacements, four experiments were conducted under supercritical conditions [37, 136, 138, 145] and one under liquid conditions [133], with no imbibition displacements were conducted at gaseous conditions. Literature shows no imbibition experiments have been performed under gaseous, liquid, and supercritical CO_2 conditions to investigate the impact of fluid pressure, temperature, and salinity on two-phase flow characteristics as a function the CO_2 phase.

2.6 References

1. Farokhpoor R, Bjørkvik BJ, Lindeberg E, Torsæter O. CO_2 wettability behavior during CO_2 sequestration in saline aquifer-an experimental study on minerals representing sandstone and carbonate. Energy Procedia. 2013;37:5339-51.

2. Nikolov A, Wasan D. Wetting–dewetting films: The role of structural forces. Advances in colloid and interface science. 2014;206:207-21.

3. Wasan D, Nikolov A, Kondiparty K. The wetting and spreading of nanofluids on solids: Role of the structural disjoining pressure. Current Opinion in Colloid & Interface Science. 2011;16(4):344-9.

4. Gambaryan-Roisman T. Liquids on porous layers: wetting, imbibition and transport processes. Current Opinion in Colloid & Interface Science. 2014;19(4):320-35.

5. Vizika O, Rosenberg E, Kalaydjian F. Study of wettability and spreading impact in three-phase gas injection by cryo-scanning electron microscopy. JPSE. 1998;20(3):189-202.

6. Boinovich L, Emelyanenko A. Wetting and surface forces. Advances in colloid and interface science. 2011;165(2):60-9.

7. Drelich J, Miller JD, Good RJ. The effect of drop (bubble) size on advancing and receding contact angles for heterogeneous and rough solid surfaces as observed with sessile-drop and captive-bubble techniques. Journal of Colloid and Interface Science. 1996;179(1):37-50.

8. Bonn D, Eggers J, Indekeu J, Meunier J, Rolley E. Wetting and spreading. Reviews of modern physics. 2009;81(2):739.

9. Wikipedia.org. Lotus effect 2017 [Water on the surface of a lotus leaf]. Available from: https://en.wikipedia.org/wiki/Lotus_effect.

10. Yang D, Gu Y, Tontiwachwuthikul P. Wettability determination of the crude oil–reservoir brine– reservoir rock system with dissolution of CO_2 at high pressures and elevated temperatures. Energy & Fuels. 2008;22(4):2362-71.

11. Chaudhuri RG, Paria S. Dynamic contact angles on PTFE surface by aqueous surfactant solution in the absence and presence of electrolytes. Journal of colloid and interface science. 2009;337(2):555-62.

12. Kaveh NS, Rudolph ESJ, van Hemert P, Rossen WR, Wolf KH. Wettability evaluation of a CO_2/water/Bentheimer sandstone system: Contact angle, dissolution, and bubble size. Energy & Fuels. 2014;28(6):4002-20.

13. Ramiasa M, Ralston J, Fetzer R, Sedev R. The influence of topography on dynamic wetting. Advances in colloid and interface science. 2014;206:275-93.

14. Korhonen JT, Huhtamäki T, Ikkala O, Ras RH. Reliable measurement of the receding contact angle. Langmuir: the ACS journal of surfaces and colloids. 2013;29(12):3858-63.

15. Decker E, Frank B, Suo Y, Garoff S. Physics of contact angle measurement. Colloids and Surfaces A: Physicochemical and Engineering Aspects. 1999;156(1):177-89.

16. Alotaibi MB, Nasralla RA, Nasr-El-Din HA. Wettability studies using low-salinity water in sandstone reservoirs. SPE Reservoir Evaluation & Engineering. 2011;14(06):713-25.

17. Singhal A, Dranchuk P. Wettability control of glass beads. The Canadian Journal of Chemical Engineering. 1975;53(1):3-8.

18. Anderson W. Wettability literature survey-part 2: Wettability measurement. JPT. 1986;38(11):1,246-1,62.

19. Espinoza DN, Santamarina JC. Water-CO_2-mineral systems: Interfacial tension, contact angle, and diffusion—Implications to CO_2 geological storage. Water resources research. 2010;46(7).

20. Chalbaud CA, Lombard J-MN, Martin F, Robin M, Bertin HJ, Egermann P, editors. Two phase flow properties of brine-CO_2 systems in a carbonate core: Influence of wettability on Pc and kr. SPE/EAGE Reservoir characterization and simulation conference; 2007.

21. Chi S, Morsi B, Klinzing G, Chiang S. Study of interfacial properties in the liquid carbon dioxide-water-coal system. Energy & Fuels. 1988;2(2):141-5.

22. Yang D, Tontiwachwuthikul P, Gu Y. Interfacial interactions between reservoir brine and CO_2 at high pressures and elevated temperatures. Energy & Fuels. 2005;19(1):216-23.

23. Bachu S, Bennion DB. Interfacial tension between CO_2, freshwater, and brine in the range of pressure from (2 to 27) MPa, temperature from (20 to 125)° C, and water salinity from (0 to 334 000) mg· L− 1. Journal of Chemical & Engineering Data. 2008;54(3):765-75.

24. Leelamanie D, Karube J. Soil-water contact angle as affected by the aqueous electrolyte concentration. Soil Science and Plant Nutrition. 2013;59(4):501-8.

25. Yang D, Gu Y, Tontiwachwuthikul P. Wettability determination of the reservoir brine− reservoir rock system with dissolution of CO_2 at high pressures and elevated temperatures. Energy & Fuels. 2007;22(1):504-9.

26. MoldMaking technology. Solving the Part-Sticking Challenge 2017 [Available from: http://www.moldmakingtechnology.com/articles/solving-the-part-sticking-challenge.

27. Al-Hadhrami HS, Blunt MJ, editors. Thermally induced wettability alteration to improve oil recovery in fractured reservoirs. SPE/DOE Improved Oil Recovery Symposium; 2000.

28. Bandara UC, Tartakovsky AM, Palmer BJ. Pore-scale study of capillary trapping mechanism during CO_2 injection in geological formations. IJGGC. 2011;5(6):1566-77.

29. Bennion DB, Bachu S, editors. Drainage and imbibition CO_2/brine relative permeability curves at reservoir conditions for high-permeability carbonate rocks. SPE Annual Technical Conference and Exhibition; 2010.

30. Berg RR. Capillary pressures in stratigraphic traps. AAPG Bulletin. 1975;59(6):939-56.

31. Schowalter TT. Mechanics of secondary hydrocarbon migration and entrapment. AAPG Bulletin. 1979;63(5):723-60.

32. Aqil Muhammad Yusof and Azelin Mohamed Noor. The topography of petroleum reservoirs 2018 [cited 2018 14-2-2018]. Available from: http://www.mssa.org.my/site/index.php?option=com_content&view=article&id=162&Itemid=224.

33. Wollenweber J, Alles S, Busch A, Krooss B, Stanjek H, Littke R. Experimental investigation of the CO_2 sealing efficiency of caprocks. IJGGC. 2010;4(2):231-41.

34. Li S, Dong M, Li Z, Huang S, Qing H, Nickel E. Gas breakthrough pressure for hydrocarbon reservoir seal rocks: implications for the security of long-term CO_2 storage in the Weyburn field. Geofluids. 2005;5(4):326-34.

35. Kwelle SO. Experimental studies on resistance to fluid displacement in single pores [PhD. Thesis]: The University of Edinburgh, Edinburgh, UK; 2017.

36. Price J, Smith B. Geologic storage of carbon dioxide–staying safely underground. International Energy Agency (IEA) Greenhouse Gas R & D Programme. 2008.

37. Saeedi A, Rezaee R, Evans B, Clennell B. Multiphase flow behaviour during CO_2 geo-sequestration: Emphasis on the effect of cyclic CO_2–brine flooding. JPSE. 2011;79(3):65-85.

38. Dance T. Assessment and geological characterisation of the CO_2 CRC Otway Project CO_2 storage demonstration site: From prefeasibility to injection. Marine and Petroleum Geology. 2013;46:251-69.

39. Kazemifar F, Blois G, Kyritsis DC, Christensen KT. Quantifying the flow dynamics of supercritical CO_2–water displacement in a 2D porous micromodel using fluorescent microscopy and microscopic PIV. Advances in Water Resources. 2015.

40. Hangx S, van der Linden A, Marcelis F, Bauer A. The effect of CO_2 on the mechanical properties of the captain sandstone: geological storage of CO_2 at the Goldeneye field (UK). IJGGC. 2013;19:609-19.

41. Kuo C-w, Perrin J-C, Benson SM, editors. Effect of gravity, flow rate, and small scale heterogeneity on multiphase flow of CO_2 and brine. SPE Western Regional Meeting; 2010.

42. Preston BL, Jones RN. Climate change impacts on Australia and the benefits of early action to reduce global greenhouse gas emissions: CSIRO Canberra; 2006.

43. Shukla R, Ranjith P, Haque A, Choi X. A review of studies on CO_2 sequestration and caprock integrity. Fuel. 2010;89(10):2651-64.

44. NOAA Research. Trends in Atmospheric Carbon Dioxide 2018 [Global Carbon Dioxide Concentration Trend]. Available from: https://www.esrl.noaa.gov/gmd/ccgg/trends/global.html.

45. Bachu S. Geological sequestration of anthropogenic carbon dioxide: applicability and current issues. Geological perspectives of global climate change. 2001(47):285-303.

46. Hatzignatiou D, Riis F, Berenblyum R, Hladik V, Lojka R, Francu J. Screening and evaluation of a saline aquifer for CO_2 storage: Central Bohemian Basin, Czech Republic. IJGGC. 2011;5(6):1429-42.

47. Delshad M, Wheeler MF, Kong X, editors. A critical assessment of CO_2 injection strategies in saline aquifers. SPE Western Regional Meeting; 2010.

48. Gozalpour F, Ren S, Tohidi B. CO_2 EOR and storage in oil reservoir. Oil & gas science and technology. 2005;60(3):537-46.

49. Kaveh NS, Wolf K, Ashrafizadeh S, Rudolph E. Effect of coal petrology and pressure on wetting properties of wet coal for CO_2 and flue gas storage. IJGGC. 2012;11:S91-S101.

50. Akbarabadi M, Piri M. Relative permeability hysteresis and capillary trapping characteristics of supercritical CO_2/brine systems: An experimental study at reservoir conditions. Advances in Water Resources. 2013;52:190-206.

51. Akbarabadi M, Piri M. Geologic storage of carbon dioxide: an experimental study of permanent capillary trapping and relative permeability. In Proceedings of International Symposium of the Society of Core Analysts; Austin, Texas, USA. 18–21 September 2011. p. 18-21.

52. Riazi M, Sohrabi M, Bernstone C, Jamiolahmady M, Ireland S. Visualisation of mechanisms involved in CO_2 injection and storage in hydrocarbon reservoirs and water-bearing aquifers. Chemical Engineering Research and Design. 2011;89(9):1827-40.

53. Chang L-C, Tsai J-P, Shan H-Y, Chen H-H. Experimental study on imbibition displacement mechanisms of two-phase fluid using micro model. Environmental Earth Sciences. 2009;59(4):901.

54. Carbon Capture UaSC. Principles of storage 2017 [Diagram of the capture of CO_2 from factories to its transportation in ships, temporary storage ("buffer" stocks) and pipeline transportation. The diagram then shows three types of storage: in unexploited coal seams, deep saline aquifers, and depleted oil or natural gas fields.]. Available from: http://www.captage-stockage-valorisation-co2.fr/en/principles-storage.

55. The University of Southampton. Geological storage of CO_2 into oceanic crust 2017 [http://www.southampton.ac.uk/oes/research/projects/geological_storage_of_co2_into_oceanic_crust.page].

56. Kneafsey TJ, Pruess K. Laboratory flow experiments for visualizing carbon dioxide-induced, density-driven brine convection. Transport in porous media. 2010;82(1):123-39.

57. Krevor S, Pini R, Zuo L, Benson SM. Relative permeability and trapping of CO_2 and water in sandstone rocks at reservoir conditions. Water Resources Research. 2012;48(2).

58. Chalbaud C, Robin M, Lombard J, Martin F, Egermann P, Bertin H. Interfacial tension measurements and wettability evaluation for geological CO_2 storage. Advances in Water Resources. 2009;32(1):98-109.

59. Li Z, Dong M, Li S, Huang S. CO_2 sequestration in depleted oil and gas reservoirs—caprock characterization and storage capacity. Energy Conversion and Management. 2006;47(11):1372-82.

60. De Silva P, Ranjith P. A study of methodologies for CO_2 storage capacity estimation of saline aquifers. Fuel. 2012;93:13-27.

61. Ren B, Sun Y, Bryant S. Maximizing local capillary trapping during CO_2 injection. Energy Procedia. 2014;63:5562-76.

62. Wang D, Dong B, Breen S, Zhao M, Qiao J, Liu Y, et al. Review: Approaches to research on CO_2/brine two-phase migration in saline aquifers. Hydrogeology Journal. 2015;23(1):1-18.

63. Wang S, Edwards IM, Clarens AF. Wettability phenomena at the CO_2-brine-mineral interface: implications for geologic carbon sequestration. Environ Sci Technol. 2013;47(1):234-41.

64. Zhang D, Song J. Mechanisms for geological carbon sequestration. Procedia IUTAM. 2014;10:319-27.

65. Chalbaud C, Robin M, Lombard J, Martin F, Egermann P, Bertin H. Interfacial tension measurements and wettability evaluation for geological CO_2 storage. Advances in Water Resources. 2009;32(1):98-109.

66. Burnside N, Naylor M. Review and implications of relative permeability of CO2/brine systems and residual trapping of CO_2. IJGGC. 2014;23:1-11.

67. Liu N, Ghorpade SV, Harris L, Li L, Grigg RB, Lee RL, editors. The effect of pressure and temperature on brine-CO_2 relative permeability and IFT at reservoir conditions. In Proceedings of the SPE Eastern Regional Meeting; Morgantown, WV, USA, 13–15 October 2010: SPE: Houston, TX, USA, 2010.

68. Soroush M, Wessel-Berg D, Kleppe J, editors. Effects of wetting behaviour on residual trapping in CO_2-brine systems. SPE Western Regional & AAPG Pacific Section Meeting 2013 Joint Technical Conference; 2013.

69. Grigg RB, Svec RK, editors. CO_2 transport mechanisms in CO_2/brine coreflooding. SPE Annual Technical Conference and Exhibition; 2006.

70. Al-Menhali A, Niu B, Krevor S, editors. The Effect of reservoir conditions on wetting and multiphase flow properties in CO_2-brine-rock system. International Petroleum Technology Conference; 2015: International Petroleum Technology Conference.

71. YorkMix. Residual-trapping-media 2017 [https://www.yorkmix.com/uncategorized/a-rock-solid-way-for-yorkshire-to-counter-climate-change/attachment/residual-trapping-media/.

72. Basbug B, Gumrah F, Oz B, editors. Simulating the effects of deep saline aquifer properties on CO_2 sequestration. Canadian International Petroleum Conference; 2005: Petroleum Society of Canada.

73. CO_2 CRC. Injection & storage 2017 [http://old.co2crc.com.au/aboutccs/stor_trapping.html.

74. Dullien FA. Porous media: fluid transport and pore structure: Academic press; 1979.

75. Scheidegger AE. The Physics of Flow Through Porous Media1958. 353 p.

76. Pini R, Benson SM. Simultaneous determination of capillary pressure and relative permeability curves from core-flooding experiments with various fluid pairs. Water Resources Research. 2013;49(6):3516-30.

77. Heaviside J, Black C, editors. Fundamentals of relative permeability: experimental and theoretical considerations. SPE Annual Technical Conference and Exhibition; 1983.

78. Anderson WG. Wettability literature survey part 5: the effects of wettability on relative permeability. JPT. 1987;39(11):1,453-1,68.

79. Al-Aulaqi T, Fisher Q, Grattoni C, Al-Hinai SM, editors. Wettability alteration by brine salinity and temperature in reservoir cores. SPE Saudi Arabia Section Technical Symposium and Exhibition; 2013.

80. Crain's Petrophysical Handbook (CPH). Relative Permeability 2017 [Available from: https://www.spec2000.net/09-relperm.htm.

81. American Association of Petroleum Geologists. EOR (Enhanced Oil Recovery) 2017 [Available from: https://ugmsc.wordpress.com/2010/09/15/eor-enhanced-oil-recovery/.

82. Bondor P. Applications of carbon dioxide in enhanced oil recovery. Energy Conversion and Management. 1992;33(5):579-86.

83. Terry RE. Enhanced oil recovery. Encyclopedia of physical science and technology. 2001;18:503-18.

84. Daripa P, Paşa G. On capillary slowdown of viscous fingering in immiscible displacement in porous media. Transport in porous media. 2008;75(1):1-16.

85. Al Adasani A, Bai B. Analysis of EOR projects and updated screening criteria. JPSE. 2011;79(1-2):10-24.

86. Xu W, Ayirala SC, Rao DN. Compositional dependence of wetting and contact angles in solid-liquid-liquid systems under realistic environments. The Canadian Journal of Chemical Engineering. 2006;84(1):44-51.

87. Shahrabadi A, Bagherzadeh H, Roostaie A, Golghanddashti H, editors. Experimental investigation of HLP nanofluid potential to enhance oil recovery: A mechanistic approach. SPE International Oilfield Nanotechnology Conference and Exhibition; 2012.

88. U.S. Energy Information Administration (EIA). EIA projects 48% increase in world energy consumption by 2040 2017 [World energy consumption by source, 1990-2040]. Available from: https://www.eia.gov/todayinenergy/detail.php?id=26212.

89. Ahmadi MA, Hasanvand Mz, Behbahani SS, Nourmohammad A, Vahidi A, Amiri M, et al. Effect of operational parameters on the performance of carbonated water injection: Experimental and numerical modeling study. The Journal of Supercritical Fluids. 2015.

90. Lashkarbolooki M, Ayatollahi S, Riazi M. The impacts of aqueous ions on interfacial tension and wettability of an asphaltenic–acidic crude oil reservoir during smart water injection. Journal of Chemical & Engineering Data. 2014;59(11):3624-34.

91. Fink JK. Enhanced Oil Recovery. 2012:459-517.

92. Nobakht M, Moghadam S, Gu Y. Effects of viscous and capillary forces on CO_2 enhanced oil recovery under reservoir conditions. Energy & Fuels. 2007;21(6):3469-76.

93. Voormeij DA, Simandl GJ. Geological, ocean, and mineral CO_2 sequestration options: a technical review. Geoscience Canada. 2004;31(1).

94. Blunt M, Fayers FJ, Orr FM. Carbon dioxide in enhanced oil recovery. Energy Conversion and Management. 1993;34(9-11):1197-204.

95. Bennion DB, Bachu S, editors. The impact of interfacial tension and pore size distribution/capillary pressure character on CO_2 relative permeability at reservoir conditions in CO_2-brine systems. In Proceedings of the SPE/DOE Symposium on Improved Oil Recovery; Tulsa, OK, USA, 22–26 April 2006: SPE: Houston, TX, USA, 2006.

96. Singh R, Gupta A, Mohanty KK, Huh C, Lee D, Cho H, editors. Fly Ash Nanoparticle-Stabilized CO_2-in-Water Foams for Gas Mobility Control Applications. SPE Annual Technical Conference and Exhibition; 2015.

97. Jikich SJ. CO_2 EOR: Nanotechnology for mobility control studied. JPT. 2012;64(07):28-31.

98. Tokunaga TK. DLVO-based estimates of adsorbed water film thicknesses in geologic CO_2 reservoirs. Langmuir: the ACS journal of surfaces and colloids. 2012;28(21):8001-9.

99. Shu G, Dong M, Chen S, Luo P. Improvement of CO_2 EOR performance in water-wet reservoirs by adding active carbonated water. JPSE. 2014;121:142-8.

100. Sehbi BS, Frailey SM, Lawal AS, editors. Analysis of factors affecting microscopic displacement efficiency in CO_2 floods. SPE Permian Basin Oil and Gas Recovery Conference; 2001.

101. Enick RM, Olsen DK, Ammer JR, Schuller W, editors. Mobility and conformance control for CO_2 EOR via thickeners, foams, and gels-A Literature review of 40 years of research and pilot tests. SPE Improved Oil Recovery Symposium; 2012.

102. Todd M, Grand G. Enhanced oil recovery using carbon dioxide. Energy conversion and management. 1993;34(9):1157-64.

103. Srivastava R, Huang S, Dyer S, Mourits F, editors. Heavy oil recovery by subcritical carbon dioxide flooding. SPE Latin America/Caribbean Petroleum Engineering Conference; Buenos Aires, Argentina, 27–29 April 1994: SPE: Houston, TX, USA, 1994.

104. Holm L. Status of CO_2 and hydrocarbon miscible oil recovery methods. JPT. 1976;28(01):76-84.

105. Velasquez D, Rey O, Manrique E, editors. An overview of carbon dioxide sequestration in depleted oil and gas reservoirs in Florida, USGS Petroleum Province 50. 4th LACCEI International Latin American and Caribbean Conference for Engineering and Technology (LACCEI 2006), Mayagüez, Puerto Rico; 2006.

106. Sarma H. Viscous fingering: one of the main factors behind poor flood efficiencies in petroleum reservoirs. Powder technology. 1986;48(1):39-49.

107. Kueper BH, Frind EO. An overview of immiscible fingering in porous media. Journal of Contaminant Hydrology. 1988;2(2):95-110.

108. Khalil F, Asghari K. Application of CO_2-foam as a means of reducing carbon dioxide mobility. Journal of Canadian petroleum technology. 2006;45(05).

109. Müller N. Supercritical CO_2-brine relative permeability experiments in reservoir rocks—Literature review and recommendations. Transport in porous media. 2011;87(2):367-83.

110. Yu J, Liu N, Li L, Lee RL, editors. Generation of nanoparticle-stabilized supercritical CO_2 foams. Carbon Management Technology Conference; 2012: Carbon Management Technology Conference.

111. Yu J, An C, Mo D, Liu N, Lee RL, editors. Foam mobility control for nanoparticle-stabilized supercritical CO_2 foam. SPE Improved Oil Recovery Symposium; 2012.

112. Lenormand R, Touboul E, Zarcone C. Numerical models and experiments on immiscible displacements in porous media. Journal of Fluid Mechanics. 1988;189(165-187):37-8.

113. Peters EJ, Flock DL. The onset of instability during two-phase immiscible displacement in porous media. SPE Journal. 1981;21(02):249-58.

114. Zhang C, Oostrom M, Wietsma TW, Grate JW, Warner MG. Influence of viscous and capillary forces on immiscible fluid displacement: Pore-scale experimental study in a water-wet micromodel demonstrating viscous and capillary fingering. Energy & Fuels. 2011;25(8):3493-505.

115. Institute for Energy Technology. CO_2 EOR tracers 2017 [Available from: https://www.ife.no/en/ife/ife_images/ife_co2_senter_ill/ife_co2_eor_tracers_1/view.

116. Lenormand R, Zarcone C, editors. Role of roughness and edges during imbibition in square capillaries. SPE annual technical conference and exhibition; 1984.

117. Chandler R, Koplik J, Lerman K, Willemsen JF. Capillary displacement and percolation in porous media. Journal of Fluid Mechanics. 1982;119:249-67.

118. Fenwick DH, Blunt MJ. Three-dimensional modeling of three phase imbibition and drainage. Advances in Water Resources. 1998;21(2):121-43.

119. Levine JS, Matter JM, Goldberg DS, Lackner KS, Supp MG, Ramakrishnan T. Two phase brine-CO_2 flow experiments in synthetic and natural media. Energy Procedia. 2011;4:4347-53.

120. Qi R, Laforce T, Blunt M. Carbon dioxide (CO_2) injection design to maximize underground reservoir storage and enhanced oil recovery (EOR). Developments and innovation in carbon dioxide (CO_2) capture and storage technology (Ed MM Maroto-Valer), Woodhead Publishing Series in Energy, Oxford. 2010:169-84.

121. Jobard E, Sterpenich J, Pironon J, Corvisier J, Jouanny M, Randi A. Experimental simulation of the impact of a thermal gradient during geological sequestration of CO_2: The COTAGES experiment. IJGGC. 2013;12:56-71.

122. Ma J, Petrilli D, Manceau J-C, Xu R, Audigane P, Shu L, et al. Core scale modelling of CO_2 flowing: identifying key parameters and experiment fitting. Energy Procedia. 2013;37:5464-72.

123. Xu R, Luo S, Jiang P. Pore scale numerical simulation of supercritical CO_2 injecting into porous media containing water. Energy Procedia. 2011;4:4418-24.

124. Bachu S. Sequestration of CO_2 in geological media: criteria and approach for site selection in response to climate change. Energy conversion and management. 2000;41(9):953-70.

125. Saraji S, Piri M, Goual L. The effects of SO_2 contamination, brine salinity, pressure, and temperature on dynamic contact angles and interfacial tension of supercritical CO_2/brine/quartz systems. IJGGC. 2014;28:147-55.

126. Sohrabi M, Jamiolahmady M, Al Quraini A, editors. Heavy oil recovery by liquid CO_2/water injection. EUROPEC/EAGE Conference and Exhibition; London, UK 11–14 June 2007: SPE: Houston, TX, USA, 2007.

127. Nourpour Aghbash V, Ahmadi M, editors. Evaluation of CO_2-EOR and Sequestration in Alaska West Sak Reservoir Using Four-Phase Simulation Model. SPE Western Regional Meeting; Bakersfield, CA, USA, 21–23 March 2012: SPE: Houston, TX, USA, 2012.

128. Frailey SM, Grube JP, Seyler B, Finley RJ, editors. Investigation of liquid CO_2 sequestration and EOR in low temperature oil reservoirs in the Illinois basin. SPE/DOE Symposium on Improved Oil Recovery; Tulsa, OK, USA, 17–21 April 2004: SPE: Houston, TX, USA, 2004.

129. Islam A, Chevalier S, Sassi M. Experimental and numerical studies of CO_2 injection Into water-Saturated porous medium: Capillary to viscous to fracture fingering phenomenon. Energy Procedia. 2013;37:5511-9.

130. Jiang L, Yu M, Liu Y, Yang M, Zhang Y, Xue Z, et al. Behavior of CO_2/water flow in porous media for CO_2 geological storage. Magnetic Resonance Imaging. 2017;37:100-6.

131. Yu M, Song Y, Jiang L, Li W. CO_2/Water Displacement in Porous Medium Under Pressure and Temperature Conditions for Geological Storage. Energy Procedia. 2014;61:282-5.

132. Song Y, Jiang L, Liu Y, Yang M, Zhao Y, Zhu N, et al. An experimental study on CO_2/water displacement in porous media using high-resolution magnetic resonance imaging. IJGGC. 2012;10:501-9.

133. Alemu BL, Aker E, Soldal M, Johnsen Ø, Aagaard P. Influence of CO_2 on rock physics properties in typical reservoir rock: A CO_2 flooding experiment of brine saturated sandstone in a CT-scanner. Energy Procedia. 2011;4:4379-86.

134. Zhang C, Oostrom M, Grate JW, Wietsma TW, Warner MG. Liquid CO_2 displacement of water in a dual-permeability pore network micromodel. Environmental science & technology. 2011;45(17):7581-8.

135. Manceau J-C, Ma J, Li R, Audigane P, Jiang P, Xu R, et al. Two-phase flow properties of a sandstone rock for the CO_2/water system: Core-flooding experiments, and focus on impacts of mineralogical changes. Water Resources Research. 2015;51(4):2885-900.

136. Berg S, Oedai S, Ott H. Displacement and mass transfer between saturated and unsaturated CO_2–brine systems in sandstone. IJGGC. 2013;12:478-92.

137. Suekane T, Soukawa S, Iwatani S, Tsushima S, Hirai S. Behavior of supercritical CO_2 injected into porous media containing water. Energy. 2005;30(11):2370-82.

138. Chang C, Zhou Q, Xia L, Li X, Yu Q. Dynamic displacement and non-equilibrium dissolution of supercritical CO_2 in low-permeability sandstone: An experimental study. IJGGC. 2013;14:1-14.

139. Suenaga H, Nakagawa K. Analysis of two-phase flow properties of sandstones to evaluate their suitability for geologic storage of CO_2. Energy Procedia. 2011;4:4323-30.

140. Krevor S, Pini R, Benson SM. Measurement of the multiphase flow properties of the CO_2 brine system for carbon sequestration. Energy Procedia. 2013;37:4499-503.

141. Herring AL, Andersson L, Newell D, Carey J, Wildenschild D. Pore-scale observations of supercritical CO_2 drainage in Bentheimer sandstone by synchrotron x-ray imaging. IJGGC. 2014;25:93-101.

142. Wang D, Zhao M, Song Y, Xu H, Ma X. Influence of capillary pressure and injection rate as well as heterogeneous and anisotropic permeability on CO_2 transport and displacement efficiency in water-saturated porous media. Energy Procedia. 2013;37:3945-51.

143. Pentland C, El-Maghraby R, Georgiadis A, Iglauer S, Blunt M. Immiscible displacements and capillary trapping in CO_2 storage. Energy Procedia. 2011;4:4969-76.

144. Perrin J-C, Benson S. An experimental study on the influence of sub-core scale heterogeneities on CO_2 distribution in reservoir rocks. Transport in porous media. 2010;82(1):93-109.

145. Shi J-Q, Xue Z, Durucan S. Supercritical CO_2 core flooding and imbibition in Tako sandstone—Influence of sub-core scale heterogeneity. IJGGC. 2011;5(1):75-87.

146. Ott H, Pentland C, Oedai S. CO_2–brine displacement in heterogeneous carbonates. IJGGC. 2015;33:135-44.

147. Cao SC, Dai S, Jung J. Supercritical CO_2 and brine displacement in geological carbon sequestration: Micromodel and pore network simulation studies. IJGGC. 2016;44:104-14.

148. Ott H, de Kloe K, Marcelis F, Makurat A. Injection of supercritical CO_2 in brine saturated sandstone: pattern formation during salt precipitation. Energy Procedia. 2011;4:4425-32.

149. Okabe H, Tsuchiya Y, Mihama-ku H, Shinjyuku-ku O, editors. Experimental investigation of residual CO_2 saturation distribution in carbonate rock. International symposium of the society of core analysts, Abu Dhabi, UAE; 2008.

150. Rosenbauer RJ, Koksalan T, Palandri JL. Experimental investigation of CO_2–brine–rock interactions at elevated temperature and pressure: implications for CO_2 sequestration in deep-saline aquifers. Fuel processing technology. 2005;86(14):1581-97.

151. Zhao DF, Liao XW, Yin DD. An experimental study for the effect of CO_2-brine-rock interaction on reservoir physical properties. Journal of the Energy Institute. 2015;88(1):27-35.

152. Wang K, Xu T, Wang F, Tian H. Experimental study of CO_2-brine-rock interaction during CO_2 sequestration in deep coal seams. Int J Coal Geo. 2016.

153. Shiraki R, Dunn TL. Experimental study on water-rock interactions during CO_2 flooding in the Tensleep Formation, Wyoming, USA. Applied Geochemistry. 2000;15(3):265-79.

154. Pini R, Krevor SC, Benson SM. Capillary pressure and heterogeneity for the CO_2/water system in sandstone rocks at reservoir conditions. Advances in Water Resources. 2012;38:48-59.

155. Perrin J-C, Falta RW, Krevor S, Zuo L, Ellison K, Benson SM. Laboratory experiments on core-scale behavior of CO_2 exolved from CO_2-saturated brine. Energy Procedia. 2011;4:3210-5.

156. Rathmell J, Stalkup F, Hassinger R, editors. A laboratory investigation of miscible displacement by carbon dioxide. Fall meeting of the SPE of AIME; 1971.

157. Beeson DM, Ortloff GD. Laboratory investigation of the water-driven carbon dioxide process for oil recovery. 1959.

158. Wang X, Gu Y. Oil Recovery and permeability reduction of a tight sandstone reservoir in immiscible and miscible CO_2 flooding processes. Industrial & Engineering Chemistry Research. 2011;50(4):2388-99.

159. Jha K. A laboratory study of heavy oil recovery with carbon dioxide. Journal of Canadian Petroleum Technology. 1986;25(02).

160. Sankur V, Creek JL, Di Julio SS, Emanuel AS. A Laboratory study of Wilmington tar Zone CO_2 injection project. 1986.

161. Moradi B, Awang M, Sabil K, Shoushtari M, Moradi P, Ajdari H, et al., editors. Liquid carbon dioxide flooding in low temperature oil reservoirs. SPE Asia Pacific Oil and Gas Conference and Exhibition; 2013.

162. Arshad A, Al-Majed AA, Menouar H, Muhammadain AM, Mtawaa B. Carbon dioxide (CO_2) miscible flooding in tight oil reservoirs: A case study. 2009/1/1/. SPE; 2009.

163. Chung F, Jones R, Burchfield T, editors. Recovery of viscous oil under high pressure by CO_2 displacement: A laboratory study. International meeting on petroleum engineering; 1988: SPE.

164. Huang ET, Tracht JH, editors. The displacement of residual oil by carbon dioxide. SPE Improved Oil Recovery Symposium; 1974; Tulsa, Oklahoma, 22–24 April 1974: SPE: Houston, TX, USA, 1974.

165. Cao M, Gu Y. Oil recovery mechanisms and asphaltene precipitation phenomenon in immiscible and miscible CO_2 flooding processes. Fuel. 2013;109:157-66.

166. Liu Y, Teng Y, Jiang L, Zhao J, Zhang Y, Wang D, et al. Displacement front behavior of near miscible CO_2 flooding in decane saturated synthetic sandstone cores revealed by magnetic resonance imaging. Magnetic resonance imaging. 2017;37:171-8.

167. Lashkarbolooki M, Vaezian A, Hezave AZ, Ayatollahi S, Riazi M. Experimental investigation of the influence of supercritical carbon dioxide and supercritical nitrogen injection on tertiary live-oil recovery. The Journal of Supercritical Fluids. 2016;117:260-9.

168. Bayat M, Lashkarbolooki M, Hezave AZ, Ayatollahi S. Investigation of gas injection flooding performance as enhanced oil recovery method. Journal of Natural Gas Science and Engineering. 2016;29(Supplement C):37-45.

169. Hammond PS, Unsal E. Spontaneous and forced imbibition of aqueous wettability altering surfactant solution into an initially oil-wet capillary. Langmuir: the ACS journal of surfaces and colloids. 2009;25(21):12591-603.

170. Salimi H, Bruining J. The Influence of heterogeneity, wetting, and viscosity ratio on oil recovery from vertically fractured reservoirs. SPE Journal. 2011;16(02):411-28.

171. Sheng JJ. Review of surfactant enhanced oil recovery in carbonate reservoirs. Advances in Petroleum Exploration and Development. 2013;6(1):1-10.

172. Morrow NR, Mason G. Recovery of oil by spontaneous imbibition. Current Opinion in Colloid & Interface Science. 2001;6(4):321-37.

173. Roustaei A, Bagherzadeh H. Experimental investigation of SiO_2 nanoparticles on enhanced oil recovery of carbonate reservoirs. Journal of Petroleum Exploration and Production Technology. 2014;5(1):27-33.

174. Pickell J, Swanson B, Hickman W. Application of air-mercury and oil-air capillary pressure data in the study of pore structure and fluid distribution. SPE Journal. 1966;6(01):55-61.

175. Yu L, Wardlaw NC. The influence of wettability and critical pore-throat size ratio on snap—off. Journal of Colloid and Interface Science. 1986;109(2):461-72.

176. Scanziani A, Singh K, Blunt MJ, Guadagnini A. Automatic method for estimation of in situ effective contact angle from X-ray micro tomography images of two-phase flow in porous media. Journal of Colloid and Interface Science. 2017;496:51-9.

177. Tang G-Q, Morrow NR. Influence of brine composition and fines migration on crude oil/brine/rock interactions and oil recovery. JPSE. 1999;24(2):99-111.

178. Lenormand R, Zarcone C, Sarr A. Mechanisms of the displacement of one fluid by another in a network of capillary ducts. J Fluid Mech. 1983;135(34):337-53.

179. Dong M, Dullien FA, Dai L, Li D. Immiscible displacement in the interacting capillary bundle model part ii. applications of model and comparison of interacting and non-interacting capillary bundle models. Transport in Porous media. 2006;63(2):289-304.

3 Chapter 3: Materials and Methods

3.1 Contact Angle Measurements

3.1.1 Materials

All the salts (NaCl, KCl and $CaCl_2.2H_2O$) used for the contact angle measurements were analytical reagent grade and purchased from SIGMA-ALDRICH, except magnesium chloride ($MgCl_2.6H_2O$) which was supplied by Fisher Scientific (UK). Both the microscopic glass slides (Thermo Fisher Scientific UK, 10143562CE) and the micro-glass tubes (Thermo Fisher Scientific UK, TWL-611-010M) were made of glass. Each micro-glass tube has a wall thickness of 1.5 mm and an outer diameter of 6 mm. The composition of both the plain glass microscopic slides and the micro-glass tubes were white soda-lime glass (SiO_2: 72.20%, Na_2O: 14.30%, CaO: 6.40%, K_2O: 1.20%, MgO: 4.30%, Al_2O_3: 1.20%, Fe_2O_3: 0.03% and SO_3: 0.30%) [1].

3.1.2 Cleaning Procedures and Manufacturing of Capillary Tubes

Glass microscopic slides and glass capillary tubes were cleaned with hot water for 2-3 minutes under tap pressure, then rinsed thoroughly with deionized water. To avoid potential surface contamination, disposable gloves were used during handling and conducting contact angle measurements. The glass samples were placed under intensified heat (550 °C) until they became red in colour to remove any trace of organic contamination [2]. To prepare micro-glass tubes, glass tubes were melted on a butane flame (Butane Battery, D2-BS 0167) and stretched to a long distance to obtain a uniform micron-sized glass pore. The diameters of the glass capillaries investigated ranged from 100 to 1000 µm. To avoid contamination, micro-capillary tubes and microscopic slides were stored in a dust proof closure and used as soon as possible for contact angle measurements. Each time, the measurements were conducted on a new microscopic glass slide and a new micro-sized glass tube.

3.1.3 Sessile Drop Method for Contact Angle Measurement on a Flat Surface

The static contact angle on a flat glass surface, as shown in Figure 3-1, was measured with the sessile drop technique. To minimize the effect of the droplet size, a liquid drop of 0.5 µl volume was placed carefully on the glass substrate using a pipette to reduce the vibration on

the measurement. The 0.5 µl liquid drop has a radius of less than 2.7 mm. This means that the gravity effects on the drop shape can be neglected, according to Spyridon and Kranias' calculations [3]. An average of five measurements was taken for each liquid drop to obtain reliable results. These measurements were repeated two to three times. The captured images were analysed using the Fta32 software (First Ten Angstroms). Since some liquid drops showed a non-spherical shape, the non-spherical fit mode instead of the spherical mode fit was used for image analysis. To minimize the effect of water evaporation on the measured contact angles, the static contact angles were measured as quickly as possible.

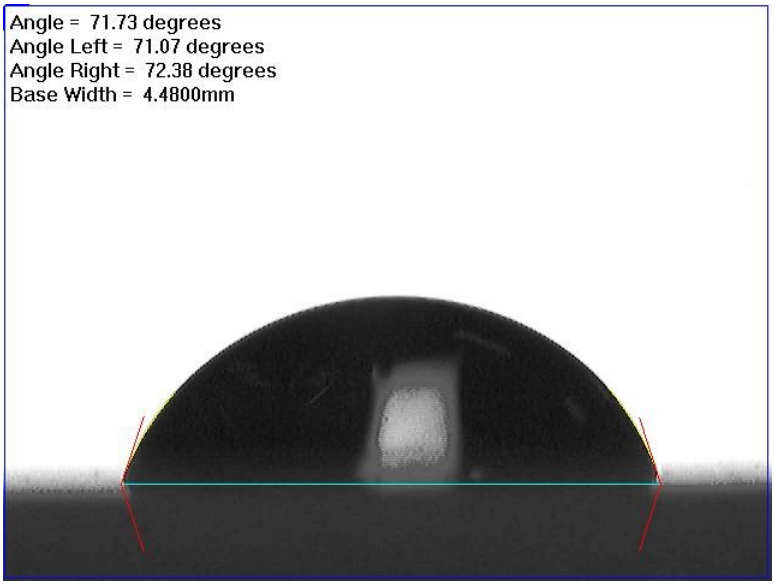

Figure 3-1: Contact angle on a flat glass surface

3.1.4 Microscopic Imaging Technique for Contact Angle Measurement in a Micron-sized Pore

The static contact angle inside a single capillary tube, as shown in Figure 3-2, was measured with the experimental rig shown in Figure 3-3. The experiment was begun by placing the micro-glass tube under the microscope and several microlitres of the electrolyte solution were fed into one end of the capillary by a microfluidic syringe (Hamilton, 701 ASN 10 10 µl). The liquid imbibes into the capillary tube under its own capillary pressure at ambient conditions. When the imbibition process and the movement of liquid stopped, an image of the meniscus was captured. A microscope (Brunel Microscopes Ltd.) equipped with a digital camera (AM7023, DinoEye) was used to capture the microscopic image of the meniscus height. The quality of the meniscus image of a small volume of liquid is highly dependent on the measurement method. Thus, a LED light source placed under the glass capillary was used

to improve the quality of the image. The effect of evaporation on the contact angle inside the micro-tubes can be neglected since the process lasted less than 10 seconds for the measurement of each image. An average of 30-40 images was taken for each concentration and for all the micro-tubes, which ranged from 100 to 1000 µm. The measurements were repeated two to three times to confirm their reliability.

The use of a cylindrical tube would cause a degree of meniscus image distortion problem [1]. Therefore, a simple and robust method proposed by Cheong et al. was used to determine the contact angle and minimize the image distortion issues in contact angle analysis [4]. Cheong et al.'s equation requires only the radius of the capillary tube and meniscus height to determine the contact angle of small volumes [4].

$$\theta = \tan^{-1}\left(\frac{r^2-h^2}{2rh}\right) \tag{3-1}$$

In Eq.3-1, Θ is the contact angle, r the radius of the capillary tube (mm), and h the height of the capillary meniscus (mm). To evaluate the measurement error of the method, Eq. 3-1 was rearranged and differentiated as follows:

$$\delta\theta = \tan^{-1}\left(-\frac{r^2+h^2}{2rh^2(1+\tan\theta)}\right)\delta h = -\frac{2r}{r^2+h^2}\delta h \tag{3-2}$$

Based on the knowledge that $h = r(1-sin\theta)/cos\theta$, Eq. 3-2 can be rewritten as follows:

$$\delta\theta = \frac{-2k}{r}\delta h, \text{ where } K = \frac{1+sin}{2}\theta \tag{3-3}$$

Eq. 3-3 shows the sources of error. Where r refers *to* the dimension of the capillary, K represents the wetting characteristics of the liquid, and δh denotes the imaging spatial resolution of the microscope system. Eq. 3-3 shows that as capillary tube diameter increases, the accuracy of the measurement of contact angle will increase; nonetheless, there is a limit to increasing this at the expense of losing the capillary effect. Moreover, in order to overcome the degree of the image distortion problem, the LED light was delivered from the liquid end up to the meniscus in a dark background [4]. As a result, the utmost boundary of the liquid-gas interface was well lighted and focused to get a clear two-phase interfacial line. This principle is similar to that used in measuring micro-bubble size [5], micro ice crustal in aqueous solution [6] and the size of a plant cell or a microcapsule in water under a microscope [7].

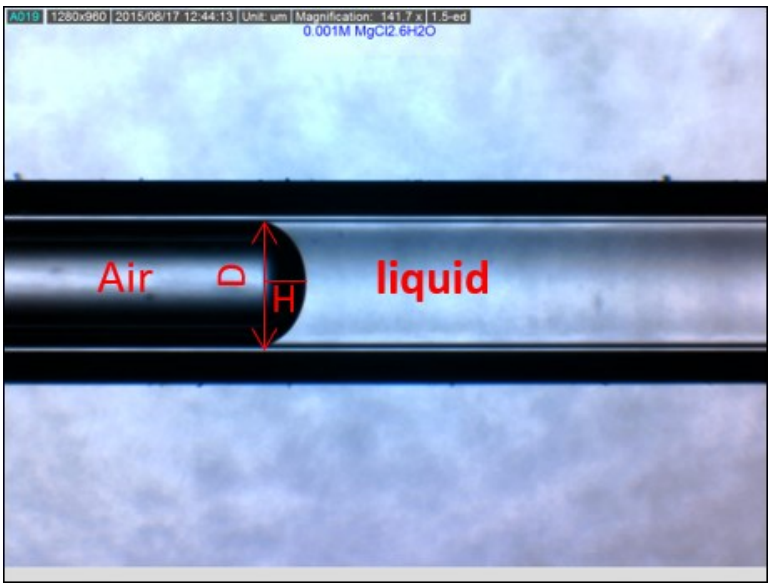

Figure 3-2: Contact angle inside a glass micro-capillary tube

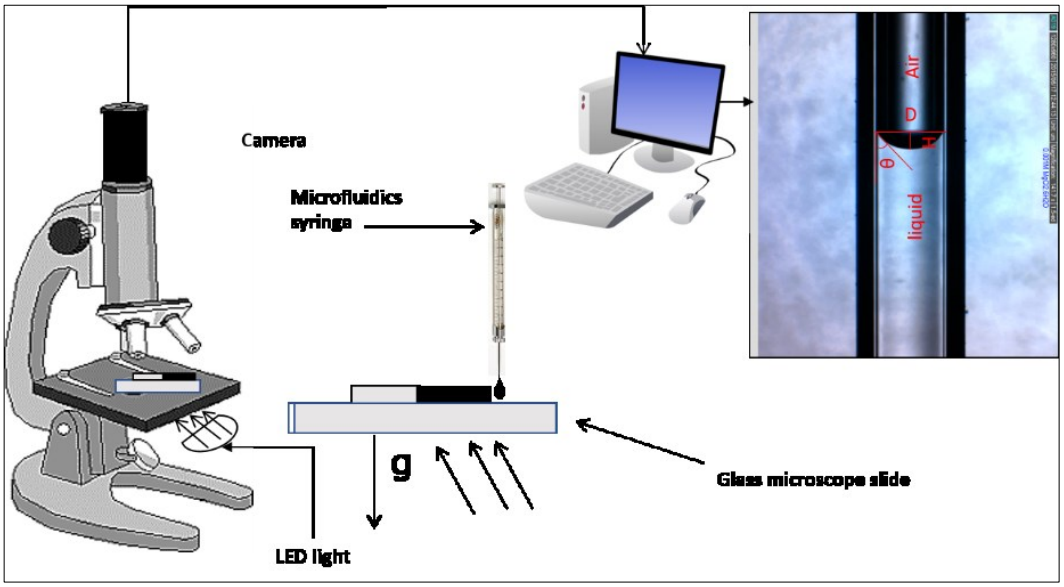

Figure 3-3: Experimental setup for the study of static contact angle in a glass tube (the vector g shows the direction of gravity)

3.2 CO_2 flooding

3.2.1 Liquid

Deionized water, brine solutions (1% NaCl, 5% NaCl, 1% $CaCl_2$), and crude oil were used in this study. The crude oil was provided by BP Exploration Operating Company Limited, but due to confidentiality, the specified properties of the oil sample cannot be disclosed.

3.2.2 Sandstone Core Sample

Figure 3-4 shows the sandstone core sample from the Guillemot A field in the North Sea that was used in both CO_2-water drainage and imbibition water-CO_2 displacements. The diameter of the core sample is 2.54 cm and the length is 7.62 cm. The average porosity and absolute water permeability of the core sample were about 14% and 15.8 millidarcys, respectively. The pore volume and porosity were calculated using the weight difference between the dry and the water-saturated core sample. More information about the core sample description can be found in Appendix C.

For drainage CO_2-oil displacements, a sandstone core sample of 2.54 cm diameter and 7.62 cm long was used. The average porosity and absolute water permeability of the core sample were about 20% and 28.9 mD, respectively. The Berea core sample wettability was altered to an oil-wet state by ageing the core inside the BP crude oil at 80 $^{\circ}$C for more than eight months.

Figure 3-4: The North Sea sandstone core sample used in this study

3.2.3 CO_2 Core Flooding Experimental Set-up

Figure 3-5 shows the core-flooding setup used to conduct both CO_2–drainage and imbibition displacements. The experimental system consists of two high-pressure syringe pumps (Teledyne ISCO, Lincoln, NE, United States), capable of injection rates ranging from 0.0001 to 25 ml/min. During the drainage displacements, the ISCO pump CO_2 was used for the injection

of CO_2 while the ISCO pump water was used for the collection of water (oil) and CO_2; this order was the opposite during the imbibition displacements.

The experimental rig composes also of a core holder, a pressure gauge mounted on the core holder to measure the confining pressure, a water bath (Grant instruments GD 100) to control the temperature with a precision of ± 0.02 ˚C, an overburden pressure pump (CM400) to deliver the confining pressure, a vacuum pump (Edwards, Model E2M5) to remove the trapped gas, and a LabVIEW software system; the software was built to acquire the data from the pressure transducers (UNIK, 0-100 bar with a precision of ± 0.1% of BSL) at the inlet and outlet side of the core sample.

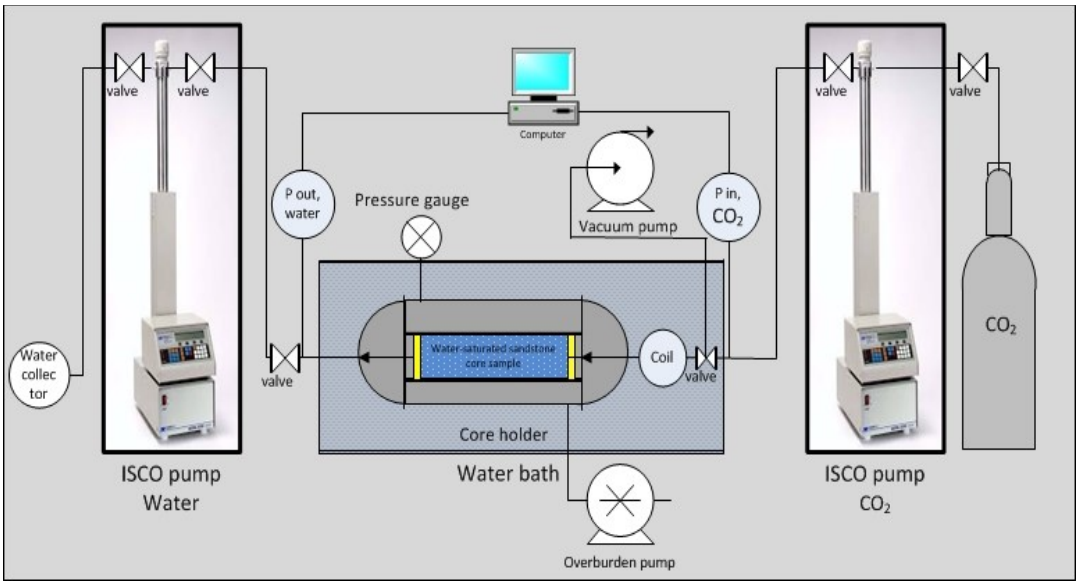

Figure 3-5: The experimental setup for CO_2–water displacements, CO_2–oil displacements and Water–CO_2 displacements

3.2.3.1 CO_2- Water /Oil Displacements Procedure

It should be noted that the following procedures are applied for all CO_2-water drainage displacements, CO_2-oil drainage displacements, and water-CO_2 imbibition displacements unless it is stated.

The core sample was wrapped into a shrinkable Teflon tube followed by a rubber sleeve and then fixed inside the core holder. Then, the core holder was mounted horizontally inside the water bath. To prevent fluid bypassing, a confining pressure of about 135 bar, which is always higher than the pore pressure, was applied to the core with the confining pump. Next, the

temperature was controlled by the heater and the vacuum pump was connected to the system to remove the trapped gas. To fully saturate the core sample with water or oil during the drainage displacements, an about 40-60 pore volumes (PVs) of water or oil was injected at a high-differential pressure of 80-90 bar; to achieve this differential pressure, the water displacement was conducted by utilizing a 0.2 μm membrane (Nuclepore Track-Etch Membrane-Whatman) while the oil displacements was conducted at a constant pressure mode. To obtain heat equilibrium, the water bath temperature was set to the required degree and the system was left overnight at the experimental temperature. Prior to each flooding experiment, a constant pressure was applied to the entire system with the syringe pump at each end. After having the experimental pressure, the system was left for about 20 mins to ensure that temperature stabilization has been achieved throughout the system.

Later, the mode of the injected pump was changed from a constant pressure mode to a constant flowrate mode to inject CO_2 or water into the core at a constant injection rate to displace the fluid saturated core sample. The injected CO_2 volumes and the collected fluid volumes were recorded every 30 seconds (s). During the experiment, the inlet and outlet pressure transducer readings were recorded every 6 s, using the LabVIEW software, in order to calculate the differential pressure across the core sample. When the experiment was finished, the volumes of fluids produced were measured to calculate the residual water (oil) saturation using the mass balance principles. Later, the weight of the core sample was measured using a Sartorius weighing scale with a resolution of 0.0001g to confirm the residual saturation measurements.

3.3 References

1. Li X, Fan X, Brandani S. Difference in pore contact angle and the contact angle measured on a flat surface and in an open space. Chemical Engineering Science. 2014;117:137-45.

2. Fisher LR, Lark PD. An experimental study of the Washburn equation for liquid flow in very fine capillaries. Journal of Colloid and Interface Science. 1979;69(3):486-92.

3. Spyridon Kranias KG, France. Effect of drop volume on static contact angles. 2012.

4. Cheong BH-P, Ng TW, Yu Y, Liew OW. Using the meniscus in a capillary for small volume contact angle measurement in biochemical applications. Langmuir: the ACS journal of surfaces and colloids. 2011;27(19):11925-9.

5. Fan X, Zhang Z, Li G, Rowson N. Attachment of solid particles to air bubbles in surfactant-free aqueous solutions. Chemical engineering science. 2004;59(13):2639-45.

6. Fan X, Ten P, Clarke C, Bramley A, Zhang Z. Direct measurement of the adhesive force between ice particles by micromanipulation. Powder technology. 2003;131(2):105-10.

7. Rosinski S, Grigorescu G, Lewinska D, Ritzén L, Viernstein H, Teunou E, et al. Characterization of microcapsules: recommended methods based on round-robin testing. Journal of microencapsulation. 2002;19(5):641-59.

4 Chapter 4: Gaseous CO_2-Water Drainage Displacements

4.1 Introduction

Investigations of multiphase flow characteristics of gaseous CO_2-water-sandstone system is of practical importance. This is because the injected CO_2 for the purpose of sequestration or enhancing oil recovery can exist in a gaseous state (GCO_2) (e.g., Alabama Black Warrior Basin:~70 bar, 22.85 °C) [1]. Moreover, any leakage of CO_2 from deeper storage would inevitably result in a phase change to a gaseous CO_2 state [2, 3].

In comparison to liquid and supercritical states of CO_2, CO_2 in a gaseous state is most likely to characterize by the highest capillary forces and the lowest viscous forces. Therefore, these properties are likely to have a different influence on the injection, displacement, and migration, storage capacity and security of CO_2. However, the literature shows that the multiphase flow properties of gaseous CO_2-water-sandstone system are scarcely investigated [4-6]. Moreover, although it is practically important, the literature shows no detailed experimental investigations into the dynamic pressure evolution and displacement efficiency of gaseous CO_2 when it is injected into a water saturated core sample [7].

During this chapter, laboratory dynamic drainage experiments were performed by injecting pure CO_2 into a deionised water-saturated sandstone core sample to investigate the impact of fluid pressure, temperature, and CO_2 injection rate on the differential pressure profile, water production, and endpoint effective and relative permeabilities of CO_2. This study also highlights the impact of capillary and viscous forces on the pressure and production data as well as shows the conditions when the capillary forces or viscous forces dominate the flow. During these dynamic displacements, the transient pressure at the inlet and outlet sides of the core and the transient outflow rates of water and CO_2 were measured and analysed.

4.2 Results and Discussions

To gain a deep insight into the dynamic behaviour of GCO_2-water drainage displacements under various fluid pressure, temperature, and CO_2 injection rate conditions; the inlet and outlet pressure, CO_2 and water outflow rates, the residual water saturation and endpoint effective and relative permeabilities of CO_2 were measured and analysed. The difference

between the pressure transducer readings at the inlet and outlet sides of the core sample was used to calculate the differential pressure.

The most influential forces that affect the differential pressure of a horizontally conducted CO_2-water displacement are the capillary forces and viscous forces. The capillary forces, which are responsible for the entrapment of one phase by another during immiscible displacements in a porous media [8, 9], arise from the presence of the interface between the immiscible fluids [10] and dominate the multiphase flow, especially in low permeability rocks and fractured reservoirs [11]. The capillary forces are controlled by the CO_2-water interfacial tension, contact angle (i.e. wetting status), pore diameter and geometry [8, 10, 12, 13]; more information about interfacial or surface tension concept can be seen in Appendix B- Section B.3; about wettability more information can be found in Chapter 2- Section 2.1 and Appendix B.1 and B.2. On the other hand, the viscous forces are controlled mainly by the viscosity of both displacing and displaced fluids, velocity of fluids in pores, amount of each fluid (i.e. the length of CO_2 invasion) in pores, and properties of the core sample (e.g. frontal area, permeability, and length).

Espinoza and Santamarina [14] proposed the following equation to account for the impact of the capillary and viscous forces on the differential pressure during CO_2-water flooding as follows:

$$\Delta P = P_{CO2} - P_{water} = 4\,\frac{\sigma_{CO_2-water}\,COS\theta}{d} + v\,\frac{32\,L}{d^2}\left(\frac{l_{CO_2}\mu_{CO_2} + l_{water}\mu_{water}}{L}\right) \quad (4\text{-}1)$$

where ΔP is the differential pressure across the core sample (Pa). P_{CO2} and P_{water} are the pressures of CO_2 phase and water phase, respectively. $\sigma_{CO2\text{-}water}$ is the CO_2-water interfacial tension (mN/m), Θ the contact angle, d (m) the diameter of the largest effective pore [15-18], L (m) the length of the core sample, l (m) the length of CO_2 or water phase inside the core sample, v (m/sec) the fluid velocity in the pores, and μ (Pa·s) the viscosity of the fluids.

The first right-hand term of Eq.4-1 refers to the Young-Laplace equation, which accounts for the capillary forces, while the second term refers to the Poiseuille's equation [14, 19], which account for the viscous forces. For small injection rate and high viscosity contrast conditions, Eq.4-1 can be reduced to the Young-Laplace equation [19] as follows:

$$\Delta P = P_{CO2} - P_{water} = 4\,\frac{\sigma_{CO_2-water}\,COS\theta}{d} \quad (4\text{-}2)$$

The Young-Laplace equation is used to determine the critical pressure point, which is the differential pressure required for the displacing fluid to enter the core sample for the first time. A non-wetting fluid cannot enter the core sample unless its pressure becomes higher than the critical pressure point [18].

In addition to the Young–Laplace equation, a number of analytical capillary pressure formulations have been used to explain laboratory results [20, 21]. Among them, the Leverett's J-function has been intensively used to convert all the capillary pressure (P_c) data, as a function of the invaded fluid saturation, to a universal curve.

$$J(S^*_g) = \frac{P_c}{\sigma cos\theta}\sqrt{\frac{k}{\emptyset}} = a(S^*_g)^{-b} \quad (4\text{-}3)$$

where

$$S^*_g = \frac{S_g - S_{gr}}{1 - S_{gr}} \quad (4\text{-}4)$$

where S^*_g is the effective or normalized gas saturation, S_g the gas saturation and S_{gr} the residual gas saturation, and. a and b are coefficients. $\sqrt{\frac{k}{\emptyset}}$ is the pore geometry factor or (hydraulic radius), which has a similar dimension to the pore radius and is used to correlate petrophysical properties such as relative permeability and saturation.

In this chapter, the experimental results have been categorized into four main sections. The first three sections present and discuss the impact of the experimental fluid pressure, temperature and CO_2 injection rate on the differential pressure profile and production behaviour while the fourth section discusses their influence on the CO_2 endpoint effective and relative permeabilities and residual water saturation. It should be noted that during this chapter, we use the term low and high-fluid pressure to refer to the experiments conducted at pressures less and higher than 50 bar, respectively. The term low and high temperature refers to the experiments performed at less or higher than 33 °C, respectively. The term low, medium and high injection rates refers to the experiments performed at injection rate ranging from 0.1 to 0.2 ml/min, from 0.3 to 0.6 ml/min, and from 1 to 2 ml/min, in sequence. The corresponding time refers to the time required to reach the maximum-differential

pressure at the start of the experiment. The quasi-differential pressure denotes the average differential pressure at the end of the experiment.

4.2.1 Pressure Behaviour of GCO_2-Water Displacements

In this section, the impact of fluid pressure, temperature, and CO_2 injection rate on the differential pressure profile are presented and discussed.

4.2.1.1 Effect of Fluid Pressure on the Differential Pressure Profile of GCO_2-Water Drainage Displacements

Figure 4-1 presents the impact of increasing fluid pressure on the differential pressure profile of GCO_2-water drainage displacements. Several trends are identifiable (A-C). Firstly, the differential pressure profile at all fluid pressures is characterized by a high initial increase immediately followed by a steep rapid reduction and then followed by a quasi-differential pressure drop. Secondly, there are multiple oscillations of these cycles. The frequency of these oscillating cycles increases as fluid pressure increases along with a rise in the values of the maximum and quasi-differential pressures.

A) The high initial increase in the differential pressure can be related to the capillary pressure. This is because the injection of gaseous CO_2 into the core sample generates an initial increase in differential pressure to overcome the capillary entry pressure for the invasion of gaseous CO_2 [22]. The following reduction in the differential pressure profile reflects the impact of the reduction in both capillary forces and viscous forces. The reduction in the capillary forces can be associated with the reduction in the pore resistance to CO_2 flow as the number of pores opened by CO_2 is increased [23]. This agrees very well with Kwell's finding, who noticed a high reduction in the differential pressure profile as the CO_2-water interfaces are displaced out of microcapillary tubes [23]. The reduction in the viscous forces can be related to the combined effect of the dynamic change in the relative permeability of gaseous CO_2 and water and the high replacement of a more viscous fluid (water) with a less viscous fluid (CO_2) [22]. Replacing water by CO_2 at a high rate can be related to the high mobility ratio (because of the high viscosity contrast), and gas expansion effects, which generate an increase in volumetric CO_2 injection rate inside the core sample.

The gas expansion can be related to the density change of the injected CO_2 due to the temperature difference between the experimental conditions inside and outside the water bath. The density of the injected CO_2 varies as the CO_2 enters the water bath dependent on the fluid pressure and the temperature difference from the pump to the sample. The density ratio (d_r) suggested by Perrin and Benson [24] has been used to calculate the CO_2 injection rate inside the core sample. For instance, at an experimental pressure of 40 bar, an injection rate of 1 cm^3/min at 20 °C becomes 1.108 cm^3/min at 33 °C. However, at an experimental pressure of 70 bar and the same injection rate and temperature conditions, it becomes 3.288 cm^3/min.

$$d_r = \frac{{\rho_{CO2}}^{20\,^{\circ}C,40\ bars}}{{\rho_{CO2}}^{33^{\circ}C,40\ bars}} \tag{4-5}$$

B) Figure 4-1 shows that the differential pressure profiles are characterized by multiple differential pressure (PD) oscillations. The appearance of the oscillations in the differential pressure profile can be related to the impact of the capillary forces at the trailing end of each CO_2-water slug during CO_2 flooding [25] or the capillary end effects.

According to Nutt, the impact of the capillary forces at the trailing end of the CO_2-water slug is governed by the wetting status of the injected fluid. If a non-wetting fluid (e.g. CO_2) is injected, then the capillary forces will work in an opposite direction to the applied viscous forces. Thus, as water depletion is progressed, the applied viscous forces will drop until they become less than the capillary forces. Upon reaching this point, the flow of non-depleted capillaries is possibly blocked by the capillary forces [25]. This blockage occurs due to a re-imbibition process of the wetting phase inside the core sample, which was noticed by Hildenbrand et al [26]. Hildenbrand et al. observed that the re-imbibition process occurs when the excess pressure in the non-wetting phase declines after the gas breakthrough [26], as shown in Figure 4-2. This re-imbibition process occurs in a progressive manner starting with the smallest pores and continuing to the larger pores, leading to the successive loss of the interconnected flow-paths, which, in turn, leads to a progressive decline in the non-wetting phase relative permeability. Finally, when the last interconnected flow-path for the non-wetting phase is blocked, the permeability of the non-wetting phase will drop to zero [26]. According to Hildenbrand et al., this re-imbition process can result in a residual water saturation when certain-gas filled pores become isolated as a result of interrupting the flow pathways. The maximum differential pressure required to open the flow paths again can be

used to determine the largest effective pore radius and, hence, the sealing efficiency of the rock [26].

Therefore, since the core sample used during these displacements is water-wet, then the pressure of the injected CO_2 had to build up to a certain level to overcome the capillary forces that blocked the CO_2 outflow rate [25]. Due to the high compressibility nature of the gaseous CO_2, the injected CO_2 will accumulate inside the core sample and the connections pipes until the differential pressure becomes high enough to overcome the capillary forces. Once the blocked capillaries are opened to flow, the cumulative CO_2 will expel the liquid drops that block the pores out of the core sample quickly; the rate of expulsion is expected to increase with the fluid pressure. The development of the PD oscillations phenomenon is highly influenced by the core sample properties and the injection rate due to their strong impact on both capillary and viscous forces. Thus, this phenomenon is expected to be reduced when the injection rate, i.e. viscous pressure drop, becomes high enough to overcome the capillary forces [25]. However, due to the cyclic reduction of the viscous pressure drop (i.e. viscous forces) to the level that becomes insufficient to overcome the capillary forces, this phenomenon of oscillations can occur often.

Nevertheless, since the GCO_2-water displacements are strongly influenced by the capillary end effects and viscous instabilities [27], it might be suggested that the appearance of the oscillations is due to the impact of capillary end effects. The capillary end effects occur at both inlet and outlet faces of the core sample, but their impact becomes more severe at the outlet face. According to Müller, the capillary end effects can never be entirely prevented but can be reduced [27]. The impact of capillary end effects and viscous instabilities can be reduced when the following scaling coefficient (Eq.4-6) proposed by Rapoport and Leas for stabilized floods becomes greater than one.

$$Lu\mu \geq 1 \qquad (4\text{-}6)$$

where L is the length of the medium (cm), u the Darcy velocity (cm/min), and μ the displacing phase viscosity (cp) [28]. Eq.4-6 indicates that as the magnitude of the scaling coefficient increases, the impact of the capillary end effect reduces. The scaling coefficients for the 40, 50, and 70 bar displacements are 0.0773, 0.0844, and 0.285, respectively. The scaling coefficients increased significantly as the fluid pressure increased from 40 and 50 bar to 70

bar, which indicates a reduction in the impact of capillary end effects with increasing fluid pressure. However, since the data from Figure 4-1 show an increase in the frequency of the PD oscillations with increasing fluid pressure, this indicates that the capillary end effects are not responsible for this phenomenon. In addition, the disappearance of the oscillations at lower injection rate as shown in Figure 4-6 further supports the idea that the oscillations phenomenon is not because of the capillary end effects.

C) Figure 4-1 also shows that increasing fluid pressure led to an increase in the rate of the PD oscillations along with increases in the values of the maximum and quasi-differential pressures and a reduction in the corresponding time. The extent of the changes in the PD oscillations, maximum and quasi-differential pressures and corresponding time is a function of the magnitude of the experimental pressure with their values increasing with increasing fluid pressure. For illustration, it can be noted that as the fluid pressure increased from 40 to 50 bar, the rate of the PD oscillations increased by around 33% and the maximum-differential pressure increased by about 2.50%. The quasi-differential pressure was constant at around 1 bar. The corresponding time declined by approximately 17%. However, as the fluid pressure increased from 50 to 70 bar, the PD oscillations substantially increased by 225%, the maximum-differential pressure raised by around 9% and the quasi-differential pressure increased by 165%. The corresponding time dropped considerably by around 78%. The high reduction in the corresponding time with increasing fluid pressure can be related mainly to increasing gaseous CO_2 density and injection rate inside the core sample due to the expansion effect. As gaseous CO_2 becomes denser, it needs lesser time to be compressed to the required pressure.

The increase in the maximum and quasi-differential pressures with increasing fluid pressure can be related mainly to the magnitudes of both viscous and capillary forces. According to Eq.4-1, as the fluid pressure increases the viscous forces increase (due to the increase in CO_2 viscosity and the injection rate inside the core sample due to expansion impact), while the capillary forces reduce (because of the reduction in the CO_2-water interfacial tension (IFT) [29] and the increase in the contact angle [30] due to increasing CO_2 solubility [31, 32]). Thus, the increase observed in the differential pressures is the net result of the increase in the viscous forces and the reduction in the capillary forces. Reducing capillary forces with

increasing pressure is expected to cause a reduction in the extent of differential pressure increase.

The increase in the PD oscillations means the frequency of liquid drops expelled out of the core sample is increased. This can be associated mainly with the reduction in the capillary forces and the increase in gas density with increasing pressure. Increasing the gas density and reducing capillary forces mean less time was needed to reach a differential pressure value which was enough to overcome the capillary forces; thus, increasing the frequency of the PD oscillations.

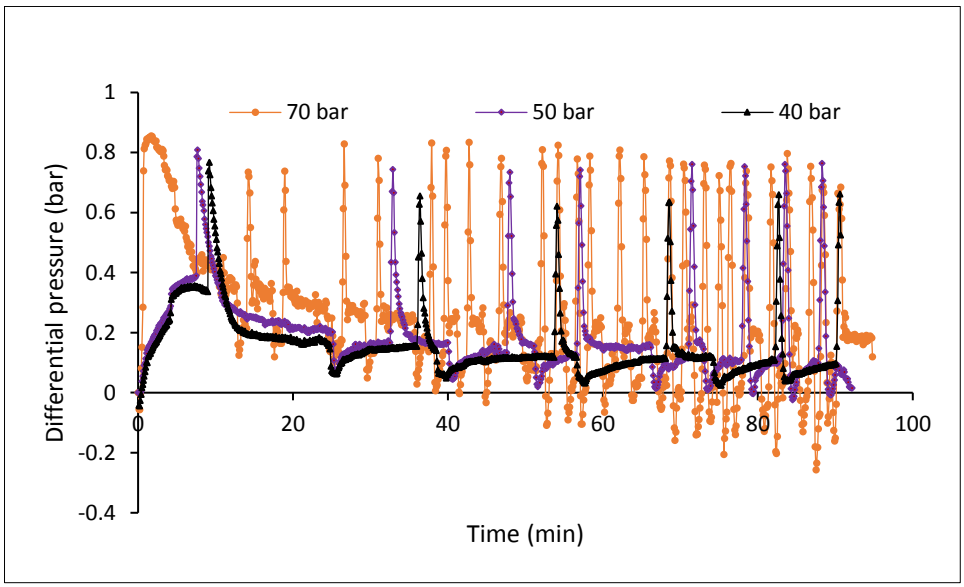

Figure 4-1: Effect of fluid pressure on the differential pressure profile of GCO_2-water displacements conducted at 0.4 ml/min and 33 °C

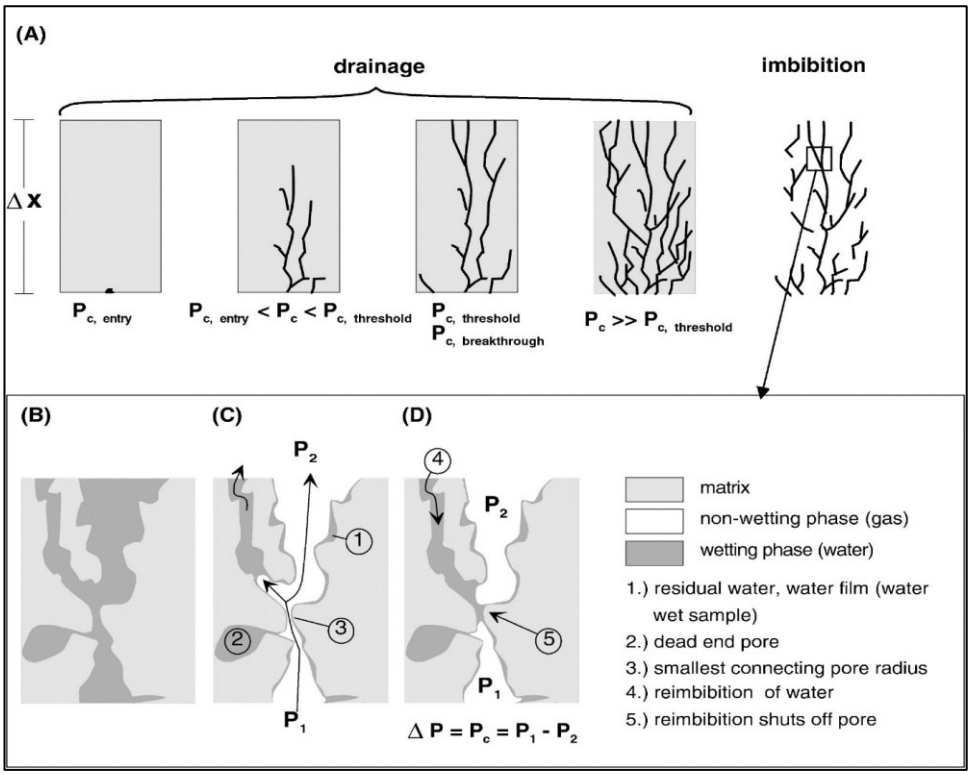

Figure 4-2: Re-imbibition process in fine-grained rocks (schematic re-imbibition); (A) drainage, (B) initially water-saturated sample, (C) gas breakthrough, (D) re-imbibition [26]

4.2.1.2 Effect of Temperature on the Differential Pressure Profile of GCO_2-Water Displacements

Figure 4-3 presents the impact of increasing the experimental temperature on the differential pressure profile. The results show that the increase in the temperature has a significant impact on the differential pressure profile. Firstly, increasing the temperature increases the frequency of the PD oscillations. At an experimental temperature of 29 °C, the differential pressure profile experienced no oscillations. However, as the temperature increased to 31 °C, the oscillations appeared for the first time. A further increase in the temperature to 33 °C caused the number of oscillations to increase by double. Secondly, the increase in the experimental temperature prompts an increase in the magnitude of the maximum-differential pressure. The quasi-differential pressure was almost constant due to the slight impact of both capillary forces and viscous forces at the end of core flooding.

The appearance and frequency of the PD cycles with increasing temperature have three potential explanations. The first potential reason behind the onset of the oscillations is the increase in the capillary forces despite the slight increase in viscous forces under these

conditions. The increase in temperature leads to an increase in the CO_2-water IFT [33] with a reduction in the contact angle [32] due to the decline in the CO_2 solubility [31, 32] as well as a slight increase in CO_2 viscosity, and a slight increase in CO_2 injection rate inside the core sample due to expansion effect. For illustration, as the experimental temperature increased from 29 to 31 °C, the CO_2-water IFT increases from to 42.9 to 44.42 mN/m, CO_2 viscosity increases very slightly from 16.72 to 16.755 × [10^{-6}(Pa·s)] and CO_2 injection inside the core sample increased from around 0.45 to 0.46 ml/min. However, a further increase in the temperature to 33 °C caused the IFT to decrease to 34.1 mN/m [34], CO_2 viscosity to increase to 16.805 × [10^{-6}(Pa·s)] and CO_2 injection to increase to 0.466 ml/min.

The second possible reason might be related to the fluctuating behaviour in the CO_2-water IFT when the experimental temperature is in the vicinity of the critical point [31], as shown in Figure 4-4. The third potential reason is that increasing temperature might result in an increase in the movement of CO_2 molecules. This is because each individual molecule has more energy as it becomes hotter, according to the Kinetic molecular theory [35]. A high energetic CO_2 molecule might open the closed flow path quicker, due to the increase in capillary forces, and hence increased the frequency of the PD oscillations. The results indicate that for the sandstone core sample (from the Guillemot A field, North Sea) used in these experiments and under the aforementioned experimental conditions, the onset temperature point of the oscillations is around 31 °C. The characteristics of the sandstone sample, e.g. pore sample distribution, play a key role in the onset of the PD oscillations phenomenon since they have a direct influence on the magnitude of both capillary and viscous forces.

The data also reveals that as the experimental temperature increased from 29 to 31 °C, the maximum-differential pressure increased by around 12.5% (from 0.72 to 0.81 bar) and the corresponding time dropped by around 9.1% (from 12.1 to 11 min). However, increasing the temperature from 31 to 33 °C caused the differential pressure to decline slightly by 1.23% (from 0.82 to 0.81 bar) and the corresponding time dropped by 30% (from 11 to 7.7 min). The increase and decrease in the maximum-differential pressure can be related mainly to the increase or decrease in the capillary forces due to CO_2-water IFT, as stated above. The highest reduction in the corresponding time occurred as the temperature increased to 33 °C. This can be related to the highest reduction in the CO_2-water interfacial tension [31], as shown in Figure 4-4.

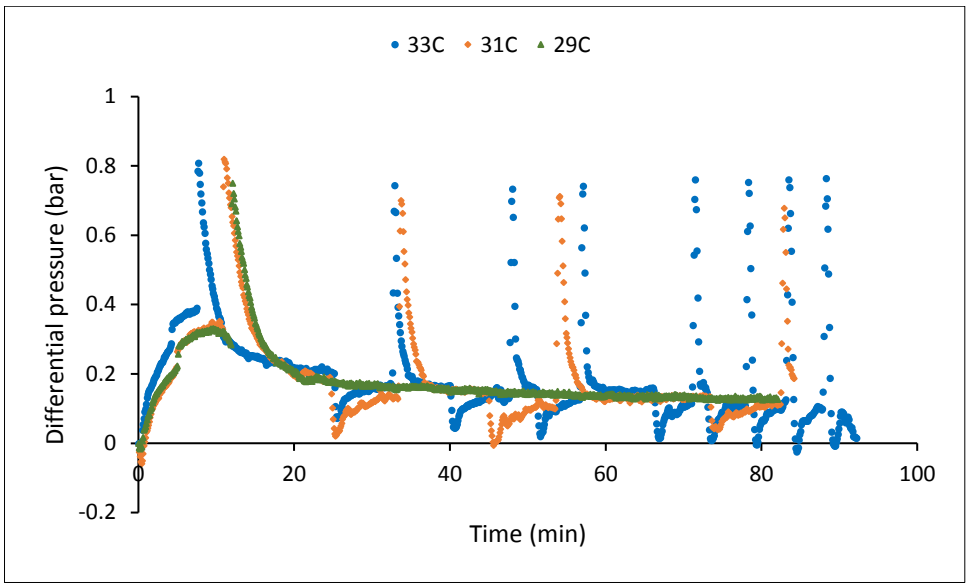

Figure 4-3: Effect of temperature on the differential pressure profile of GCO_2-water displacements conducted at 50 bar and 0.4 ml/min

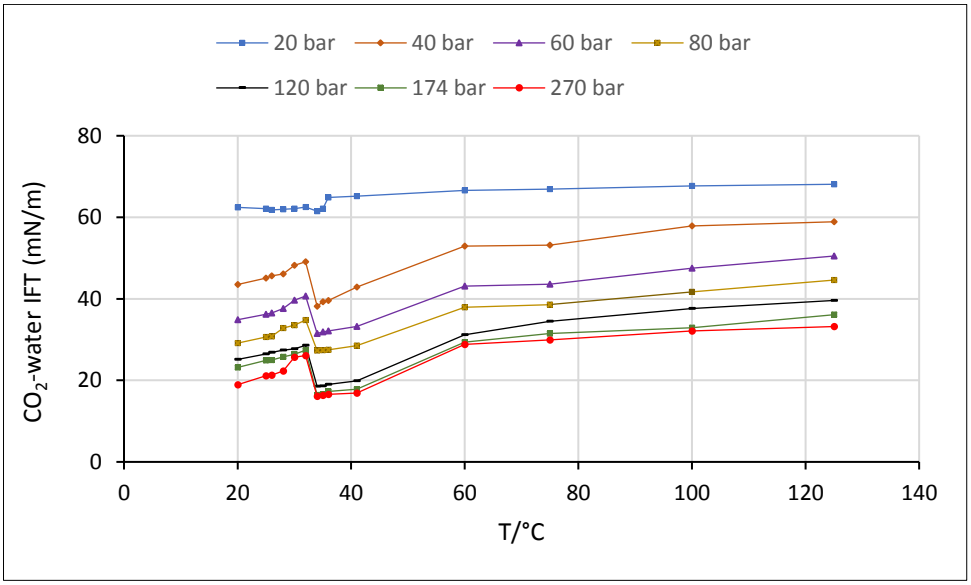

Figure 4-4: Interfacial tension for CO_2-Pure Water Systems adopted from [34]

To further investigate the effect of the temperature on the differential pressure profile, and especially on the PD oscillations, more GCO_2-water displacement experiments were conducted under high-pressure of 70 bar and higher temperature conditions.

The data from Figure 4-5 shows that increasing the experimental temperature by 12° (from 33 to 45 °C) at high-pressure caused no further increase in the rate of the PD oscillations. Yet, it instigated a very slight increase in the maximum and quasi-differential pressures with a

small reduction in the corresponding time. The maximum differential pressure increased by only 4.2% (from 0.854 to 0.89 bar) and the quasi-differential pressure increased by 4.81% (from 0.208 to 0.218 bar). The corresponding time declined by around 17% (from 1.8 to 1.5 min).

The data showed no further increase in the PD oscillations occurred when there are no fluctuations in the IFT as the temperature increased from 33 to 45 °C, as shown in Figure 4-4. This suggests that the IFT fluctuations might have highly influenced the frequency of PD oscillations.

The increase in the differential pressures can be related to the increase in the capillary forces (because of the increasing CO_2-water interfacial tension and the reducing contact angle [32]), and the slight increase in the viscous forces (because of the increasing injection rate). The magnitude of the viscous forces might have slightly declined because of the slight reduction in CO_2 viscosity with increasing temperature. For illustration, as the experimental temperature increased from 33 to 45 °C, the CO_2-water IFT increases slightly from around 29.15 to around 33.4 mN/m [31] and the CO_2 injection rate inside the core sample increased from 1.315 to 1.748 ml/min but the viscosity decreases from 20.743 to 19.05 × [10^{-6}(Pa·s)].

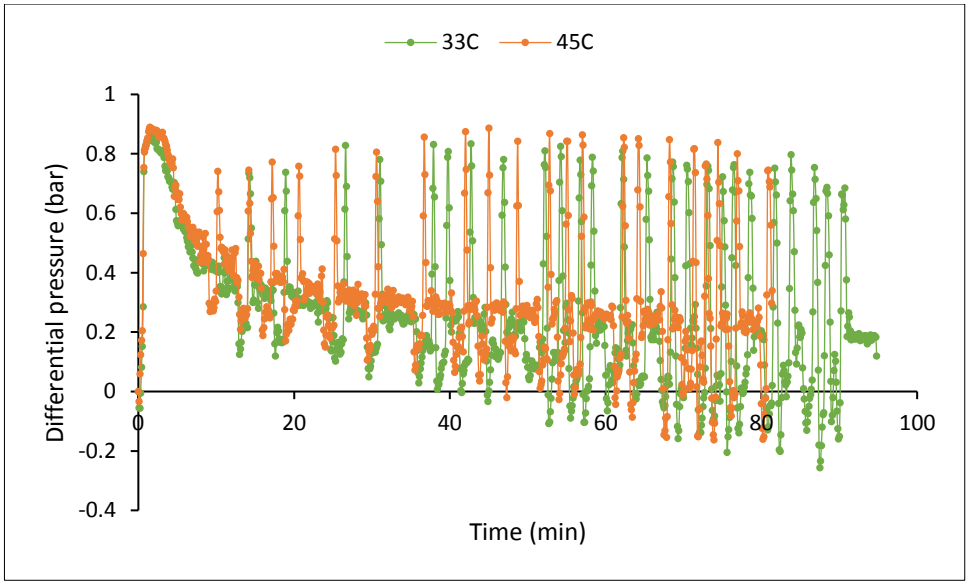

Figure 4-5: Effect of temperature on the differential pressure profile of GCO_2-water displacements conducted at 70 bar and 0.4 ml/min.

4.2.1.3 Effect of CO_2 Injection Rate on the Differential Pressure Profile of GCO_2-Water Core Floodings.

Figure 4-6, Figure 4-7 and Figure 4-8 show the impact of increasing CO_2 injection rate on the differential pressure profile. The results show that increasing the injection rate has a significant impact on the differential pressure profile, mainly during the early stages of CO_2 flooding. The data show several important observations (A-E).

A) The results from Figure 4-6 and Figure 4-7 show that the higher the injection rate, the higher the maximum differential pressure is. Increasing the injection rate caused a slight increase in the quasi-differential pressure; it caused a decrease in the corresponding time at low injection rates and an increase at high injection rates. For illustration, as the CO_2 injection rate increased from 0.1 to 0.2 ml/min, the maximum-differential pressure increased by 33.54% (from 0.161 to 0.215 bar), and the quasi-differential pressure increased by 5.88% (from 0.068 to 0.072 bar) while the corresponding time reduced by almost half (from 13.5 to 6.5 min). However, as the CO_2 injection rate increased from 1 to 2 ml/min, the maximum-differential pressure increased by around 44% (from 0.833 to 1.201 bar), the quasi-differential pressure increased by around 15% (from 0.254 to 0.291 bar), and the corresponding time increased by 12% (from 3.3 to 3.7 min). The increase in the corresponding time at high injection rates despite the increase in the CO_2 injection rate can be related to the high increase in the magnitude of the maximum-differential pressure as well as the low-density nature of gaseous CO_2. Since the injected gaseous CO_2 was at low pressure (40 bar), it needed a longer time to reach the higher maximum-differential pressure of 1.201 bar during the 2 ml/min-displacement.

B) The data from Figure 4-6 and Figure 4-7 show that as the injection rate increased by tenfold (from 0.1 to 1 ml/min, and from 0.2 to 2 ml/min), the quasi-differential pressure increased by only around fourfold (from 0.068 to 0.254 bar, and from 0.072 to 0.291 bar). This might be related to a potential increase in the relative permeability with increasing injection rate [22, 36] that leads to a reduction in the viscous pressure drop.

C) The data, previously shown in Figure 4-1, show that the differential pressure profile of the 40 bar-experiments is characterized by PD oscillations at 0.4 ml/min CO_2 injection rate. Surprisingly, the data from Figure 4-6 and Figure 4-7 show no PD oscillations at lower and

higher CO_2 injection rates. The disappearance of the PD oscillations at higher injection rates (e.g. 1-2 ml/min) can be related to the high increase in the pressure drop due to viscous forces. Thus, the viscous forces impeded the capillary forces, which are responsible for the PD oscillations phenomenon observed [25]. On the other hand, at lower CO_2 injection rates (e.g. 0.1 to 0.2 ml/min), CO_2 might flow through preferential inlet and outlet pores [37] which are characterized by low resistance to CO_2 flow and by less capillary forces. Consequently, CO_2 does not need to pass through the smallest channels that are characterized by higher CO_2 flow resistance and higher capillary forces, hence avoiding the impact of the capillary forces that cause the oscillations.

D) To look in detail at the unexpected results regarding the appearance and disappearance of the PD oscillations and the impact of CO_2 injection rate on the differential pressure profile, further experiments were conducted at 40 bar and over a more detailed range of injection rates, as shown in Figure 4-8. It should be noted that the 0.4 ml/min GCO_2-water displacement is repeated to make sure that the observations were not an experimental error.

The results from Figure 4-8 show clearly that the PD oscillations occurred only at 0.4 ml/min for the experiments conducted at a low pressure of 40 bar. Overall, the data confirm that the increase in the injection rate produces an increase in the maximum-differential pressure and a reduction in its corresponding time for this range of injection rates. The quasi-differential pressure reduced slightly due to the potential increase in the relative permeabilities [22, 36].

The data from Figure 4-8 can be divided into two groups. The first group includes the experiments conducted at CO_2 injection rates of 0.3 and 0.4 ml/min while the second group involves the experiments performed at 0.5 and 0.6 ml/min. As the CO_2 injection rate increased for the first lower injection rate group, the maximum-differential pressure was almost constant at around 0.76 bar but the corresponding time reduced by 25% (from around 20 to 15 min). The second higher injection rate group was characterized by a constant maximum-differential pressure of 0.938 bar and a constant corresponding time of 6.5 min. Thus, the data shows that shifting the CO_2 injection rate from the first to the second group caused the maximum-differential pressure to increase by 23.42% and the corresponding time to reduce by around 57%. The increase in the maximum-differential pressure with shifting the CO_2 injection rate might be related to the properties of the core sample. It might have

occurred because as the injection rate increased from the first to the second group, the maximum-differential pressure had to further increase to open new preferential flow paths for the injected CO_2 [37]. The nearly constant maximum-differential pressure for each group might indicate a minimal impact for the viscous forces on the differential pressure at low pressures. It indicates also that the expected increase in the maximum-differential pressure due to increasing injection rate is reduced by the potential increase in the relative permeability due to the increasing injection rate [22, 36].

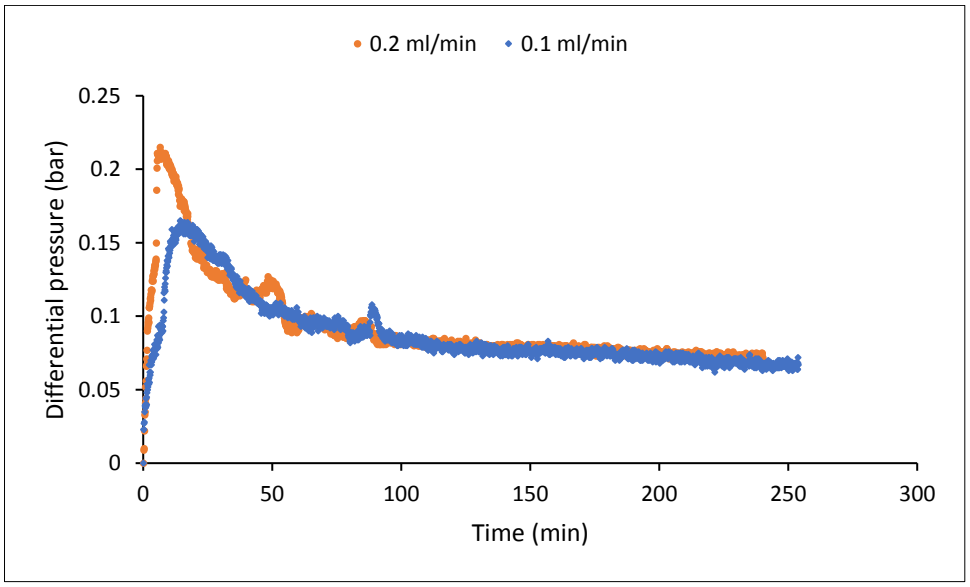

Figure 4-6: Effect of injection rate on the differential pressure profile of GCO_2-water displacements conducted at 40 bar and 33 °C

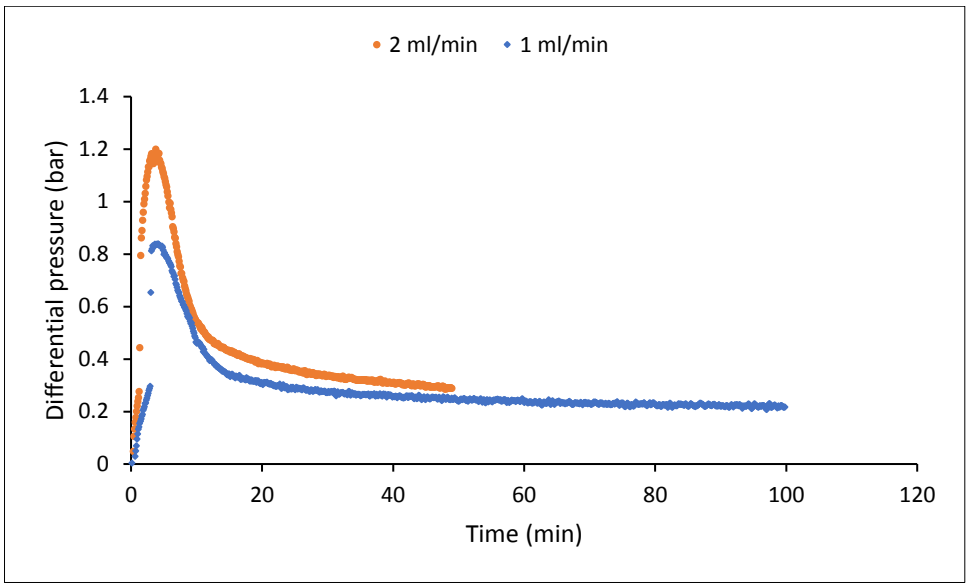

Figure 4-7: Effect of CO_2 injection rate on the differential pressure profile of GCO_2-water displacements conducted at 40 bar and 33 °C

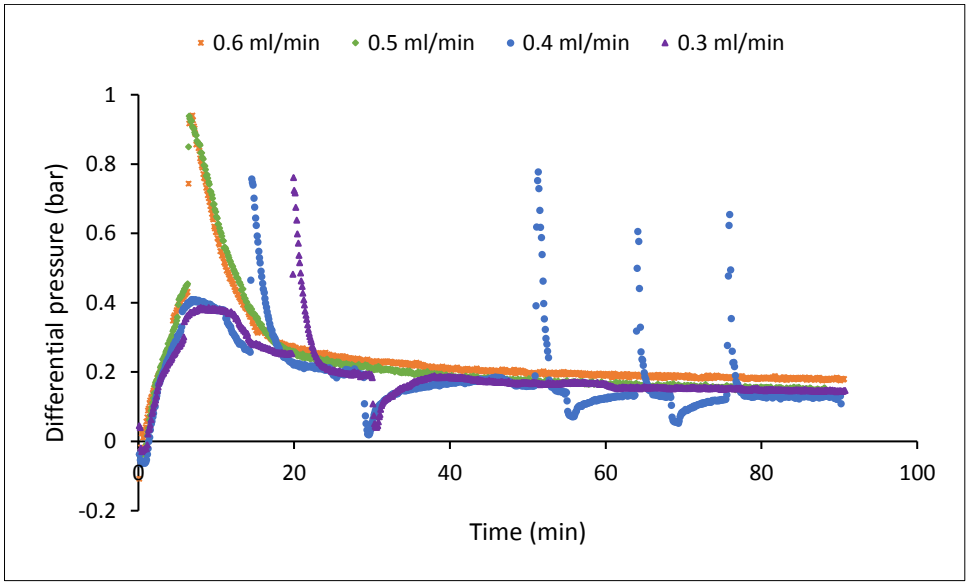

Figure 4-8: Effect of CO_2 injection rate on the differential pressure profile of GCO_2-water displacements conducted at 40 bar and 33 °C

E) To further investigate the effect of CO_2 injection rate on the differential pressure profile and the phenomenon of the PD oscillations particularly, a second set of GCO_2-water displacements have been performed at a higher pressure (70 bar). To enable a clear comparison, the data is presented in two figures: Figure 4-9 and Figure 4-10.

E.1) The data shows clearly that conducting GCO_2-water displacements at higher pressure (70 bar) caused the PD oscillations to appear over a wider range of CO_2 injection rates (from 0.2 to 1 ml/min). It shows also that the change in the maximum and quasi-differential pressures, corresponding time and PD oscillations are dependent on the range of the injection rate; the highest change in the differential pressures occurred as the injection rate increased from 0.4 to 1 ml/min. For illustration, as the CO_2 injection rate increased from 0.4 to 1 ml/min, the maximum-differential pressure increased considerably by around 258% (from 0.845 to 3.024 bar) and the quasi-differential pressure increased by around 224.5% (from 0.265 to 0.86 bar). The corresponding time prolonged by 140% (from 1 to 2.4 min) despite the increase in the injection rate. The frequency of the PD oscillations was almost constant for the last 20 min of both experiments. The increase in the maximum and quasi-differential pressures can be attributed to the increase in the viscous forces; the increase in the corresponding time can be related to the high increase in the magnitude of the maximum differential pressure.

E.2) On the other hand, as the CO_2 injection rate increased from 0.2 to 0.4 ml/min, the maximum-differential pressure was almost constant at around 0.85 bar, the quasi-differential pressure slightly increased, the corresponding time slightly reduced, and the frequency of the PD oscillations considerably decreased but the magnitude of the PD oscillations significantly increased from around 0.25 to 0.825 bar. The nearly constant maximum-differential pressure (0.85 bar) at low injection rates (0.2 to 0.4 ml/min)-core floodings shows a negligible impact for the viscous forces on the differential pressure at the conditions investigated. However, the reduction in the frequency of the PD oscillations might be attributed to CO_2 flow through preferential flow paths.

The frequency of the PD oscillations might depend to a considerable extent on the core sample properties, the change in CO_2 distribution due to the change in the CO_2 injection rate, and the associated operational conditions. For illustration, as the CO_2 injection rate increased from 0.2 to 0.4 ml/min, the CO_2 might have distributed over a wider range of capillaries. Consequently, as the viscous pressure drop declined because of water depletion, the CO_2 flow inside the smaller capillaries was blocked due to their higher resistance to CO_2 flow. Later, as the pressure drop continued, the CO_2 flow in larger capillaries was blocked, too. Ultimately, it came to the point when all capillaries were blocked by the capillary forces [25,

26]. Thus, the increase in CO_2 distribution with increasing injection rate might have led to prolonging the time required for the capillary forces to block the CO_2 production from all opened interconnected flow paths. As a result, since the volume of the opened capillaries were larger with increasing injection rate from 0.2 to 0.4 ml/min; therefore, the frequency of the PD oscillations was reduced.

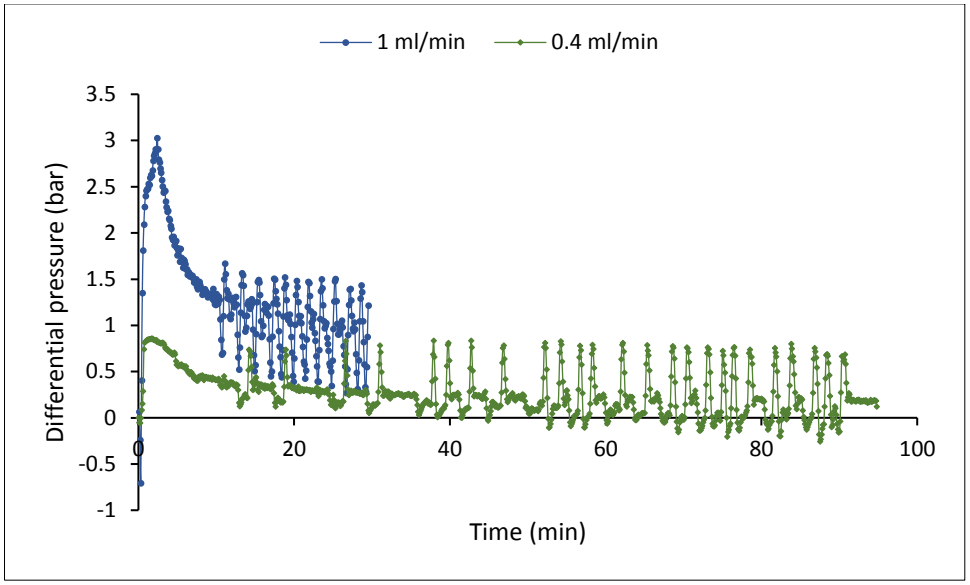

Figure 4-9: Effect of CO_2 injection rate on the differential pressure profile of GCO_2-water displacements conducted at 70 bar and 33 °C

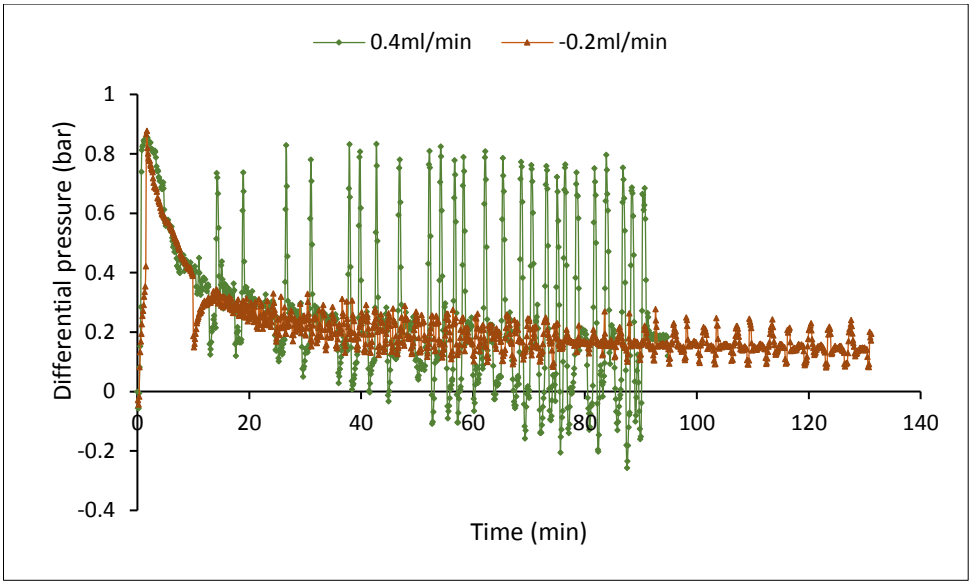

Figure 4-10: Effect of CO_2 injection rate on the differential pressure profile of GCO_2-water displacements conducted at 70 bar and 33 °C

In summary, fluid pressure, temperature and CO_2 injection rate exert significant influences on the differential pressure profile of the GCO_2-water drainage displacements. The differential pressure profile at all fluid pressures, temperatures and injection rates is characterized by a high initial increase immediately followed by a steep rapid pressure reduction and then by a quasi-pressure drop. The differential pressure is controlled by the interplay of both capillary and viscous forces. The increase in capillary forces leads to the appearance of the PD oscillations (the onset points) while the increase in viscous forces causes their impedance.

There are multiple cycles of these oscillations and the occurrence and frequency of these oscillations vary with fluid pressure, temperature and injection rate. The frequency of these oscillating cycles increases as fluid pressure and fluid temperature increase but vary with injection rate and seem to be fluid pressure dependent. These oscillations only occurred at 0.4 ml/min at low pressures (i.e. 40 bar), but the cycles appear over a wider range of injection rates at higher pressures (i.e. 70 bar). The maximum-differential pressure reached during each cycle increases with increasing fluid pressure, temperature and injection rate.

4.2.2 Water Production Behaviour of GCO_2-Water Displacement

During this section, the impact of fluid pressure, temperature, and CO_2 injection rate on the transient outflow rates and the cumulative produced volumes of water and CO_2 are presented and discussed.

4.2.2.1 Effect of Fluid Pressure on GCO_2-Water Production Behaviour

Figure 4-11 and Figure 4-12 present the impact of increasing fluid pressure on the cumulative produced volumes while Figure 4-13 present the impact of increasing fluid pressure on the transient outflow rates. The data show that the cumulative produced volumes of low-fluid pressure displacements are less than the cumulative injected volumes, while the cumulative produced volumes of high-fluid pressure displacements are higher than the cumulative injected volumes. The increase in fluid pressure results in increasing the cumulative produced volumes and decreasing the time needed to achieve most of the water production along with decreasing the magnitude of the highest transient outflow rates but increasing their frequency.

The data from Figure 4-11 demonstrates that for low-fluid pressure displacements, the cumulative produced volumes are always less than the cumulative injected volumes; this can be related to the low displacement efficiency, the less expansion effect, and the high mass transfer rate and diffusion of CO_2 in water [38]. Increasing fluid pressure caused a slight increase in the cumulative produced volumes. As the fluid pressure increased from 40 to 50 bar, the cumulative produced volumes increased by approximately 8% (2.336 ml). The increase in the cumulative volumes with increasing fluid pressure can be associated with increasing displacement efficiency and CO_2 expansion effect.

Figure 4-12 shows that for higher-fluid pressure displacements, the cumulative produced volumes are always higher than the cumulative injected volumes; this can be attributed to the high displacement efficiency and high expansion effect. Increasing fluid pressure led to a considerable increase in the cumulative produced volumes. As the fluid pressure increased from 50 to 70 bar, the cumulative produced volumes increased remarkably by around 26.85%. For the 50 bar -displacement, the cumulative produced volumes were less than the cumulative injected CO_2 volumes by approximately 19.56% (5.72 ml). However, for the experiment conducted at a higher pressure of 70 bar, the cumulative produced volumes were higher than the cumulative injected CO_2 volumes by approximately 7.25% (2.7432 ml).

Figure 4-12 also shows that the increase in fluid pressure results in a decrease in the time needed to achieve most of the water production. For the 70 bar-displacement, the increase in cumulative produced volumes occurred during the first 5 min. After 5 min, the cumulative produced volumes and the cumulative injected CO_2 volumes experienced a linear relation trend. The increase observed in the cumulative produced volumes can be related mainly to the water production; this is because after this period (around 5 min) until the end of the displacements, the cumulative produced and injected volumes were identical. The similarity between the cumulative injected and produced volumes means that CO_2 volumes cannot cause an increase in the cumulative volumes under these experimental conditions. This is because the CO_2 produced shrinks again to its original injected volume after leaving the core sample.

Figure 4-13 shows that the increase in fluid pressure leads to a decrease in the magnitude of the highest transient outflow rates but an increase in their frequency. As the fluid pressure

increased from 50 to 70 bar, the highest transient outflow rate decreased by around 31% (from 0.734 ml/min at 48 min to 0.507 ml/min at 47 min, in sequence) but the time lapse between the successive oscillations decreased, i.e. the frequency increased. On average, the time lapse was 10 min and 4 min for the 50 and 70 bar experiments, respectively. This might be related to the ratio of the magnitude of the capillary forces to the magnitude of the viscous forces [25], for more information see Section 4.2.1.1.

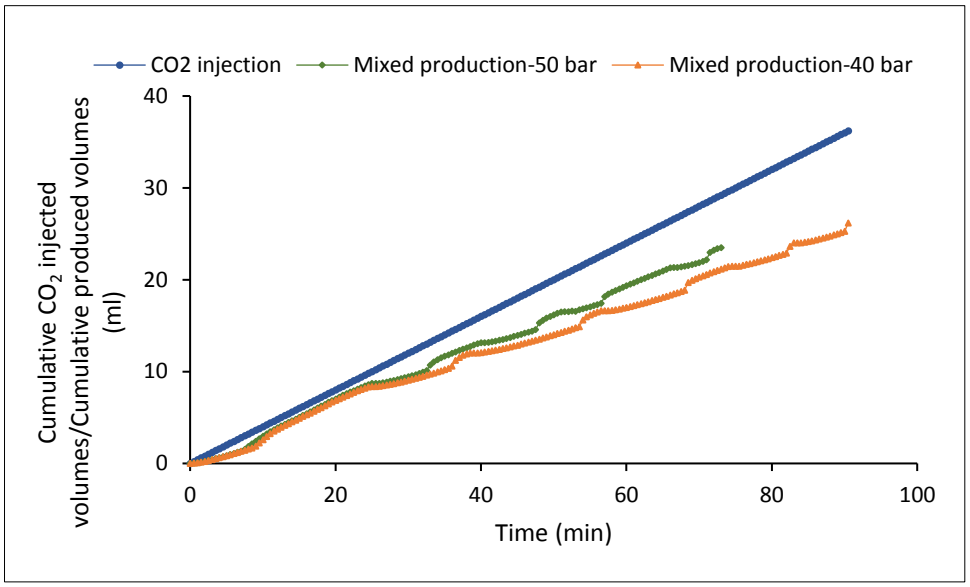

Figure 4-11: Effect of fluid pressure on the cumulative produced volumes of water and CO_2 for GCO_2-water experiments conducted at 0.4 ml/min and 33 °C

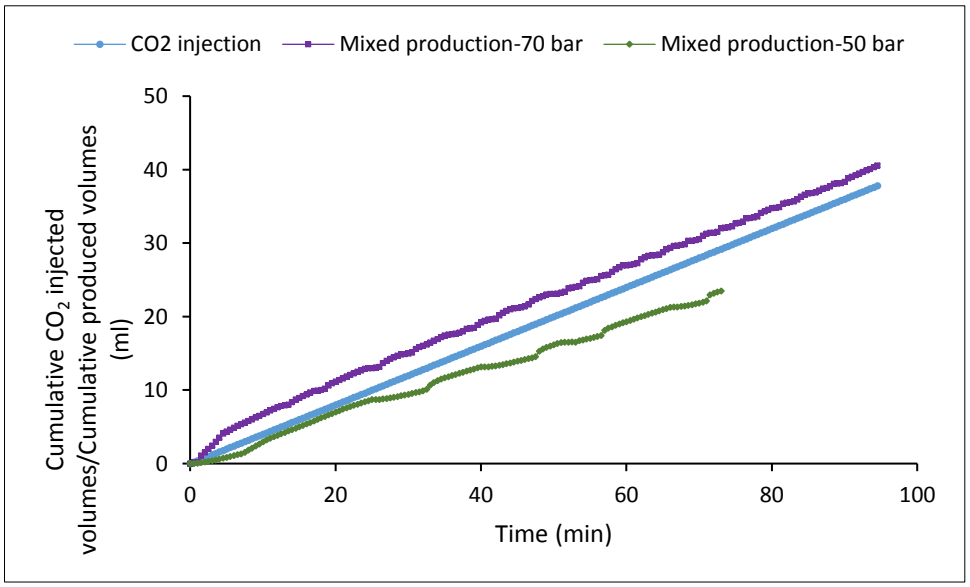

Figure 4-12: Effect of fluid pressure on the cumulative produced volumes of water and CO_2 for GCO_2-water experiments conducted at 0.4 ml/min and 33 °C

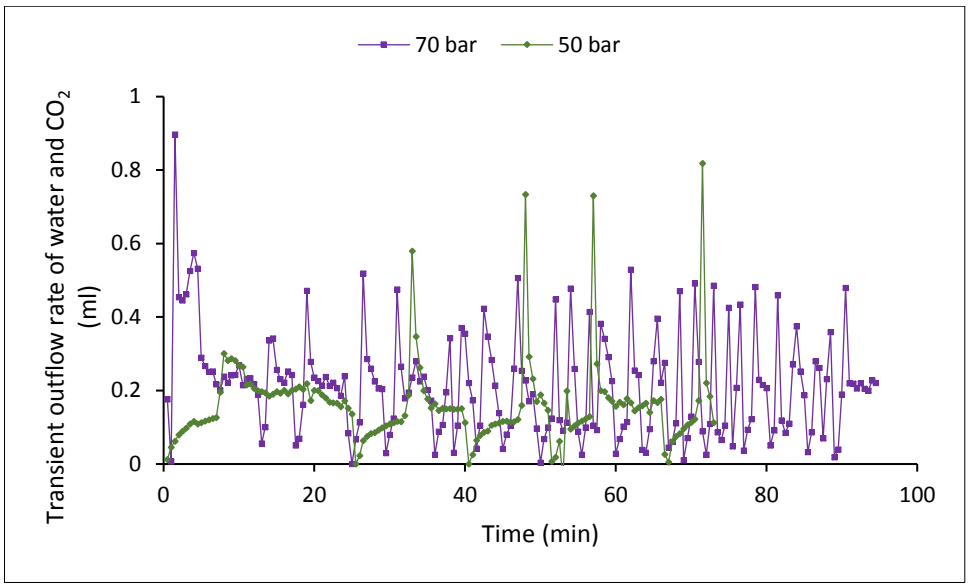

Figure 4-13: Effect of fluid pressure on transient outflow rates for low and high-fluid pressure GCO_2-water experiments conducted at 0.4 ml/min and 33 °C

4.2.2.2 Effect of Temperature on GCO_2-Water Production Behaviour

It should be noted that to avoid repeatability, only some of the typical experiments are presented here. Figure 4-14 and Figure 4-15 present the impact of increasing temperature on the cumulative produced volumes and the transient outflow rates, respectively. The data show that increasing temperature caused a considerable increase in the cumulative produced volumes and in the magnitude of the highest transient outflow rates for the displacements conducted at low-fluid pressures. As the temperature increased from 33 to 45 °C for the 40 bar-experiments, the cumulative produced volumes increased by around 17% (3.45 ml) and the highest transient outflow rates increased by around 15.6% (from 0.63 to 0.747 ml/min at 36.5 min), as shown in Figure 4-14 and Figure 4-15.

On the other hand, Figure 4-16 shows the impact of increasing temperature on the cumulative produced volumes for experiments conducted at high-fluid pressure. The data show that increasing temperature from 33 to 45 °C for the high-fluid pressure (70 bar) experiments, showed no practical change in the cumulative produced volumes, as shown in Figure 4-16, for more information see Section 4.2.1.2. The increase in the cumulative volumes with increasing temperature suggests that high-temperature environments will result in reducing the mass of the stored CO_2.

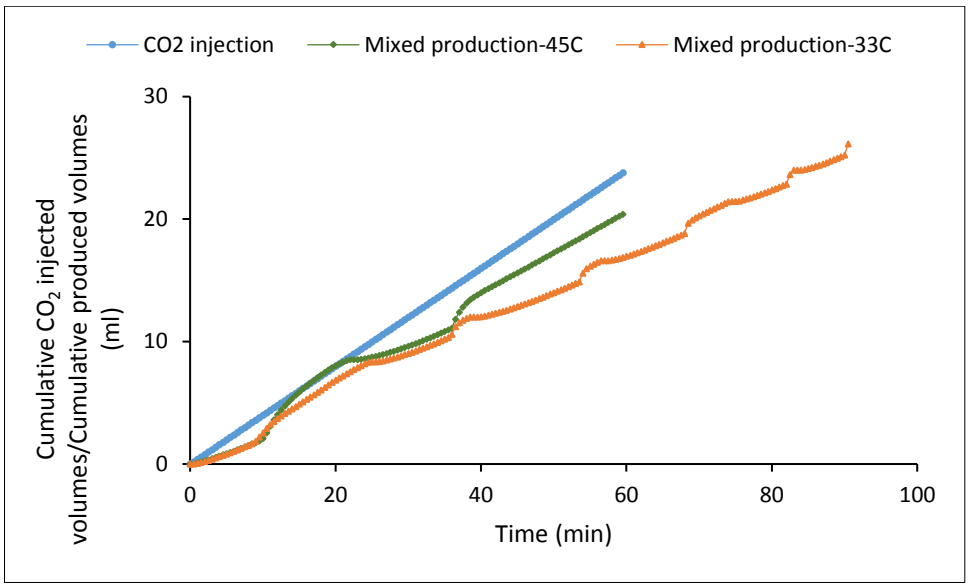

Figure 4-14: Effect of temperature on the cumulative produced volumes of water and CO_2 for GCO_2-water experiments conducted at 40 bar and 0.4 ml/min

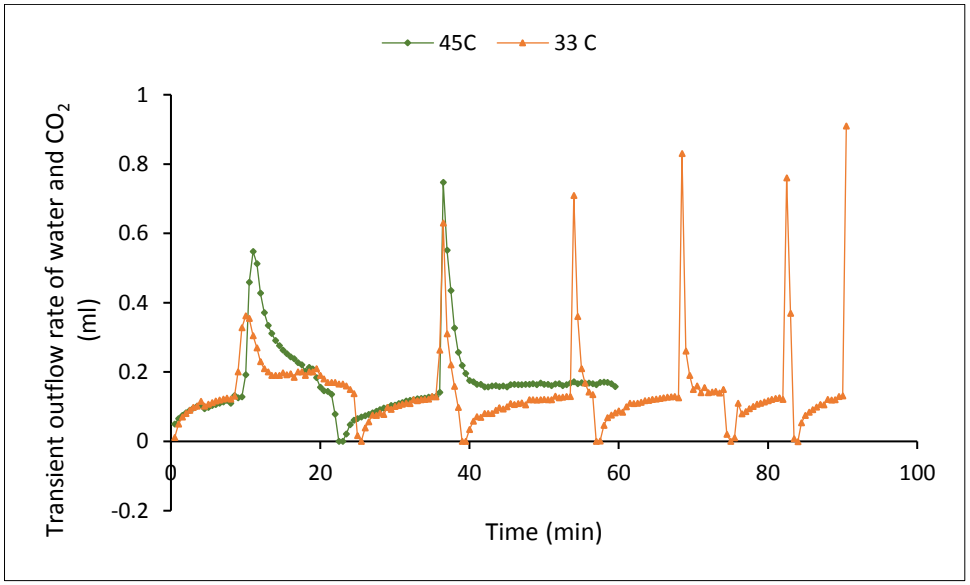

Figure 4-15: Effect of temperature on transient outflow rates for GCO_2-water experiments conducted at 40 bar and 0.4ml/min

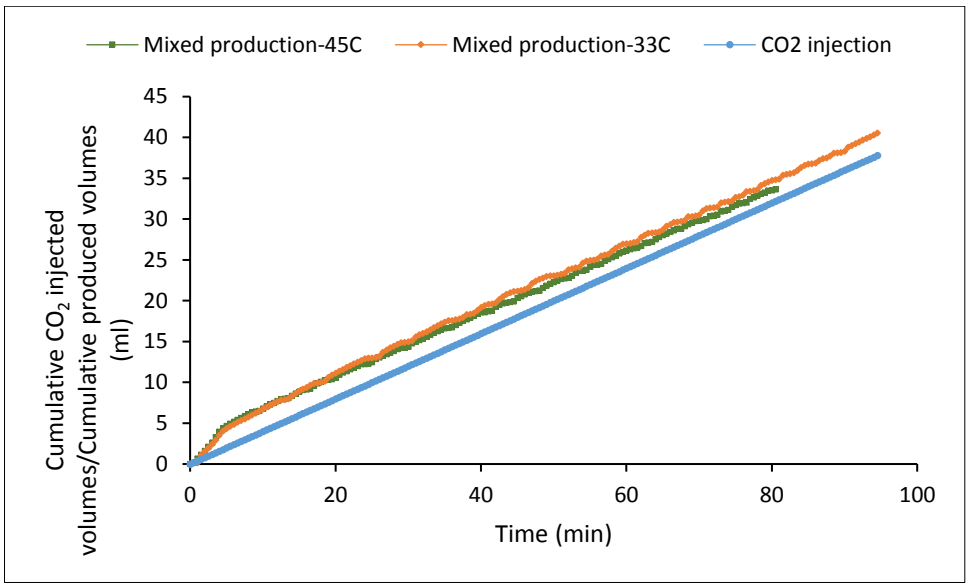

Figure 4-16: Effect of temperature on the cumulative produced volumes of water and CO_2 for GCO_2-water experiments conducted at 70 bar and 0.4ml/min

4.2.2.3 Effect of CO_2 Injection Rate on GCO_2-Water Production Behaviour

Figure 4-17 and Figure 4-18 show the cumulative produced volumes and the transient out flowrates for experiments conducted at 50 bar and 1 ml/min. These Figures have been compared with the data of the 50 bar-0.4 ml/min-displacements presented in Figure 4-11 and Figure 4-15.

The data from Figure 4-11 and Figure 4-15 as well as Figure 4-17 and Figure 4-18 show that as the CO_2 injection rate increases, the difference between the cumulative injected volumes and the cumulative produced volumes decreased significantly (i.e. the cumulative produced volumes increased), the time required to achieve most of the water recovery decreased, and the oscillations in the transient outflow rates disappeared. When the CO_2 injection rate increased from 0.4 to 1 ml/min for the 50 bar-experiment, the difference decreased by around 88% (from 5.72 ml to about 0.69 ml). The increase in the cumulative produced volumes can be related to increasing displacement efficiency. The disappearance of the transient outflow rate oscillations as the CO_2 injection rate increased can be related to the decrease in the ratio of the magnitude of the capillary forces to the magnitude of the viscous forces. Consequently, no blockage of interconnected flow paths occurred because of the high viscous pressure gradient [25].

The data from Figure 4-17 and Figure 4-18 show that the highest increase in the production trends occurred during the period from 0 to 10 min. After around 12 min, the production and the injection trends become equals. This might indicate the precise time when the majority of water production occurred.

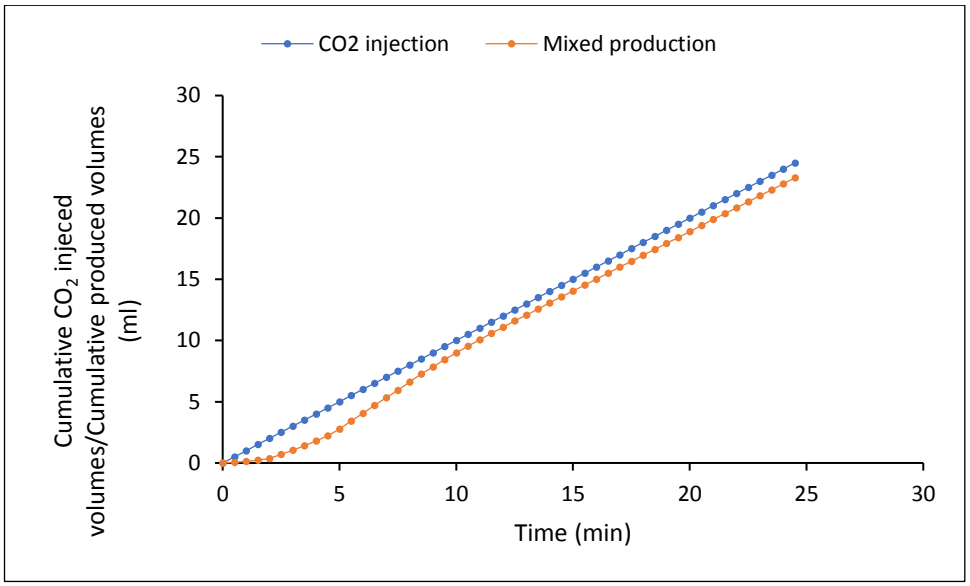

Figure 4-17: The cumulative produced volumes of water and CO_2 and the cumulative injected volumes of CO_2 for a GCO_2-water displacement conducted at 50 bar-1 ml/min-33 °C

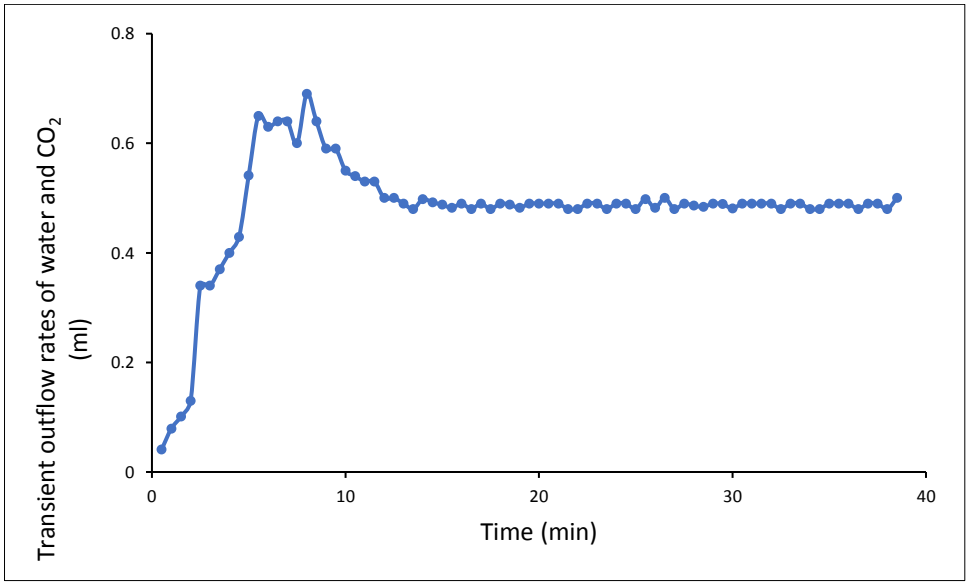

Figure 4-18: Transient outflow rate for a GCO_2-water experiment conducted at 50 bar -1 ml/min-33 °C

In summary, the cumulative produced volumes are less than the cumulative injected volumes for low-fluid pressure displacements, while the cumulative produced volumes are

higher than the cumulative injected volumes for high-fluid pressure displacements. Increasing fluid pressure, temperature, and CO_2 injection rate resulted in increasing the cumulative produced volumes. Increasing fluid pressure and injected rate led to decrease the time needed to achieve most of the water production. Increasing fluid pressure caused a reduction in the magnitude of the highest transient outflow rates while increasing temperature caused an increase in them.

4.2.3 Effect of Fluid pressure, Temperature and CO_2 Injection Rate on Endpoint Effective and Relative Permeabilities of CO_2 and Residual Water Saturation

The effective and relative permeabilities of CO_2 are significantly important to the determination of the efficiency and integrity of CO_2 sequestration in subsurface formations [39, 40]. At the end of the flooding experiment, the volume of the water produced was measured, and the residual water saturation was calculated. Then, the core sample was weighed to confirm the residual water saturation calculations. To calculate the endpoint effective (relative) CO_2 permeability using Darcy's law, the average quasi-differential pressure and the average CO_2 outflow rate of the last period were used [22, 36]. The CO_2 viscosity at the experimental pressure and temperature was calculated using the Peace software website [41].

The results from Table 4-1 shows that both endpoint relative permeability (K_{rCO2}) [42] and residual water saturation (S_{wr}) are dependent on the experimental conditions at which they are measured. The S_{wr} was in the range of 0.38 to 0.42 while the K_{rCO2} was less than 0.25. Busch and Müller obtained a low relative permeability for CO_2, too [39]. Such low relative permeability would tend to decrease injectivity but increase displacement efficiency [43].

The results from Table 4-1 show that in general the increase in fluid pressure, temperature, and injection rate led to an increase in the K_{rCO2} and a decline in the S_{wr}. In case of increasing fluid pressure and temperature, the high increase in the K_{rCO2} can be attributed mainly to the high increase in the volumetric CO_2 injection rate inside the core sample due to the high impact of the gas expansion effect [44, 45]. This increase in volumetric CO_2 injection rate might result in forcing the CO_2 to flow through a wider range of the core sample pores.

Regarding the S_{wr}, the displacements efficiency is controlled by many factors that include relative permeability, wetting conditions, viscous fingering, gravity segregation, amount of crossflow/mass transfer [46], mobility ratio (*M*), and capillary number (*Ca*) [47]. For the GCO_2-water displacement investigated both *Ca* and *M* are small, which suggest a capillary fingering regime [47], more information about *Ca* and *M* can be found in Section 2.4.1.1.4-Chapter 2. The reduction observed in the S_{wr} can be attributed mainly to the increase in the *Ca* and the reduction in *M*. This is because the *Ca* and *M* are the most influential dimensionless parameters that govern GCO_2-water core flooding displacement [47]. As the *Ca* increases, the impact of capillary forces compared to viscous forces decreases. The balance between the viscous forces and capillary forces governs the pore scale drainage displacements [48]. The capillary forces are responsible for the trapping of the injected CO_2 [9, 49]. Thus, decreasing the capillary forces (e.g. due to the reduction in the interfacial tension) will lower the S_{wr} (i.e. enhance the fluid displacements) [50]. On the other hand, reducing the *M* can result in a more uniform displacement of water by CO_2 [51], which can result in reducing the S_{wr}. The data from Table 4-1 show that the increase in the *Ca* and the reduction in *M* can lead to a reduction in the S_{wr} even when the change in both *Ca* and *M* is small. Ding and Kantzas observed that the critical *Ca* for the gas-water system is 2E-8 [52].

The results from Table 4-1 show that increasing the fluid pressure from 40 to 70 bar at 33 °C and 0.4 ml/min caused the K_{rCO2} to increase by around 0.099 and the S_{wr} to decrease by around 0.047. The largest increase in K_{rCO2} and the highest reduction in the S_{wr} occurred as the fluid pressure increased from low-fluid pressure displacements (40 and 50 bar) to high-fluid pressure displacements (70 bar). The observed trend of the K_{rCO2} and S_{wr} are in agreement with the findings of Liu et al. and Bennion and Bachu [51, 53]. Liu et al also observed an increase in the endpoint relative permeability of CO_2 with increasing pressure [53]. Bennion and Bachu observed an increase in the K_{rCO2} and increase in the maximum endpoint CO_2 saturation (i.e. a decrease in S_{wr}) with increasing pressure; they attributed that to the reduction in IFT with increasing pressure [51]. The observed trend of the K_{rCO2} and S_{wr} can also be associated with the relatively high increase in the *Ca* and the high reduction in the *M*.

The results from Table 4-1 show that increasing temperature led to an increase in the K_{rCO2}. However, increasing temperature caused a reduction in the S_{wr} for the displacements

conducted at high-fluid pressure (70 bar) and over a high-temperature increase (33-45 °C). Nonetheless, for the experiments conducted at low-fluid pressure (50 bar) and over a small temperature increase (29-33 °C), the trend of the S_{wr} is dependent on the magnitude of the experimental temperature. For the high-fluid pressure displacements, when the temperature increased from 33 to 45 °C at 70 bar, the K_{rCO2} increased by around 0.035 and the S_{wr} decreased by around 0.02. The reduction in S_{wr} for the 70 bar displacements can be attributed also to the increase in the *Ca* and the reduction in the *M*. For low-fluid pressure displacements, as the temperature increased slightly from 29 to 33 °C at 50 bar, the K_{rCO2} increased by around 0.016. Nevertheless, the S_{wr} value was between around 0.40 and 0.41. The S_{wr} saturation slightly increased by around 0.01 as the temperature increased from 29 to 31 °C, and then slightly decreased by about 0.005 as the temperature increased from 31 to 33 °C. The slight increase in the S_{wr} might be related to the slight reduction in the *Ca* as well as the impact of the capillary forces, which can be seen through the appearance of the PD oscillations when the temperature increased to 31 °C, see Section 4.2.1.2 for more information; the PD oscillations might result in hindering water production to a slight extent. On the other hand, the slight reduction in the S_{wr}, when the temperature further increased to 33 °C, can be associated with the relatively high increase in the *Ca* as well as the slight reduction in the *M*.

Overall, the results from Table 4-1 shows that the increase in the CO_2 injection rate caused an increase in the K_{rCO2} and a reduction in the S_{wr}. Increasing the injection rate from 0.1 to 2 ml/min at 40 bar and 33 °C resulted in an increase in the K_{rCO2} by around 0.0157 and a reduction in the S_{wr} by around 0.05. These findings agree with those in Chang et al. and Akbarabadi and Piri [22, 36]. However, for the core flooding at 0.4 ml/min or less, the S_{wr} trend is not clear. Moreover, the K_{rCO2} of the experiments conducted at 40 bar-0.2 ml-33 °C does not fit linearly in the trend. Increasing the injection rate from 0.6 to 1 ml/min resulted in the highest reduction in the S_{wr}. This can be corresponded to the high increase in the *Ca* from around 7.9 E-8 to 1.3 E-7. For the core flooding performed at 70 bar and 33 °C, increasing the injection rate from 0.2 to 1 ml/min caused a very slight reduction in the S_{wr} by 0.0077. However, the K_{rCO2} increased substantially as the injection rate increased from 0.2 to 0.4 ml/min. Nevertheless, as the injection rate increased to 1 ml/min, a significant reduction in the K_{rCO2} happened again, the reason is not clear. The very slight reduction in the S_{wr} might be because only a slight increase occurred in the *Ca* and that *M* was constant.

Table 4-1: Effect of fluid pressure, temperature, and CO_2 injection rate on endpoint effective and relative permeabilities of gaseous CO_2 and residual water saturation

Parameter	Experiment	K_{fCO2}	K_{rCO2}	S_{wr}	M	Ca
Fluid Pressure Effect	40 bar-0.4 ml/min-33 °C	1.768	0.113	0.4244	46.26	5.265E-08
	50 bar-0.4 ml/min-33 °C	1.987	0.127	0.4089	44.56	6.250E-08
	70 bar-0.4 ml/min-33 °C	2.613	0.212	0.3779	36.10	2.504E-07
Temperature Effect	50 bar-0.4 ml/min-29 °C	1.507	0.096	0.4012	48.69	4.748E-08
	50 bar-0.4 ml/min-31 °C	1.738	0.111	0.4147	46.57	4.698E-08
	50 bar-0.4 ml/min-33 °C	1.987	0.127	0.4089	44.56	6.250E-08
	70 bar-0.4 ml/min-33 °C	2.613	0.212	0.3779	36.10	2.547E-07
	70 bar-0.4 ml/min-45 °C	3.675	0.247	0.3566	31.34	2.714E-07
Injection Rate Effect	40 bar-0.1 ml/min-33 °C	0.67	0.043	0.38	46.26	1.316E-08
	40 bar-0.2 ml/min-33 °C	1.265	0.081	0.446	46.26	2.632E-08
	40 bar-0.3 ml/min-33 °C	0.955	0.061	0.436	46.26	3.948E-08
	40 bar-0.4 ml/min-33 °C	1.493	0.095	0.4244	46.26	5.265E-08
	40 bar-0.5 ml/min-33 °C	1.528	0.097	0.436	46.26	6.581E-08
	40 bar-0.6 ml/min-33 °C	1.535	0.098	0.4167	46.26	7.897E-08
	40 bar-1 ml/min-33 °C	1.793	0.114	0.3837	46.26	1.316E-07
	40 bar-2 ml/min-33 °C	3.13	0.20	0.391	46.26	2.632E-07
	70 bar-0.2 ml/min-33 °C	2.421	0.154	0.3798	36.10	1.273E-07
	70 bar-0.4 ml/min-33 °C	3.625	0.167	0.3779	36.10	2.547E-07
	70 bar-1 ml/min-33 °C	1.976	0.128	0.3721	36.10	6.368E-07

4.3 Summary

In this chapter, the effect of fluid pressure, temperature, and CO_2 injection rate on the dynamic pressure evolution and displacement efficiency during the gaseous CO_2 flooding of a water-saturated sandstone core sample have been investigated in detail. The results indicate that the parameters investigated have a moderate to significant influence on the differential pressure profile, cumulative produced volumes, endpoint CO_2 relative and effective permeabilities and residual water saturation.

For all fluid pressures, temperatures, and CO_2 injection rates, the differential pressure profiles are characterized by a sharp increase followed immediately by a steep pressure reduction, and, finally, by a gradual pressure reduction. The differential pressure profiles are controlled by the interplay of both capillary and viscous forces. The capillary forces produce cyclic oscillations within the differential pressure and fluid production data; the increase in viscous forces impede the appearance of these oscillations.

The appearance and frequency of the oscillations depend on the fluid pressure, temperature, and CO_2 injection rates. The increase in fluid pressure (from 40 to 70 bar) caused an increase in the frequency of the oscillations. Temperature has a significant effect on the cyclic oscillations, which depends to a considerable extent on the fluid pressure. At 50 bar, there was only one cycle with no further oscillation cycles at the lowest temperature of 29 °C, but at 31 °C and 33 °C the increasing temperature resulted in an increase in the frequency of the oscillations and increase in the maximum differential pressure values. The differential pressure oscillation cycles exhibited a very interesting response to varying injection rate and as with temperature, they are dependent on the fluid pressure. At 40 bar, the oscillations were only observed at an injection rate of 0.4 ml/min, whereas at 70 bar the oscillations occurred at all injection rates tested (0.2, 0.4, and 1ml/min).

In general, the increase in fluid pressure, temperature, and CO_2 injection rate led to an increase in the maximum and quasi-differential pressures, the magnitude of the increase in the differential pressures is dependent on the associated fluid pressure, temperature, and injection rate. For displacements conducted at 50 bar, the differential pressure increased as the temperature increased from 29 to 31 °C but decreased as the temperature further increased to 33 °C. Increasing fluid pressure and temperature caused a reduction in the time required to achieve the maximum-differential pressure at the start of the experiment, i.e. corresponding time. Nevertheless, increasing injection rate caused the corresponding time to decrease at low injection rates and increase at high injection rates.

The cumulative produced volumes at the lower-fluid pressure GCO_2-water displacements (e.g. 40-50 bar) are always less than the cumulative injected volumes. On the other hand, the cumulative produced volumes at the higher-fluid pressure (70 bar) displacements are always

higher than the cumulative injected volumes. Increasing fluid pressure, temperature, and injection rate caused an increase in the cumulative produced volumes. Increasing fluid pressure and injection rate reduced the time required to achieve most of the water production. Increasing fluid pressure led to a decrease in the magnitude of the highest transient outflow rates, and vice versa for temperature; increasing injection rate caused the disappearance of the cyclic oscillations.

In general, the increase in fluid pressure, temperature, and CO_2 injection rate led to an increase in the endpoint CO_2 relative permeability (K_{rCO2}) and a decline in the residual water saturation (S_{wr}). The residual water saturation was in ranges of 0.38 to 0.42 while the CO_2 K_{rCO2} was less than 0.25.

4.4 References

1. Saraji S, Piri M, Goual L. The effects of SO_2 contamination, brine salinity, pressure, and temperature on dynamic contact angles and interfacial tension of supercritical CO_2/brine/quartz systems. IJGGC. 2014;28:147-55.

2. Edlmann K, Bensabat J, Niemi A, Haszeldine R, McDermott C. Lessons learned from using expert elicitation to identify, assess and rank the potential leakage scenarios at the Heletz pilot CO_2 injection site. IJGGC. 2016;49:473-87.

3. Miocic JM, Gilfillan SM, Roberts JJ, Edlmann K, McDermott CI, Haszeldine RS. Controls on CO_2 storage security in natural reservoirs and implications for CO_2 storage site selection. IJGGC. 2016;51:118-25.

4. Islam A, Chevalier S, Sassi M. Experimental and Numerical Studies of CO_2 Injection Into Water-Saturated Porous Medium: Capillary to Viscous to Fracture Fingering Phenomenon. Energy Procedia. 2013;37:5511-9.

5. Jiang L, Yu M, Liu Y, Yang M, Zhang Y, Xue Z, et al. Behavior of CO_2/water flow in porous media for CO_2 geological storage. Magnetic Resonance Imaging. 2017;37:100-6.

6. Yu M, Song Y, Jiang L, Li W. CO_2/Water Displacement in Porous Medium Under Pressure and Temperature Conditions for Geological Storage. Energy Procedia. 2014;61:282-5.

7. Rezaei N, Firoozabadi A. Pressure evolution and production performance of waterflooding in n-heptane-saturated fired Berea cores. SPE Journal. 2014;19(04):674-86.

8. Chatzis I, Morrow NR. Correlation of capillary number relationships for sandstone. SPE Journal. 1984;24(05):555-62.

9. Akbarabadi M, Piri M. Relative permeability hysteresis and capillary trapping characteristics of supercritical CO_2/brine systems: An experimental study at reservoir conditions. Advances in Water Resources. 2013;52:190-206.

10. Bikkina P, Wan J, Kim Y, Kneafsey TJ, Tokunaga TK. Influence of wettability and permeability heterogeneity on miscible CO_2 flooding efficiency. Fuel. 2016;166:219-26.

11. Schembre JM, Kovscek AR. A technique for measuring two-phase relative permeability in porous media via X-ray CT measurements. JPSE. 2003;39(1-2):159-74.

12. Alkan H, Cinar Y, Ülker E. Impact of capillary pressure, salinity and in situ conditions on CO_2 injection into saline aquifers. Transport in porous media. 2010;84(3):799-819.

13. Fulcher Jr RA, Ertekin T, Stahl C. Effect of capillary number and its constituents on two-phase relative permeability curves. JPT. 1985;37(02):249-60.

14. Espinoza DN, Santamarina JC. Water-CO_2-mineral systems: Interfacial tension, contact angle, and diffusion—Implications to CO_2 geological storage. Water resources research. 2010;46(7).

15. Chiquet P, Broseta DF, Thibeau S, editors. Capillary alteration of shaly caprocks by carbon dioxide. In Proceedings of the SPE Europec/EAGE Annual Conference; Madrid, Spain, 13–16 June 2005: SPE: Houston, TX, USA, 2005.

16. Chiquet P, Daridon J-L, Broseta D, Thibeau S. CO_2/water interfacial tensions under pressure and temperature conditions of CO_2 geological storage. Energy Conversion and Management. 2007;48(3):736-44.

17. Farokhpoor R, Bjørkvik BJA, Lindeberg E, Torsæter O. Wettability behaviour of CO_2 at storage conditions. IJGGC. 2013;12:18-25.

18. Han F, Busch A, van Wageningen N, Yang J, Liu Z, Krooss BM. Experimental study of gas and water transport processes in the inter-cleat (matrix) system of coal: anthracite from Qinshui Basin, China. Int J Coal Geo. 2010;81(2):128-38.

19. Li X. Experimental studies on pore wetting and displacement of fluid by CO_2 in porous media [doctoral thesis]: University of Edinburgh, Edinburgh, UK; 2015.

20. Behrenbruch P, Huu MTD, Hoang TG, Bui KD, editors. Modelling of drainage capillary pressure: A comparative study of various analytical capillary pressure formulations in matching laboratory results. In Proceedings of the SPE Asia Pacific Oil & Gas Conference and Exhibition; Perth, Australia, 25–27 October 2016: SPE: Houston, TX, USA, 2016.

21. Parvazdavani M, Abbasi S, Zare-Reisabadi M. Experimental study of gas–oil relative permeability curves at immiscible/near miscible gas injection in highly naturally fractured reservoir. Egyptian Journal of Petroleum. 2017;26(1):171-80.

22. Chang C, Zhou Q, Xia L, Li X, Yu Q. Dynamic displacement and non-equilibrium dissolution of supercritical CO_2 in low-permeability sandstone: An experimental study. IJGGC. 2013;14:1-14.

23. Kwelle SO. Experimental studies on resistance to fluid displacement in single pores [PhD. Thesis]: The University of Edinburgh, Edinburgh, UK; 2017.

24. Perrin J-C, Benson S. An experimental study on the influence of sub-core scale heterogeneities on CO_2 distribution in reservoir rocks. Transport in porous media. 2010;82(1):93-109.

25. Nutt C, editor The physical basis of the displacement of oil from porous media by other fluids: a capillary bundle model. Proceedings of the Royal Society of London A: Mathematical, Physical and Engineering Sciences; 1982.

26. Hildenbrand A, Schlömer S, Krooss B. Gas breakthrough experiments on fine-grained sedimentary rocks. Geofluids. 2002;2(1):3-23.

27. Müller N. Supercritical CO_2-brine relative permeability experiments in reservoir rocks—Literature review and recommendations. Transport in porous media. 2011;87(2):367-83.

28. Fathollahi A, Rostami B. Carbonated water injection: Effects of silica nanoparticles and operating pressure. Can J Chem Eng. 2015;93:1949–56.

29. Georgiadis A, Maitland G, Trusler JM, Bismarck A. Interfacial tension measurements of the (H2O+ CO_2) system at elevated pressures and temperatures. Journal of Chemical & Engineering Data. 2010;55(10):4168-75.

30. Banerjee S, Hassenklöver E, Kleijn JM, Cohen Stuart MA, Leermakers FA. Interfacial tension and wettability in water–carbon dioxide systems: Experiments and self-consistent field modeling. The Journal of Physical Chemistry B. 2013;117(28):8524-35.

31. Bennion DB, Bachu S, editors. The impact of interfacial tension and pore size distribution/capillary pressure character on CO_2 relative permeability at reservoir conditions in CO_2-brine systems. In Proceedings of the SPE/DOE Symposium on Improved Oil Recovery; Tulsa, OK, USA, 22–26 April 2006: SPE: Houston, TX, USA, 2006.

32. Yang D, Gu Y, Tontiwachwuthikul P. Wettability determination of the reservoir brine− reservoir rock system with dissolution of CO_2 at high pressures and elevated temperatures. Energy & Fuels. 2007;22(1):504-9.

33. Iglauer S, Mathew MS, Bresme F. Molecular dynamics computations of brine-CO_2 interfacial tensions and brine-CO_2-quartz contact angles and their effects on structural and residual trapping mechanisms in carbon geo-sequestration. J Colloid Interface Sci. 2012;386(1):405-14.

34. Bachu S, Bennion DB. Interfacial tension between CO_2, freshwater, and brine in the range of pressure from (2 to 27) MPa, temperature from (20 to 125) °C, and water salinity from (0 to 334 000) mg· L− 1. Journal of Chemical & Engineering Data. 2008;54(3):765-75.

35. Physics Do. Q & A: Temperature and Water Molecules | Department of Physics | the University of Illinois at Urbana-Champaign 2017 [Available from: https://van.physics.illinois.edu/qa/listing.php?id=1497.

36. Akbarabadi M, Piri M. Geologic storage of carbon dioxide: an experimental study of permanent capillary trapping and relative permeability. In Proceedings of International Symposium of the Society of Core Analysts; Austin, Texas, USA. 18–21 September 2011. p. 18-21.

37. Gunde AC, Bera B, Mitra SK. Investigation of water and CO_2 (carbon dioxide) flooding using micro-CT (micro-computed tomography) images of Berea sandstone core using finite element simulations. Energy. 2010;35(12):5209-16.

38. Plug W-J, Bruining J. Capillary pressure for the sand–CO_2–water system under various pressure conditions. Application to CO_2 sequestration. Advances in Water Resources. 2007;30(11):2339-53.

39. Busch A, Müller N. Determining CO_2/brine relative permeability and capillary threshold pressures for reservoir rocks and caprocks: Recommendations for development of standard laboratory protocols. Energy Procedia. 2011;4:6053-60.

40. Rathnaweera T, Ranjith P, Perera M. Effect of salinity on effective CO_2 permeability in reservoir rock determined by pressure transient methods: An experimental study on Hawkesbury sandstone. Rock Mechanics and Rock Engineering. 2015;48(5):2093-110.

41. Peace software. 2017 [http://www.peacesoftware.de/einigewerte/co2_e.html].

42. Armstrong RT, McClure J, Berill M, Rücker M, Schlüter S, Berg S. Flow regimes during immiscible displacement. Petrophysics. 2017;58(01):10-8.

43. Levine JS, Matter JM, Goldberg DS, Lackner KS, Supp MG, Ramakrishnan T. Two phase brine-CO_2 flow experiments in synthetic and natural media. Energy Procedia. 2011;4:4347-53.

44. Rostami B, Kharrat R, Ghotbi C, Tabatabaie S. Gas-oil relative permeability and residual oil saturation as related to displacement instability and dimensionless numbers. Oil & Gas Science and Technology–Revue de l'Institut Français du Pétrole. 2010;65(2):299-313.

45. Skauge A, Håskjold G, Thorsen T, Aarra M, editors. Accuracy of gas-oil relative permeability from two-phase flow experiments. In Proceedings of International Symposium of the Society of Core Analysts; Calgary, AB, Canada, 7–10 September, 1997.

46. Chukwudeme EA, Hamouda AA. Enhanced oil recovery (EOR) by miscible CO_2 and water flooding of asphaltenic and non-asphaltenic oils. Energies. 2009;2(3):714-37.

47. Kazemifar F, Blois G, Kyritsis DC, Christensen KT. Quantifying the flow dynamics of supercritical CO_2–water displacement in a 2D porous micromodel using fluorescent microscopy and microscopic PIV. Advances in Water Resources. 2015.

48. Heaviside J, Black C, editors. Fundamentals of relative permeability: experimental and theoretical considerations. SPE Annual Technical Conference and Exhibition; 1983.

49. Bachu S, Shaw J. Evaluation of the CO_2 Sequestration capacity in Alberta's oil and gas reservoirs at depletion and the effect of underlying aquifers. Journal of Canadian Petroleum Technology. 2003;42(09).

50. Ahmadi MA, Hasanvand Mz, Behbahani SS, Nourmohammad A, Vahidi A, Amiri M, et al. Effect of operational parameters on the performance of carbonated water injection: Experimental and numerical modeling study. The Journal of Supercritical Fluids. 2015.

51. Bennion DB, Bachu S, editors. Dependence on temperature, pressure, and salinity of the IFT and relative permeability displacement characteristics of CO_2 injected in deep saline aquifers. SPE Annual Technical Conference and Exhibition; 2006.

52. Ding M, Kantzas A. Capillary number correlations for gas-liquid systems. Journal of Canadian Petroleum Technology. 2007;46(02).

53. Liu N, Ghorpade SV, Harris L, Li L, Grigg RB, Lee RL, editors. The effect of pressure and temperature on brine-CO_2 relative permeability and IFT at reservoir conditions. In Proceedings of the SPE Eastern Regional Meeting; Morgantown, WV, USA, 13–15 October 2010: SPE: Houston, TX, USA, 2010.

5 Chapter 5: Liquid CO_2-Water Drainage Displacements

5.1 Introduction

CO_2 in its liquid state can be injected into deep oceanic waters (depths > 3000 m) [1] for CO_2 storage purposes. Liquid CO_2 can also be used as a working fluid to enhance oil recovery in deep and cold formations (e.g., West Sak reservoir: ~110-125 bar, 23.9 °C [2, 3]) and in high-temperature reservoirs [4]. Hamdi and Awang showed a significant enhancement in the displacement efficiency can occur when a low-temperature CO_2 (i.e. liquid CO_2) is injected into a hot reservoir (+ 93 °C) [4].

In comparison to gaseous and supercritical CO_2 phases, liquid CO_2 may be characterized by the highest viscous forces and the lowest capillary forces. This is due to the high density and viscosity, and the relatively high contact angle and less interfacial tension due to the low solubility of CO_2 in water. The low capillary forces and high capillary forces are likely to have a positive impact on displacement efficiency but not on CO_2 integrity.

Despite its practical importance, the literature shows only a scarce research has been allocated to investigate the multiphase flow characteristics of liquid CO_2-water-sandstone system [5-9]. In this study, experimental investigations have been allocated to explore the impact of fluid pressure, temperature, salinity, and CO_2 injection rate on multiphase flow characteristics (differential pressure profile, production profile, displacement efficiency, and endpoint effective and relative permeabilities of CO_2) when a pure liquid CO_2 is injected into a water or brine (1% NaCl, 1% $CaCl_2$, and 5% NaCl) saturated sandstone core sample. The results of this study can help in highlighting the impact of the capillary forces and viscous forces on the multiphase phase flow properties investigated and in showing the conditions when capillary forces or viscous forces dominate the flow. The findings of this study would be of interest for the injection, migration, displacement, storage capacity and security of liquid CO_2 in sandstone formations.

5.2 Results and Discussions

In order to have a deep insight into the two-phase flow characteristics when liquid CO_2 is injected into sandstone formations, the effect of fluid pressure, temperature, CO_2 injection rate and salinity on the differential pressure profile, production behaviour, residual water saturation and endpoint CO_2 effective and relative permeabilities have been investigated. The experimental data has been categorized into four main sections. The first main section explains the pressure and the production behaviour for a typical liquid (L) CO_2-water displacement. Section two to three deal with the impact of fluid pressure, temperature, CO_2 injection rate and salinity on the differential pressure profile and production behaviour; while section four deal with their influence on the endpoint CO_2 effective and relative permeabilities and residual water saturation. During this chapter, the corresponding time refers to the time needed to reach the maximum-differential pressure. The quasi-differential pressure refers to the differential pressure at the end of the core flooding. It should be noted that to avoid repeatability, the background information about differential pressure profile and the governing equations presented in Chapter 4-Section 4.2 are used here.

5.2.1 Pressure and Production Behaviour for Typical Liquid CO_2-Water Displacement

To gain a deep understanding of the dynamic behaviour of LCO_2-water displacement, the pressure and production behaviour for a typical LCO_2-water displacement conducted at 60 bar, 0.4 ml/min, and 20 °C will be discussed.

5.2.1.1 Pressure Behaviour for a Typical LCO_2-Water Displacement

Figure 5-1 shows the pressure data for a typical LCO_2-water displacement. The results show that the pressure data can be categorized easily into three distinct periods of only water production, mixed (water and CO_2) production, and only CO_2 production. The pressure data will be discussed according to these periods.

Prior to the commencing of the first production period, i.e. before CO_2 breakthrough into the core sample, and during the very first time of 0.4 min, the inlet and outlet pressures increased sharply by around 0.769 and 0.451 bar, respectively. The sharp rise of the inlet pressure, which propagates quickly to the outlet face, was because of the first contact of CO_2 with the frontal face of the core sample. The differential pressure corresponding to this sharp rising

was around 0.271 bar. The brief time of 0.4 min before CO_2 breakthrough can be associated with the low entry pressure and the high density of liquid CO_2 phase. The high density of liquid CO_2 phase means a brief time is required for LCO_2 to be compressed to the required pressure.

During the following period of 6 seconds (s), from 0.4 to 0.5 min, the differential pressure increased sharply by 0.192 bar to reach its highest value of 0.463 bar. This further increase in the differential pressure might have been required to force CO_2 to enter smaller pores to provide enough space for the injected CO_2.

The next interval that lasted for around 6.5 min, from 0.4 to 6.9 min, corresponded to the first period of only water production. Generally, the first period is characterized by a gradual reduction in the pressure data. This gradual reduction can be related to the reduction in the applied viscous forces due to the replacement of water (a more viscous fluid) by CO_2 (a less viscous fluid). Nonetheless, during the first interval of 24 s, from 0.5 to 0.9 min, the pressure data was characterized by a sharp decline; the drop in the inlet pressure was higher than that in the outlet pressure. The inlet pressure dropped by 0.379 bar while the outlet pressure decreased by 0.297 bar. This sharp decline indicates the start of CO_2 invasion in the core sample. 0

During the following period from 0.9 to 2.2 min, the pressure data increased again, by about 0.077 bar, to enable the injected CO_2 to continue its water displacement. During the next interval from 2.2 to 6.9 min, the differential pressure decreased again by around 0.042 bar. The highest reduction occurred again in the inlet pressure readings. The inlet pressure decreased by 0.066 bar whilst the outlet pressure declined by about third of the inlet pressure value; it decreased by 0.024 bar.

The second period of mixed production (water and CO_2 production) lasted for about 22 min. It lasted from around 6.9 to 29.3 min. The differential pressure dropped by approximately 0.181 bar; and, most of its reduction (around 66%) occurred during the first 7.4 min. The inlet pressure readings dropped by around 0.205 bar while the outlet pressure readings decreased by around 0.024, which is around the tenth of the inlet pressure reduction. The pressure drop in this period might be related to the reduction in both capillary and viscous forces. The

reduction in the capillary forces occurred as more capillary pores were opened to flow [10]; the continuous reduction in the viscous forces was due to the continuous increase in the CO_2 saturation at the expense of water saturation; i.e. leading to an increase in the relative permeability of CO_2 but reducing that of water.

The third period lasted from 29.3 min to the end of the experiment. This period is characterized by a quasi-differential pressure, especially on the outlet side. The inlet pressure reduced by 0.032 bar while the outlet pressure declined only by 0.005 bar.

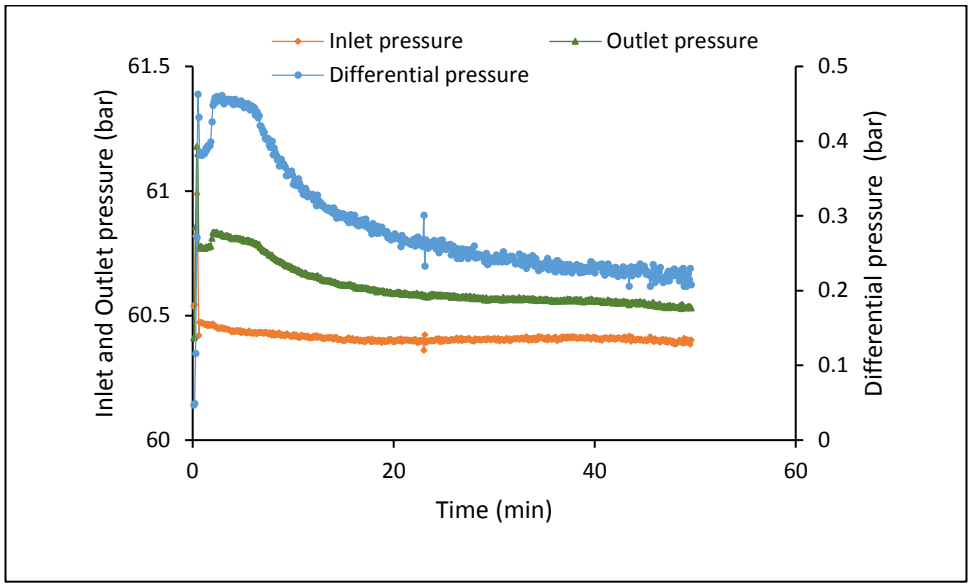

Figure 5-1: Inlet, outlet, and differential pressure profiles of a LCO_2-water displacement conducted at 60 bar, 0.4 ml/min, and 20 °C

A.1.1.1 Production Behaviour for the Typical LCO_2-Water Displacement

Figure 5-2, Figure 5-3 and Figure 5-4 present the transient outflow rate of water and CO_2, cumulative volumes, and water recovery profiles for the LCO_2-water displacement presented in Section 5.2.1, respectively.

The data from Figure 5-2 show that the transient outflow rates of water and CO_2 were more or less equal to the injection rate of CO_2 (0.4 ml/min). Consequently, the cumulative injected volumes and the cumulative produced volumes of the LCO_2-water displacement were identical, as shown in Figure 5-3. The identicalness might be because of the slight impact of the dissolution and diffusion of liquid CO_2 in the water on the production behaviour [11]. This is because the mass transfer rate and the diffusion of the liquid CO_2 in water are negligible [11].

The data from Figure 5-2 show also the limits of the three distinct periods of only water production, mixed production of water and CO_2, and finally only CO_2 production period, respectively. The displaced volumes of water during these three periods: [0.4-6.9], [6.9-29.3], and [29.3-49.5] minutes were 2.59, 0.84, and ≈ 0 ml, respectively. These produced volumes were accounted for 75, 25, and 0 % of the total water production, which corresponded to 50, 16, and 0 % of the total core pore volume, as shown in Figure 5-4. The average flowrates during the three periods were 0.4, 3.65×10^{-2}, and 0 ml/min, respectively.

The data from Figure 5-4 show also that the LCO_2-water displacement required 2.32 pore volumes (PVs) of liquid CO_2 to be injected to achieve the highest water recovery of 65.9%. During the first production period, i.e. before the CO_2 breakthrough out of the core sample, the water recovery percentages was 50.37%. To obtain this recovery percentage, the LCO_2-water displacement required about 0.54 PVs of liquid CO_2 to be injected. During the mixed production period, the water recovery percentage was around 16.3%. This required about 1.7 PVs of liquid CO_2 to be injected during a period of around 23 min.

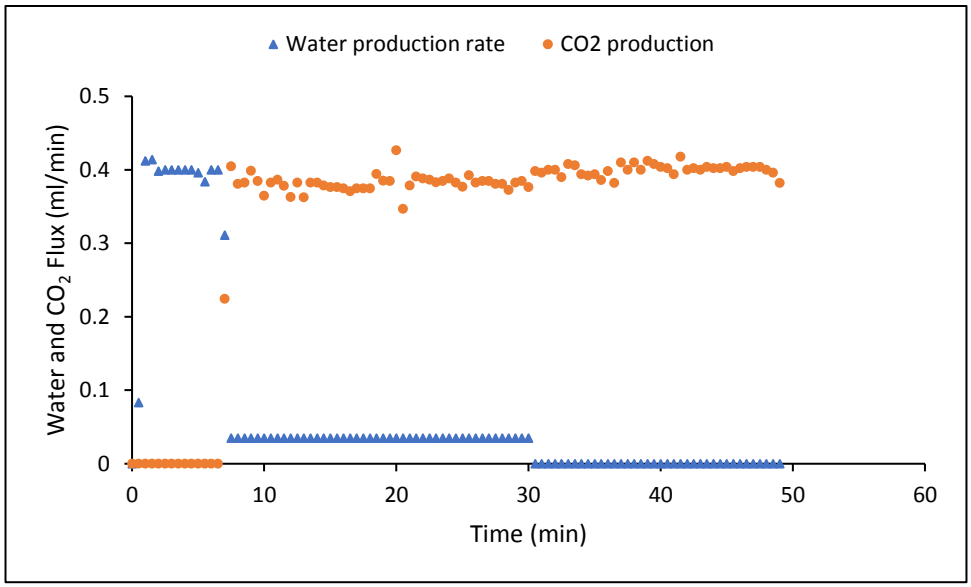

Figure 5-2: Transient flowrates of water and CO_2 profiles of a LCO_2-water displacement conducted at 60 bar, 0.4 ml/min and 20 °C

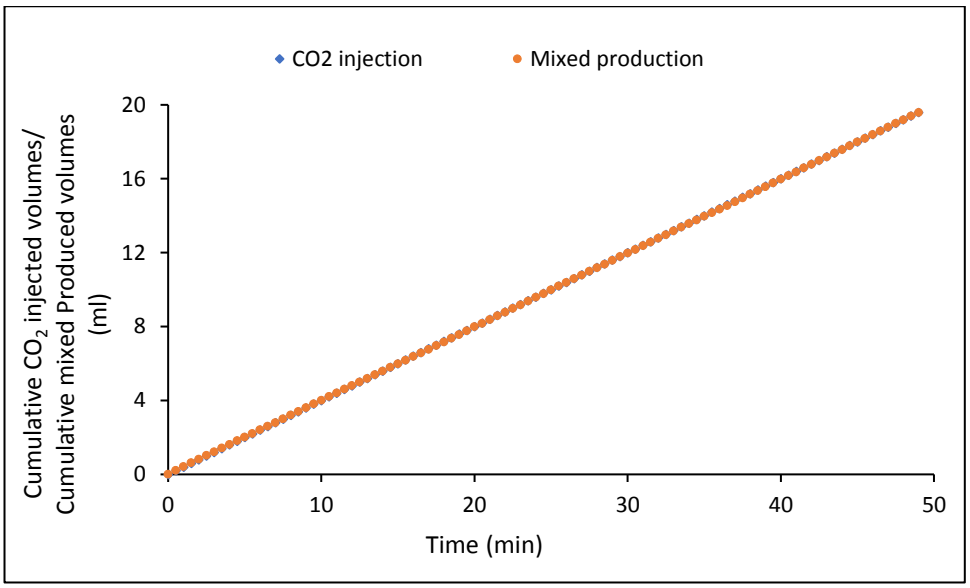

Figure 5-3: Cumulative injected volumes of CO_2 and cumulative volumes of produced water and CO_2 of a LCO_2-water displacement conducted at 60 bar, 0.4 ml/min and 20 °C

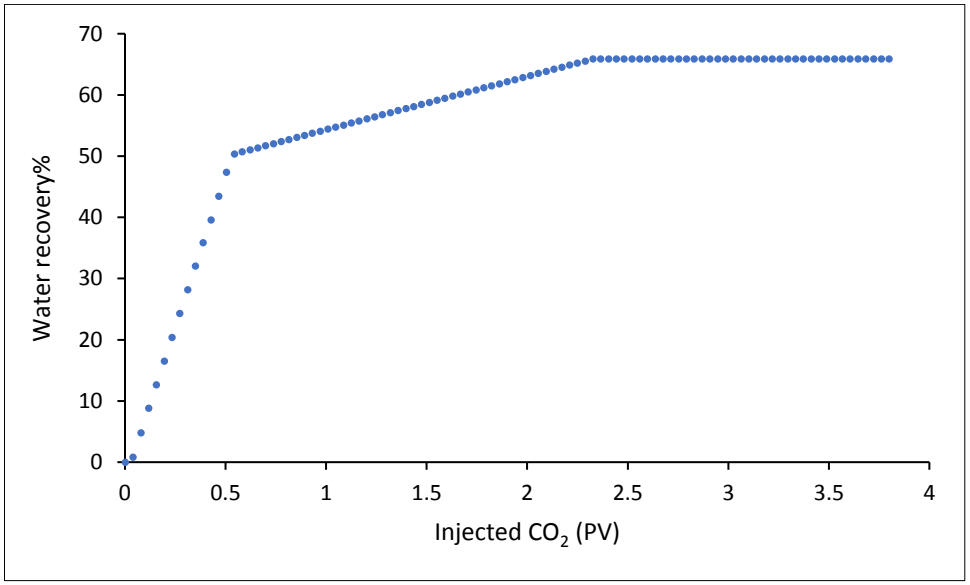

Figure 5-4: Water recovery profile of a LCO_2-water displacement conducted at 60 bar, 0.4 ml/min and 20 °C

5.2.2 Differential Pressure Profile of Liquid CO_2-Water Drainage Displacements

To examine the effect of fluid pressure, experimental temperature, salinity (brine concentration and valency), and CO_2 injection rate on the differential pressure and production behaviour, series of LCO_2-water (brine) displacements were conducted at various

fluid pressures (60, 70 and 90 bar), different experimental temperatures (20 and 29 °C) and various CO_2 injection rates (0.1, 0.4 and 1ml/min).

5.2.2.1 Effect of Fluid Pressure on the Differential Pressure Profile of Liquid CO_2-Water Displacements

Figure 5-5 and Figure 5-6 present the impact of increasing fluid pressure on the differential pressure profile. The results show that for all fluid pressures, the differential pressure profile experienced a sharp increase that is followed by a quasi-stable pressure reduction for a while; and then, it experienced a high-pressure reduction that is followed by a gradual pressure reduction.

Increasing the fluid pressure led to an increase in the differential pressure profile, which further increased with the injection rate. For illustration, as the fluid pressure increased from 60 to 70 bar, the differential pressure during the early times of the flooding increased by around 11% (from around 0.45 to 0.5 bar) for the displacements conducted at 0.4 ml/min and by around 14% (from around 1.58 to 1.8 bar) for the displacements performed at 1 ml/min; however, the differential pressure at the end of the displacements increased by around 11% (from 0.222 to 0.247 bar) for the displacements conducted 0.4 ml/min and by around 17.5% (from 0.706 to 0.829 bar) for the displacements conducted at 1 ml/min.

According to Eq.4-1-Chapter 4, the most likely reason behind the increase in the differential pressure profile is the increase in the applied viscous forces. This is because the increase observed in the differential pressure profile is the net result of the increase in the viscous forces and the reduction in the capillary forces. With increasing pressure, the viscous forces increase due to increasing CO_2 viscosity while the capillary forces decrease due to reducing CO_2-water interfacial tension (from around 34.9 to 29.7 mN/m), and increasing contact angle owing to increasing CO_2 solubility [12].

To confirm that the increase in the differential pressure profile with increasing pressure is because of increasing the viscous forces due to increasing CO_2 viscosity, the data presented in Figure 5-5 were normalized against CO_2 viscosity. The result was an identical trend between the pressure profile of both 60 and 70 bar-experiments, as shown in Figure 5-7. This confirms that in the case of liquid CO_2-water displacements, viscous forces are more influential than capillary forces as fluid pressure increases.

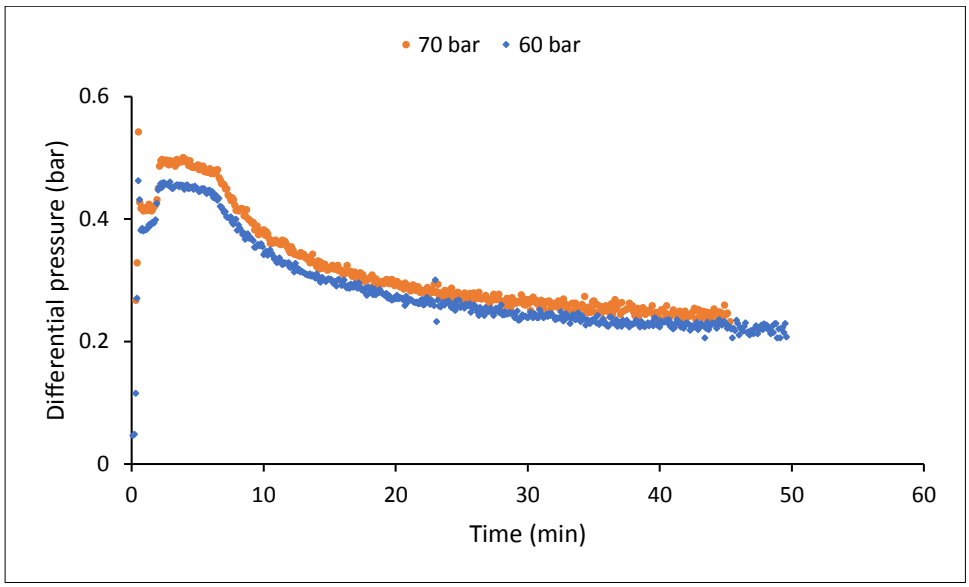

Figure 5-5: Effect of fluid pressure on the differential pressure profile of LCO_2-water displacements conducted at 0.4 ml/min and 20 °C

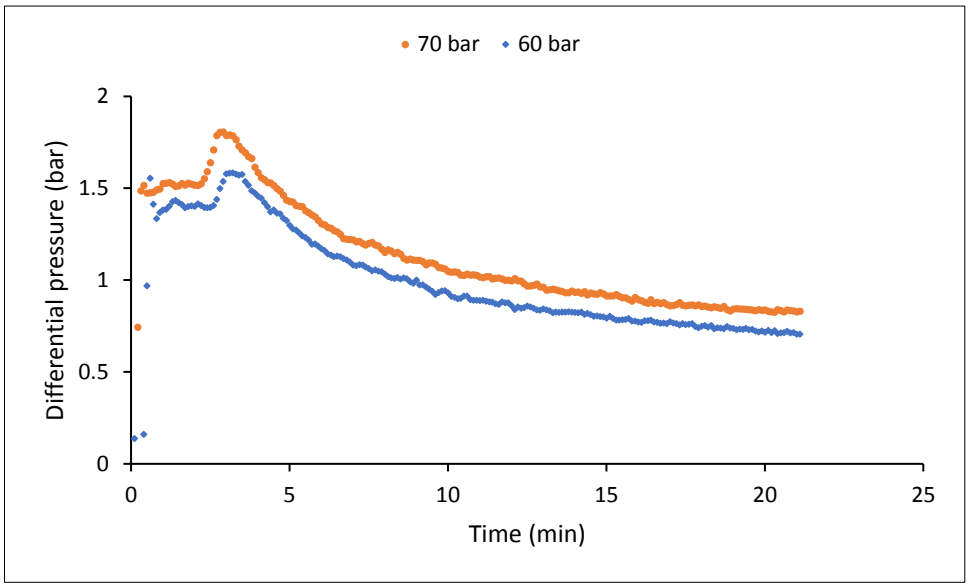

Figure 5-6: Effect of fluid pressure on the differential pressure profile of LCO_2-water displacements conducted at 1 ml/min and 20 °C

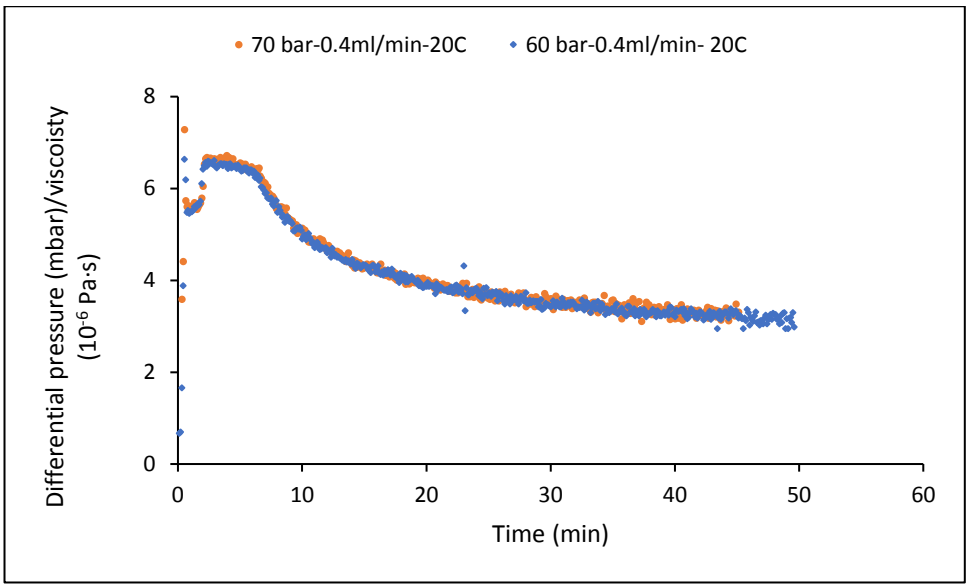

Figure 5-7: A viscosity normalised differential pressure profiles of LCO_2-water displacements conducted at 20 °C and 0.4 ml/min

5.2.2.2 Effect of Temperature on the Differential Pressure Profile of Liquid CO_2-Water Displacements

Figure 5-8 presents the impact of increasing temperature on the differential pressure profile. The results show that the differential pressure profile was stable during the first period that lasted for about 16 min, was reducing overtime during the mixed period, and was increasing over time during the last period; consequently, after around 200 min, the differential pressure profile of the 29 °C-experiment became higher than that of the 20 °C-experiment. Moreover, the results reveal that increasing temperature generated oscillations in the differential pressure profiles. The increase in the differential pressure profile is likely to occur because of the blocking of the CO_2 outflow paths when the viscous forces become less than the capillary forces [13]. The second possible reason is that, after around 180 min, the impact of viscous forces might become higher than that of capillary forces as most of the water was displaced; thereby CO_2 was flowing through opened pores [10]. The oscillations might have occurred as the energy of the CO_2 molecules increased with increasing temperature.

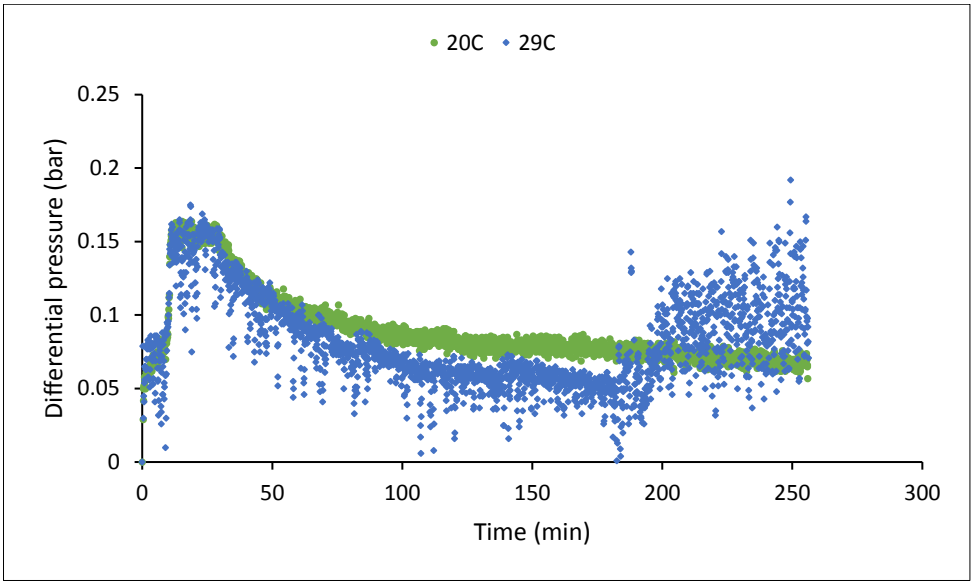

Figure 5-8: Effect of temperature on the differential pressure profile of LCO_2-water displacements conducted at 90 bar and 0.1 ml/min

5.2.2.3 Effect of CO_2 Injection Rate on the Differential Pressure Profile of Liquid CO_2-Water Displacements

Figure 5-9 and Figure 5-10 show the impact of increasing CO_2 injection rate on the differential pressure profile; while Figure 5-11 presents the dynamic change in the differential pressure profile with increasing injection rate. The increase in injection rate led to three identifiable trends (A-C):

A) The data from Figure 5-9 and Figure 5-10 show that increasing injection rate resulted in a considerable increase in the differential pressure, which slightly decreased (by around 3%) as the fluid pressure increased. For illustration, increasing the injection rate for the 60 bar-experiments caused the maximum-differential pressure to increase by more than 236% (from 0.463 to 1.554 bar) and the quasi-differential pressure to increase by 240% (from 0.208 to 0.707 bar), as shown in Figure 5-9. Nonetheless, increasing the injection rate for the 70 bar-experiments caused the maximum-differential pressure to increase by around 233% bar (from 0.543 to 1.807 bar) and the quasi-differential pressure to increase by 237% (from 0.247 to 0.832 bar), as shown in Figure 5-10. According to Eq.4-1-Chapter 4, the observed increase in the maximum and quasi-differential pressures can be related only to the increase in viscous forces due to the increase in the CO_2 injection rate. However, the reduction observed in the differential pressures with the fluid pressure can be associated with the reduction in the

capillary forces with increasing fluid pressure, see Section 4.2.2.1–chapter 4 for more information.

B) The data from Figure 5-11 show that increasing CO_2 injection rate from 0.4 to 1 ml/min caused the differential pressure to increase by more than 3.5 times, except for the first 5 min interval. During this interval, the ratio of the differential pressures decreased quickly from around 3.5 to 2.5 times. The quick reduction in the differential pressure might reflect the high replacement of the water (a more viscous fluid) by CO_2 (a less viscous one) and the high increase in the CO_2 relative permeability at the expense of water relative permeability. After more than 5 min until the end of the experiment, the differential pressure ratio profiles presented in Figure 5-11 experienced a quasi-steady profile. This indicates that the majority of water production happened during the first 5 min, therefore the capillary and viscous forces experienced a slight reduction (as most waters were produced and most capillaries were opened to flow [10]) leading to a small reduction in the differential pressure profile ratio.

C) The data from Figure 5-9 and Figure 5-10 show that increasing injection rate caused a high spike in the differential pressure profile after the initial increase, which is immediately followed by a sharp reduction and then by a gradual reduction. The spikes in the differential pressure immediately before CO_2 breakthrough might have occurred because of the sweeping of water inside the pipeline segments [14] or it might happen because the injected

CO_2 had to open new flow paths after the initial entry as the available space was not sufficient for the injected CO_2, which depends on the core sample properties.

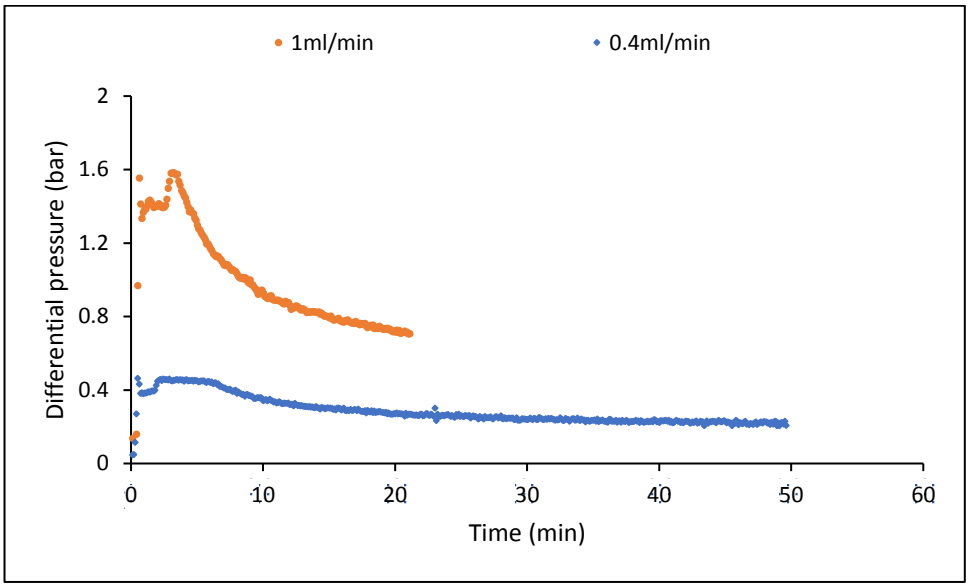

Figure 5-9: Effect of CO_2 injection rate on the differential pressure profile of LCO_2-water displacements conducted at 60 bar and 20 °C

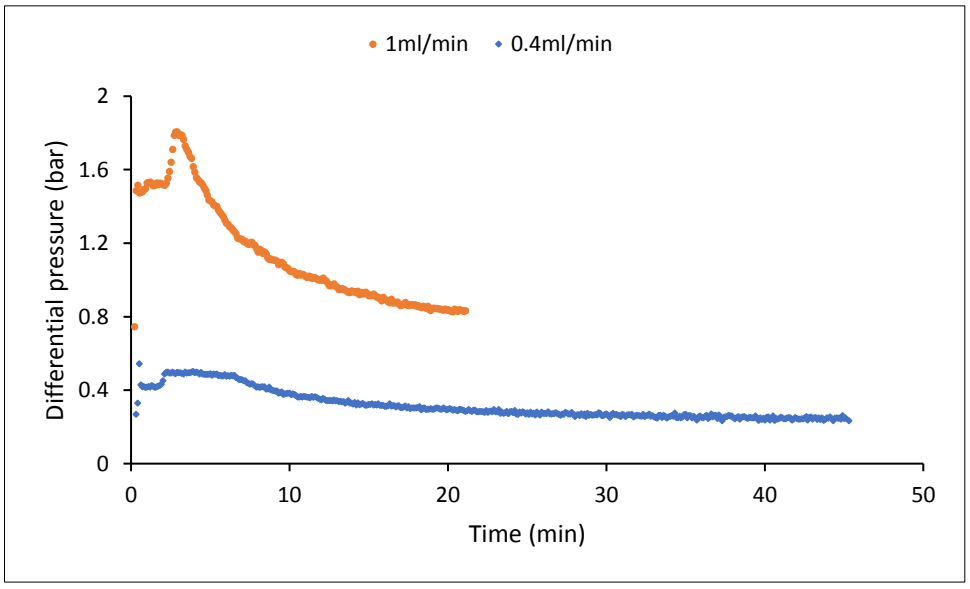

Figure 5-10: Effect of CO_2 injection rate on the differential pressure profile of LCO_2-water displacements conducted at 70 bar and 20 °C

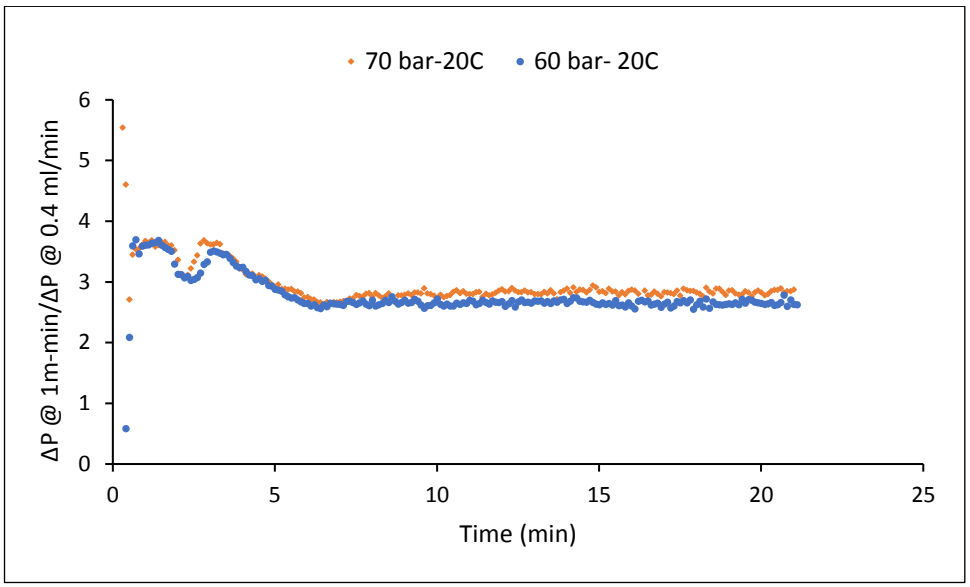

Figure 5-11: The ratio of the differential pressure of 1 ml/min-experiment to the differential pressure of the 0.4 ml/min-experiment for LCO_2-water displacements conducted at 60 and 70 bar and 20 °C

5.2.2.4 Effect of Salinity on the differential pressure profile of liquid CO_2-brine (water) displacements

Figure 5-12 and Figure 5-13 present the impact of salinity (brine concentration and valency) on the differential pressure profile at different injection rates. The results reveal that increasing brine concentration and valency caused a slight increase in the differential pressure profile with a slight change in the differential pressure profile, mainly during the first period.

Figure 5-12 shows that increasing brine concentration and valency led to a slight increase in the differential pressure profile, primarily during the first period. Overall, the order of the differential pressure was as follows: LCO_2-1% $CaCl_2$ > LCO_2-5% NaCl > LCO_2-1% NaCl > LCO_2-DIW displacement. The order of the differential pressure was according to the cations arrangement in terms of their order of impact on the increase in surface tension: Cs^+ <Rb^+ <NH^{4+} <K^+ <Na^+ <Li^+ <Ca^{2+} Mg^{2+} [15]. According to Eq.4-1-Chapter 4, the increase in the differential pressure can be related largely to the increase in the capillary forces because of increasing surface tension with increasing brine concentration and valency. The viscous forces are not expected to have an impact on the differential pressure as no practical change is expected to occur in viscosity with adding slight amounts of brine to the deionised water.

Figure 5-13 shows that both deionised water and 1% NaCl displacements showed similar differential pressure profiles. On the other hand, both 1% $CaCl_2$ and 5% NaCl–displacements profiles were characterized by almost identical profiles; their profiles were characterized by a spike before starting declining, for more information about the spikes see Section 5.2.2.3-observation C.

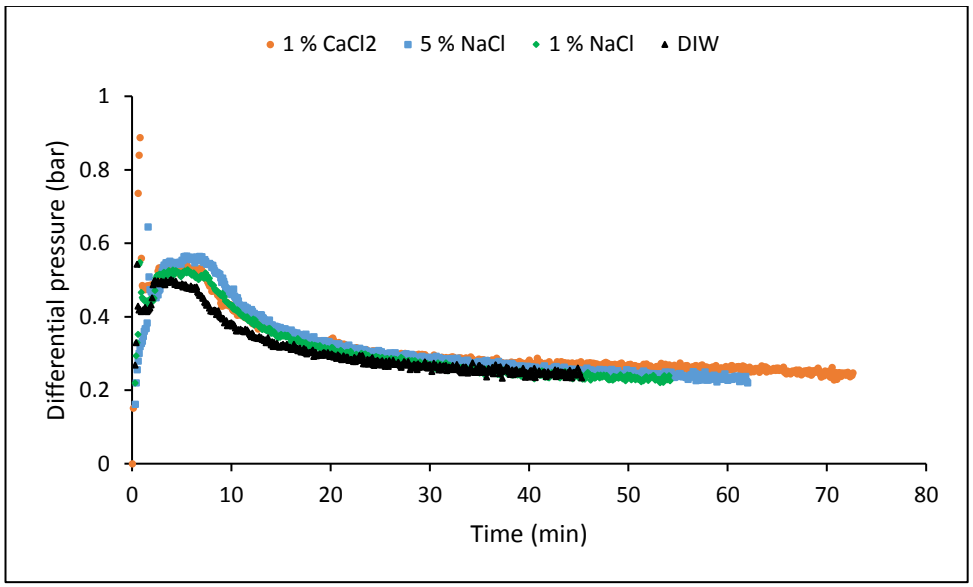

Figure 5-12: Effect of salinity on the differential pressure profile of LCO_2-brine (DIW) displacements conducted at 70 bar, 0.4 ml/min, and 20 °C

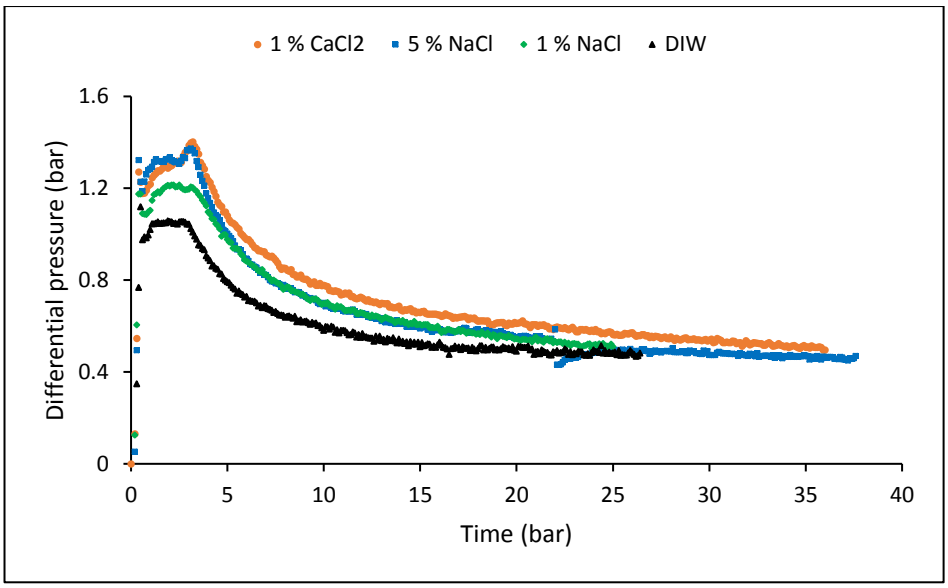

Figure 5-13: Effect of salinity on the differential pressure profile of LCO_2-brine (water) displacements conducted at 70 bar, 1 ml/min, and 20 °C

In summary, the differential pressure profile experienced a sharp increase that is followed by a quasi-stable pressure reduction for a while; and then, it experienced a high-pressure reduction that is followed by a gradual pressure reduction. The differential pressure profiles are characterized by: (a) no change in their shape with increasing pressure, (b) an increase in the differential pressure profile at the end of the displacements with increasing temperature, (c) spikes in the differential pressure profile, after the initial increase, with increasing injection rate, and (d) only slight changes, mainly during the first period, with increasing salinity (brine concentration and valency).

The differential pressure profile: (a) slightly increased with increasing pressure; this slight increase increased with the injection rate, (b) was stable during the first period, decreased during the mixed period, and increased again during the last period with increasing temperature, (c) considerably increased with increasing injection rate, mainly during the first five minutes; this considerable increase was slightly decreased by around 0.3% as the fluid pressure increased from 60 to 70 bar, and (d) slightly increased, mainly during the first period, with increasing salinity. The order of the differential pressure profile with increasing salinity was as follows: LCO_2-1% $CaCl_2$ > LCO_2-5% NaCl > LCO_2-1% NaCl > LCO_2-DIW displacement.

5.2.3 Water Production Behaviour of Liquid CO_2-Water (brine) Displacements

In this section, we will discuss the effect of fluid pressure, temperature, CO_2 injection rates, and water salinity on water production behaviour.

5.2.3.1 Effect of Fluid Pressure on Water Production Behaviour during LCO_2 Injection.

Figure 5-14, Figure 5-15 and Figure 5-16 present the transient outflow rates, cumulative volumes, and water recovery profiles of LCO_2-water displacements, respectively.

The data from Figure 5-14 and Figure 5-15 show that increasing fluid pressure led to a slight reduction in both the transient outflow rates of water and CO_2 and the cumulative produced volumes. As the pressure increased from 60 to 70 bar, the cumulative produced volumes at the end of the experiments decreased slightly by around 0.373 ml. This slight reduction can be related to the increase in solubility and compressibility of liquid CO_2 with increasing fluid pressure [16, 17].

The data from Figure 5-16 show that increasing fluid pressure caused a slight increase in the total water recovery with a very slight increase in the amount of water production and the length of the first period. As the fluid pressure increased from 60 to 70 bar, the water recovery (W_R) increased by around 2% (from 65.9 to 67.87%), the water production of the first period increased by 0.003 PVs (from about 0.503 to 0.506 PVs), and the length of the first period increased by 0.2 min (from around 6.5 to 6.7 min) due to the slight decrease in the viscosity ratio. The slight increase in the total water production might be related to the increase in the capillary number (*Ca*) and the slight decrease in the viscosity ratio (*M*). The *Ca* increases with the increase in the viscous forces (because of increasing viscosity) and the reduction in the capillary forces (owing to increasing contact angle and reducing CO_2-water interface with increasing CO_2 solubility [18-20]). As the fluid pressure increased from 60 to 70 bar at a constant temperature of 20 °C, CO_2 viscosity increased from 69.72 to 74.54 × [10^{-6} (Pa·s)], the CO_2-water IFT decreased from 34.9 to 30 mN/m, the *M* decreased from 14.33 to 13.4 and the *Ca* increased from 2.175 to 2.73 × 10^{-7}.

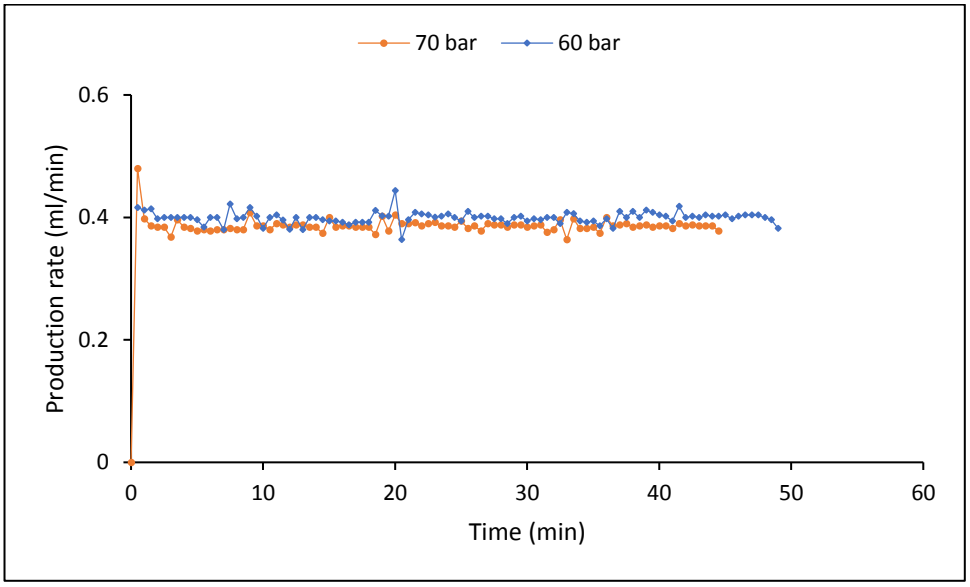

Figure 5-14: Effect of fluid pressure on the transient outflow rates of water and CO_2 of LCO_2-water displacements conducted at 0.4 ml/min and 20 °C

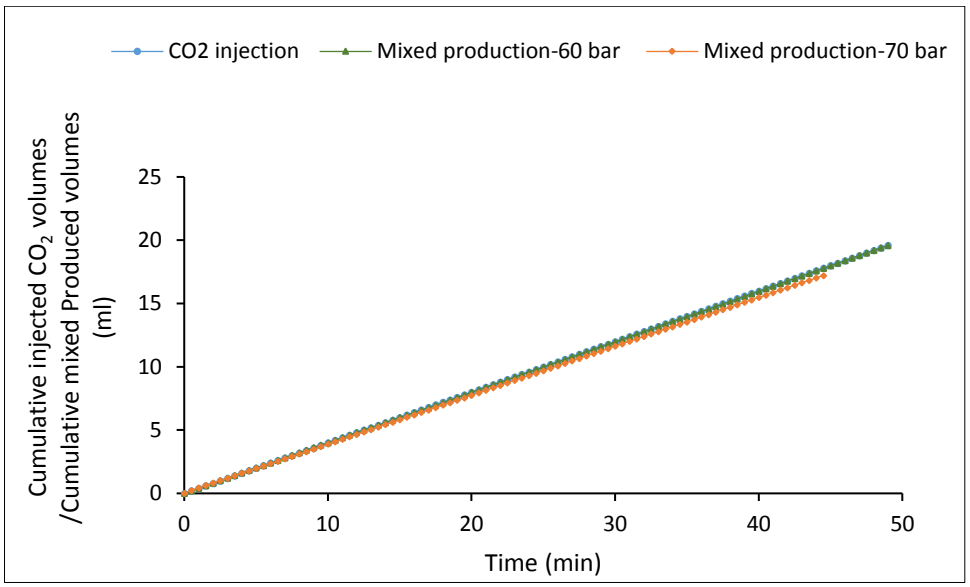

Figure 5-15: Effect of fluid pressure on the cumulative produced volumes of water and CO_2 of LCO_2-water displacements conducted at 0.4ml/min and 20 °C

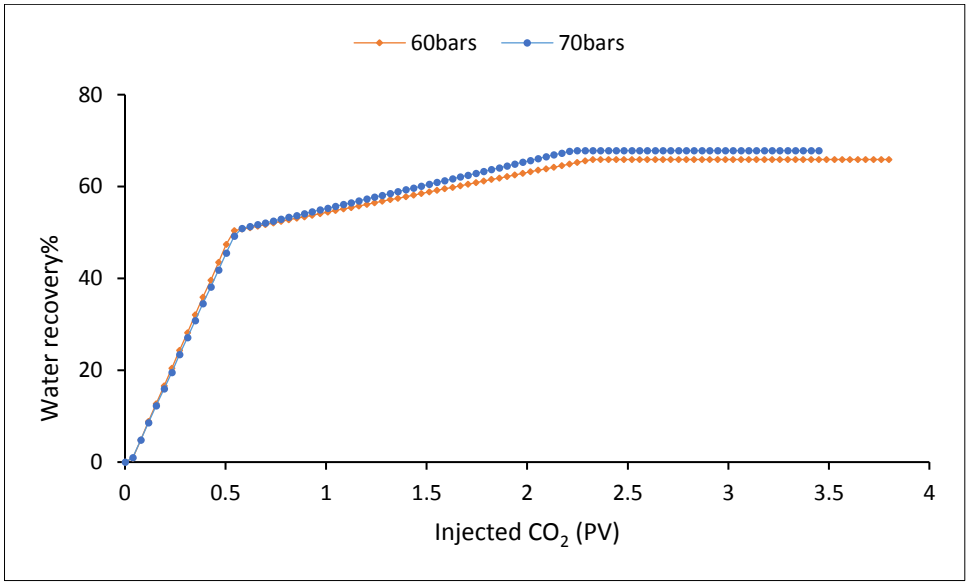

Figure 5-16: Effect of fluid pressure on the water recovery profile of LCO_2-water displacements conducted at 0.4 ml/min and 20 °C

5.2.3.2 Effect of Temperature on Water Production Behaviour during LCO_2 Injection

Figure 5-17 presents the effect of increasing temperature on the cumulative produced volumes. The data reveals that the cumulative injected volumes of liquid CO_2 were much higher than the cumulative produced volumes. The increase in temperature did not accompany by a noticeable change in the cumulative produced volumes due to the high-density nature of liquid CO_2 phase, especially at high pressures (e.g. 90 bar). The difference

between the injected and produced cumulative volumes might be related to the increase in the CO_2 compressibility and the solubility of CO_2 in water, especially at high pressure [18-20]. It should be noted that the water recovery profile and the transient outflow rate data were not presented here to avoid repeatability as they were similar to those presented in the fluid pressure section above.

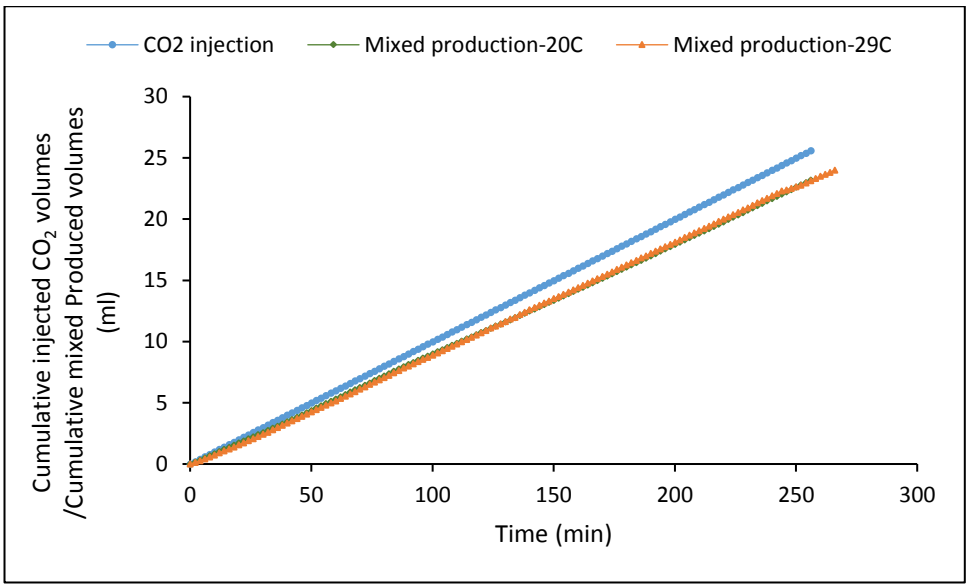

Figure 5-17: Effect of temperature on the cumulative produced volumes of water and CO_2 of LCO_2-water displacements conducted at 90 bar and 0.1 ml/min

5.2.3.3 Effect of CO_2 Injection rate on Water Production Behaviour during LCO_2 Injection

The data from Figure 5-2, Figure 5-3 and Figure 5-4 as well as Figure 5-18, Figure 5-19 and Figure 5-20 exhibit the impact of increasing CO_2 injection rate on the transient outflow rates, cumulative produced volumes and water recovery profiles. It should be noted that only the data of the LCO_2-water displacement conducted at CO_2 injection rates of 1 ml/min are presented here as that of 0.4 ml/min was discussed in Section 5.2.1.1. The results show that the increase in the injection rate caused an increase in the water recovery but caused no observable change in the behaviour of the transient flowrates of water and CO_2 and the cumulative produced volumes.

The data from Figure 5-2 and Figure 5-18 and Figure 5-4 and Figure 5-20 show that increasing CO_2 injection rate led to: (I) a reduction in the time of the only water production period (from around 6.9 to 3.5 min) and that of mixed period (from about 23 to 6.5 min), (II) a reduction

in the amount of water production during only production period (from 50.37 to 49%) but an increase in that of mixed period (from to 16.3 to 17.38%), and (III) an increase in the total W_R by around 3.4% (from 65.9 to 69.38%) [21] and a reduction in the amount of injected CO_2 to achieve that by around 48% (from 2.32 to 1.98 PVs). The increase in the W_R with increasing injection rate can be associated with (a) the increase in the *Ca*, from about 2.175 to 5.437 × 10^{-7}, due to the increase in the viscous forces, and (b) the occurrence of a uniform CO_2 front that leads to an improvement in CO_2 displacement efficiency [5]. The results suggest that if the goal of CO_2 injection is to enhance displacement efficiency, then high injection rates might be a better option.

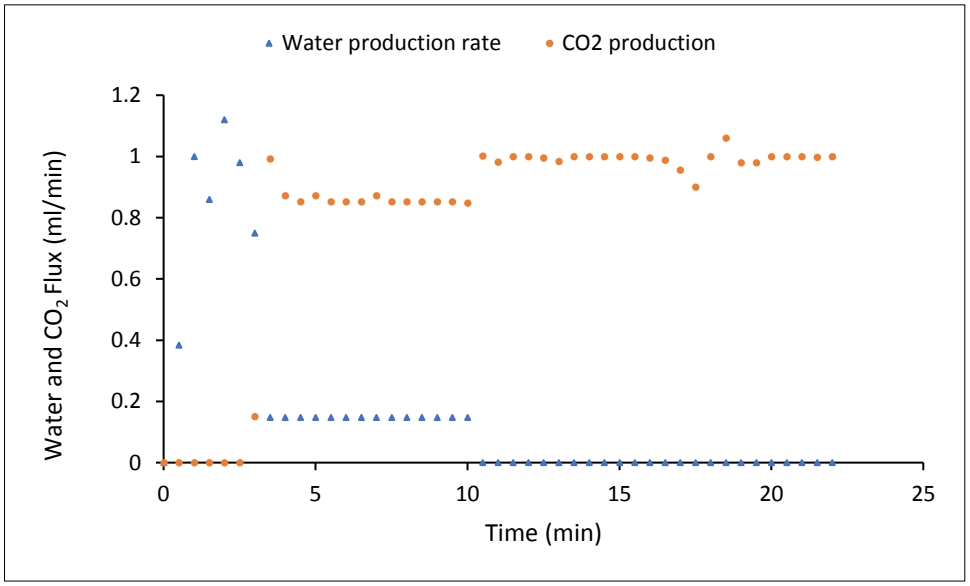

Figure 5-18: Transient flowrates of water and LCO_2 of a LCO_2-water displacement conducted at 60 bar, 1 ml/min, and 20 °C

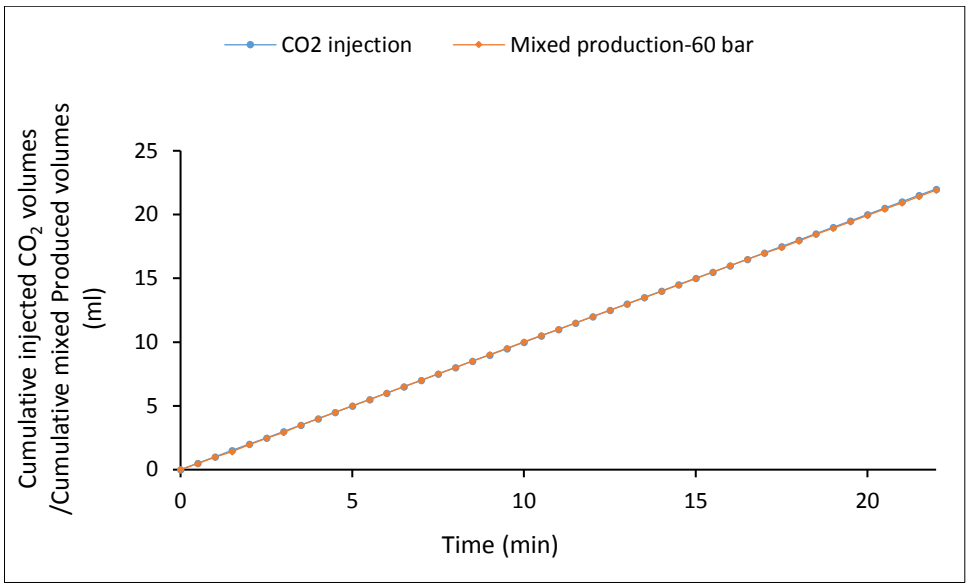

Figure 5-19: Cumulative injected volumes of CO_2 and cumulative produced volumes of water and CO_2 of a LCO_2-water displacement conducted at 60 bar, 1 ml/min, and 20 °C

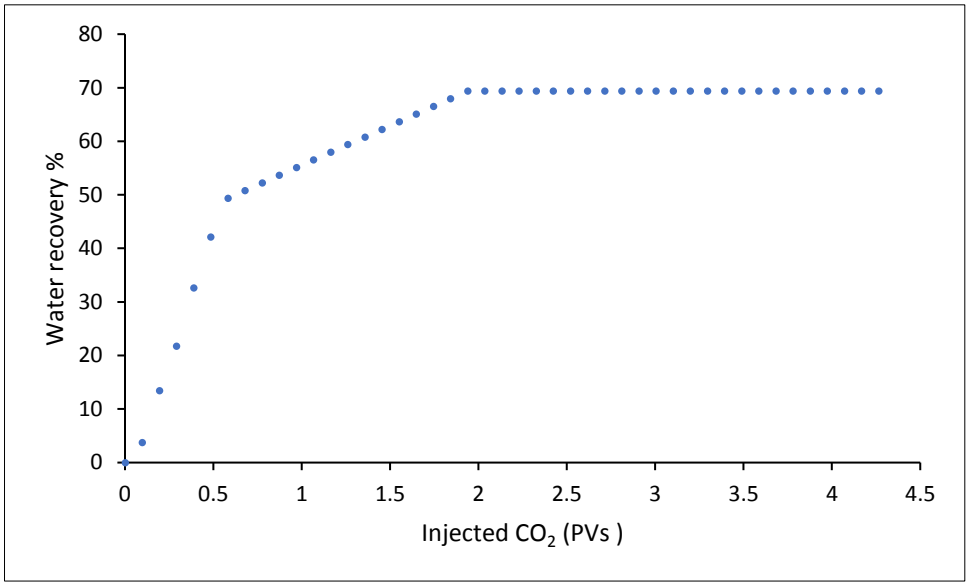

Figure 5-20: Water recovery profile of a LCO_2-water displacement conducted at 60 bar, 1 ml/min, and 20 °C

5.2.3.4 Effect of Salinity on Water Production Behaviour during LCO_2 Injection

Figure 5-21 presents the effect of salinity on the cumulative produced volumes. The data reveals that the cumulative injected volumes of CO_2 were higher than the cumulative produced volumes. The increase in brine concentration and valency caused a slight decrease in the cumulative produced volumes. The cumulative produced volumes were decreased by around 0.42, 0.62, and 1.07 ml when 1% NaCl, 1% $CaCl_2$, and 5% NaCl brine solutions was

used instead of deionised water, respectively. This might be associated with the reduction in brine recovery due to the increase in capillary forces with the increase in the interfacial tension [15]. However, the reduction in the cumulative produced volumes cannot be associated with increasing CO_2 solubility since solubility decreases with increasing salinity [22, 23].

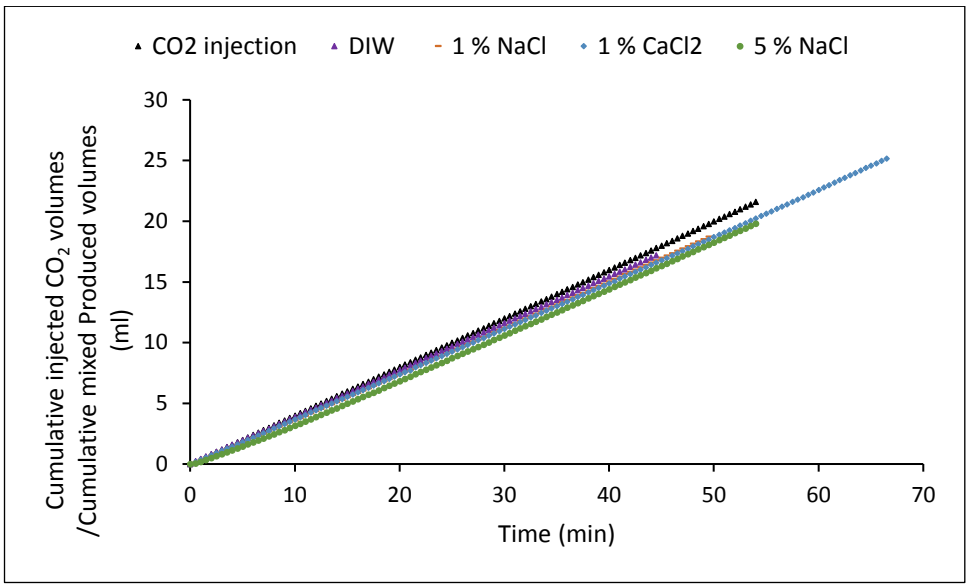

Figure 5-21: Effect of salinity on the cumulative injected volumes of CO_2 and the cumulative produced volumes of water and CO_2 volumes of LCO_2-water displacements conducted at 70 bar, 0.4 ml/min, and 20 °C

In summary, the cumulative produced volumes: (a) decreased slightly with increasing fluid pressure and salinity, and (b) showed no noticeable change with increasing temperature and injection rate. W_R increased as fluid pressure and injection rate increased. With increasing injection rate, the amount of the injected CO_2 to achieve the highest W_R was reduced.

5.2.4 Effect of Fluid Pressure, Temperature, CO_2 Injection Rate, and Salinity on Endpoint CO_2 Effective and Relative Permeabilities and Water (Brine) Recovery

It should be noted that the same procedures presented in Chapter 4 for measuring and calculating the residual water saturation and endpoint effective and relative permeabilities of CO_2 are followed here. The data in Table 5-1 show the effect of fluid pressure, temperature, salinity, and CO_2 injection rate on the endpoint CO_2 effective and relative permeabilities and water recovery.

Table 5-1: Effect of fluid pressure, temperature, salinity, and CO_2 injection rate on the endpoint CO_2 effective and relative permeabilities and water recovery

Parameter	Experiment	K_{fCO2} (md)	K_{rCO2}	W_R	M	Ca
Fluid Pressure Effect	LCO_2-DIW-60 bar-0.4 ml-20 °C	3.188	0.203	0.659	14.33	2.175E-07
	LCO_2-DIW-70 bar-0.4 ml-20 °C	3.064	0.195	0.6787	13.4	2.734E-07
	LCO_2-DIW-60 bar-1 ml-20 °C	2.307	0.147	0.6938	14.33	5.437E-07
	LCO_2-DIW-70 bar-1 ml-20 °C	2.271	0.145	0.701	13.4	6.835E-07
Temperature Effect	LCO_2-DIW-90 bar-0.1 ml-20 °C	3.185	0.203	0.653	12.24	6.923E-08
	LCO_2-DIW-90 bar-0.1 ml-29 °C	1.760	0.112	0.661	12.73	6.124E-08
Injection Rate Effect	LCO_2-DIW-60 bar-0.4 ml-20 °C	3.188	0.203	0.659	14.33	2.174E-07
	LCO_2-DIW-60 bar-1 ml-20 °C	2.307	0.147	0.6938	14.33	5.437E-07
Salinity Effect	LCO_2-DIW-70 bar-0.4 ml-20 °C	3.248	0.195	0.6787	13.4	
	LCO_2-1% NaCl-70 bar-0.4 ml-20 °C	3.180	0.203	0.6514	13.4	
	LCO_2-5% NaCl-70 bar-0.4 ml-20 °C	2.991	0.191	0.6254	13.4	
	LCO_2-1% $CaCl_2$-70 bar-0.4 ml-20 °C	2.845	0.181	0.616	13.4	

Table 5-1 shows that the water recovery (W_R) was in ranges of 0.616-0.6938 (i.e. residual water saturation 0.3062-0.384) while the endpoint CO_2 relative permeability (K_{rCO2}) was in ranges of 0.112-0.203. Table 5-1 shows that increasing fluid pressure and CO_2 injection rate caused an increase in the W_R; the highest increase occurred with increasing the injection rate. On the other hand, the increase in the experimental temperature and water salinity caused a decrease in the W_R; the highest reduction occurred with increasing the salinity. The W_R increased by around 0.02 as the fluid pressure increased from 60 to 70 bar at 0.4 ml/min and by about 0.007 as the fluid pressure increased from 60 to 70 bar at 1 ml/min. The W_R

increased by around 0.035 as the injection rate increased from 0.4 to 1 ml/min at 60 bar. Nevertheless, the W_R decreased by around 0.008 as the temperature increased from 20 to 29 °C at 90 bar. The W_R decreased by about 0.027, 0.053, and 0.063 when 1% NaCl, 5% NaCl, and 1% $CaCl_2$ brine solutions were used instead of deionised water, respectively.

The efficiency of water displacement (i.e. W_R) depends on many parameters such as permeability, displacement pattern, injection rate, stability of the displacement front, *Ca*, and *M* [5, 7]. The increase in injection rate can enhance production by changing the displacement pattern from capillary to viscous fingering, stabilizing the displacement front, and forcing the injected CO_2 to displace water from low permeability formations [7]. However, the most influential parameters that determine the displacement efficiency of CO_2-water core flooding are the Ca and M [24]. The data from Table 5-1 show that the increase in the W_R with the increasing fluid pressure and injection rate and the reduction in the W_R with the increasing temperature can be associated with the *Ca* and *M* data. However, the *Ca* data are not available for the set of data dealing with the salinity impact as contact angle data are not available. Nevertheless, the reduction in water recovery with increasing the salinity can be attributed to the increase in capillary forces due to increasing CO_2-brine interfacial tension [15].

On the other hand, the increase in fluid pressure, experimental temperature, injection rate and salinity led to a reduction in the K_{rCO2}, which is opposite to gaseous CO_2 behaviour as stated in Section 4.2.3 Chapter 4. The highest reduction in the K_{rCO2} occurred with increasing temperature whiles the lowest occurred with increasing pressure. As the CO_2 injection rate increased, the percentage of the reduction in the K_{rCO2} with fluid pressure decreased; this can be related to increasing viscous forces at the expense of the capillary forces, thereby reducing the entrapment impact of capillary forces. The K_{rCO2} decreased by around 0.008 as the fluid pressure increased from 60 to 70 bar at 0.4 ml/min and decreased by about 0.002 as the fluid pressure increased from 60 to 70 bar at 1 ml/min. It decreased by around 0.091 as the temperature increased from 20 to 29 °C at 90 bar. It decreased by around 0.056 as the injection rate increased from 0.4 to 1 ml/min at 60 bar. It decreased by about 0.004, and 0.014 when 5% NaCl, and 1% $CaCl_2$ solutions were used instead of deionised water, respectively. However, using 1% NaCl instead of deionised water showed a slight increase in the K_{rCO2} by about 0.008. The reduction in the K_{rCO2} with increasing temperature and salinity

might be related to the increase in the capillary forces and hence reducing the sweeping efficiency. However, this cannot explain the reduction in the K_{rCO2} with increasing pressure and injection rate, the reason for this reduction is not clear. The reduction in the K_{rCO2} with increasing salinity agrees with the findings of Rathnaweera et al. [25].

5.3 Summary

In this chapter, the effect of fluid pressure, temperature, CO_2 injection rate, and salinity (brine concentration and valency) on the two-phase flow characteristics when liquid CO_2 is injected into a water or brine-saturated sandstone core sample have been investigated in detail. The results indicate that the parameters investigated showed a moderate to significant influence on the differential pressure profile, water recovery, endpoint CO_2 effective and relative permeabilities, and cumulative produced volumes. The results indicate that the capillary forces have less impact on the differential pressure profiles than viscous forces when fluid pressure, temperature and injection rate increase but the capillary forces have more impact when salinity increases.

The differential pressure profile is characterized by a sharp increase followed by a stable pressure reduction and then by a high-pressure reduction that is followed by a gradual pressure reduction. The differential pressure profiles were characterized by: (a) no change in their shape with increasing pressure, (b) an increase in the differential pressure profile at the end of the displacements with increasing temperature, (c) spikes in the differential pressure profile, after the initial increase, with increasing injection rate, and (d) only slight changes, mainly during the first period, with increasing salinity.

The differential pressure profile: (a) slightly increased with increasing pressure; this slight increase increased with the injection rate, (b) was stable during the first period, decreased during the mixed period, and increased again during the last period with increasing temperature, (c) considerably increased with increasing injection rate, mainly during the first five minutes; this considerable increase was slightly decreased, by around 0.3%, as the fluid pressure increased from 60 to 70 bar, and (d) slightly increased, mainly during the first period, when brine concentration and valency increased. The order of the differential pressure with increasing salinity was as follows: LCO_2-1% $CaCl_2$ > LCO_2-5% NaCl > LCO_2-1% NaCl > LCO_2-DIW displacement.

The cumulative produced volumes: (a) decreased slightly with increasing fluid pressure and salinity and (b) showed no noticeable change with increasing temperature and injection rate. With increasing injection rate, the amount of the injected CO_2 to achieve the highest water recovery was reduced.

The water recovery (W_R) was in ranges of 0.616-0.6938 (i.e. residual water saturation 0.3062-0.38.4) while the endpoint CO_2 relative permeability (K_{rCO2}) was in ranges of 0.112-0.203. The results show that increasing fluid pressure and injection rate caused an increase in the W_R; the largest increase occurred with increasing the injection rate. On the other hand, the increase in the experimental temperature and water salinity caused a decrease in the W_R; however, the largest reduction occurred with increasing salinity.

Nevertheless, the increase in fluid pressure, experimental temperature, CO_2 injection rate, and salinity led to a reduction in the K_{rCO2}; the highest reduction in the K_{rCO2} occurred with increasing temperature whilst the lowest occurred with increasing fluid pressure. As the CO_2 injection rate increased, the percentage of the reduction in the K_{rCO2} decreased with increasing fluid pressure.

5.4 References

1. Teng H, Yamasaki A. Mass transfer of CO_2 through liquid CO_2–water interface. International journal of heat and mass transfer. 1998;41(24):4315-25.

2. Sohrabi M, Jamiolahmady M, Al Quraini A, editors. Heavy oil recovery by liquid CO_2/water injection. EUROPEC/EAGE Conference and Exhibition; London, UK 11–14 June 2007: SPE: Houston, TX, USA, 2007.

3. Nourpour Aghbash V, Ahmadi M, editors. Evaluation of CO_2-EOR and Sequestration in Alaska West Sak Reservoir Using Four-Phase Simulation Model. SPE Western Regional Meeting; Bakersfield, CA, USA, 21–23 March 2012: SPE: Houston, TX, USA, 2012.

4. Hamdi Z, Awang M. Comparison of liquid CO_2 injection with a common tertiary recovery method using non-isothermal simulations. ICIPEG 2016: Springer; 2017. p. 61-70.

5. Song Y, Jiang L, Liu Y, Yang M, Zhao Y, Zhu N, et al. An experimental study on CO_2/water displacement in porous media using high-resolution magnetic resonance imaging. IJGGC. 2012;10:501-9.

6. Levine JS, Matter JM, Goldberg DS, Lackner KS, Supp MG, Ramakrishnan T. Two phase brine-CO_2 flow experiments in synthetic and natural media. Energy Procedia. 2011;4:4347-53.

7. Zhang C, Oostrom M, Grate JW, Wietsma TW, Warner MG. Liquid CO_2 displacement of water in a dual-permeability pore network micromodel. Environmental science & technology. 2011;45(17):7581-8.

8. Alemu BL, Aker E, Soldal M, Johnsen Ø, Aagaard P. Influence of CO_2 on rock physics properties in typical reservoir rock: A CO_2 flooding experiment of brine saturated sandstone in a CT-scanner. Energy Procedia. 2011;4:4379-86.

9. Manceau J-C, Ma J, Li R, Audigane P, Jiang P, Xu R, et al. Two-phase flow properties of a sandstone rock for the CO_2/water system: Core-flooding experiments, and focus on impacts of mineralogical changes. Water Resources Research. 2015;51(4):2885-900.

10. Kwelle SO. Experimental studies on resistance to fluid displacement in single pores [PhD. Thesis]: The University of Edinburgh, Edinburgh, UK; 2017.

11. Plug W-J, Bruining J. Capillary pressure for the sand–CO_2–water system under various pressure conditions. Application to CO_2 sequestration. Advances in Water Resources. 2007;30(11):2339-53.

12. Bachu S, Bennion DB. Interfacial tension between CO_2, freshwater, and brine in the range of pressure from (2 to 27) MPa, temperature from (20 to 125) °C, and water salinity from (0 to 334 000) mg· L− 1. Journal of Chemical & Engineering Data. 2008;54(3):765-75.

13. Nutt C, editor. The physical basis of the displacement of oil from porous media by other fluids: a capillary bundle model. Proceedings of the Royal Society of London A: Mathematical, Physical and Engineering Sciences; 1982: The Royal Society.

14. Chang C, Zhou Q, Xia L, Li X, Yu Q. Dynamic displacement and non-equilibrium dissolution of supercritical CO_2 in low-permeability sandstone: An experimental study. IJGGC. 2013;14:1-14.

15. Chalbaud C, Robin M, Lombard JM, Martin F, Egermann P, Bertin H. Interfacial tension measurements and wettability evaluation for geological CO_2 storage. Advances in Water Resources. 2009;32(1):98-109.

16. Bennion DB, Bachu S, editors. The impact of interfacial tension and pore size distribution/capillary pressure character on CO_2 relative permeability at reservoir conditions in CO_2-brine systems. In Proceedings of the SPE/DOE Symposium on Improved Oil Recovery; Tulsa, OK, USA, 22–26 April 2006: SPE: Houston, TX, USA, 2006.

17. Tokunaga TK, Wan J. Capillary pressure and mineral wettability influences on reservoir CO_2 capacity. Reviews in mineralogy and geochemistry. 2013;77(1):481-503.

18. Li X. Experimental studies on pore wetting and displacement of fluid by CO_2 in porous media. 2015.

19. Espinoza DN, Santamarina JC. Water-CO_2-mineral systems: Interfacial tension, contact angle, and diffusion—Implications to CO_2 geological storage. Water resources research. 2010;46(7).

20. Chiquet P, Daridon J-L, Broseta D, Thibeau S. CO_2/water interfacial tensions under pressure and temperature conditions of CO_2 geological storage. Energy Conversion and Management. 2007;48(3):736-44.

21. Cao SC, Dai S, Jung J. Supercritical CO_2 and brine displacement in geological carbon sequestration: Micromodel and pore network simulation studies. IJGGC. 2016;44:104-14.

22. Ji X, Zhu C. CO_2 storage in deep saline aquifers. Chapter 10 in Novel Materials for Carbon Dioxide Mitigation Technology. 2015:299-332.

23. De Silva G, Ranjith P, Perera M. Geochemical aspects of CO_2 sequestration in deep saline aquifers: A review. Fuel. 2015;155:128-43.

24. Kazemifar F, Blois G, Kyritsis DC, Christensen KT. Quantifying the flow dynamics of supercritical CO_2–water displacement in a 2D porous micromodel using fluorescent microscopy and microscopic PIV. Advances in Water Resources. 2015.

25. Rathnaweera T, Ranjith P, Perera M. Effect of salinity on effective CO_2 permeability in reservoir rock determined by pressure transient methods: An experimental study on Hawkesbury sandstone. Rock Mechanics and Rock Engineering. 2015;48(5):2093-110.

6 Chapter 6: Supercritical CO_2-Water Drainage Displacements

6.1 Introduction

Due to the high pressure and temperature conditions of most of the formations suitable for CO_2 sequestration and enhanced oil recovery projects, the injected CO_2 will be in a supercritical state. Thus, widening our understanding about multiphase flow characteristics of supercritical (Sc) CO_2-water displacement would be of high practical importance.

Literature review shows a wide range of investigations for multiphase characteristics [1-21]. However, despite its high importance, no investigations have been focused on the dynamic pressure evolution and displacement efficiency when CO_2 in its supercritical state is flooded into a water-saturated sandstone core sample. This study deals with the impact of fluid pressure, temperature, and CO_2 injection rate on multiphase flow characteristics (i.e. differential pressure profile, water production profile, residual water saturation, and effective and relative permeabilities of CO_2). One of the main aims of this investigation is to shed more light on the impact of capillary forces and viscous forces on the two-phase flow characteristics and highlights the conditions at which the capillary forces or viscous forces become more dominant. The results would be of an essential importance for evaluating the capacity and the long-term fate of CO_2 storage in saline aquifers as well as migration, displacement, and injectivity of CO_2 in geologic formations [18, 22].

6.2 Results and Discussions

In this chapter, the experimental data has been categorized into four main sections. The first three sections deal with the impact of the fluid pressure, temperature, and CO_2 injection rate on the differential pressure profile and production behaviour; while the fourth section deal with their influence on the endpoint CO_2 effective and relative permeabilities and residual water saturation. It should be noted that during this study, the corresponding time refers to the time needed to reach the maximum-differential pressure at the beginning of CO_2 flooding. The quasi-differential pressure refers to the average differential pressure measured at the end of the core flooding.

6.2.1 Effect of Fluid Pressure on the Differential Pressure Profile of $ScCO_2$-Water Core-Flooding Displacements

To have a thorough understanding about the effect of fluid pressure on the differential pressure and water recovery of $ScCO_2$-water displacements, experiments were conducted under various fluid pressures (75-90 bar), temperatures (33 and 45 °C), and CO_2 injection rates (0.1,0.4, and 1 ml/min). The discussion of the fluid pressure data will be presented in two sections depending on the experimental temperature.

6.2.1.1 Effect of Fluid Pressure on the Differential Pressure Profile of $ScCO_2$-Water Displacements Conducted at 33 °C

Figure 6-1, Figure 6-2, and Figure 6-3 show the impact of increasing fluid pressure on the differential pressure profile. The data show several important observations (from A to D):

A) Generally, for all fluid pressures, the differential pressure is characterized by a sharp increase followed by a strong reduction and then by a gradual reduction, i.e. quasi-steady reduction [13]. A similar behaviour has been reported by Bikini et al. [23], see Section 4.2.1.1 in Chapter 4 for more information about the potential reasons for increasing and decreasing the differential pressure.

B) The data from Figure 6-1, Figure 6-2, and Figure 6-3 show that increasing fluid pressure caused a substantial drop in the maximum and quasi-differential pressures along with an increase or a decrease in the corresponding time depending on the CO_2 injection rate; the corresponding time increased with the fluid pressure at an injection rate of 0.1 ml/min and decreased at an injection rate of 0.4 ml/min and higher. For illustration, the data from Figure 6-1 exhibit that as the fluid pressure increased from 75 to 90 bar at 0.1 ml/min injection rate, the maximum-differential pressure dropped by around 72% (from 0.36 to 0.102 bar) and the quasi-differential pressure decreased by around 69.5% (from 0.154 to 0.047 bar) but the corresponding time increased by around 66% (from 6.5 to 10.8 min). The data from Figure 6-2 show that as the fluid pressure increased from 75 to 90 bar at 0.4 ml/min, the maximum-differential pressure dropped by around 46.6% (from 1.121 to 0.599 bar), the quasi-differential pressure declined by around 39% (from 0.363 to 0.221 bar), and the corresponding time reduced by around 68.4% (from 1.9 to 0.6 min). The data from Figure 6-3 show that increasing the fluid pressure from 75 to 80 bar and then to 90 bar at 1 ml/min,

caused the maximum-differential pressure to drop by around 40% (from 2.492 to 1.496 bar), the quasi-differential pressure to decline by around 38% (from 0.994 to 0.614), and the corresponding time to decline by around 15.6% (from 3.2 to 2.7 min).

According to Eq.4-1-Chapter 4, the reduction observed in the differential pressure profile is the net result of the reduction in the capillary forces and the increase in the viscous forces with increasing fluid pressure. The reduction in the capillary forces with increasing pressure is owing to the reduction in the CO_2-water interfacial tension, as shown in Figure 4-4-Chapter 4, and the increase in contact angle because of the increase in CO_2 solubility, as shown in Figure 6-4, [24-26]. The increase in the viscous forces with increasing fluid pressure is due to the increase in CO_2 viscosity [27]. For illustration, increasing the fluid pressure from 75 to 90 bar caused the $ScCO_2$ viscosity to increase from 33.3095 to 53.837 × [10^{-6} (Pa·s)] [27] and the CO_2-water interfacial tension (IFT) to reduce from around 28 to 25 mN/m [28]. The IFT dataset showed a slight reduction in the interfacial tension, around 3 Nm/m, with increasing fluid pressure. As a result, the reduction observed in the differential pressure with increasing fluid pressure might be related mainly to the increase in contact angle. This is in agreement with the findings by Yang et al. [29], Liu et al. [30], and Jung and Wan [26]. Yang et al. [29] and Liu et al. [30] noticed that using a supercritical CO_2 with reservoir rocks leads to a higher alteration towards a less water-wetting state in comparison to gaseous and liquid CO_2. Moreover, Jung and Wan [26] found that contact angle increases significantly with increasing fluid pressure up to 100 bar when the fluid pressure is higher than the critical pressure of CO_2 (larger than 73.8 bar) but remains fairly constant when the fluid pressure is less than the critical pressure or above 100 bar.

Regarding the change in the corresponding time, the increase observed in the corresponding time at low injection rate (0.1 ml/min) can be linked to the transformation of supercritical CO_2-water behaviour to liquid CO_2 behaviour; the transformation can result in reducing the mobility ratio, more discussion will follow later. However, the reduction in the corresponding time at higher injection rate (0.4 ml/min) is likely to be related to the reduction in the magnitude of the maximum differential pressure with increasing fluid pressure.

B.1) The aforementioned data from Figure 6-1, Figure 6-2, and Figure 6-3 showed that the drop in the maximum-differential pressure with increasing fluid pressure was always higher

than that in the quasi-differential pressure. This can be related to the fact that the dynamic reduction in both capillary and viscous forces at the end of the displacement is less than that at the start of the displacement.

B.2) The results from Figure 6-1, Figure 6-2, and Figure 6-3 showed also that as the CO_2 injection rate increased, the reduction in the differential pressure, due to increasing fluid pressure, decreased. This is because the reduction observed in the differential pressure profile is the net result of the increase in the viscous forces and the reduction in the capillary forces with increasing fluid pressure. Thus, with increasing injection rate, the contribution of the viscous forces to the net pressure drop increases at the expense of the capillary forces [31], thereby leading to a less reduction in the differential pressure.

C) The data from Figure 6-1, Figure 6-2 and Figure 6-3 show also that as the fluid pressure increased, the differential pressure profile of the $ScCO_2$-water displacements transformed from the likeness of gaseous CO_2 behaviour to liquid CO_2 behaviour. The differential pressure profile of the 75 bar-experiment is remarkably similar to that of a typical high-fluid pressure gaseous CO_2-water displacement, see Section 4.2.1.1 in Chapter 4, while that of the 90 bar-experiment is virtually identical to that of a typical liquid CO_2-water displacement, see Section 5.2.1.2 in Chapter 5. The $ScCO_2$ transformation occurs at lower fluid pressures with increasing the CO_2 injection rate from 0.1 to 0.4 ml/min. For the 0.1 ml/min-displacements, the transition towards liquid CO_2 behaviour occurred at 90 bar. Nonetheless, for the 0.4 ml/min-displacements, it started from 77 bar. The similarity to gaseous or liquid CO_2 behaviour has been decided mainly on the rate of reduction in the differential pressure during early times of flooding; gaseous CO_2 displacements are characterized by a high-pressure drop at early stages while liquid CO_2 displacements are characterized by a slight pressure drop. The impact of increasing injection rate on the differential pressure profile can be related to the increase in viscous pressure drop, leading to a reduction in the total pressure drop as stated above. As a result, this led to the appearance of the liquid CO_2-like differential pressure profile, which is characterized by gradual pressure drop at initial stages of CO_2 flooding.

The transformation of the differential pressure profile with increasing fluid pressure suggests that the capillary and viscous properties of supercritical CO_2 phase become similar to that of gaseous CO_2 phase at low fluid pressures and similar to that of liquid CO_2 phase at high fluid pressures; liquid CO_2 is characterized by higher viscous forces and lesser capillary forces in

comparison to gaseous CO_2. With increasing fluid pressure, the viscous forces of the supercritical CO_2 phase become higher while the capillary forces become lesser. This is because the increase in fluid pressure leads to an increase in the CO_2 density and viscosity as well as a decrease in the interfacial tension and an increase in the contact angle due to increasing CO_2 solubility [32, 33].

Moreover, the transformation towards liquid CO_2 behaviour might have occurred because the wettability behaviour of liquid and supercritical CO_2 phases might become very close to each other at high-pressure conditions. The wettability of the core sample with supercritical and liquid CO_2 might have been altered towards hydrophobic wetting status at high pressures. This potential wettability alteration might have occurred due to (a) the increase in fluid pressure in case of supercritical CO_2 (as illustrated above) [26, 29], and (b) the CO_2 phase transformation in case of liquid CO_2 [24]. Yang et al. observed that as gaseous CO_2 transforms to a liquid CO_2 state, the wettability of the system becomes hydrophobic [24].

D) The data from Figure 6-1 show that increasing fluid pressure caused an increase in the differential pressure profile of the 90 bar-experiment until it became slightly higher than the differential pressure profile of the 80 bar-experiment after about 180 min. The reason is not entirely clear. However, the first possible explanation is that as water depletion progressed, and, hence, the viscous pressure drop across the core sample diminished, the flow of the non-depleted capillaries was partially blocked by the capillary forces [34]. As a result, the pressure of the CO_2 had to build up to a certain level to overcome the capillary forces. The second possible explanation is that, after around 180 min, the impact of viscous forces became higher than that of capillary forces. This is because most of the water was displaced, leaving the bypassed water to concentrate inside the smallest pores while the larger pores to be occupied by the injected CO_2 [2]. Consequently, the impact of the capillary forces was significantly reduced [35].

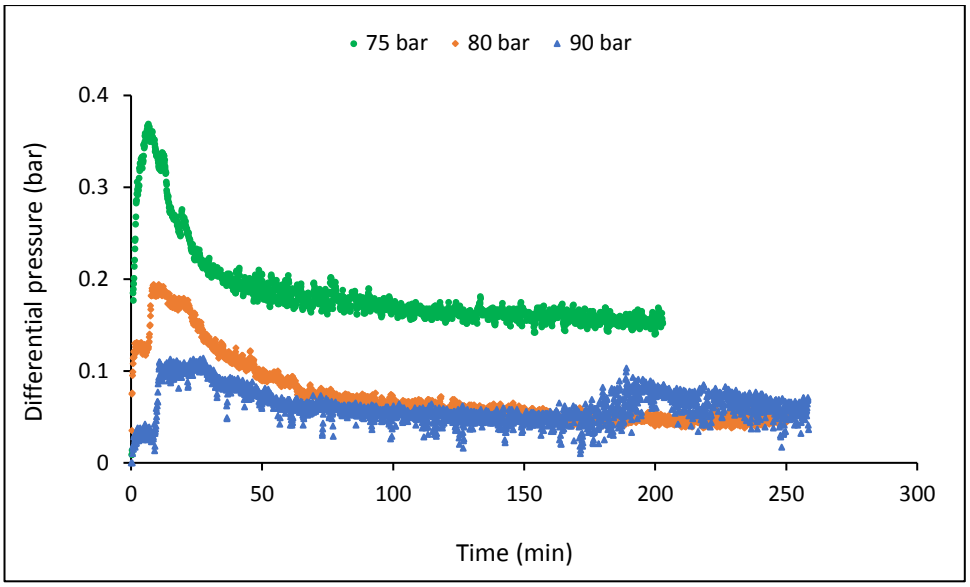

Figure 6-1: Effect of fluid pressure on the differential pressure profile of $ScCO_2$-water displacements conducted at 0.1 ml/min and 33 °C

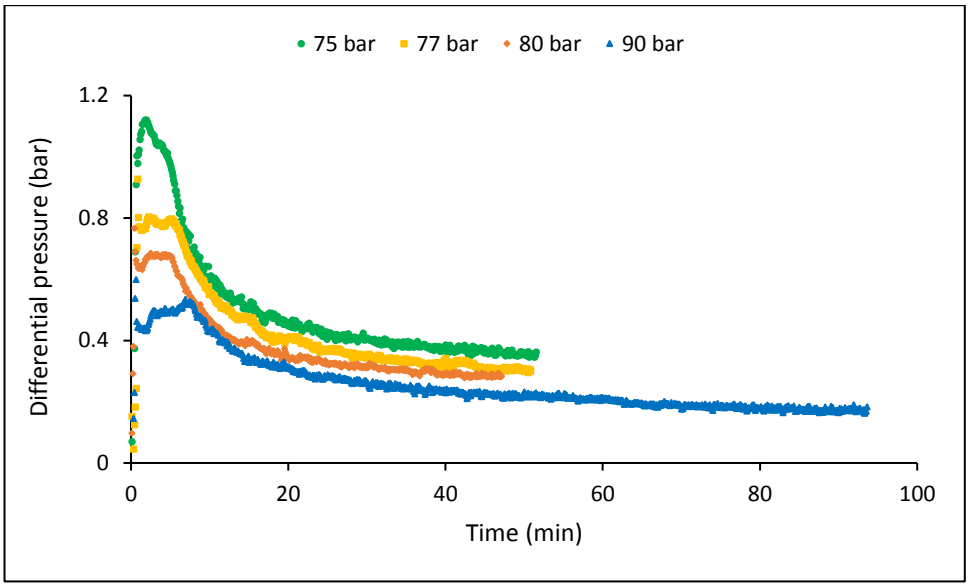

Figure 6-2: Effect of fluid pressure on the differential pressure profile of $ScCO_2$-water displacements conducted at 0.4 ml/min and 33 °C

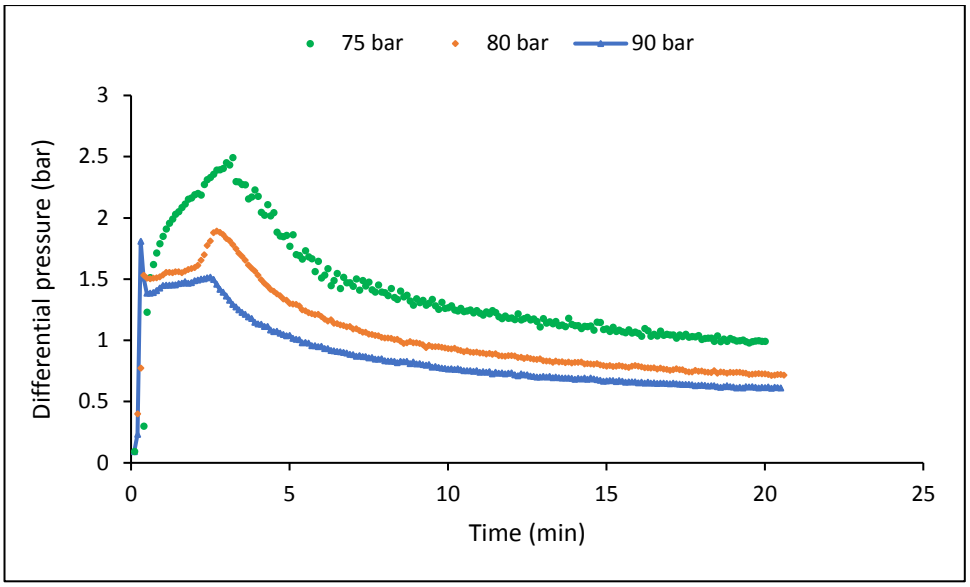

Figure 6-3: Effect of fluid pressure on the differential pressure profile of $ScCO_2$-water displacements conducted at 1 ml/min and 33 °C

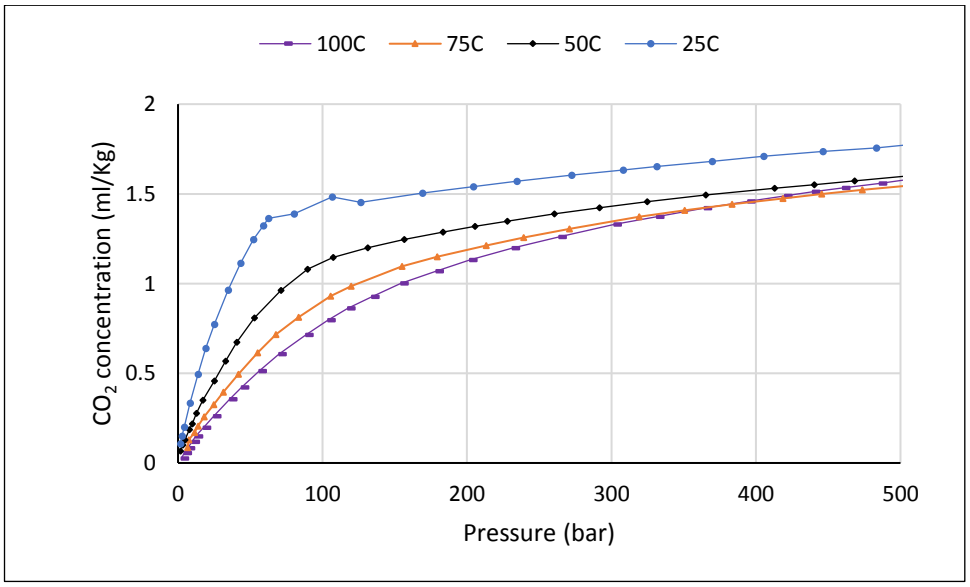

Figure 6-4: CO_2 solubility in water [36]

6.2.1.2 Effect of Fluid Pressure on the Differential Pressure Profile of $ScCO_2$-Water Displacements Conducted at 45 °C

Figure 6-5 presents the effect of increasing fluid pressure on the differential pressure at a higher temperature (45 °C). Overall, in comparison to the experiments conducted under lower temperature (33 °C) conditions, the differential pressure profile of the higher temperature (45 °C) displacements becomes more similar to gaseous CO_2 behaviour than liquid CO_2 behaviour.

The data from Figure 6-5 shows that the differential pressure profile experienced the highest reduction within the first three to five minutes of running the experiments and reached a quasi-pressure state after around 20 min. This indicates that most of the water recovery happened during the first five minutes of running the coreflooding. As a result, the differential pressure profile of the 80 and 90 bar-experiments became almost identical after about 3.3 min. These nearly identical pressure profiles might have occurred because the reduction in the differential pressure profile due to the decline of the capillary forces was equalled by the increase in the differential pressure profile due to the increase of the viscous forces with increasing fluid pressure. This suggests that in comparison to capillary forces, the viscous forces played a vital role at later stages of the displacements, for more information see Section 6.2.1.1- observation D.

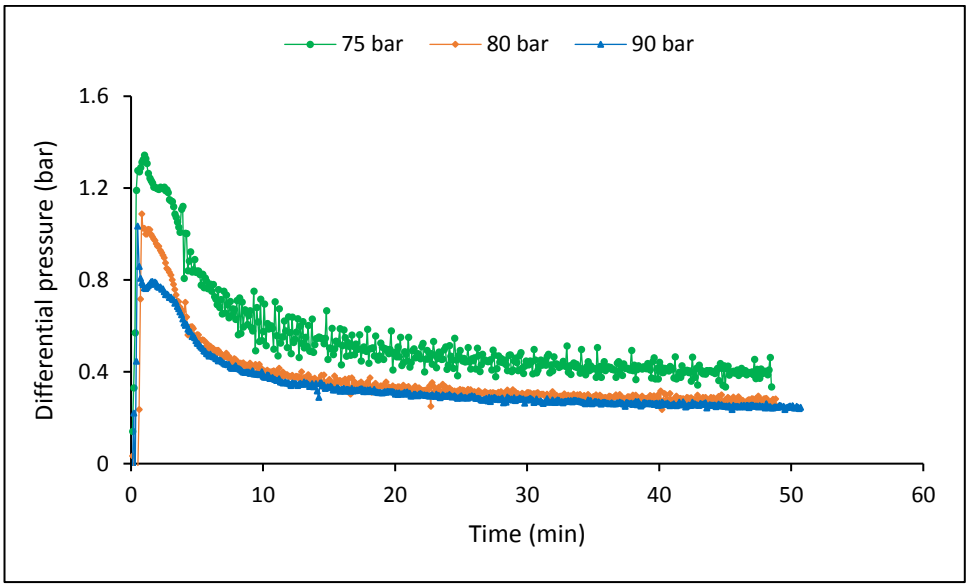

Figure 6-5: Effect of fluid pressure on the differential pressure profile of $ScCO_2$-water displacements conducted at 0.4 ml/min, and 45 °C

6.2.1.3 Effect of Temperature on the Differential Pressure Profile of $ScCO_2$-Water Drainage Displacements

To have a deep understanding of the effect of temperature on the differential pressure and water recovery of $ScCO_2$-water displacements, series of experiments were conducted under different temperatures (33 and 45 °C), different injection rates (0.1, 0.4, and 1ml/min), and different fluid pressures (75 and 90 bar) conditions. Figure 6-6, Figure 6-7, Figure 6-8, and

Figure 6-9 show the impact of increasing temperature on the differential pressure profile. The data show a set of important observations (A-C):

A) The data from Figure 6-6 show that in contrary to the fluid pressure effects, increasing temperature, from 33 to 45 °C at 90 bar, caused the differential pressure profile to transform to the likeness of gaseous CO_2 behaviour.

B) The data from Figure 6-6, Figure 6-7, and Figure 6-8 show that the increase in temperature produced a remarkable increase in the maximum and quasi-differential pressures; this increase increased with the injection rate. The reduction or increase in the corresponding time is dependent on the CO_2 injection rate; the corresponding time decreased with the temperature at an injection rate of 0.1 ml/min and increased with temperature at an injection rate of 0.4 ml/min and higher; which is opposite to the impact of fluid pressure as stated above. The data from Figure 6-6 shows that as the temperature increased from 33 to 45 °C at 0.1 ml/min and 90 bar, the maximum-differential pressure increased by around 133% (from around 0.11 to 0.256 bar) but the corresponding times dropped by around 44.5% (from around 11 to 6.1 min). The quasi-differential pressure was almost identical after about 200 min. The data from Figure 6-7 shows that for the displacements conducted at 0.4 ml/min, increasing the temperature from 33 to 55 °C at 90 bar caused the maximum-differential pressure to rise by around 75.5% (from 0.599 to 1.051 bar), the quasi-differential pressure to increase by 54% (from 0.224 to 0.345 bar), and the corresponding time to extend by around 17% (from 0.6 to 0.7 ml/min). The corresponding time of both 33 and 45 °C-displacements was equal and their differential profiles were almost identical during the last period. The data from Figure 6-8 shows that for the displacements conducted at 1 ml/min, increasing the temperature from 33 to 55 °C at 90 bar led the maximum-differential pressure to increase by around 246.6% (from 0.786 to 2.724 bar), the quasi-differential pressure to increase by about 201% (from 0.299 to 0.901 bar), and the corresponding time to extend by 47% (from 1.7 to 2.5 min).

According to Eq.4-1-Chapter 4, the increase observed in the differential pressure profile with increasing temperature can be related mainly to the increase in the capillary forces and slightly to the increase in the applied viscous forces. The increase in the capillary forces with increasing temperature is due to the increase in the CO_2-water interfacial tension and the

reduction in the contact angle because of the reduction in CO_2 solubility, as shown in Figure 6-4, [24, 28]. On the other hand, the slight increase in the viscous forces with increasing temperature, despite the reduction in the CO_2 dynamic viscosity, is because of increasing the volumetric CO_2 injection rate due to expansion impact. For the experiments conducted at 90 bar-0.4 ml/min, as the temperature increased from 33 to 55 °C, the IFT increased from 25 to 28 mN/m and the volumetric CO_2 injection rate inside the core sample increased from 0.506 to 1.296 ml/min but the CO_2 viscosity decreased from 53.837 to 22.26 × [10^{-6} (Pa·s)][27].

C) The results from Figure 6-9 show that increasing temperature from 33 to 45 °C at a lower fluid pressure (75 bar) led to the appearance of the differential pressure oscillations for the first time in addition to the increase in the maximum and quasi-differential pressures. As the temperature further increased to 55 °C, the magnitude of the oscillations increased. Increasing the temperature from 33 to 55 °C caused the maximum-differential pressure to increase by around 29% (from 1.12 to 1.444 bar), the quasi-differential pressure to increase by about 21% (from 0.367 to 0.444 bar), and the corresponding times to prolong by 175% (from 1 to 1.17 min). The differential pressure oscillations are likely to appear because of the reduction in the ratio of the viscous forces to capillary forces. Thus, the viscous forces became higher than the capillary forces and, as a result, the water flow paths were closed [34].

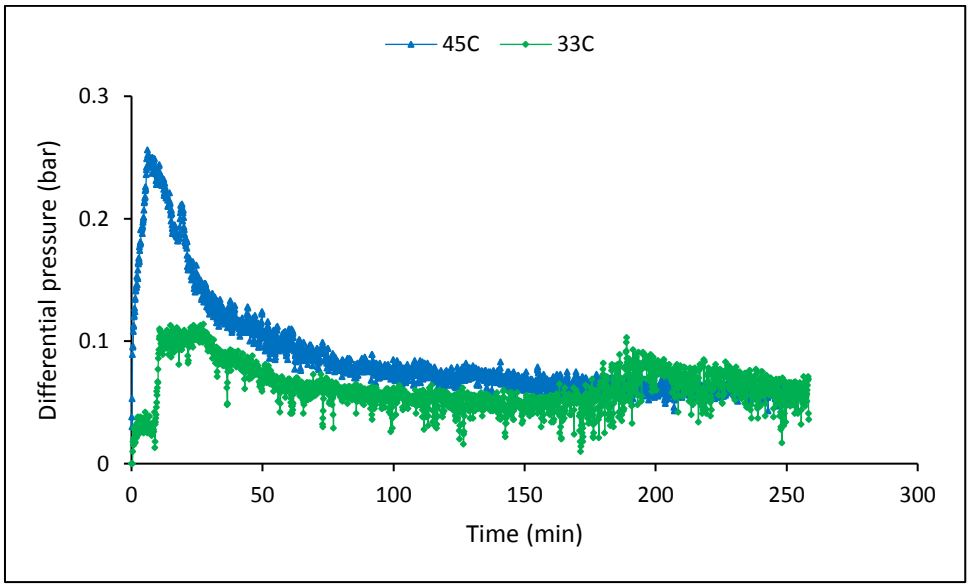

Figure 6-6: Effect of temperature on the differential pressure profile of $ScCO_2$-water displacements conducted at 90 bar and 0.1 ml/min

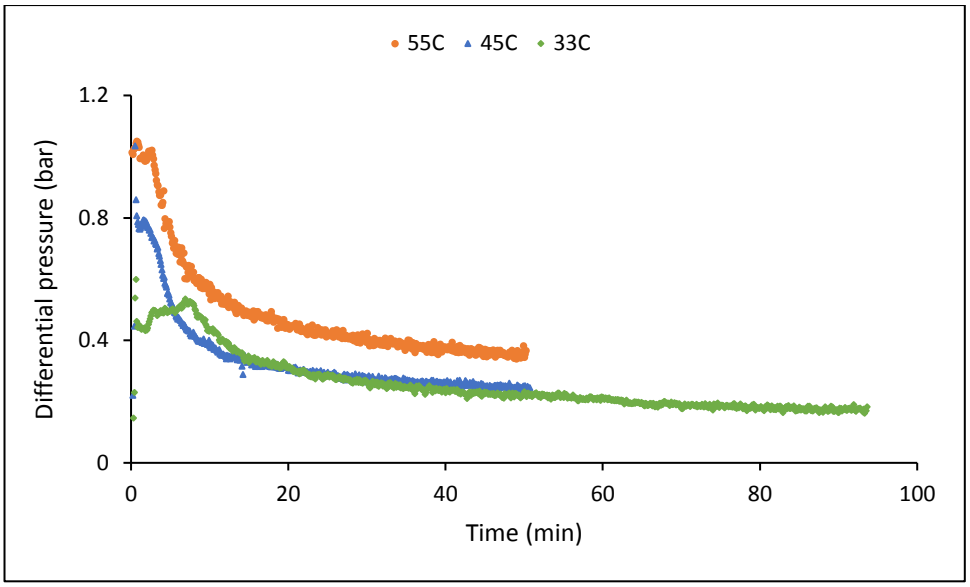

Figure 6-7: Effect of temperature on the differential pressure profile of $ScCO_2$-water displacements conducted at 90 bar and 0.4 ml/min

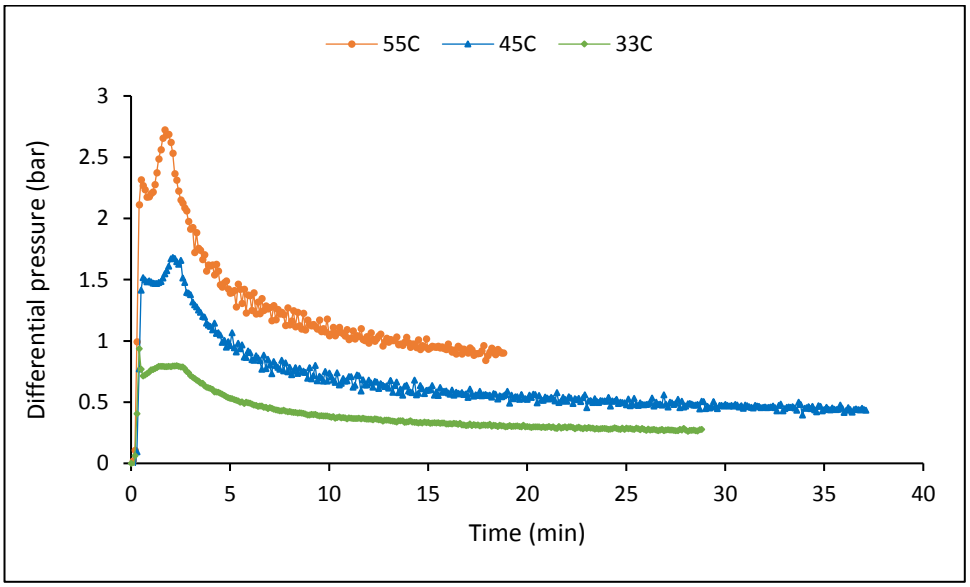

Figure 6-8: Effect of temperature on the differential pressure profile of $ScCO_2$-water displacements conducted at 90 bar and 1 ml/min

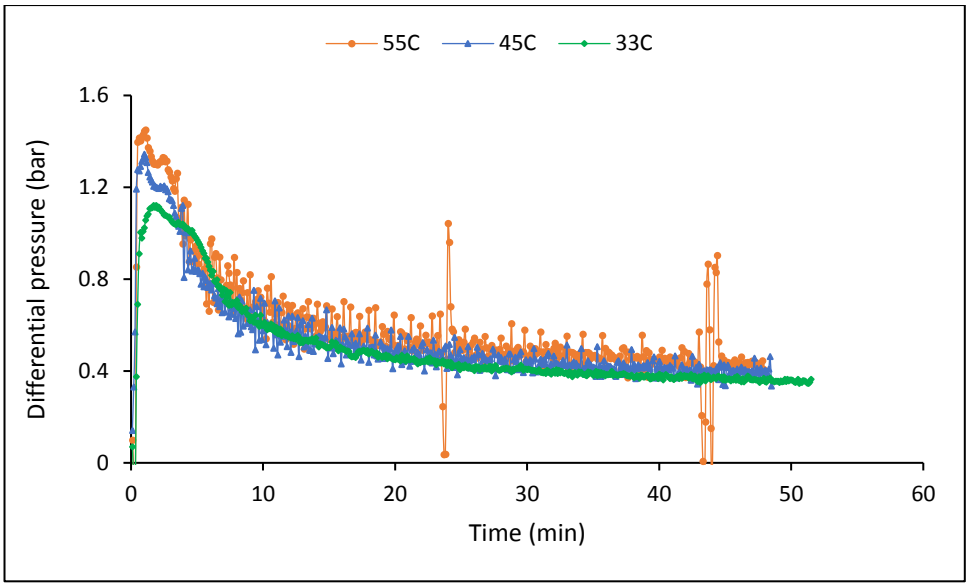

Figure 6-9: Effect of temperature on the differential pressure profile of $ScCO_2$-water displacements conducted at 75 bar and 0.4 ml/min

6.2.1.4 Effect of CO_2 Injection Rate on the Differential Pressure Profile of $ScCO_2$-Water Drainage Displacements

To investigate the effect of CO_2 injection rate on the differential pressure profile and water recovery of $ScCO_2$-water displacements, three series of experiments were performed under various fluid pressures (74 and 90 bar), temperatures (33 and 45 °C), and injection rates (0.1, 0.4, and 1ml/min). Figure 6-10, Figure 6-11, and Figure 6-12 present the effect of increasing CO_2 injection rate on the differential pressure profile under different pressure and temperature conditions. The results show two main observations (A-B):

A) The data show that increasing injection rate caused a considerable increase in the maximum and quasi-differential pressures, this considerable increase increased with the associated temperature and reduced with the associated fluid pressure. The decrease or increase in the corresponding time with increasing injection rate is dependent on the fluid pressure and temperature; the corresponding time decreased under low-temperature (33 °C) and high-fluid pressure (90 bar) conditions but increased under higher-temperature (45 °C) and higher-fluid pressure (90 bar) conditions. The data show that as the injection rate increased from 0.4 to 1 ml/min: (I) the maximum-differential pressure increased by 56% (from 0.599 to 0.935 bar), the quasi-differential pressure was constant, and the corresponding time reduced by 33.33% (from 0.6 to 0.4 min) for the displacements

conducted at 90 bar and 33 °C, as shown in Figure 6-10; (II), the maximum-differential pressure increased by around 62% (from 1.035 to 1.674 bar), the quasi-differential pressure increased by around 85.5% (from 0.234 to 0.434 bar), and the corresponding time increased by 340% (from 0.5 to 2.2 min) for the displacements conducted at 90 bar and 45 °C, as shown in Figure 6-11; and (III) the maximum-differential pressure increased by about 111% (from 1.16 to 2.4446 bar), the quasi-differential pressure by 129% (from around 0.271 to 0.621 bar), and the corresponding time was constant for the displacements conducted at 74 bar and 45 °C, as shown in Figure 6-12.

According to Eq.4-1-Chapter 4, the increase observed in the differential pressure can be related to the increase in the viscous forces because of increasing injection rate, the magnitude of the increase is dependent on the associated fluid pressure and temperature conditions; the highest increase occurred at low pressure and high-temperature conditions. The reduction in corresponding time at low-temperature and high-pressure conditions can be related to the low maximum-differential pressure because of the transformation of the $ScCO_2$-water displacement behaviour to the likeness of a liquid CO_2-water displacement; while the increase in the corresponding time at high-temperature and high-pressure conditions can be associated with the high maximum-differential pressure because of the transformation of the $ScCO_2$-water displacement profile to the likeness of a gaseous CO_2-water displacement.

B) The data in Figure 6-11 show also that increasing the injection rate to 1 ml/min caused a spike in the differential pressure profile, for more information about the potential reasons can be found in Section 5.2.2.3 in Chapter 5-observation C. Moreover, the data from Figure 6-11 also show that the differential pressure profile of the 0.4 and 0.6 ml/min experiments became nearly identical, during the last period, after around 14 min. This suggests that the effect of pressure drop due to viscous forces became negligible after around 14 min.

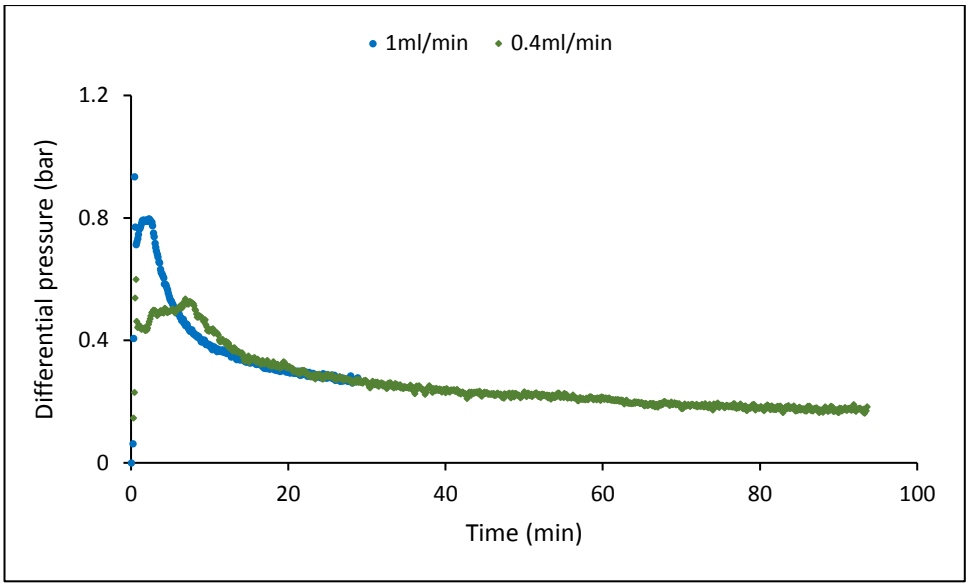

Figure 6-10: Effect of CO_2 injection rate on the differential pressure profile of $ScCO_2$-water displacements conducted at 90 bar and 33 °C

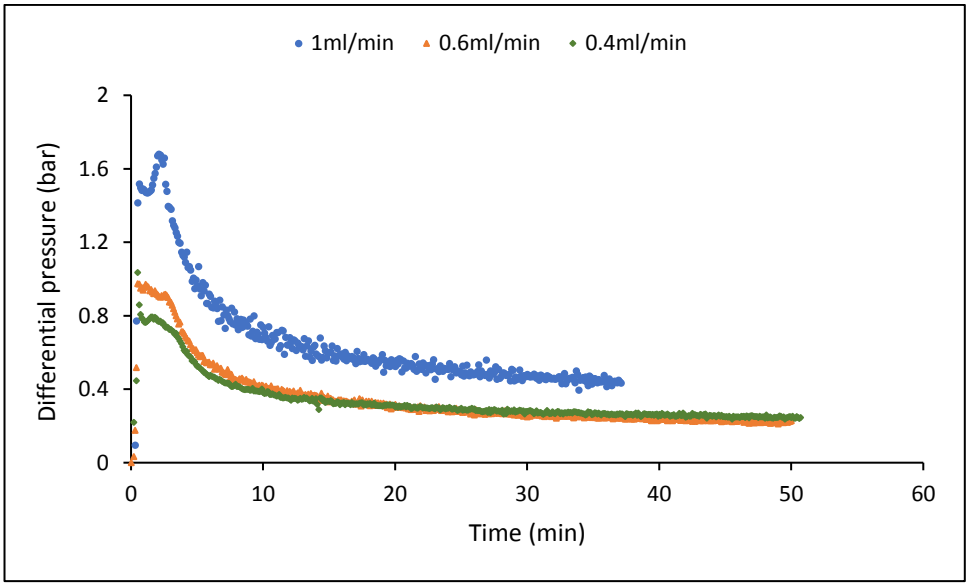

Figure 6-11: Effect of CO_2 injection rate on the differential pressure profile of $ScCO_2$-water displacements conducted at 90 bar and 45 °C

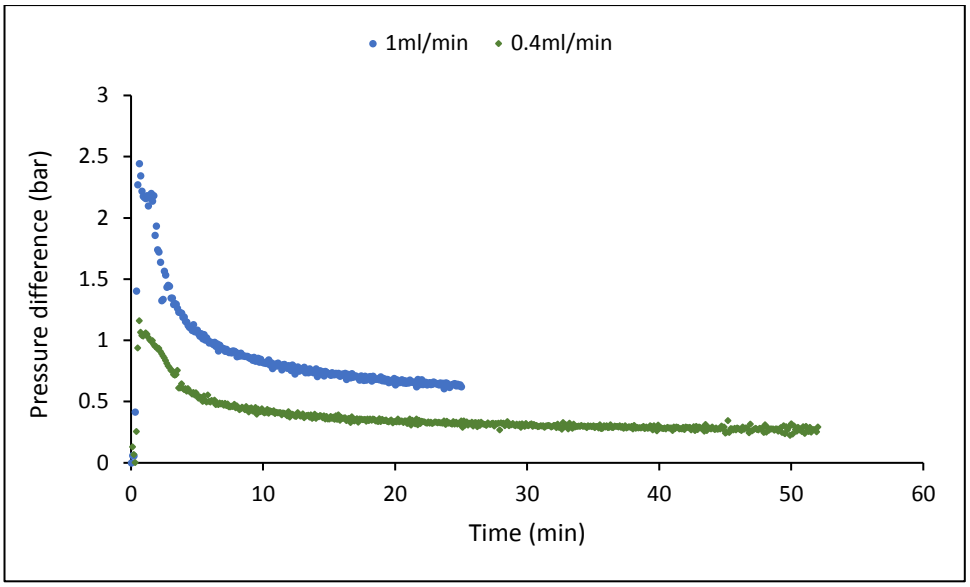

Figure 6-12: Effect of CO_2 injection rate on the differential pressure profile of $ScCO_2$-water displacements conducted at 74 bar and 45 °C

In summary, generally, for all fluid pressures, temperatures, and CO_2 injection rates, the differential pressure is characterized by a sharp increase followed by a steep pressure drop and then by a gradual reduction. Increasing fluid pressure caused the differential pressure profile of the $ScCO_2$-water displacements to transform to the likeness of liquid CO_2 behaviour. Contrariwise, increasing temperature caused it to transform to the likeness of gaseous CO_2 behaviour. Increasing injection rate causes the transition from gaseous to liquid CO_2 behaviour to occur at lower fluid pressures. Increasing fluid pressure caused a slight change in the differential pressure profile; the differential pressure profile of the 90 bar-experiment increased until it became slightly higher than the differential pressure profile of the 80 bar-experiment at the end of the flooding. Increasing temperature at a lower fluid pressure (75 bar) displacements caused the appearance of the differential pressure oscillations. The increase in the injection rate caused spikes in the differential pressure profile.

Increasing fluid pressure caused a substantial drop in the maximum and quasi-differential pressures; this drop decreased with the injection rate. On the other hand, increasing injection rate and temperature caused a considerable increase in the maximum and quasi-differential pressures; this considerable increase is dependent on the concomitant operational conditions. For increasing temperature, the maximum and quasi-differential pressures increased with the injection rate. With increasing injection rate, the maximum and quasi-differential pressures increased with the temperature and reduced with the fluid pressure.

The results indicate a higher impact for the capillary forces than viscous forces on the differential pressure profile when fluid pressure and temperature increase. As the injection rate increased significantly, the impact of viscous forces become more influential.

The magnitude of the corresponding time is dependent on many factors such as the operational conditions (e.g. fluid pressure, temperature, and CO_2 injection rate) and the core sample and fluids properties. This is because of the direct impact of the above factors on the capillary entry pressure (due to their influence on the CO_2-water interfacial tension and core sample wettability), density of the injected fluid, and expansion effect. For illustration, a displacement characterizes by lower entry pressure, dense CO_2, and high injection rate will need much less corresponding time to reach its maximum-differential pressure. Increasing injection rate caused the corresponding time to decrease at low-temperature (33 °C) and high-fluid pressure (90 bar) conditions but increase at high-temperature (45 °C) and high-fluid pressure (90 bar) conditions. For increasing fluid pressure and temperature, the decrease or increase in the corresponding time is dependent on the associated injection rate. For increasing the fluid pressure, the corresponding time increased at an injection rate of 0.1 ml/min but decreased at an injection rate of 0.4 ml/min and higher. However, with increasing the temperature, the corresponding time decreased at an injection rate of 0.1 ml/min but increased at an injection rate of 0.4 ml/min and higher.

6.2.2 Water Production Behaviour of $ScCO_2$-Water Displacements

This section deals with the impact of fluid pressure, temperature, and CO_2 injection rate on water production behaviour.

6.2.2.1 Effect of Fluid Pressure on Water Production Behaviour during $ScCO_2$ Injection

Figure 6-13 presents the effect of increasing fluid pressure on the cumulative produced volumes. The data show that the increase in fluid pressure led to a reduction in the cumulative produced volumes. As the fluid pressure increased, the difference between the cumulative produced volumes and the cumulative injected volumes decreased. The difference was 1.9, 0.75, 0.38, and-0.363 for the experiments performed at 75, 77, 80, and 90 bar, respectively. The 75 bar-experiment corresponded to the highest difference while the 90 bar-experiment corresponded to the lowest. For the experiments performed at 75, 77,

and 80 bar, the cumulative produced volumes were higher than the cumulative injected volumes. As the fluid pressure increased to 90 bar, the cumulative produced volumes became less than the cumulative injected volumes. The high cumulative produced volumes at low pressures mean less volume of CO_2 can be stored at these conditions. However, if the goal is to enhance oil production by reducing the cost of CO_2 then low pressures is a better choice. The increase observed in the cumulative produced volumes can be related mainly to the increase in CO_2 compressibility and solubility with increasing pressure [37, 38].

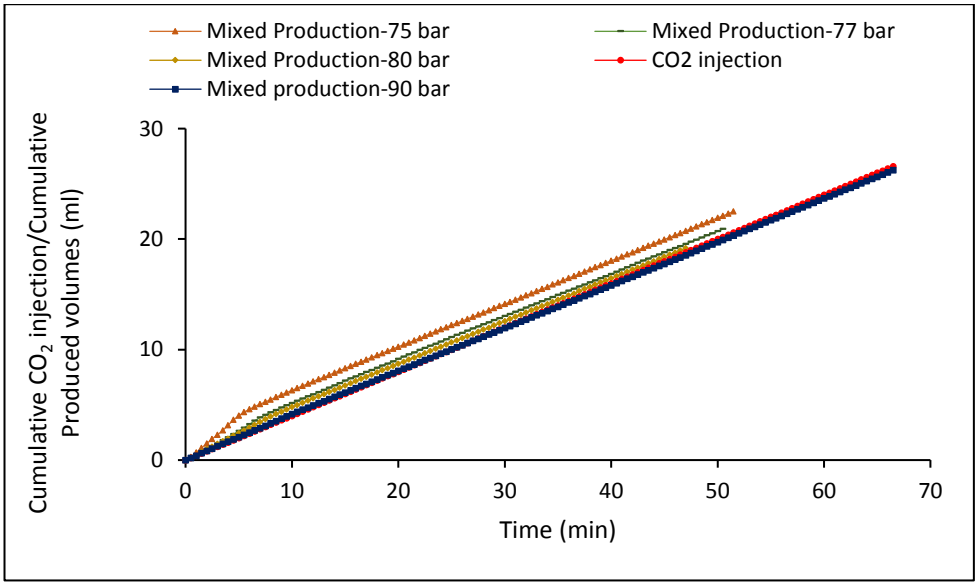

Figure 6-13: Effect of fluid pressure on the cumulative produced volumes for water and CO_2 for $ScCO_2$-water displacements conducted at 0.4 ml/min, and 33 °C

6.2.2.2 Effect of Temperature on Water Production Behaviour during $ScCO_2$ Injection

The effect of increasing temperature on the cumulative produced volumes is shown in Figure 6-14. The data show that as the temperature increased, the cumulative produced volumes increased considerably. As the temperature increased from 33 °C to 55 °C, the cumulative produced volumes increased by around 10.6% (from 20.2 to 22.338 ml). The increase in the cumulative produced volumes can be attributed to the increasing gas expansion and reducing CO_2 solubility because of increasing temperature. The increase in cumulative produced means less CO_2 can be stored in hot temperature environments.

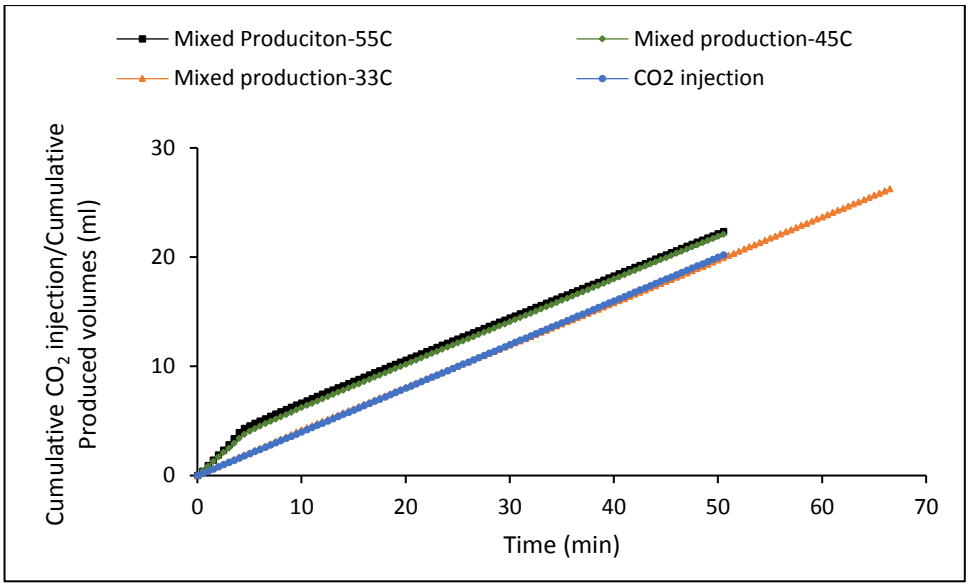

Figure 6-14: Effect of temperature on the cumulative produced volumes of water and CO_2 of $ScCO_2$-water displacements conducted at 90 bar and 0.4 ml/min

6.2.2.3 Effect of CO_2 injection rate on Water Production Behaviour during $ScCO_2$ Injection

Figure 6-15 shows the effect of increasing temperature on the cumulative produced volumes. The impact of CO_2 injection rate was obtained by comparing the data from Figure 6-14 and Figure 6-15. The results show that as the injection rate increased, from 0.1 to 0.4 ml/min, the cumulative produced volumes increased. The cumulative produced volumes increased by around 9% (from 22.627 to 24.662 ml) at 33 °C and increased by around 2.7% (from 13.711 to 14.078 ml) at 45 °C. The increase in the cumulative volume with increasing injection rate can be related to the increase in water recovery due to the increase in the viscous forces at the expense of capillary forces, which try to reduce production by hindering water mobilization of porous media.

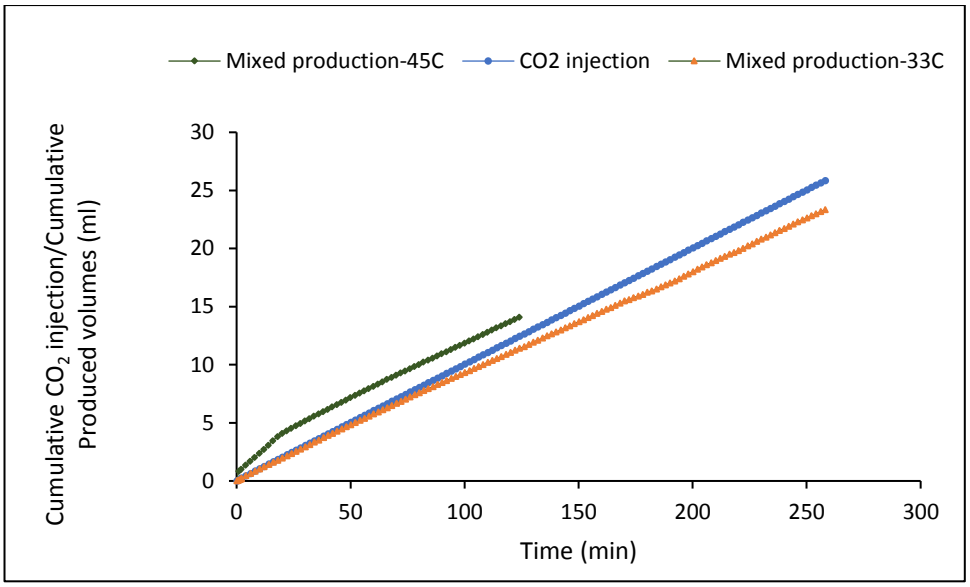

Figure 6-15: Effect of temperature on the cumulative produced volumes of water and CO_2 for $ScCO_2$-water displacements conducted at 90 bar and 0.1 ml/min

In summary, the increase in fluid pressure led to a reduction in the cumulative produced volumes. On the other hand, increasing temperature and injection rate caused an increase in the cumulative produced volumes.

6.2.3 Effect of Fluid Pressure, Temperature, and CO_2 Injection Rate on Endpoint CO_2 Effective and Relative Permeabilities and Residual Water Saturation during $ScCO_2$ Injection

In this section, the same procedures that were presented in Chapter 4-Section 4.2.3 for measuring and calculating the endpoint CO_2 effective and relative permeabilities and residual water saturation are followed here.

Table 6-1 presents the endpoint effective and relative permeabilities of supercritical CO_2 as well as the residual water saturation as a function of fluid pressure, temperature, and CO_2 injection rate. The results show that both CO_2 endpoint relative permeability (K_{rCO2}) [14] and residual water saturation (S_{wr}) are dependent on the experimental conditions at which they are measured. The S_{wr} was in ranges of 0.34 to 0.41 while the K_{rCO2} was less than 0.37. Akbarabadi and Piri as well as Busch and Müller observed a low relative permeability for CO_2 [39, 40]. Such low relative permeability would tend to decrease injectivity while increasing displacements efficiency [18]. The results showed a remarkable impact for the parameters investigated on the K_{rCO2} but a less impact on the S_{wr}. The amount of the injected volumes

showed no impact on the S_{wr} trend. The logarithmic values of the viscosity (M) and capillary numbers (Ca) ranged from1.14 to1.48 and from -6.13 to-7.21, respectively, as shown in Figure 6-16. This shows that the invasion pattern of this study is capillary fingering regime [41], as shown in Figure 2-18 in Chapter 2.

In general, increasing fluid pressure led to an increase in the K_{rCO2}. This is in agreement with the findings of Bennion and Bachu [42]. The magnitude of the increase in the K_{rCO2} with increasing fluid pressure depends on the concomitant injection rate and temperature; the K_{rCO2} decreased with increasing the injection rate and experimental temperature. The highest increase occurred with low injection rate and low temperature. As the fluid pressure increased from 75 to 90 bar at 33 °C, the K_{rCO2} increased: (I) by about 0.114 for the 0.1 ml/min-displacements, (II) by around 0.08 for the 0.4 ml/min-displacements, and (III) by approximately 0.07 for the 1 ml/min-displacements. However, as the fluid pressure increased from 75 to 90 bar at 45 °C, the K_{rCO2} increased by about 0.046 for the 0.4 ml/min-displacements. The reduction in the K_{rCO2} as the temperature increased from 33 to 45 °C might be associated with the increase in the capillary forces which hinder water production. It should be noted that Liu et al also observed an increase in the K_{rCO2} with increasing fluid pressure [30]. Bennion and Bachu noticed also an increase in the K_{rCO2} and the maximum endpoint CO_2 saturation (i.e. a reduction in the S_{wr}) and attributed that to decreasing interfacial tension with increasing pressure [42].

The results from Table 6-1 show that in compassion to its impact on K_{rCO2}, the fluid pressure showed a lesser influence on the S_{wr} [42]. Increasing the fluid pressure from 75 to 90 bar at 33 °C resulted in decreasing the S_{wr}: (I) by 0.027 for the 0.1 ml/min displacements, (II) by 0.015 for the 0.4 ml/min displacements, and (III) by 0.016 for the 1 ml/min displacements. Increasing the fluid pressure from 75 to 90 bar at 45 °C and 0.4 ml/min produced a reduction in the S_{wr} by 0.025. The main reasons behind the reduction in the S_{wr} are the increase in the Ca and the reduction in the M as illustrated in Table 6-1. It should be noted that the displacement conducted at 80 bar-0.1 ml/min-33 °C showed the lowest S_{wr} of 0.343 and the highest K_{rCO2} of around 0.223, the reason is not entirely to us. However, this might be related to the transition from gaseous to liquid CO_2 behaviour as the fluid pressure increased from 75 to 80 bar and then to 90 bar, as shown in Figure 6-1.

The results from Table 6-1 show that the impact of the temperature on the K_{rCO2} is dependent largely on the associated fluid pressure and injection rate. The K_{rCO2} showed a declining trend with increasing temperature at high-fluid pressures (90 bar) but an increasing trend at lower-fluid pressures (75 bar). With increasing the fluid temperature, the percentage of the reduction in the K_{rCO2} at high-fluid pressures increased with the injection rate. For the 90 bar-core floodings, increasing temperature from 33 to 45 °C at low injection rate (0.1ml/min) caused the K_{rCO2} to decrease by around 0.081. As the temperature increased from 33 to 55 °C, the K_{rCO2} dropped by about 0.121 for the 0.4ml/min-displacements and by 0.239 for the 1 ml/min-displacements. On the other hand, for the 75 bar-core floodings, as the temperature increased from 33 to 55 °C, the K_{rCO2} increased slightly by around 0.015; the reason is not entirely clear. However, it might be also associated with the slight increase in pressure drop despite the high reduction in CO_2 viscosity with increasing temperature; the slight increase in pressure drop might be associated with the transfer of supercritical CO_2 behaviour towards gaseous CO_2 behaviour, especially under high-temperature and low-fluid pressure conditions, as shown in Figure 6-9. It should be noted that there is no consensus in the literature about the effect of temperature on the relative permeability. For illustration Bennion and Bachu [37] observed a reduction in the relative permeability with increasing temperature. On the other hand, Lee et al observed almost no change in the relative permeability with increasing temperature [43].

Generally, the results from Table 6-1 show that the increase in temperature led to an increase in the S_{wr}. The magnitude of the increase depends on the associated fluid pressure and injection rate. Overall, as the temperature increased, the increase in the S_{wr} increased with the injection rate and fluid pressure. As the temperature increased from 33 to 45 °C, the S_{wr} increased by 0.004 for the experiments conducted at 90 bar and 0.1 ml/min. When the temperature increased from 33 to 55 °C, the S_{wr} increased by 0.021 for the experiments conducted at 90 bar and 0.4 ml/min, by 0.041 for the experiments conducted at 90 bar and 1 ml/min, and by 0.018 for the experiments conducted at 75 bar and 0.4 ml/min and. Overall, the reduction in the K_{rCO2} and the increase in S_{wr} can be related to the reduction in the Ca and the increase in the M.

In general, the results from Table 6-1 show that the increase in the CO_2 injection rate caused a rise in the K_{rCO2} and a reduction in the S_{wr}. These findings agree qualitatively with those

obtained by Chang et al. and Akbarabadi and Piri [2, 40]. As the injection rate increased, the change in the K_{rCO2} and S_{wr} increased with the fluid pressure but decreased with the temperature. Overall, as the injection rate increased from 0.1 to 1 ml/min, the K_{rCO2} increased by about 0.0384 for the 75 bar-33 °C-core floodings, by around 0.1341 for the 90 bar-33 °C-core floodings, by about 0.0168 for the 74 bar-45 °C-core floodings, and by 0.084 for the 90 bar-45 °C-core floodings. The S_{wr} decreased by 0.033, 0.034, 0.006, and 0.012 for the above experiments, respectively. Since M is constant, the reduction in the S_{wr} can be related mainly to the increase observed in the *Ca*. On the other hand, the displacements conducted at 80 bar showed an opposite behaviour. As the injection rate increased from 0.1 to 1ml/min, the K_{rCO2} decreased by 0.08 and the S_{wr} increased by 0.041. The reason is not entirely clear. However, this might be related to the transition from gaseous to liquid CO_2 behaviour as the fluid pressure increased from 75 to 80 bar and then to 90 bar, see Figure 6-1.

Table 6-1: Effect of fluid pressure, temperature, and CO_2 injection rate on the endpoint effective (K_{fCO2}) and relative permeabilities (K_{rCO2}) of supercritical CO_2 and residual water saturation (S_{wr}).

Parameter	Experiment	K_{fCO2}	K_{rCO2}	S_{wr}	*Ca*	*M*	Injected CO_2 (ml)
Fluid Pressure Effect	75 bar-0.1 ml/min-33 °C	1.095	0.0698	0.411	6.417E-08	22.47	20.19
	80 bar-0.1ml/min-33°C	3.495	0.223	0.343	6.613E-08	16.31	24.7
	90 bar-0.1ml/min-33°C	2.880	0.1837	0.384	7.413E-08	13.91	25.82
	75 bar-0.4ml/min-33°C	1.858	0.1185	0.372	2.566E-07	22.47	20.6
	77 bar-0.4ml/min-33°C	2.207	0.1408	0.374	2.594E-07	19.53	19.84
	80 bar-0.4ml/min-33°C	2.388	0.1523	0.372	2.645E-07	16.31	18.36
	90 bar-0.4ml/min-33°C	3.128	0.1995	0.357	2.965E-07	13.91	37.36
	75 bar-1ml/min-33°C	1.696	0.1082	0.366	6.417E-07	22.47	20
	80 bar-1ml/min-33°C	2.307	0.14715	0.362	6.613E-07	16.31	20.5
	90 bar-1ml/min-33°C	2.815	0.1795	0.35	7.413E-07	13.91	20.3
	75 bar-0.4ml/min-45°C	1.897	0.1201	0.39	2.577E-07	29.59	19.52
	80 bar-0.4ml/min-45°C	2.714	0.1730	0.363	2.497E-07	27.93	19.24
	90 bar-0.4ml/min-45°C	2.619	0.1670	0.365	2.467E-07	20.62	20.04

Temperature Effect	90 bar-0.1ml/min-33°C	3.677	0.2345	0.384	7.413E-08	13.91	25.82
	90 bar-0.1ml/min-45°C	2.404	0.1533	0.388	6.168E-08	20.62	25.14
	90 bar-0.4ml/min-33°C	4.019	0.2563	0.357	2.965E-07	13.91	37.36
	90 bar-0.4ml/min-45°C	2.629	0.1677	0.365	2.467E-07	20.62	20
	90 bar-0.4ml/min-55°C	2.123	0.1354	0.378	2.445E-07	22.73	20.08
	90 bar-1ml/min-33°C	5.780	0.3686	0.35	7.413E-07	13.91	20.3
	90 bar-1ml/min-45°C	2.918	0.1861	0.374	6.168E-07	20.62	36.7
	90 bar-1ml/min-55°C	2.032	0.1296	0.391	6.114E-07	22.73	18.8
	75 bar-0.4ml/min-33°C	1.921	0.1225	0.372	2.566E-07	22.47	20.6
	75 bar-0.4ml/min-45°C	1.995	0.1272	0.39	2.577E-07	29.59	19.4
	75 bar-0.4ml/min-55°C	2.160	0.1378	0.39	2.641E-07	25.91	19.16
Injection Rate Effect	75 bar-0.1ml/min-33°C	1.095	0.0698	0.411	6.417E-08	22.47	20.19
	75 bar-0.4ml/min-33°C	1.921	0.1225	0.372	2.566E-07	22.47	20.6
	75 bar-1ml/min-33°C	1.696	0.1082	0.378	6.417E-07	22.47	20
	90 bar-0.1ml/min-33°C	3.677	0.2345	0.384	7.41E-08	13.91	25.82
	90 bar-0.2ml/min-33°C	1.755	0.1119	0.386	1.48E-07	13.91	17.24
	90 bar-0.4ml/min-33°C	4.019	0.25632	0.357	2.97E-07	13.91	37.36
	90 bar-1ml/min-33°C	5.78	0.3686	0.35	7.41E-07	13.91	20.3
	74 bar-0.4ml/min-45°C	2.902	0.1851	0.39	2.60E-07	29.94	25
	74 bar-1ml/min-45°C	3.166	0.2019	0.384	6.50E-07	29.94	20.56
	90 bar-0.1ml/min-45°C	2.404	0.1533	0.368	6.17E-08	20.62	25.14
	90 bar-0.4ml/min-45°C	2.629	0.1677	0.365	2.47E-07	20.62	19.76
	90 bar-0.6ml/min-45°C	4.333	0.2764	0.353	3.70E-07	20.62	29.63
	90 bar-1ml/min-45°C	3.711	0.2367	0.356	6.17E-07	20.62	37.1
	80 bar-0.1ml/min-33°C	3.569	0.2276	0.343	6.613E-08	16.31	24.7
	80 bar-0.4ml/min-33°C	2.388	0.1523	0.372	2.645E-07	16.31	18.36
	80 bar-1ml/min-33°C	2.307	0.1472	0.384	6.613E-07	16.31	20.5

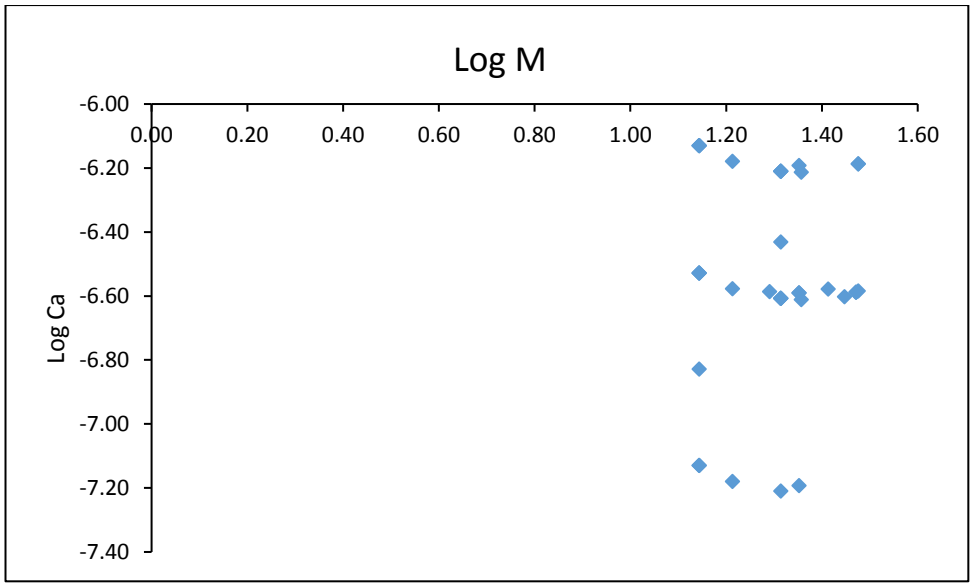

Figure 6-16: Capillary number (*Ca*) against viscosity ratio (*M*) on a logarithmic scale for the experiments presented in Table 6-1.

6.3 Summary

This study investigated the impact of fluid pressure, temperature, and CO_2 injection rate on the dynamic pressure evolution and displacement efficiency during the injection of supercritical CO_2 into a water-saturated sandstone core sample. The experiments also highlight the impact of both capillary and viscous forces on multiphase flow characteristics (i.e. pressure and production data) of $ScCO_2$-water displacements. The results show a moderate to considerable impact of the parameters investigated on multiphase flow characteristics. The extent of the impact of each parameter (e.g. fluid pressure) is a function of the associated parameters (e.g. temperature and injection rate). The results show a higher impact for capillary forces than viscous forces on multiphase flow characteristics when fluid pressure and temperature increase. As the injection rate increased significantly, the impact of viscous forces become more influential.

In general, the results show that for all fluid pressures, temperatures, and CO_2 injection rates the differential pressure is characterized by a sharp increase followed by a steep pressure drop and then by a gradual reduction. Increasing fluid pressure caused the differential pressure profile of the $ScCO_2$-water displacements to transform to the likeness of liquid CO_2 behaviour. On contrary, increasing temperature caused it to transform to the likeness of gaseous CO_2 behaviour. Increasing injection rate causes the transition from gaseous to liquid

CO_2 behaviour to occur at lower pressures. Increasing fluid pressure caused a slight change in the differential pressure profile; the differential pressure profile of the 90 bar-experiment increased until it became slightly higher than the differential pressure profile of the 80 bar-experiment at the end of the flooding. Increasing temperature at a lower fluid pressure (75 bar) caused the appearance of the differential pressure oscillations. Increasing injection rate caused spikes in the differential pressure profile.

Increasing fluid pressure caused a substantial drop in the maximum and quasi-differential pressures; this large drop decreased with the injection rate. On the other hand, increasing injection rate and temperature caused a considerable increase in the maximum and quasi-differential pressures; this considerable increase is dependent on the concomitant operational conditions. For increasing temperature, the maximum and quasi-differential pressures increased with the injection rate. For increasing injection rate, the maximum and quasi-differential pressures increased with the temperature and reduced with the fluid pressure.

Increasing injection rate influences the time required to reach the maximum differential pressure, i.e. the corresponding time. With increasing CO_2 injection rate, the corresponding time decreases under low-temperature (33 °C) and high-fluid pressures (90 bar) conditions but increase under higher-temperature (45 °C) and high-fluid pressure (90 bar) conditions. For increasing fluid pressure and temperature, the decrease or increase in the corresponding time is dependent on the associated CO_2 injection rate. For increasing the fluid pressure, the corresponding time increased at an injection rate of 0.1 ml/min and decreased at an injection rate of 0.4 ml/min and higher. However, for increasing the temperature, the corresponding time decreased at an injection rate of 0.1 ml/min and increased at an injection rate of 0.4 ml/min and higher.

The increase in fluid pressure led to a reduction in the cumulative produced volumes. On the other hand, increasing temperature and CO_2 injection rate caused an increase in the cumulative produced volumes.

The results show that both endpoint relative CO_2 permeability (K_{rCO2}) and residual water saturation (S_{wr}) are dependent on the experimental conditions at which they are measured.

The S_{wr} was in ranges of 0.34 -0.41 while the K_{rCO2} was less than 0.37. The results showed a remarkable impact for the parameters investigated on the K_{rCO2} with a lesser impact on the S_{wr}. The amount of the injected volumes showed no impact on the S_{wr} trend. Based on logarithmic values of the mobility ratio (*M*) and capillary number (*Ca*), the invasion pattern of this study is capillary fingering regime. Increasing fluid pressure caused an increase in the K_{rCO2} and a reduction in the S_{wr}; the magnitude of the increase in the K_{rCO2} with increasing fluid pressure depends on the associated injection rate and temperature conditions. However, increasing temperature led to an increase in the S_{wr}. The K_{rCO2} showed a declining trend with increasing temperature at high fluid pressures (90 bar) but an increasing trend at lower fluid pressures (75 bar); the magnitude of the change in K_{rCO2} and S_{wr} depends on the associated fluid pressure and injection rate conditions. The increase in the CO_2 injection rate caused a rise in the K_{rCO2} and a reduction in the S_{wr}. As the injection rate increased, the change in the K_{rCO2} and S_{wr} increased with the fluid pressure but decreased with the temperature.

6.4 Reference

1. Berg S, Oedai S, Ott H. Displacement and mass transfer between saturated and unsaturated CO_2–brine systems in sandstone. IJGGC. 2013;12:478-92.

2. Chang C, Zhou Q, Xia L, Li X, Yu Q. Dynamic displacement and non-equilibrium dissolution of supercritical CO_2 in low-permeability sandstone: An experimental study. IJGGC. 2013;14:1-14.

3. Suenaga H, Nakagawa K. Analysis of two-phase flow properties of sandstones to evaluate their suitability for geologic storage of CO_2. Energy Procedia. 2011;4:4323-30.

4. Suekane T, Soukawa S, Iwatani S, Tsushima S, Hirai S. Behavior of supercritical CO_2 injected into porous media containing water. Energy. 2005;30(11):2370-82.

5. Krevor S, Pini R, Benson SM. Measurement of the multiphase flow properties of the CO_2 brine system for carbon sequestration. Energy Procedia. 2013;37:4499-503.

6. Herring AL, Andersson L, Newell D, Carey J, Wildenschild D. Pore-scale observations of supercritical CO_2 drainage in Bentheimer sandstone by synchrotron x-ray imaging. IJGGC. 2014;25:93-101.

7. Wang D, Zhao M, Song Y, Xu H, Ma X. Influence of capillary pressure and injection rate as well as heterogeneous and anisotropic permeability on CO_2 transport and displacement efficiency in water-saturated porous media. Energy Procedia. 2013;37:3945-51.

8. Pentland C, El-Maghraby R, Georgiadis A, Iglauer S, Blunt M. Immiscible displacements and capillary trapping in CO_2 storage. Energy Procedia. 2011;4:4969-76.

9. Alemu BL, Aker E, Soldal M, Johnsen Ø, Aagaard P. Influence of CO_2 on rock physics properties in typical reservoir rock: A CO_2 flooding experiment of brine saturated sandstone in a CT-scanner. Energy Procedia. 2011;4:4379-86.

10. Saeedi A, Rezaee R, Evans B, Clennell B. Multiphase flow behaviour during CO_2 geo-sequestration: Emphasis on the effect of cyclic CO_2–brine flooding. JPSE. 2011;79(3):65-85.

11. Perrin J-C, Benson S. An experimental study on the influence of sub-core scale heterogeneities on CO_2 distribution in reservoir rocks. Transport in porous media. 2010;82(1):93-109.

12. Shi J-Q, Xue Z, Durucan S. Supercritical CO_2 core flooding and imbibition in Tako sandstone—Influence of sub-core scale heterogeneity. IJGGC. 2011;5(1):75-87.

13. Ott H, Pentland C, Oedai S. CO_2–brine displacement in heterogeneous carbonates. IJGGC. 2015;33:135-44.

14. Armstrong RT, McClure J, Berill M, Rücker M, Schlüter S, Berg S. Flow regimes during immiscible displacement. Petrophysics. 2017;58(01):10-8.

15. Cao SC, Dai S, Jung J. Supercritical CO_2 and brine displacement in geological carbon sequestration: Micromodel and pore network simulation studies. IJGGC. 2016;44:104-14.

16. Ott H, de Kloe K, Marcelis F, Makurat A. Injection of supercritical CO_2 in brine saturated sandstone: Pattern formation during salt precipitation. Energy Procedia. 2011;4:4425-32.

17. Pini R, Krevor SC, Benson SM. Capillary pressure and heterogeneity for the CO_2/water system in sandstone rocks at reservoir conditions. Advances in Water Resources. 2012;38:48-59.

18. Levine JS, Matter JM, Goldberg DS, Lackner KS, Supp MG, Ramakrishnan T. Two phase brine-CO_2 flow experiments in synthetic and natural media. Energy Procedia. 2011;4:4347-53.

19. Edlmann K, Haszeldine S, McDermott C. Experimental investigation into the sealing capability of naturally fractured shale caprocks to supercritical carbon dioxide flow. Environmental earth sciences. 2013;70(7):3393-409.

20. Zheng XL, Mahabadi N, Yun TS, Jang J. Effect of capillary and viscous force on CO_2 saturation and invasion pattern in the microfluidic chip. Journal of Geophysical Research-Solid Earth. 2017;122(3):1634-47.

21. Song Y, Jiang L, Liu Y, Yang M, Zhao Y, Zhu N, et al. An experimental study on CO_2/water displacement in porous media using high-resolution magnetic resonance imaging. IJGGC. 2012;10:501-9.

22. Wang D, Dong B, Breen S, Zhao M, Qiao J, Liu Y, et al. Review: Approaches to research on CO_2/brine two-phase migration in saline aquifers. Hydrogeology Journal. 2015;23(1):1-18.

23. Bikkina P, Wan J, Kim Y, Kneafsey TJ, Tokunaga TK. Influence of wettability and permeability heterogeneity on miscible CO_2 flooding efficiency. Fuel. 2016;166:219-26.

24. Yang D, Gu Y, Tontiwachwuthikul P. Wettability determination of the reservoir brine− reservoir rock system with dissolution of CO_2 at high pressures and elevated temperatures. Energy & Fuels. 2007;22(1):504-9.

25. Plug W-J, Bruining J. Capillary pressure for the sand–CO_2–water system under various pressure conditions. Application to CO_2 sequestration. Advances in Water Resources. 2007;30(11):2339-53.

26. Jung J-W, Wan J. Supercritical CO_2 and ionic strength effects on wettability of silica surfaces: Equilibrium contact angle measurements. Energy & Fuels. 2012;26(9):6053-9.

27. Peace software. 2017 [http://www.peacesoftware.de/einigewerte/co2_e.html].

28. Bachu S, Bennion DB. Interfacial tension between CO_2, freshwater, and brine in the range of pressure from (2 to 27) MPa, temperature from (20 to 125) °C, and water salinity from (0 to 334 000) mg· L− 1. Journal of Chemical & Engineering Data. 2008;54(3):765-75.

29. Yang D, Tontiwachwuthikul P, Gu Y. Interfacial interactions between reservoir brine and CO_2 at high pressures and elevated temperatures. Energy & Fuels. 2005;19(1):216-23.

30. Liu N, Ghorpade SV, Harris L, Li L, Grigg RB, Lee RL, editors. The effect of pressure and temperature on brine-CO_2 relative permeability and IFT at reservoir conditions. In Proceedings of theSPE Eastern Regional Meeting; Morgantown, WV, USA, 13–15 October 2010: SPE: Houston, TX, USA, 2010.

31. Rezaei N, Firoozabadi A. Pressure evolution and production performance of waterflooding in n-heptane-saturated fired Berea cores. SPE Journal. 2014;19(04):674-86.

32. Plug W-J, Bruining J. Capillary pressure for the sand–CO_2–water system under various pressure conditions. Application to CO_2 sequestration. Advances in Water Resources. 2007;30(11):2339-53.

33. Espinoza DN, Santamarina JC. Water-CO_2-mineral systems: Interfacial tension, contact angle, and diffusion—Implications to CO_2 geological storage. Water resources research. 2010;46(7).

34. Nutt C, editor. The physical basis of the displacement of oil from porous media by other fluids: a capillary bundle model. Proceedings of the Royal Society of London A: Mathematical, Physical and Engineering Sciences; 1982.

35. Kwelle SO. Experimental studies on resistance to fluid displacement in single pores [Ph.D. Thesis]: The University of Edinburgh, Edinburgh, UK; 2017.

36. Parkhurst DL, Appelo CAJ. Description of input and examples for PHREEQC version 3-a computer program for speciation, batch-reaction, one-dimensional transport, and inverse geochemical calculations 2017 [cited 2017 1 December]. Available from: https://wwwbrr.cr.usgs.gov/projects/GWC_coupled/phreeqc/phreeqc3-html/phreeqc3-77.htm.

37. Bennion DB, Bachu S, editors. The impact of interfacial tension and pore size distribution/capillary pressure character on CO_2 relative permeability at reservoir conditions in CO_2-brine systems. In Proceedings of the SPE/DOE Symposium on Improved Oil Recovery; Tulsa, OK, USA, 22–26 April 2006: SPE: Houston, TX, USA, 2006.

38. Tokunaga TK, Wan J. Capillary pressure and mineral wettability influences on reservoir CO_2 capacity. Reviews in Mineralogy and Geochemistry. 2013;77(1):481-503.

39. Busch A, Müller N. Determining CO_2/brine relative permeability and capillary threshold pressures for reservoir rocks and caprocks: Recommendations for development of standard laboratory protocols. Energy Procedia. 2011;4:6053-60.

40. Akbarabadi M, Piri M. Geologic storage of carbon dioxide: an experimental study of permanent capillary trapping and relative permeability. In Proceedings of International Symposium of the Society of Core Analysts; Austin, Texas, USA. 18–21 September 2011. p. 18-21.

41. Zhang C, Oostrom M, Wietsma TW, Grate JW, Warner MG. Influence of viscous and capillary forces on immiscible fluid displacement: Pore-scale experimental study in a water-wet micromodel demonstrating viscous and capillary fingering. Energy & Fuels. 2011;25(8):3493-505.

42. Bennion DB, Bachu S, editors. Dependence on temperature, pressure, and salinity of the IFT and relative permeability displacement characteristics of CO_2 injected in deep saline aquifers. SPE Annual Technical Conference and Exhibition; 2006.

43. Lee Y, Kim K, Lee T, Sung W, Park Y, Lee J. Analysis of CO_2 endpoint relative permeability and injectivity by change in pressure, temperature, and phase in saline aquifer. Energy Sources, Part A: Recovery, Utilization, and Environmental Effects. 2009;32(1):83-99.

7 Chapter 7: CO_2-Oil Drainage Displacements

7.1 Introduction

Since CO_2 has been in use for several decades, extensive laboratory studies [1, 2], numerical simulations [3], and field applications of CO_2 flooding have been conducted in various light, medium [4], and heavy oil reservoirs [5]. However, despite its high importance and the extensive research on CO_2–oil displacements, the literature review shows that investigations allocated to CO_2–oil displacements [4, 6-18] have widely overlooked the analysis of the pressure data in core flooding [19]. Moreover, the literature review also reveals that CO_2–oil displacements were conducted either under gaseous, liquid, or supercritical CO_2 conditions with the exception of a few experiments that were conducted under more than one CO_2 state. To the best of the authors' knowledge, there is no study that has been conducted to examine the effect of the CO_2 phase on the dynamic pressure evolution and the oil recovery performance during CO_2–oil drainage core floodings.

In this study, drainage experiments were performed by injecting pure CO_2 (under gaseous, liquid, and supercritical CO_2 condition) into an oil-saturated Berea sandstone core sample to investigate the effect of the CO_2 phase, fluid pressure, temperature, and CO_2 injection rate on multiphase flow characteristics, especially focusing on the differential pressure profile, cumulative produced volumes, residual oil saturation, and endpoint effective and relative permeabilities of CO_2. This study shed more light on the impact of capillary and viscous forces on multiphase flow characteristics and show the conditions when the capillary or viscous forces dominate the flow. The results of this study would provide deep insights into the impact of the CO_2 phase as well as operational conditions on the injectivity, migration, displacement efficiency, storage capacity, and integrity of CO_2 flooding.

7.2 Results and Discussions

To gain deep understanding of the effect of the CO_2 phase on the two-phase flow characteristics of CO_2-oil drainage displacements, the inlet and outlet pressures, the outlet CO_2 and oil flow rates, the differential pressure profile, the cumulative produced volumes, the residual oil saturation, and the endpoint effective and relative permeabilities of CO_2 were measured and analysed carefully.

In this study, the quasi-differential pressure refers to the differential pressure measured at the end of CO_2 flooding displacement. The corresponding time represents the time required to achieve the maximum-differential pressure at the start of the experiment. The data are categorized into three main sections. The first main section deals with the impact of fluid pressure, experimental temperature, and CO_2 injection rate on the differential pressure profile as a function of the CO_2 phase. The second and the third sections deal with their impact on the production data profiles and the endpoint effective and relative permeabilities of CO_2 and the residual oil saturation as a function of the CO_2 phase.

7.2.1 Differential Pressure Profile of CO_2-Oil Drainage Displacements as a Function of the CO_2 Phase

This section deals with the impact of fluid pressure, experimental temperature, and CO_2 injection rate on the differential pressure profile of gaseous (G), liquid (L), and supercritical (Sc) CO_2-oil drainage displacements.

7.2.1.1 Effect of Fluid Pressure on the Differential Pressure Profile of CO_2-Oil Displacements as a Function of the CO_2 Phase

Figure 7-1, Figure 7-3, Figure 7-4, and Figure 7-5 present the impact of increasing fluid pressure on the differential pressure profile of gaseous, liquid, and supercritical CO_2-oil drainage displacements. During the experiments, the experimental temperature and CO_2 injection rate were held constant. The data reveal three important observations (A, B, and C) that can be identified as follows:

A) Generally, for all fluid pressures, the differential pressure profile is characterized by a high increase followed by a sharp decline. The rate and the magnitude of the increase in the differential pressure profile are dependent on the CO_2 phase as well as the fluid pressure for gaseous CO_2 displacements. The slope of the reduction in the differential pressure profile decreased over time and is dependent on the CO_2 phase and the fluid pressure for the gaseous CO_2 displacements. Based on the shape of the differential pressure profile, the data are discussed and analysed in two groups. The first group deals with the low-fluid pressure GCO_2–oil displacements (fluid pressure ≤60 bar), while the second group deals with the high-

fluid pressure GCO_2–oil displacements, LCO_2–oil displacements, and $ScCO_2$–oil displacements.

A.1) Figure 7-1 shows the differential pressure profile of the low-fluid pressure GCO_2 displacements. The differential pressure profile is characterized by a slow but significant increase until its maximum value is reached (after around 1.2 pore volumes (PV) of CO_2 was injected); then, it is characterized by a slow and slight reduction over time; with the slope of the reduction decreasing over time. Increasing fluid pressure reduced the magnitude of the entry pressure and its associated time before CO_2 breakthrough. For illustration, as the fluid pressure increased from 40 to 60 bar, the entry pressure decreased from 1.196 to 0.883 bar and the associated time reduced from around 12.5 to 7.2 min. The reduction in the entry pressure and the associated time as fluid pressure increases can be related to the reduction in the capillary forces due to the reduction in the interfacial tension [20], as shown in Figure 7-2**,** and the increase in the contact angle [21], respectively.

A.2) Figure 7-3, Figure 7-4, and Figure 7-5 present the differential pressure profile of the high-fluid pressure gaseous, liquid, and supercritical CO_2–oil displacements. For all displacements, the differential pressure profile is characterized by a high increase until its maximum-differential pressure value is reached (after the injection of around 0.08–0.155 PVs of CO_2) and then followed by a steep reduction until its quasi-differential pressure value is achieved (after around 0.08–0.155 PVs). The maximum-differential pressure varied with the state of the injected CO_2. Liquid CO_2 phase gave the highest magnitudes in the maximum-differential pressure. The highest maximum-differential pressure profile of the LCO_2 displacements might be attributed to the fact that liquid CO_2 phase is less miscible with oil [6] compared to gaseous and supercritical CO_2 phases. The result of less miscibility of the liquid CO_2 was a lower reduction in the CO_2–oil interfacial tension and oil viscosity when the liquid CO_2 phase was injected. Thus, this, in turn, caused a less reduction in capillary and viscous forces leading to the highest differential pressure. Nonetheless, it might be proposed that the highest differential pressure of the LCO_2–oil displacements was because LCO_2 displacements were conducted at 20 °C, while GCO_2 and $ScCO_2$ displacements were performed at 33 °C. Thus, the large temperature difference, 13 °C, between the LCO_2 and the GCO_2 and $ScCO_2$ displacements (which caused a sharp reduction in oil viscosity) could be responsible for the difference in the differential pressure. However, this is might not be the reason because the

LCO_2 displacements performed at 29 °C, as shown in Figure 7-8, also show much higher differential pressure profile than that of GCO_2 and $ScCO_2$ displacements performed at 33 °C, despite the smaller temperature difference between them, which was only 4 °C.

The increase observed in the differential pressure after the injection of CO_2 into the core sample can be associated with the increase in pore pressure due to CO_2 invasion [22]. According to Equations 4-1 and 4-3 in Chapter 4, the reduction in the differential pressure can be related to both capillary forces and viscous forces. The reduction in the viscous forces can be related to the combined effect of the relative permeability of CO_2 and oil and the replacement of a highly viscous fluid (oil) with a less viscous one (CO_2) [22, 23]. The reduction in the capillary forces can be associated with (a) the reduction in the capillary forces due to the reduction in the interfacial tension [20] and the increase in the contact angle [21] and (b) with the number of pores that were opened to flow by CO_2, as CO_2 flooding continued after its breakthrough. This agrees with the findings of Kwelle [24], who found that the resistance of capillary pore to two-phase flow (CO_2 and water) is much greater than its resistance to single-phase flow (water or CO_2). Thus, as the number of the opened pores increased, the two-phase flow is significantly reduced, and the pore resistance to the injection of CO_2 flow is significantly reduced. Therefore, the differential pressure is sharply reduced [24]. Regarding the low-fluid pressure GCO_2 displacements, the slow and slight reduction in the differential pressure over time might indicate slow and a low-displacement efficiency for the CO_2–oil experiments performed at low-pressure conditions. The low-efficiency displacement might arise from high capillary forces due to high interfacial tension [20] and high mobility contrast at these low-pressure conditions.

B) The differential pressure profile of the low-fluid pressure GCO_2 displacement is characterized by oscillations. The frequency of these oscillations increased as fluid pressure increased; for illustration, as the fluid pressure increased from 40 to 60 bar, the oscillations increased from one to three times over the duration of the experiment, as shown in Figure 7-1. The appearance of the oscillations in the differential pressure profile can be related to the impact of the capillary forces at the trailing end of the CO_2-oil slug [23], more information can be found in Chapter 4-Section 4.2.1.1. Nonetheless, since the CO_2-oil displacements can be strongly affected by the capillary end effect and viscous instabilities [25], the appearance of the oscillations might be related to the impact of the capillary retention due to the

discontinuity of the capillary pressure [19]. The scaling coefficients for the 40 and 60 bar CO_2-oil displacements are 0.0773 and 0.411, respectively. Thus, the oscillations observed cannot be related to capillary end effects as the calculated coefficients increased not decreased with increasing fluid pressure, more information can be found about the capillary end effect in Chapter 4-Section 4.2.1.1. On the other hand, increasing the frequency of the oscillations with increasing pressure can be attributed to the reduction in the capillary forces and the increase in gas density. An increasing gas density and decreasing capillary forces mean less time was needed to reach a pressure value that is sufficient to overcome the capillary forces, i.e. less time was required to push the oil that blocks production out of the sample, and, in turn, increasing the differential pressure oscillation frequency.

C) Increasing fluid pressure led to an increase in the differential pressure profile for the displacements conducted under subcritical conditions but caused a reduction for the displacements performed at supercritical conditions. The magnitude of the change in the differential pressure profile depends on the CO_2 phase and the pressure range for the GCO_2 displacements. For subcritical displacements, the highest percentage increase occurred in the low-fluid pressure GCO_2 displacements, while the lowest occurred in the high-fluid pressure GCO_2 displacements. The corresponding time of subcritical CO_2 displacements increased while that of supercritical CO_2 displacements decreased with increasing pressure; this can be linked to the increase and decrease in the differential pressure with increasing fluid pressure, respectively.

For the low-fluid pressure GCO_2 displacements, increasing the fluid pressure from 40 to 60 bar caused the maximum-differential pressure to increase by around 93% (from 1.196 to 2.306 bar), and the differential pressure at the end of the displacements to rise by around 155% (from 0.411 to 1.049 bar), as shown in Figure 7-1. However, for the high-fluid pressure GCO_2 displacements, increasing the pressure from 65 to 70 bar caused the maximum-differential pressure to increase by around 6% (from 3.248 to 3.438 bar), the quasi-differential pressure to rise by about 30% (from 0.536 to 0.699 bar), and the corresponding time to increase by around 27% (from 1.5 to 1.9 min). For the LCO_2 displacements, as the fluid pressure increased from 70 to 90 bar, the maximum-differential pressure increased by around 49% (from 3.533 to 5.26 bar), the quasi-differential pressure increased by 37.5% (from 0.272 to 0.374 bar), and the corresponding time increased by around 6.7% from (3 to

3.2 min). On the other hand, increasing fluid pressure from 75 to 90 bar for the $ScCO_2$ displacements caused the maximum-differential pressure to decrease by 33.3% (from 2.345 to 1.564 bar), the quasi-differential pressure to decline by around 56% (from 0.134 to 0.059 bar), and the corresponding time to decrease by 36% (from 2.5 to 1.6 min).

According to Eq.4-1-Chapter 4, the increase observed in the differential pressure of the subcritical displacements as fluid pressure increased means that the impact of the viscous forces was higher than that of the capillary forces. This is because the increase observed in the differential pressure is a combination of the increase in the viscous forces and the reduction in the capillary forces. The reduction in the capillary forces with increasing fluid pressure is because of the reduction in the CO_2-oil interfacial tension (IFT) [20] and the increase in contact angle [21] due to increasing CO_2 solubility [5, 26, 27]. The increase in viscous forces as fluid pressure increased is owing to the increase in the CO_2 and oil viscosities, and the volumetric CO_2 injection rate inside the core sample due to the expansion effects (more information can be seen in Chapter 4 Section 4.2.1). Since the increase in the CO_2 and oil viscosities are expected to be slight, thus the highest increase in the differential pressure occurred as the fluid pressure increased from 40 to 60 bar during low-fluid pressure GCO_2 displacements can be related mainly to the increase in the volumetric CO_2 injection rate due to expansion effects. On the other hand, the reduction in the differential pressure of the supercritical CO_2 displacements as fluid pressure increased means that the reduction in capillary forces was higher than the increase in viscous forces. According to the J-function (Eq.4-3 in Chapter 4), the reduction in the capillary forces can be related to the reduction in the IFT, the increase in contact angle, and the reduction of CO_2 saturation. The data from Section 7.2.3 show that, as fluid pressure increased, the CO_2 saturation increased because of the reduction in residual oil saturation; therefore, the change in CO_2 saturation was not responsible for the reduction in the differential pressure. The IFT decreases with the increase in pressure and the reduction in temperature [5], as shown in Figure 7-2. No reduction in the differential pressure was observed during the subcritical displacements, despite the reduction in their IFT as fluid pressure increased. This indicates that the reduction in the IFT is not the main factor responsible for the reduction observed in the differential pressure profiles of supercritical CO_2 displacements. Thus, the only possible factor that causes the reduction in the differential pressure is the increase in contact angle. This agrees with the findings by Yang et al. [28], Liu et al. [29], and Jung and Wan [30]. Yang et al. [28] and Liu et

al. [29] observed that supercritical CO_2 has a higher ability than gaseous and liquid CO_2 to alter reservoir rocks towards less water-wetting (i.e. increase contact angle). Jung and Wan [30] found that, at a pressure higher than the CO_2 critical pressure (larger than 73.8 bar), the contact angle increases sharply with pressure rise up to 100 bar. Below the critical pressure, or above 100 bar, the contact angle remained fairly constant.

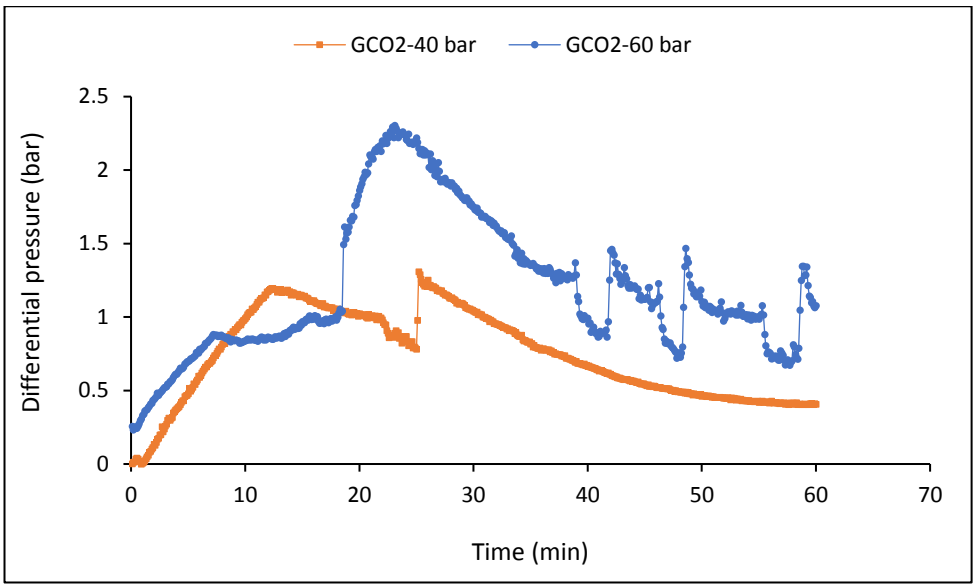

Figure 7-1: Effect of fluid pressure on the differential pressure profile of low-fluid pressure GCO_2-oil displacements conducted at 0.4 ml/min and 33 ˚C

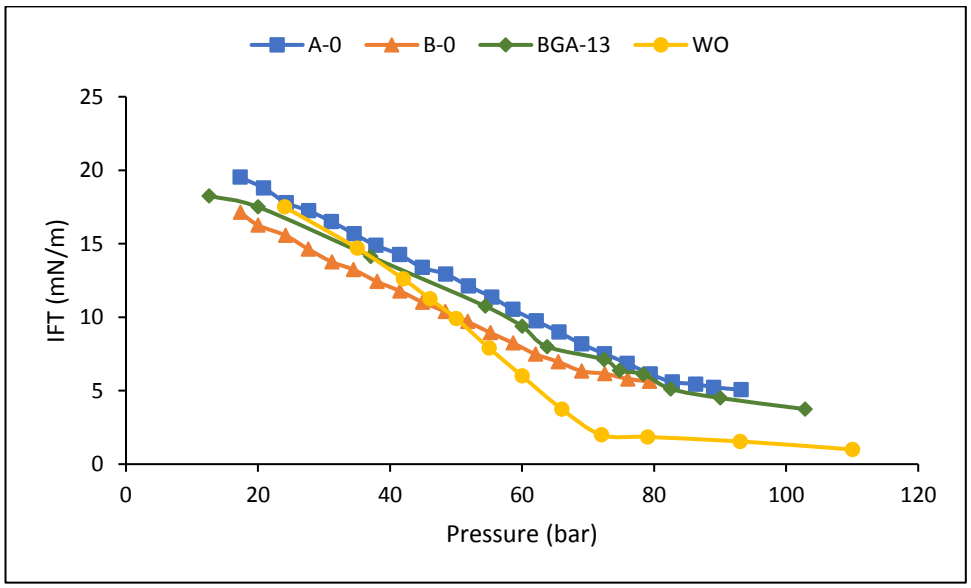

Figure 7-2: IFT tension for CO_2-crude oils (WO= Weyburn crude oil-CO_2 system against equilibrium pressure data at T=27 °C [31]; A-0 and B-0= Iranian crude oils at 49.85 °C [32]; BGA-13= Iranian crude oil at 48.85 °C [33]

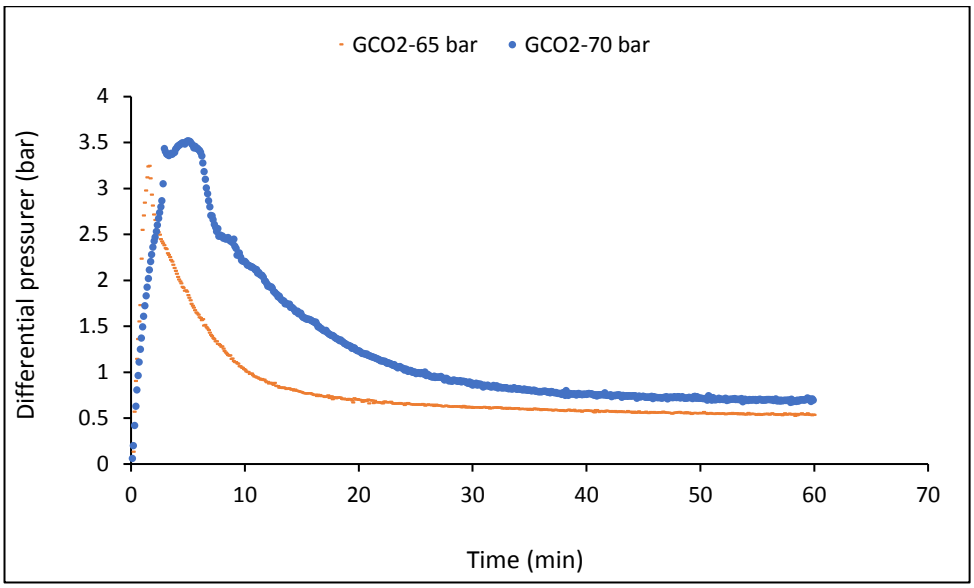

Figure 7-3: Effect of fluid pressure on the differential pressure profile of high-fluid pressure GCO_2-oil displacements conducted at 0.4 ml/min and 33 °C

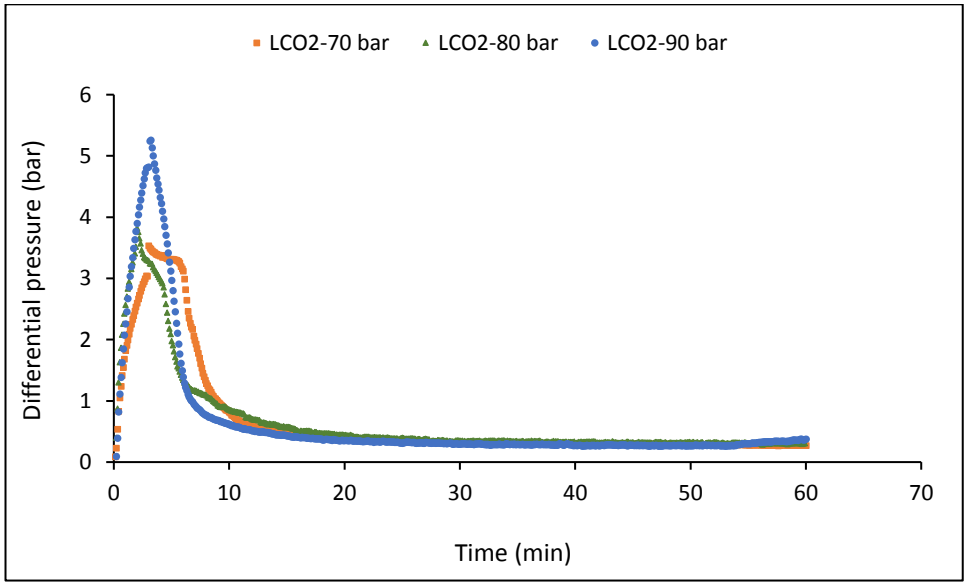

Figure 7-4: Effect of fluid pressure on the differential pressure profile of LCO_2-oil displacements conducted at 0.4 ml/min and 20 °C

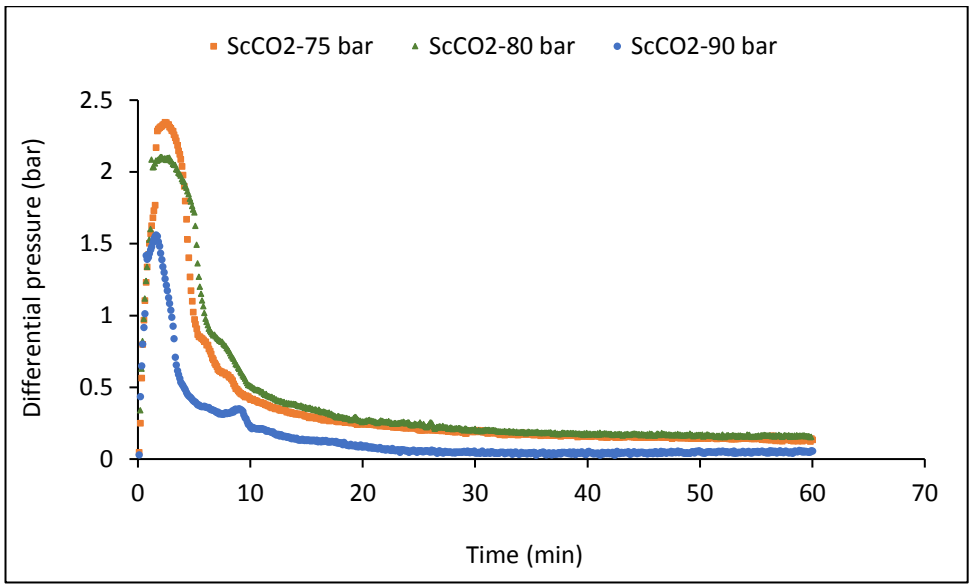

Figure 7-5: Effect of fluid pressure on the differential pressure profile of $ScCO_2$-oil displacements conducted at 0.4 ml/min and 33 °C

7.2.1.2 Effect of Temperature on the Differential Pressure Profile of CO_2-Oil Displacements as a function of the CO_2 phase

Figure 7-6, Figure 7-7, Figure 7-8, and Figure 7-9 show the effect of increasing experimental temperature on the differential pressure profile of gaseous, liquid, and supercritical CO_2-oil drainage displacements. The results reveal that increasing temperature led to a reduction in the differential pressure for both subcritical and supercritical displacements. The increase in temperature resulted in the appearance of differential pressure (PD) oscillations for the gaseous and supercritical CO_2 displacements but not for the liquid CO_2 displacements. The highest percentage reduction in the differential pressure profile as temperature increased occurred in the high-fluid pressure and then low-fluid pressure gaseous CO_2 displacements, followed by supercritical CO_2, and, then finally by liquid CO_2 displacements.

For the low-fluid pressure GCO_2 displacements conducted at 40 bar, increasing the temperature from 33 to 55 °C caused the maximum-differential pressure to decrease by around 69% (from 1.196 to 0.371 bar), the quasi-differential pressure to drop by around 81% (from 0.406 to 0.076 bar), and the corresponding time to decline by 67.5% (from 12.3 to 4 min). However, for the high-fluid pressure GCO_2 displacements performed at 70 bar, increasing the temperature from 33 to 55 °C caused the maximum-differential pressure to decrease by around 70.6% (from 3.438 to 1.01 bar), the quasi-differential pressure to decline by 88% (from 0.684 to 0.082 bar), the corresponding time to decrease by about 76% (from

2.9 to 0.7 min), and the differential pressure oscillations to appear for the first time. It should be noted that as the temperature increased from 45 to 55 °C, the quasi-differential pressure increased by around 17% (from 0.082 to 0.096 bar). This increase might be associated with the appearance of the differential pressure oscillations. The appearance of the oscillations indicates that the 55 °C-displacement is characterized by a stronger impact of the capillary forces than the 45 °C-displacement; thereby, a high quasi-differential pressure occurred in the 55 °C displacements. The appearance of the differential pressure oscillations as temperature increased can be related to the reduction in the applied viscous forces and the increase in the capillary forces due to the increasing interfacial tension [20, 31] and the decreasing contact angle [21].

For the LCO_2 displacements, as the temperature increased from 20 to 29 °C, the maximum-differential pressure decreased by around 7.6% (from 5.26 to 4.858 bar), the quasi-differential pressure declined by around 58% (from 0.365 to 0.154 bar), and the corresponding time dropped by around 37.5% (from 3.2 to 2 min). The slight reduction in the maximum-differential pressure of the liquid CO_2 displacements as temperature increased is likely to be associated with the small increase in the experimental temperature (20–29 °C), the dense-nature of liquid CO_2, and the low miscibility of liquid CO_2 with oil [6] in comparison to that of gaseous and supercritical CO_2 displacements. For the $ScCO_2$ displacements, increasing the temperature from 33 to 55 °C caused the maximum-differential pressure to decrease by 28.7% (from 1.564 to 1.115 bar), the quasi-differential pressure to decline by around 54% (from 0.059 to 0.027 bar), the corresponding time to decline by around 56% (from 1.6 to 0.7 min), and the differential pressure oscillations to appear for the first time. Importantly, the point at which the viscous forces were insufficient to overcome the capillary forces occurred at 55 °C, leading to the blockage of CO_2 production during these oscillations.

According to Eq.4-1-Chapter 4, the reduction in the maximum and quasi-differential pressures as temperature increases is the net result of the increase in capillary forces and the reduction in viscous forces. As temperature increases, the capillary forces increase because of the increasing CO_2–oil interfacial tension [20, 31] and the decreasing contact angle [21] due to the decreasing CO_2 solubility [26, 27], while the viscous forces decrease because of the decreasing viscosities of oil and CO_2. However, the change in CO_2 viscosity is likely to have little impact on the reduction in the viscous forces in comparison to that caused

by oil viscosity reduction as temperature increased. Increasing temperature caused a large reduction in the viscosity of the oil used in these displacements. The oil sample was provided by the BP Exploration Operating Company Limited, but, due to confidentiality, the specified properties of the oil sample cannot be disclosed. Increasing temperature causes only a slight change in CO_2 viscosity; the highest reduction occurred with supercritical CO_2 displacements. For illustration, increasing the temperature from 33 to 55 °C causes the CO_2 viscosity to (1) increase from 16.187 to 17.07 × [10^{-6} (Pa·s)] for the 40 bar GCO_2 displacements, (2) decrease from 20.743 to 18.9 × [10^{-6} (Pa·s)] for the 70 bar GCO_2 displacements, (3) decrease from 81.56 to 63.902 × [10^{-6} (Pa·s)] for the liquid CO_2 displacements, and (4) decrease from 53.837 to 22.26 × [10^{-6} (Pa·s)] for the 90 bar $SCCO_2$ displacements [34].

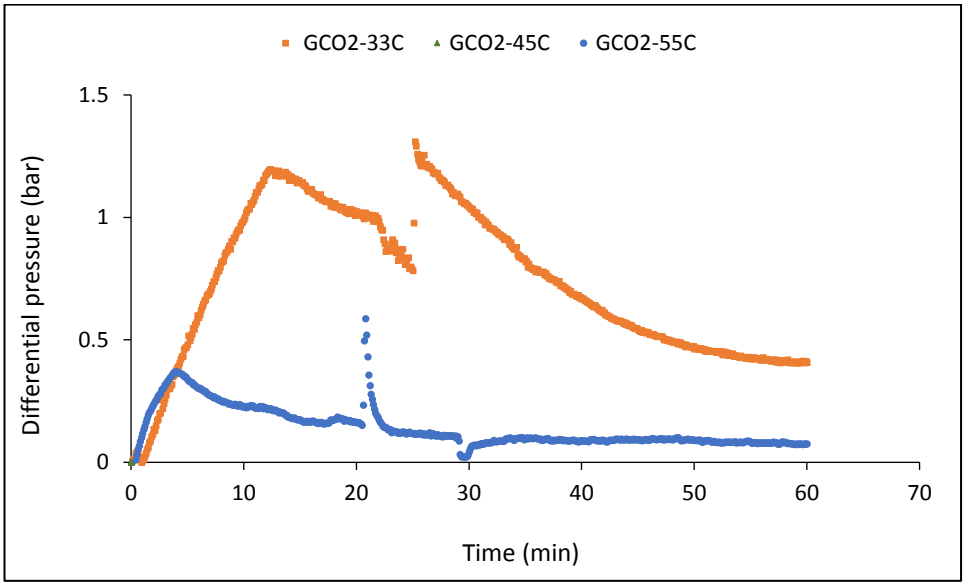

Figure 7-6: Effect of experimental temperature on the differential pressure profile of low-fluid pressure GCO_2-oil displacements conducted at 0.4 ml/min and 40 bars

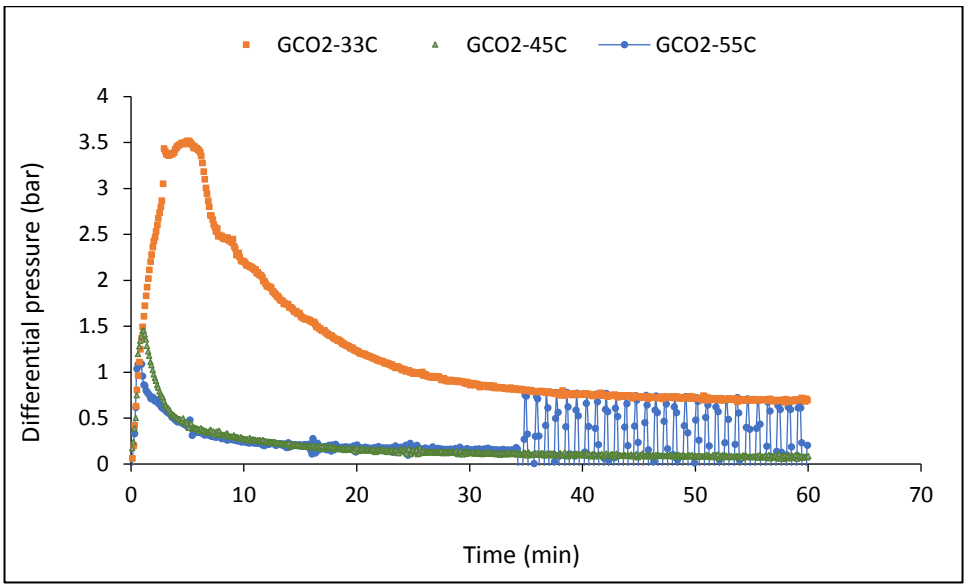

Figure 7-7: Effect of experimental temperature on the differential pressure profile of high-fluid pressure GCO_2-oil displacements conducted at 0.4 ml/min and 70 bar

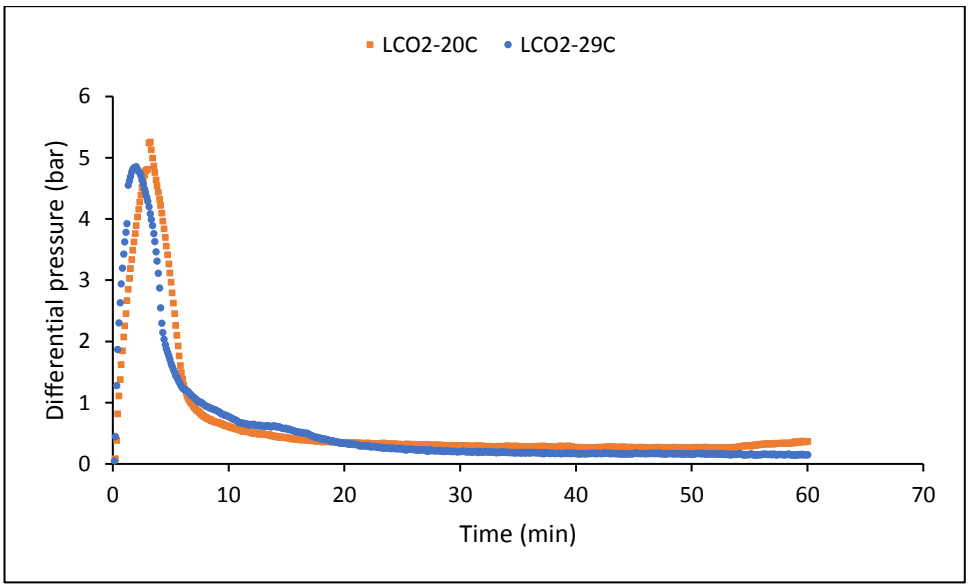

Figure 7-8: Effect of experimental temperature on the differential pressure profile of LCO_2-oil displacements conducted at 0.4 ml/min and 90 bar.

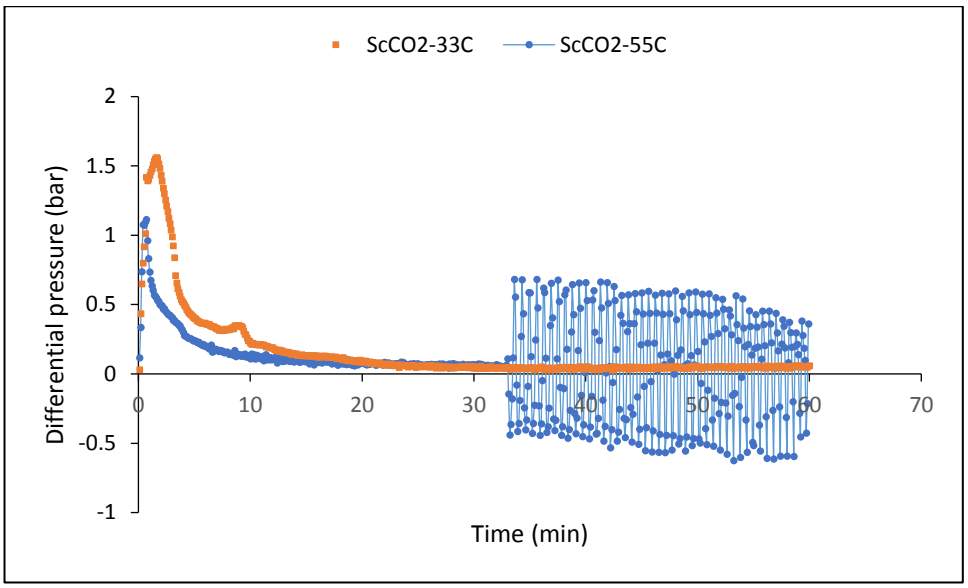

Figure 7-9: Effect of experimental temperature on the differential pressure profile of $ScCO_2$-oil displacements conducted at 0.4 ml/min and 90 bar.

7.2.1.3 Effect of CO_2 Injection Rate on the Differential Pressure Profile of CO_2-Oil Displacements as a Function of the CO_2 Phase

Figure 7-10, Figure 7-11, Figure 7-12, and Figure 7-13 show the effect of increasing CO_2 injection rate on the differential pressure profile of gaseous, liquid, and supercritical CO_2–oil drainage displacements. The results reveal that the increase in the CO_2 injection rate led to a substantial increase in the differential pressure for the displacements conducted at both subcritical and supercritical conditions. The magnitude of the increase in the differential pressure depends on the CO_2 state as well as fluid pressure range for the gaseous CO_2 displacements; the highest increase in the maximum-differential pressure occurred in the $ScCO_2$ displacements, and the lowest occurred in the high-fluid pressure GCO_2 displacements conducted at 70 bar.

For the low-fluid pressure GCO_2 displacements (40 bar), increasing the CO_2 injection rate from 0.4 to 1 ml/min caused the maximum-differential pressure to increase by around 34% (from 1.196 to 1.604 bar), the differential pressure at the end of the displacements to increase by around 166% (from 0.408 to 1.084 bar), and the corresponding time to reduce by around 57% (from 12.3 to 5.3 min). However, for the higher-fluid-pressure GCO_2 displacements performed at 70 bar, increasing the CO_2 injection rate from 0.4 to 1 ml/min caused the maximum-differential pressure to increase only by around 4.6% (from 3.438 to

3.597 bar), the quasi-differential pressure to decrease by about 31% (from 0.699 to 0.481 min), and the corresponding time to decrease by 72.4% (from 2.9 to 0.8 min). For the LCO_2 displacements, as the CO_2 injection rate increased from 0.4 to 1 ml/min, the maximum-differential pressure increased by about 94% (from 3.533 to 6.847 bar), the quasi-differential pressure declined by around 14.34% (from 0.272 to 0.233 bar), and the corresponding time decreased by around 43.33% (from 3 to 1.7 min). For the $ScCO_2$ displacements, increasing the CO_2 injection rate from 0.4 to 1 ml/min caused the maximum-differential pressure to increase by about 105% (from 1.564 to 3.211 bar), the quasi-differential pressure to increase by 54.24% (from 0.059 to 0.091), and the corresponding time to decline by 50% (from 1.6 to 0.8 min).

According to Eq.4-1-Chapter 4, the increase in the differential pressure can be related mainly to the increase in the applied viscous forces due to the increase in the CO_2 injection rate. The considerable increase observed in the differential pressure profile as CO_2 injection rate increased demonstrates the high impact of viscous forces despite the large viscosity contrast between the displacing fluid (CO_2) and the displaced one (oil). The reduction observed in the quasi-differential pressure for the high-fluid pressure GCO_2 displacements and the LCO_2 displacements is likely to be related to the increase in the endpoint relative permeability with the increasing CO_2 injection rate due to increasing viscous forces [22, 35, 36].

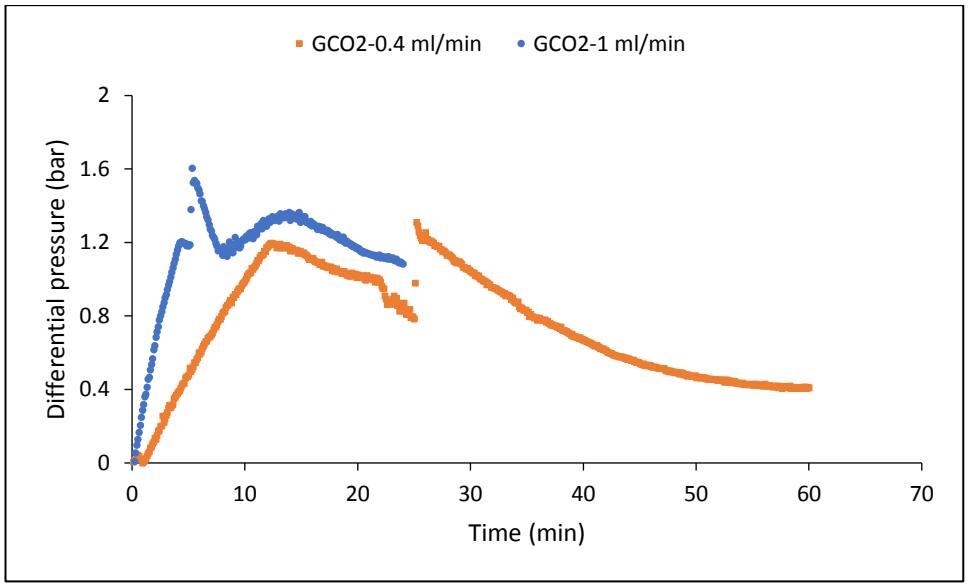

Figure 7-10: Effect of CO_2 injection rate on the differential pressure profile of low-fluid pressure GCO_2-oil displacements conducted at 40 bar and 33 °C

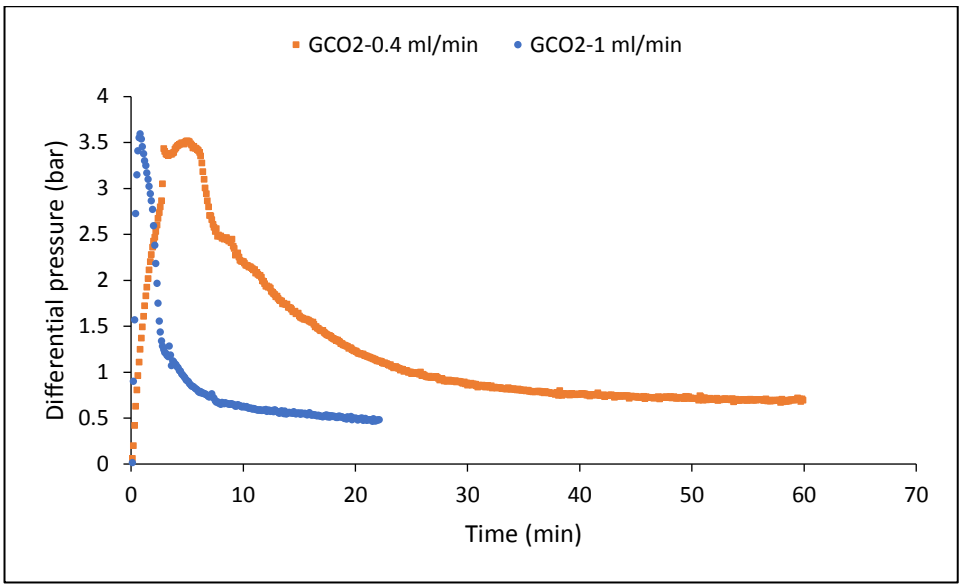

Figure 7-11: Effect of CO_2 injection rate on the differential pressure profile of high-fluid pressure GCO_2-oil displacements conducted at 70 bar and 33 °C

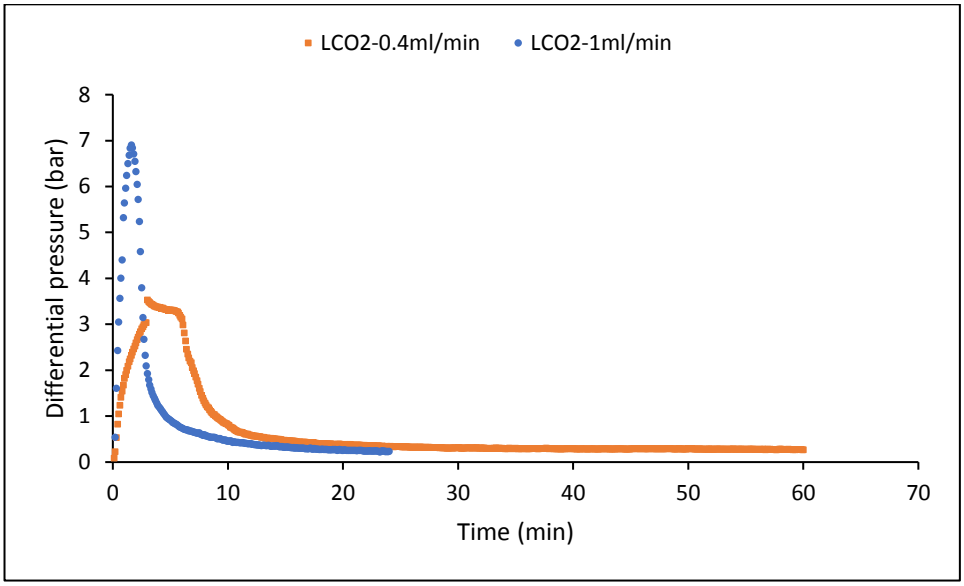

Figure 7-12: Effect of CO_2 injection rate on the differential pressure profile of LCO_2-oil displacements conducted at 70 bar and 20 ˚C

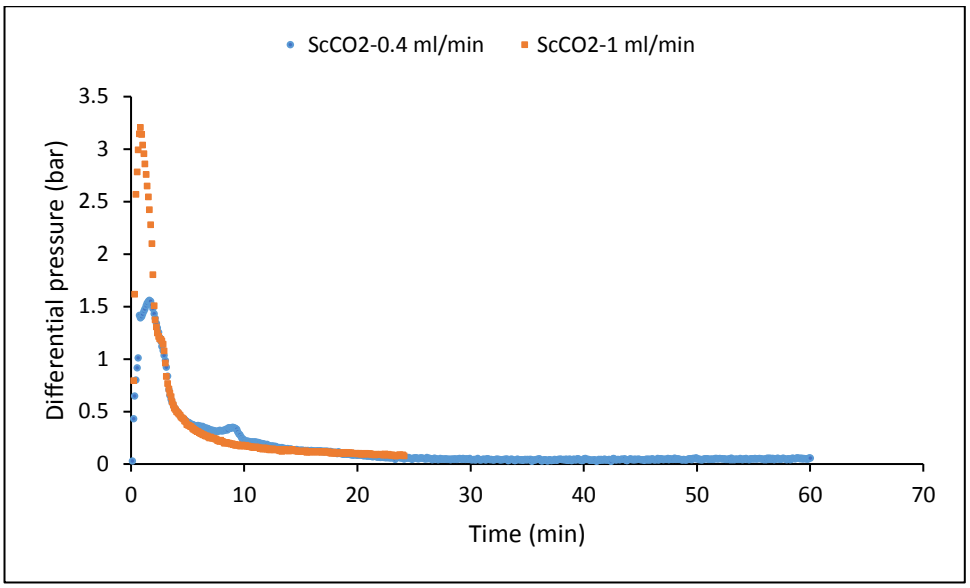

Figure 7-13: Effect of CO_2 injection rate on the differential pressure profile of $ScCO_2$-oil displacements conducted at 90 bar and 33 ˚C

7.2.2 Production Behaviour of CO_2-Oil Displacements as a Function of the CO_2 Phase

This section deals with the impact of fluid pressure and experimental temperature on the cumulative produced volumes and the transient outflow rates of CO_2 and oil of gaseous, liquid, and supercritical CO_2 displacements. To avoid repeatability, the impact of CO_2 injection rate was not presented as it was similar to those presented in the fluid pressure and temperature sections below.

7.2.2.1 Effect of Fluid Pressure on Production Behaviour of CO_2-Oil Displacements as a Function of the CO_2 Phase

Figure 7-14, Figure 7-15, Figure 7-16, and Figure 7-17 show the impact of increasing fluid pressure on the cumulative produced volumes. In general, increasing fluid pressure caused an increase in the cumulative produced volumes of low-fluid pressure GCO_2 displacements but a reduction in the cumulative produced volumes of high-fluid pressure GCO_2 displacements, LCO_2 displacements, and $ScCO_2$ displacements. For GCO_2 displacements, increasing fluid pressure reduced the time required to achieve most of the oil production.

The data from Figure 7-14 show that the increase in fluid pressure results in an increase in the cumulative produced volumes of the low-fluid pressure GCO_2-oil displacements. As the fluid pressure increased from 40 to 60 bar, the ratio of the cumulative produced volumes to

the cumulative injected volumes at the end of the displacements increased from 0.65 to 0.95. The increase is likely to be related to the increase in displacement efficiency and the impact of gas expansion.

The data from Figure 7-15, Figure 7-16, and Figure 7-17 show that increasing fluid pressure resulted in a decrease in the cumulative produced volumes of high-fluid pressure GCO_2 displacements, LCO_2 displacements, and $ScCO_2$ displacements; the highest reduction occurred in the $ScCO_2$ displacements, while the lowest occurred in the LCO_2 displacements. The cumulative produced volumes of the high-fluid pressure GCO_2 displacements at the end of the experiment were higher than the total cumulative injected volumes. On the other hand, the cumulative produced volumes of the LCO_2 and $ScCO_2$ displacements were less than the total cumulative injected volumes. The reduction observed in the cumulative produced volumes as fluid pressure increased can be related to the increase in gas compressibility and CO_2 solubility [26, 27]. As the fluid pressure increased from 65 to 70 bar for the high-fluid pressure GCO_2 displacements, the ratio of the total produced volumes to the total injected volumes at the end of displacements decreased from 1.05 to 1.02%. As the fluid pressure increased from 70 to 80 bar and then to 90 bar for the LCO_2 displacements, the ratio of the total produced volumes to the total injected volumes at the end of displacements decreased from 92.6 to 91.6% and then to around 90.6%. This means that every 10 bar increase in fluid pressure led to about 1% reduction in the cumulative produced volumes. However, as the fluid pressure increased from 75 to 80 bar and then to 90 bar for the $ScCO_2$ displacements, the ratio of the total produced volumes to total injected volumes at the end of displacements decreased from 99.5 to 97.5% and then to around 91.5%. It is worth noting that the increase in the cumulative produced volumes occurred only during the first period, and later the injection and production profiles became equal. The equality between the injection and production profiles suggests that the produced CO_2 shrinks again to its normal volume after leaving the water bath, causing no increase in the produced volumes. Thus, the increase in the cumulative produced volumes can be mainly related to oil production, which mostly occurred during the early stages of the experiments. The equality between the injection and production profiles can be used as an indicator to show when most of the oil production occurred.

The data from Figure 7-14 and Figure 7-15 indicate that increasing fluid pressure results in a decrease in the time required to achieve most of the oil production, from around 20–25 min for the low-fluid pressure GCO_2 experiments (40 and 60 bar) to around 5 min for the high-fluid pressure GCO_2 experiments (65 and 70 bar). After most of the oil production occurred, the cumulative produced volumes and the cumulative injected CO_2 volumes showed a constant linear trend with time. For the low-fluid pressure GCO_2 experiments conducted at 40 bar, the production profile is characterized by a slight increase during the first 25.5 min followed by a constant linear trend. On the other hand, the production profile of the 60 bar GCO_2 displacements is characterized by a continuous increase over time. The main reason behind the highest reductions in the production times and the increase in cumulative produced volumes over time, with the increase in fluid pressure, is the increase in CO_2 density and displacement efficiency, respectively. Increasing CO_2 density means less time was required to reach the differential pressure required for the injected CO_2 to enter the core sample for the first time.

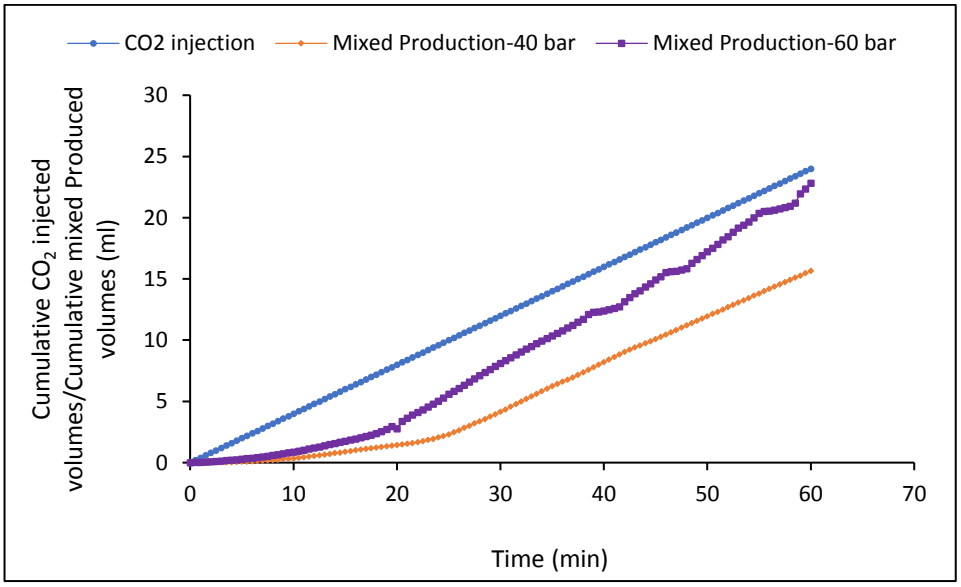

Figure 7-14: Effect of fluid pressure on the cumulative produced volumes of oil and CO_2 for low-fluid pressure GCO_2-oil displacements conducted at 33 ˚C and 0.4 ml/min

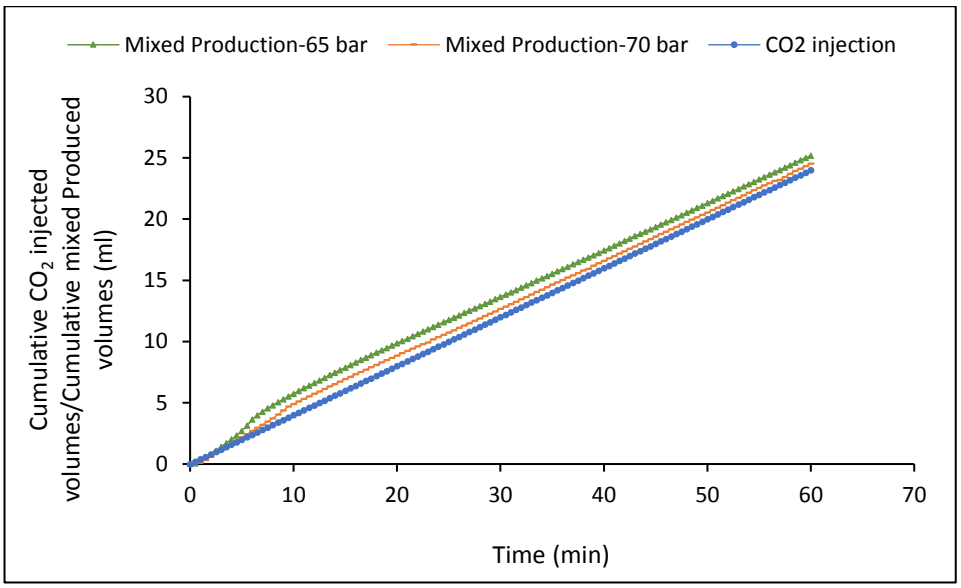

Figure 7-15: Effect of fluid pressure on the cumulative produced volumes of oil and CO_2 for high-fluid pressure GCO_2-oil displacements conducted at 33 °C and 0.4 ml/min

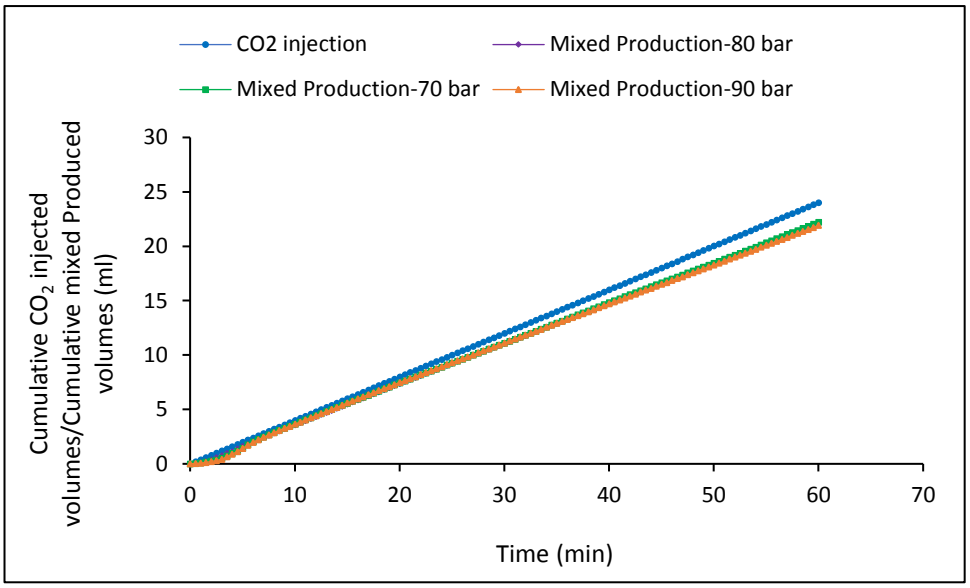

Figure 7-16: Effect of fluid pressure on the cumulative produced volumes of oil and CO_2 for LCO_2-oil displacements conducted at 20 °C and 0.4 ml/min

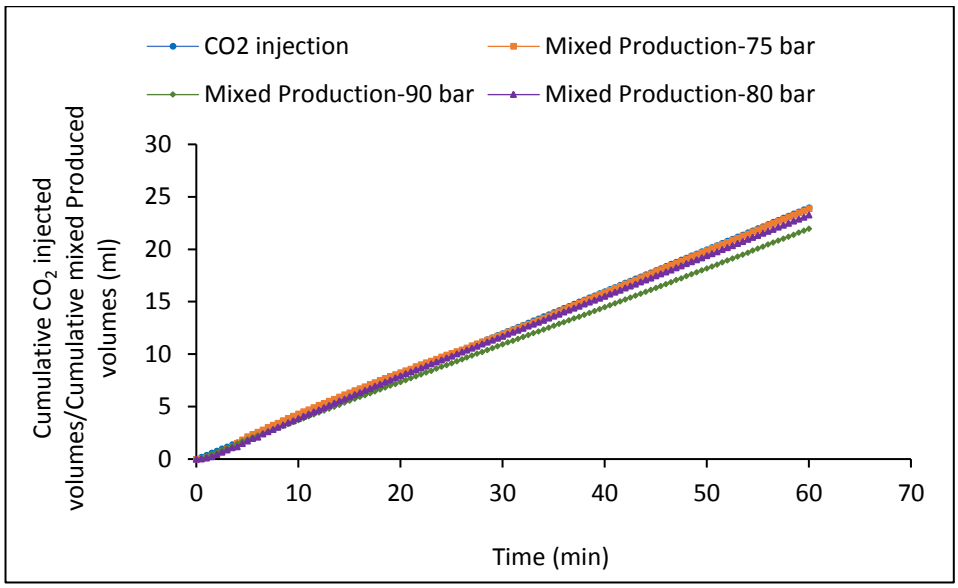

Figure 7-17: Effect of fluid pressure on the cumulative produced volumes of oil and CO_2 for $ScCO_2$-oil displacements conducted at 33 °C and 0.4 ml/min

7.2.2.2 Effect of Experimental Temperature on Production Behaviour of CO_2-Oil Displacements as a Function of the CO_2 Phase.

Figure 7-18, Figure 7-19, Figure 7-20, and Figure 7-21 show the impact of experimental increasing temperature on the cumulative produced volumes. The results reveal that increasing temperature caused an increase in the cumulative produced volumes. The data from Figure 7-18 show that the cumulative produced volumes of low-fluid pressure GCO_2 displacements (40 bar) were less than the cumulative injected volumes. On the other hand, the cumulative produced volumes of high-fluid pressure GCO_2 displacements (70 bar) were higher than the cumulative injected volume, as shown in Figure 7-19. The increase in temperature caused an increase in the cumulative produced volumes. Increasing the temperature from 45 to 55 °C for the low-fluid pressure GCO_2 displacements (40 bar) caused the ratio of the cumulative produced volumes to the cumulative injected volumes at the end of the displacements to increase from 0.51 to 0.55; nonetheless, the displacement conducted at 33 °C showed the highest ratio (0.65), the reason is not clear. As the temperature increased for the high-fluid pressure GCO_2 displacements (70 bar), the ratio of the cumulative produced volumes to the cumulative injected volumes at the end of the displacements were 1.02, 1.04, and 1.07 for the displacements conducted at 33, 45, and 55 °C, respectively. The increase observed in the cumulative produced volumes as temperature increased can be related to the increase in displacement efficiency and the decrease in gas compressibility and solubility.

The data from Figure 7-20 show that the cumulative produced volumes during LCO_2-displacements were less than the cumulative injected volumes. Nevertheless, the increase in temperature caused a very slight increase in the cumulative produced volumes. At the end of the displacements, the ratio of the cumulative produced volumes to the cumulative injected volumes were 0.914, and 0.918 for the displacements performed at 20 and 29 °C, respectively. This slight increase might reflect a slight change in CO_2 compressibility and solubility due to the low sensitivity of liquid CO_2 to pressure and temperature changes compared to gaseous and supercritical CO_2 displacements.

The data from Figure 7-21 show that for $ScCO_2$ displacements, increasing the temperature from 33 to 55 °C caused a substantial increase in the cumulative produced volumes. At the end of the displacements, the ratio of the cumulative produced volumes to the cumulative injected volumes were 0.915 and 1.06 for the displacements performed at 33 and 55 °C, respectively. As temperature increased, the behaviour of supercritical CO_2 became very similar to that of high-pressure gaseous CO_2 displacements, as shown in Figure 7-19. The similarity is because the cumulative produced volumes for both displacements were much higher than the cumulative injected volumes.

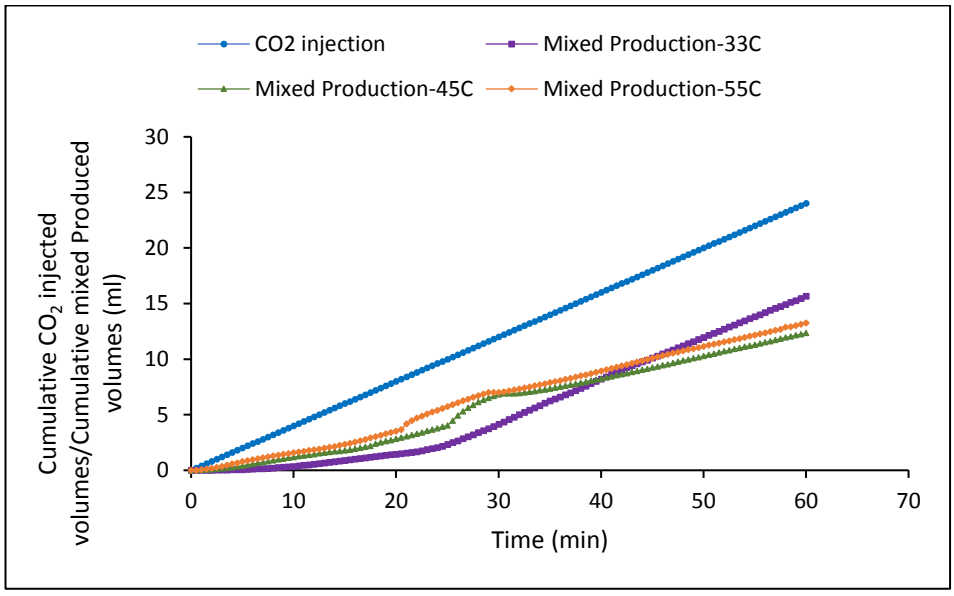

Figure 7-18: Effect of experimental temperature on the cumulative produced volumes of oil and CO_2 for low-fluid pressure GCO_2-oil displacements conducted at 40 bar and 0.4 ml/min

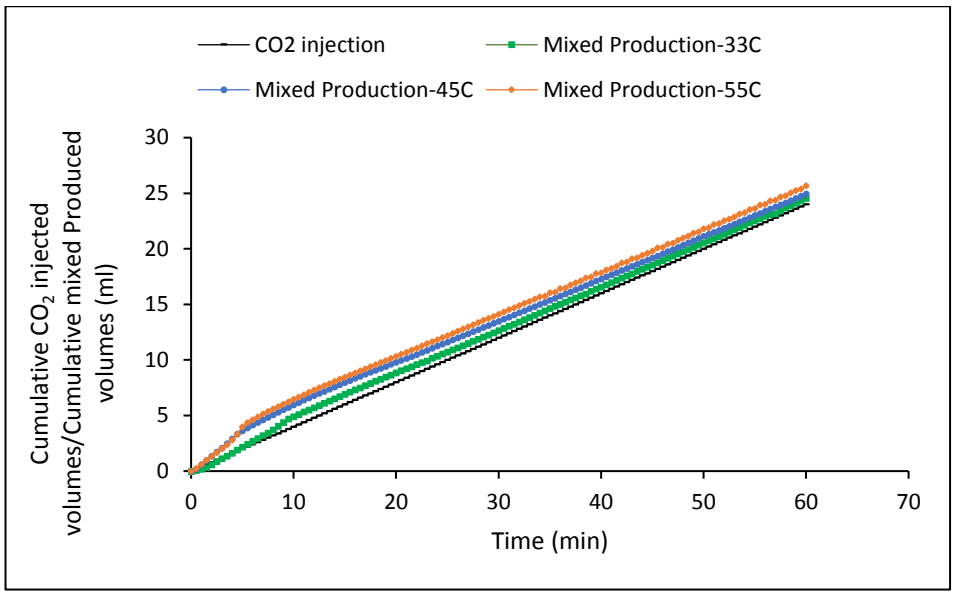

Figure 7-19: Effect of experimental temperature on the cumulative produced volumes of oil and CO_2 for high-fluid pressure GCO_2-oil displacements conducted at 70 bar and 0.4 ml/min.

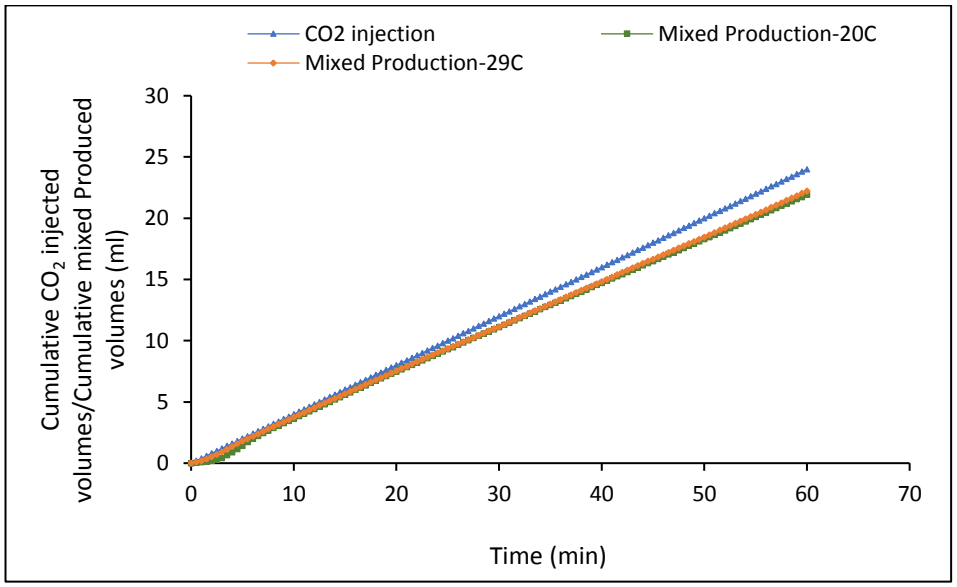

Figure 7-20: Effect of experimental temperature on the cumulative produced volumes of oil and CO_2 for LCO_2-oil displacements conducted at 90 bar and 0.4 ml/min

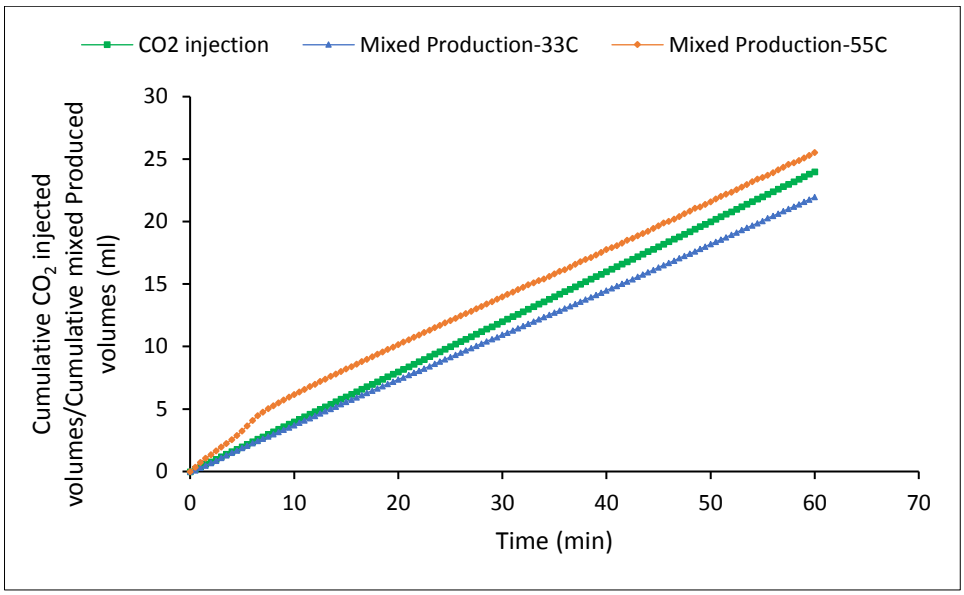

Figure 7-21: Effect of experimental temperature on the cumulative produced volumes of oil and CO_2 for $ScCO_2$-oil displacements conducted at 90 bar and 0.4 ml/min

7.2.3 Effect of Fluid Pressure, Temperature, and CO_2 Injection Rate on Endpoint CO_2 Effective and Relative Permeabilities and Oil Recovery as a Function of the CO_2 Phase

Effective and relative permeabilities of CO_2 and oil is of practical interest for CO_2 sequestration in subsurface formation, particularly important in reservoirs that are characterized by gas drive, gas cap expansion, or gas injection [35, 37]. Relative permeability data is a key factor in the determination of the efficiency, integrity, injectivity, and plume migration of CO_2 sequestration process [25, 38] as well as in the designing and making decisions for reservoir improvement [39], fluid flow in porous media [40], breakthrough time [3], and mobility of the displacing and displaced fluids [3, 25]. The change in CO_2 state is likely to change the mobility of the fluids due to its impact on viscosity and potentially its influence on relative permeability. In this study, when the flooding experiment was finished, the volume of the produced oil was measured, and the residual oil saturation was calculated. The average differential pressure and the average CO_2 outflow rate of the last period were used to calculate the endpoint effective (K_{fCO2}) and relative permeabilities (K_{rCO2}) of CO_2 using Darcy's law [22, 36]. Then, the core sample was weighed to confirm the calculated residual oil saturation (S_{or}). The CO_2 viscosity at the fluid pressure and the experimental temperature was calculated using the Peace software website [34].

Table 7-1 shows the effect of operational conditions on the endpoint CO_2 effective and relative permeabilities and oil recovery (i.e. as a function of the CO_2 phase.

Table 7-1: Effect of fluid pressure, temperature and CO_2 injection rate on the endpoint CO_2 effective and relative permeabilities and oil recovery as a function of the CO_2 phase.

Parameter	Experiment	K_{fCO2} (mD)	K_{rCO2}	Oil Recovery	S_{or}
Fluid Pressure Effect	LCO_2–oil-70 bar-0.4 ml/min-20 °C	2.782	0.096	0.44	0.56
	LCO_2–oil-90 bar-0.4 ml/min-20 °C	2.287	0.079	0.56	0.44
	GCO_2–oil-40 bar-0.4 ml/min-33 °C	0.446	0.015	0.30	0.70
	GCO_2–oil-60 bar-0.4 ml/min-33 °C	0.822	0.028	0.35	0.65
	GCO_2–oil-65 bar-0.4 ml/min-33 °C	1.417	0.049	0.40	0.60
	GCO_2–oil-70 bar-0.4 ml/min-33 °C	0.991	0.034	0.41	0.59
	$ScCO_2$–oil-75 bar-0.4 ml/min-33 °C	4.996	0.173	0.45	0.55
	$ScCO_2$–oil-80 bar-0.4 ml/min-33 °C	4.167	0.144	0.51	0.49
	$ScCO_2$–oil-90 bar-0.4 ml/min-33 °C	11.717	0.406	0.41	0.59
Temperature Effect	LCO_2–oil-90 bar-0.4 ml/min 20 °C	2.287	0.079	0.56	0.44
	LCO_2–oil-90 bar-0.4 ml/min 29 °C	4.710	0.163	0.44	0.56
	GCO_2–oil-40 bar-0.4 ml/min-33 °C	0.446	0.015	0.30	0.70
	GCO_2–oil-40 bar-0.4 ml/min-45 °C	1.572	0.054	0.33	0.67
	GCO_2–oil-40 bar-0.4 ml/min-55 °C	2.895	0.1	0.35	0.65
	GCO_2–oil-70 bar-0.4 ml/min-33 °C	0.991	0.034	0.41	0.59
	GCO_2–oil-70 bar-0.4 ml/min-45 °C	11.906	0.412	0.40	0.60
	GCO_2–oil-70 bar-0.4 ml/min-55 °C	9.870	0.342	0.43	0.57
	$ScCO_2$–oil-90 bar-0.4 ml/min-33 °C	11.717	0.405	0.41	0.59
	$ScCO_2$–oil-90 bar-0.4 ml/min-55 °C	12.413	0.430	0.47	0.53
Injection Rate Effect	LCO_2–oil-70 bar-0.4 ml/min-20 °C	2.782	0.096	0.44	0.56
	LCO_2–oil-70 bar-1 ml/min-20 °C	8.120	0.218	0.51	0.49
	GCO_2–oil-40 bar-0.4 ml/min-33 °C	0.446	0.015	0.30	0.70
	GCO_2–oil-40 bar-1 ml/min-33 °C	0.420	0.015	0.32	0.68
	GCO_2–oil-70 bar-0.4 ml/min-33 °C	0.991	0.034	0.41	0.59
	GCO_2–oil-70 bar-1 ml/min-33 °C	3.599	0.125	0.44	0.56
	$ScCO_2$–oil-90 bar-0.4 ml/min-33 °C	11.717	0.405	0.41	0.59
	$ScCO_2$–oil-90 bar-1 ml/min-33°C	18.992	0.657	0.51	0.49

The data from Table 7-1 shows that S_{or} was in ranges of 0.65–0.7, 0.56–0.6, 0.49–0.59, and 0.44-0.56 for the low-fluid pressure GCO_2–oil displacements, high-fluid pressure GCO_2–oil displacements, $ScCO_2$–oil displacements, and LCO_2–oil displacements, respectively. The lowest recovery occurred in the low-fluid pressure GCO_2–oil displacements, whilst the highest oil recovery occurred in the LCO_2–oil displacements. The data demonstrate the impact of the CO_2 phase and the operational conditions on oil recovery. The amount of oil recovery depends on many factors, including relative permeability, wetting conditions, viscous fingering, gravity tonguing, amount of crossflow/mass transfer [39], mobility ratio, and capillary number [41]. The change in CO_2 phase and the operational conditions are likely to have an influence on most of the listed factors, leading to their impact on the displacement

efficiency. The highest recovery with liquid CO_2 phase can be associated with its highest capillary number (due to its highest viscous forces and lowest capillary forces), lowest mobility ratio, and potentially its most stable displacement front compared to that of gaseous and supercritical CO_2 phases. The highest viscous forces and the lowest mobility ratio of the liquid CO_2 phase in comparison to that of gaseous and supercritical CO_2 phases can be associated with its highest viscosity, while the lowest capillary forces of the liquid CO_2 phase can be related to its lowest IFT, providing a constant contact angle for the three phases of CO_2. For illustration, for the LCO_2 displacements conducted at 90 bar and 29 °C, the GCO_2 displacements performed at 70 bar and 33 °C, and the $ScCO_2$ displacements conducted at 90 bar and 33 °C, the viscosity of the LCO_2, GCO_2, and $ScCO_2$ phases is 63.902, 20.743, and 53.837 × [10^{-6} (Pa·s)], respectively [34]. The CO_2–oil IFT decreases as pressure increases due to increases in CO_2 solubility and increases as temperature increases due to decreases in CO_2 solubility [5]. Therefore, the CO_2–oil IFT of LCO_2 displacement is less than that of GCO_2 displacements due to its higher pressure and lower temperature as well as less than that of $ScCO_2$ displacements due to its lower temperature.

On the other hand, Table 7-1 shows that the K_{rCO2} was in ranges of 0.015–0.1, 0.034–0.412, 0.144–0.657, and 0.079–0.281 for the low-fluid pressure GCO_2–oil displacements, high-fluid pressure GCO_2–oil displacements, $ScCO_2$–oil displacements, and LCO_2–oil displacements, respectively. This data also demonstrates the impact of the CO_2 phase and the operational conditions on the endpoint CO_2 relative permeabilities. In general, the lowest K_{rCO2} was observed in the low-fluid pressure GCO_2–oil displacements, whilst the highest was obtained in the $ScCO_2$ displacements. The data show also a wide range of endpoint CO_2 relative permeabilities from low to high values. The change in relative permeability with CO_2 phase and operational conditions can be related to their potential strong influence on the capillary number, viscous forces, capillary forces, flow regimes [35, 42], and capillary end effect; thus, in turn, the CO_2 phase and the operational conditions will have a strong impact on relative permeability data [29, 40, 43]. Bennion and Bachu [43], Liu et al. [29], and Parvazdavani et al. [40] observed an impact for the operational conditions on relative permeability.

On the other hand, the observed lowest endpoint relative permeabilities of the low-fluid pressure GCO_2–oil displacements are likely to be related to the impact of high capillary forces and low viscous forces (due to their higher interfacial tension and lower viscosity) in

comparison to the LCO_2 and $ScCO_2$-displacements. Nevertheless, the highest K_{rCO2} of $ScCO_2$–oil displacements is likely to be associated with the highest ability of the supercritical CO_2 phase to alter the wettability towards a less water-wetting state in comparison to gaseous and liquid CO_2 phases [28, 29] (more information can be seen in Section 7.2.1.1). Generally, the observed low K_{rCO2} and the wide range of the endpoint CO_2 relative permeabilities agree well with the findings of Moortgat et al. [3], Parvazdavani et al. [40], and Müller [25]. The results of Moortgat et al.'s simulation study suggest that the K_{rCO2} of the CO_2-rich phase may be lower than that of the oil phase [3]. However, the results of Parvazdavani et al.'s experimental and modelling study reveal a wide range of GCO_2 endpoint relative permeabilities depending on the pressure range and the core sample origin; for illustration, they found that increasing the pressure from 500 psi (34.5 bar) to 800 psi (55 bar) caused the K_{rCO2} to range from 0.34 to 0.68 for the sandstone sample and from 0.25 to 0.56 for the dolomite sample [40]. The comparison of Müller for relative permeabilities of SCO_2–brine systems showed a wide range of relative permeability data that vary between 0.07 and 1 [25].

The data from Table 7-1 show that increasing fluid pressure caused the K_{rCO2} of liquid CO_2 to decrease by about 0.017 and that of gaseous and supercritical CO_2 to increase by 0.034 and 0.261, respectively. On the other hand, increasing the fluid pressure resulted in a decrease in the S_{or} of the subcritical CO_2 phases by 0.12 and 0.11, respectively; however, it led to an increase in the S_{or} of the supercritical CO_2 phase by 0.04. It is worth mentioning that, for the GCO_2 experiments, the displacement conducted at 65 bar experienced the highest K_{rCO2} which might be related to its highest gas expansion impact and low capillary forces in comparison to other low-fluid pressure GCO_2 displacements. The highest expansion impact of the 65 bar-displacement is due to its highest density reduction as CO_2 entered the water bath (Section 7.2.1.1). However, in the $ScCO_2$ experiments, the displacement conducted at 80 bar experienced the lowest K_{rCO2} and the lowest S_{or}; the reason for this is not clear. The increase in the viscous forces can explain the increase observed in the K_{rCO2} for gaseous and supercritical CO_2 displacement, but not the reduction for liquid CO_2 displacement. The reason for the reduction might be related to the increasing dissolution of liquid CO_2 in oil as fluid pressure increased, which could result in a reduction in the amount of the free movable liquid CO_2, thus reducing its relative permeability. The increase in gaseous permeability as fluid pressure increased agrees with the finding of Parvazdavani et al. [40], who observed that

increasing fluid pressure for GCO_2–oil displacements led to a high increase in the relative permeability of GCO_2 [40]. On the other hand, the reduction and increase in the S_{or} with subcritical CO_2 phases and supercritical CO_2 phase, respectively, can be associated with the reasons behind the increase and decrease observed in the differential pressure, as shown in Figure 7-1 to Figure 7-5. The increase and reduction in the differential pressure were related to capillary and viscous forces (more information can be seen in Section 7.2.1.1). Therefore, the reduction in the S_{or} as fluid pressure increased in the case of the subcritical CO_2 phases can be associated with the increase in the viscous forces and the reduction in mobility ratio. However, the increase in S_{or} as fluid pressure increased in the case of the supercritical CO_2 might be related to the reduction in capillary forces; this indicates that capillary forces complemented viscous forces; thereby, its reduction led to a reduction in oil production [23]. The results indicate that viscous forces were dominant in subcritical CO_2 displacements, while capillary forces were dominant in supercritical CO_2 displacements.

Increasing the experimental temperature caused the K_{rCO2} of the three CO_2 phases to increase by 0.084, 0.085, 0.378, and 0.024 for the LCO_2, the low-fluid pressure GCO_2, the high-fluid pressure GCO_2, and $ScCO_2$ displacements, respectively. On the other hand, increasing the experimental temperature caused the S_{or} to increase by 0.12 for LCO_2 displacements. Nevertheless, it led to a decrease in the S_{or} by 0.05, 0.02, and 0.06 for the low-fluid pressure GCO_2, high-fluid pressure GCO_2, and $ScCO_2$ displacements, respectively. It should be noted that, for the 70 bar GCO_2 displacements, increasing temperature from 45 to 55 °C reduced the K_{rCO2} from 0.412 to 0.342; this reduction could be associated with the appearance of the differential pressure oscillations, as shown in Figure 7-7. The increase in relative permeability as temperature increased could be associated with the increase in the CO_2 injection rate [35, 42] due to expansion effect (see Section 7.2.1.1). Skauge et al. [35] and Rostami et al. [42] observed that the increase in the displacement velocity leads to a higher gas relative permeability and can slightly affect the oil relative permeability [35, 42]. The increase in the S_{or} of the LCO_2 displacements can be associated with the with the reasons behind the reduction in differential pressures due to increasing temperature, as shown in Figure 7-6 to Figure 7-9. However, the reduction in the S_{or}, i.e., increasing displacement efficiency, as temperature increased in the case of gaseous and supercritical CO_2 phases might be related to the reduction in oil viscosity as well as the increase in CO_2 injection rate inside the core sample because of the gas expansion impact. Increasing displacement efficiency can be seen

through the increase in the cumulative produced volumes of gaseous and supercritical CO_2 phases as temperature increased, see Figure 7-19 and Figure 7-21.

Increasing the CO_2 injection rate caused the K_{rCO2} of the three CO_2 phases to increase by 0.185, 0.09, and 0.252 for the LCO_2, high-fluid pressure GCO_2, and $ScCO_2$ displacements, respectively. It should be noted that, as CO_2 injection rate increased from 0.4 to 1 ml/min for the low-fluid pressure GCO_2 (40 bar), the K_{rCO2} experienced no change. The increase in the CO_2 injection rate led to the reduction of the S_{or} of the three CO_2 phases by 0.07, 0.02, 0.03, 0.1 for the LCO_2, low-fluid pressure GCO_2, high-fluid pressure GCO_2, and $ScCO_2$ displacements, respectively. The increase in the viscous forces could be the reason behind the increase in K_{rCO2} [22, 36] and the reduction in the S_{or} with increasing CO_2 injection rate [35].

7.3 Summary

In this study, the effect of fluid pressure, temperature, and CO_2 injection rate on two-phase flow characteristics have been investigated as a function of the CO_2 phase when CO_2 flooded an oil-saturated Berea sandstone core sample. The results indicate that the fluid pressure, experimental temperature, and CO_2 injection rate significantly influence the differential pressure profile, cumulative produced volumes, endpoint CO_2 effective and relative permeabilities, and oil recovery. The trend and the size of the changes depend on the CO_2 state as well the fluid pressure range for GCO_2 displacements. The data indicate that as fluid pressure increases, the capillary forces have a stronger impact on the differential pressure profile of supercritical CO_2–oil displacements than that on subcritical CO_2–oil displacements. As temperature and CO_2 injection rates increased, the viscous forces become more dominant than the capillary forces.

In summary, for all fluid pressures, temperature, and CO_2 injection rates, the differential pressure profile is characterized by a strong increase, followed by a high reduction until it reached the value of quasi-differential pressure; the rate of the increase and reduction in the differential pressure depends on the CO_2 phase and the fluid pressure range for the GCO_2 displacements. In general, liquid CO_2 phase gave the highest differential pressure magnitude. Increasing fluid pressure caused an increase in the differential pressure profile of subcritical CO_2 displacements but a reduction in that of supercritical CO_2 displacements; the magnitude

of the change in the differential pressure depends on the CO_2 phase and the fluid pressure range for GCO_2 displacements. For subcritical displacements, the highest percentage increase occurred in the low-fluid pressure GCO_2 displacements, while the lowest occurred in the high-fluid pressure GCO_2 displacements. In addition, increasing fluid pressure for low-fluid pressure GCO_2 displacements increased the frequency of the differential pressure oscillations and reduced the entry pressure and its associated time. Increasing temperature caused a reduction in the differential pressure profile for the three CO_2 phases along with the appearance of the pressure oscillations in the case of gaseous and supercritical CO_2 displacements. The magnitude of this reduction in the differential pressure depends on the CO_2 phase and the pressure range for the GCO_2 displacements; the highest reduction occurred in high-fluid pressure GCO_2 displacements, while the lowest occurred in LCO_2 displacements. The increase in CO_2 injection rate caused a substantial increase in the differential pressure of the three CO_2 phases with the highest percentage increase in the maximum-differential pressure occurred in the $ScCO_2$ displacements and the lowest in the high-fluid pressure GCO_2 displacements conducted at 70 bar.

The increase in fluid pressure caused an increase in the cumulative produced volumes of low-fluid pressure GCO_2 displacements, but a reduction in those of high-fluid pressure GCO_2, LCO_2, and SCO_2 displacements; the largest reduction occurred in the $ScCO_2$ displacements, while the lowest occurred in the LCO_2 displacements; increasing fluid pressure reduced the time required to achieve most of oil production. However, increasing temperature caused an increase in the cumulative produced volumes; the lowest increase occurred in LCO_2–oil displacements.

The residual oil saturation (S_{or}) was in ranges of around 0.44–0.7; liquid CO_2 gave the lowest, and low-fluid pressure gaseous CO_2 gave the highest. The endpoint CO_2 relative permeability (K_{rCO2}) was in ranges of about 0.015–0.657; supercritical CO_2 gave the highest, and low-pressure gaseous CO_2 gave the lowest. Increasing fluid pressure caused the K_{rCO2} of liquid CO_2 to decrease, but that of gaseous and supercritical CO_2 to increase. However, increasing fluid pressure caused the S_{or} to decrease for the subcritical CO_2 displacements but to decrease for the supercritical CO_2 displacements. Increasing the experimental temperature caused the K_{rCO2} of the three CO_2 phases to increase. However, increasing the experimental temperature caused the S_{or} to increase for liquid CO_2 displacements but to decrease for gaseous and

supercritical CO_2 displacements. Increasing CO_2 injection rate caused the K_{rCO2} of the three CO_2 phases to increase and the S_{or} to decrease.

7.4 References

1. Rathmell J, Stalkup F, Hassinger R, editors. A laboratory investigation of miscible displacement by carbon dioxide. Fall meeting of the SPE of AIME; New Orleans, LA, USA, 3–6 October 1971: SPE: Houston, TX, USA, 1971.

2. Beeson DM, Ortloff GD. Laboratory investigation of the water-driven carbon dioxide process for oil recovery. SPE-0714-0138-JPT. 1959;11:63-6.

3. Moortgat JB, Firoozabadi A, Li Z, Espósito RO. CO_2 injection in vertical and horizontal cores: measurements and numerical simulation. SPE Journal. 2013;18(02):331-44.

4. Wang X, Gu Y. Oil recovery and permeability reduction of a tight sandstone reservoir in immiscible and miscible CO_2 flooding processes. Industrial & Engineering Chemistry Research. 2011;50(4):2388-99.

5. Jha K. A laboratory study of heavy oil recovery with carbon dioxide. J Can Petrol Technol. 1986;25(02).

6. Emadi A, Sohrabi M, Farzaneh SA, Ireland S, editors. Experimental Investigation of Liquid-CO_2 and CO_2-Emulsion Application for Enhanced Heavy Oil Recovery. EAGE Annual Conference & Exhibition incorporating SPE Europec; London, UK, 10–13 June 2013: SPE: Houston, TX, USA, 2013.

7. Klins MA, Ali SMF. Oil production in shallow reservoirs by carbon dioxide injection. In Proceedings of the SPE Eastern Regional Meeting, Columbus; 1981/1/1/; Ohio, 4–6 November 1981. SPE: SPE: Houston, TX, USA, 1981.

8. Rojas G, Ali S. Dynamics of subcritical CO_2/brine floods for heavy-oil recovery. SPE Reservoir Engineering. 1988;3(01):35-44.

9. Tuo Z, Xuewei L, Zhengming Y, Xizhe L, Shuying W. Experimental analysis on reservoir blockage mechanism for CO_2 flooding. Petroleum Exploration and Development. 2015;42(4):548-53.

10. Liu Y, Teng Y, Jiang L, Zhao J, Zhang Y, Wang D, et al. Displacement front behavior of near-miscible CO_2 flooding in decane saturated synthetic sandstone cores revealed by magnetic resonance imaging. Magnetic Resonance Imaging. 2017;37:171-8.

11. Sankur V, Creek JL, Di Julio SS, Emanuel AS. A laboratory study of Wilmington tar zone CO_2 injection project. 1986;1:95-104.

12. Moradi B, Awang M, Sabil K, Shoushtari M, Moradi P, Ajdari H, et al., editors. Liquid carbon dioxide flooding in low temperature oil reservoirs. SPE Asia Pacific Oil and Gas Conference and Exhibition; Jakarta, Indonesia, 22–24 October 2013: SPE: Houston, TX, USA, 2013.

13. Arshad A, Al-Majed AA, Menouar H, Muhammadain AM, Mtawaa B. Carbon dioxide (CO_2) miscible flooding in tight oil reservoirs: A case study. In Proceedings of the SPE Kuwait International Petroleum Conference and Exhibition; 2009/1/1/; Kuwait City, Kuwait, 14–16 December 2009. SPE: Houston, TX, USA, 2009.; 2009/1/1.

14. Chung F, Jones R, Burchfield T, editors. Recovery of viscous oil under high pressure by CO_2 displacement: A laboratory study. International meeting on petroleum engineering; Tianjin, China, 1–4 November 1988: SPE: Houston, TX, USA, 1988.

15. Huang ET, Tracht JH, editors. The displacement of residual oil by carbon dioxide. SPE Improved Oil Recovery Symposium; Tulsa, Oklahoma, 22–24 April 1974: SPE: Houston, TX, USA, 1974.

16. Cao M, Gu Y. Oil recovery mechanisms and asphaltene precipitation phenomenon in immiscible and miscible CO_2 flooding processes. Fuel. 2013;109:157-66.

17. Lashkarbolooki M, Vaezian A, Hezave AZ, Ayatollahi S, Riazi M. Experimental investigation of the influence of supercritical carbon dioxide and supercritical nitrogen injection on tertiary live-oil recovery. The Journal of Supercritical Fluids. 2016;117:260-9.

18. Bayat M, Lashkarbolooki M, Hezave AZ, Ayatollahi S. Investigation of gas injection flooding performance as enhanced oil recovery method. JNGSE. 2016;29(Supplement C):37-45.

19. Rezaei N, Firoozabadi A. pressure evolution and production performance of waterflooding in n-heptane-saturated fired Berea cores. SPE Journal. 2014;19(04):674-86.

20. Georgiadis A, Maitland G, Trusler JM, Bismarck A. Interfacial tension measurements of the (H_2O+ CO_2) system at elevated pressures and temperatures. Journal of Chemical & Engineering Data. 2010;55(10):4168-75.

21. Banerjee S, Hassenklöver E, Kleijn JM, Cohen Stuart MA, Leermakers FA. Interfacial tension and wettability in water–carbon dioxide systems: Experiments and self-consistent field modeling. The Journal of Physical Chemistry B. 2013;117(28):8524-35.

22. Chang C, Zhou Q, Xia L, Li X, Yu Q. Dynamic displacement and non-equilibrium dissolution of supercritical CO_2 in low-permeability sandstone: An experimental study. International Journal of Greenhouse Gas Control. 2013;14:1-14.

23. Nutt C, editor. The physical basis of the displacement of oil from porous media by other fluids: a capillary bundle model. Proceedings of the Royal Society of London A: Mathematical, Physical and Engineering Sciences; 1982.

24. Kwelle SO. Experimental studies on resistance to fluid displacement in single pores [PhD. Thesis]: The University of Edinburgh, Edinburgh, UK; 2017.

25. Müller N. Supercritical CO_2-brine relative permeability experiments in reservoir rocks—Literature review and recommendations. Transport in porous media. 2011;87(2):367-83.

26. Bennion DB, Bachu S, editors. The impact of interfacial tension and pore size distribution/capillary pressure character on CO_2 relative permeability at reservoir conditions in CO_2-brine systems. In Proceedings of the SPE/DOE Symposium on Improved Oil Recovery; Tulsa, OK, USA, 22–26 April 2006: SPE: Houston, TX, USA, 2006.

27. Yang D, Gu Y, Tontiwachwuthikul P. Wettability determination of the reservoir brine− reservoir rock system with dissolution of CO_2 at high pressures and elevated temperatures. Energy & Fuels. 2007;22(1):504-9.

28. Yang D, Tontiwachwuthikul P, Gu Y. Interfacial interactions between reservoir brine and CO_2 at high pressures and elevated temperatures. Energy & Fuels. 2005;19(1):216-23.

29. Liu N, Ghorpade SV, Harris L, Li L, Grigg RB, Lee RL, editors. The effect of pressure and temperature on brine-CO_2 relative permeability and IFT at reservoir conditions. In Proceedings of the SPE Eastern Regional Meeting; Morgantown, WV, USA, 13–15 October 2010: SPE: Houston, TX, USA, 2010.

30. Jung J-W, Wan J. Supercritical CO_2 and ionic strength effects on wettability of silica surfaces: Equilibrium contact angle measurements. Energy & Fuels. 2012;26(9):6053-9.

31. Nobakht M, Moghadam S, Gu Y. Effects of viscous and capillary forces on CO_2 enhanced oil recovery under reservoir conditions. Energy & Fuels. 2007;21(6):3469-76.

32. Mahdavi E, Zebarjad FS, Taghikhani V, Ayatollahi S. Effects of paraffinic group on interfacial tension behavior of CO_2–asphaltenic crude oil systems. Journal of Chemical & Engineering Data. 2014;59(8):2563-9.

33. Escrochi M, Mehranbod N, Ayatollahi S. The gas–oil interfacial behavior during gas injection into an asphaltenic oil reservoir. Journal of Chemical & Engineering Data. 2013;58(9):2513-26.

34. Peace software. 2017 [http://www.peacesoftware.de/einigewerte/co2_e.html]

35. Skauge A, Håskjold G, Thorsen T, Aarra M, editors. Accuracy of gas-oil relative permeability from two-phase flow experiments. In Proceedings of International Symposium of the Society of Core Analysts; Calgary, AB, Canada, 7–10 September 1997.

36. Akbarabadi M, Piri M. Geologic storage of carbon dioxide: an experimental study of permanent capillary trapping and relative permeability. In Proceedings of International Symposium of the Society of Core Analysts; Austin, Texas, USA. 18–21 September 2011. p. 18-21.

37. Rathnaweera T, Ranjith P, Perera M. Effect of salinity on effective CO_2 permeability in reservoir rock determined by pressure transient methods: An experimental study on Hawkesbury sandstone. Rock Mechanics and Rock Engineering. 2015;48(5):2093-110.

38. Busch A, Müller N. Determining CO_2/brine relative permeability and capillary threshold pressures for reservoir rocks and caprocks: Recommendations for development of standard laboratory protocols. Energy Procedia. 2011;4:6053-60.

39. Chukwudeme EA, Hamouda AA. Enhanced oil recovery (EOR) by miscible CO_2 and water flooding of asphaltenic and non-asphaltenic oils. Energies. 2009;2(3):714-37.

40. Parvazdavani M, Masihi M, Ghazanfari M. Gas–oil relative permeability at near miscible conditions: An experimental and modeling approach. Scientia Iranica. 2013;20(3):626-36.

41. Kazemifar F, Blois G, Kyritsis DC, Christensen KT. Quantifying the flow dynamics of supercritical CO_2–water displacement in a 2D porous micromodel using fluorescent microscopy and microscopic PIV. Advances in Water Resources. 2015.

42. Rostami B, Kharrat R, Ghotbi C, Tabatabaie S. Gas-oil relative permeability and residual oil saturation as related to displacement instability and dimensionless numbers. Oil & Gas Science and Technology–Revue de l'Institut Français du Pétrole. 2010;65(2):299-313.

43. Bennion DB, Bachu S, editors. Dependence on temperature, pressure, and salinity of the IFT and relative permeability displacement characteristics of CO_2 injected in deep saline aquifers. SPE Annual Technical Conference and Exhibition; 2006.

8 Chapter 8: Water (Brine)-CO_2 Imbibition Displacements

8.1 Introduction

After the injection of CO_2 in a drainage process, the formation water will push back the injected CO_2 in an imbibition process [1, 2]. This can trap large quantities of the injected CO_2, thereby enhancing the storage capacity and security of CO_2, even leakage events were to occur [3]. This trapment is governed by the snap-off phenomenon, which depends on the capillary forces [4, 5] and relative permeability hysteresis [6-8]. The capacity of this mechanism is controlled by the effective porosity times the residual nonwetting saturation, which depends on the displacement efficiency and relative permeability. The displacement efficiency, in turn, is strongly influenced by the ratio between capillary and viscous forces and the interfacial interactions, which, in turn, are largely influenced by the change in the state of CO_2 as well as pressure, temperature, and salinity of the formation fluids.

Despite its widespread occurrence and practical importance, the literature review has shown only a little experimental research (which conducted either under gaseous, liquid, or supercritical CO_2 conditions) has been allocated to water-CO_2 imbibition displacements [9-13]. The literature review shows no such detailed experiments have been conducted to study the impact of the CO_2 phase and operational conditions on the dynamic pressure evolution and displacements efficiency when water or brine solution is injected into a CO_2 saturated sandstone core sample. In this study, the impact of fluid pressure, temperature, and salinity on the differential pressure profile, endpoint water saturation (i.e. residual CO_2 saturation), and endpoint water (brine) effective and relative permeabilities have been studied under gaseous, liquid, and supercritical conditions. The results would provide a deep insight into the impact of the CO_2 phase as well as operational conditions and salinity on the displacement efficiency, injectivity, migration, and storage capacity of CO_2.

8.2 Experimental Results on Water-CO_2 imbibition Displacements as a Function of the CO_2 Phase

To gain a deep insight into the impact of the CO_2 phase on the dynamic behaviour of CO_2 imbibition displacements (under various fluid pressure, temperature, and saline conditions),

the inlet and outlet pressures, the endpoint water saturation, and endpoint effective (relative) water permeability were measured and analysed. The experimental data has been categorized into four sections. The first three sections deal with the impact of fluid pressure, temperature, and salinity on the differential pressure profile as a function of the CO_2 phase, respectively; while the fourth section deals with their influence on the endpoint water (brine) saturation and endpoint water (brine) effective and relative permeabilities as a function of the CO_2 phase, too. In this study, the quasi-differential pressure refers to the average differential pressure measured at the end of the core flooding experiment.

8.2.1 Effect of Fluid Pressure on the Differential Pressure Profile of Water-CO_2 Displacements as a Function of the CO_2 Phase

Figure 8-1, Figure 8-2, and Figure 8-3 present the effect of fluid pressure on the differential pressure profiles during Water- gaseous (G) CO_2, Water-liquid (L) CO_2, and Water-supercritical (Sc) CO_2 dynamic imbibition displacements. During these experiments, the experimental temperature and water injection rate were maintained constant. The data show a number of important observations (A-C) as follows:

A) The results show that initially, the differential pressure increased significantly as water was injected into the core sample and reached a maximum value (1.807 to 2.773 bar) after approximately 0.37-0.49 pore volumes (PVs) of water had been injected. After reaching the maximum value, the differential pressure decreased until it reached an almost quasi-steady differential pressure after about 1-4 PVs of water had been injected. The results show that the state of the injected CO_2 governs the maximum-differential pressure and the amount of the water injected to reach the maximum and quasi-steady differential pressures. The liquid CO_2 displacements resulted in the highest magnitude in the maximum-differential pressure and required the highest amount of water to reach the maximum and quasi-steady differential pressures. Contrariwise, the gaseous CO_2 displacements showed the lowest magnitude in the differential pressure and required the least amount of water to reach the maximum and quasi-steady differential pressures.

B) The data also show that the increase in fluid pressure did not affect the shape of the differential pressure profile. However, it reduced the magnitudes of both maximum and quasi-steady differential pressures. The magnitude of reduction in the maximum and quasi-

steady differential pressures depend on the state of CO_2. The smallest reduction in the maximum-differential pressure occurred in the gaseous CO_2 displacements whereas the largest reduction occurred in the liquid CO_2 displacements followed closely by the supercritical CO_2 imbibition displacements. For the gaseous imbibition CO_2 displacements, as the fluid pressure increased from 40 to 70 bar at 33 °C, the maximum-differential pressure declined by around 4% (from around 1.882 to 1.807 bar) and the quasi-steady differential pressure dropped by 28% (from 0.26 to 0.187 bar). However, for the liquid CO_2 imbibition displacements, as the fluid pressure increased from 80 to 90 bar at 29 °C, the maximum-differential pressure decreased by 15.61% (from 2.773 to 2.34 bar) and the quasi-steady differential pressure dropped by around 62.8% (from 0.473 to 0.176 bar). Finally, for the supercritical CO_2 imbibition displacements, as the fluid pressure increased from 80 to 90 bar at 33 °C, the maximum-differential pressure reduced by 15.4% (from 2.342 to 1.981 bar) and the quasi-steady differential pressure declined by 10.6% (from 0.264 to 0.236 bar).

According to Eq.4-1 in Chapter 4, the reduction in the differential pressure with increasing fluid pressure can be related mainly to the reduction in the capillary forces. This is because the reduction observed in the differential pressure is the net result of the reduction in the capillary forces and the increase in the viscous forces. As the fluid pressure increased, the capillary forces decreased due to the reduction in the water-CO_2 interfacial tension and the increase in contact angle owing to increasing CO_2 solubility [14, 15]; while, the viscous forces increased due to increasing CO_2viscosity; the water viscosity is constant at around 7.488, 8.137, and 7.488 × [10^{-4} (Pa·s)] for the gaseous, liquid, and supercritical CO_2 displacements, respectively [16]. For the gaseous CO_2 imbibition displacements, increasing fluid pressure from 40 to 70 bars at 33 $^{\circ}$C causes the water-CO_2 IFT to decrease from around 37.1 to 29.65 mN/m, as shown in Figure 4-4 in Chapter 4, but the CO_2 viscosity to increase from 16.187 to 20.743 × [10^{-6} (Pa·s)] [16]. For the liquid CO_2 displacements, increasing fluid pressure from 80 to 90 bars at 29 $^{\circ}$C causes the IFT to decrease from around 33.15 to 31.75 mN/m [17] but the CO_2 viscosity to increase from 78.33 to 81.56 × [10^{-6} (Pa·s)]. For the supercritical CO_2 displacements, increasing fluid pressure from 80 to 90 bars at 33 $^{\circ}$C causes the IFT to decrease from around 27.2 to 25 mN/m but the CO_2 viscosity to increase from 45.876 to 53.837 × [10^{-6} (Pa·s)].

The differential pressure profiles of the liquid and supercritical CO_2 displacements seemed to be highly influenced by the contact angle, which seems not to be the case for the gaseous CO_2 displacements. This can be suggested by two observations: 1) the differential pressures of the liquid and supercritical CO_2-displacements experienced the highest reduction (around 15%) despite the slightest reduction in the IFT (≤ 2 mN/m); and 2) the differential pressures of the gaseous CO_2 displacements experienced the lowest reduction (around 4%) despite the highest reduction in the CO_2-water interfacial tension (≤ 7 mN/m). This might indicate a higher increase occurred in contact angle of the liquid and supercritical CO_2 displacements as fluid pressure increased in comparison to the gaseous CO_2 displacements [18, 19]. That is, wettability alteration in case of liquid and supercritical CO_2 imbibition displacements might be responsible for the largest portion of the reduction in the differential pressures.

C) The data also show that the response of the differential pressure to increasing fluid pressure is dependent on the CO_2 state. For the liquid CO_2 displacements conducted at 29 °C, the differential pressure profile of the lower-fluid pressure experiment (80 bar) was higher than that of the higher-fluid pressure experiment (90 bar) during the whole experiment, as shown in Figure 8-2. This indicates a strong influence for the capillary forces on the liquid CO_2 differential profiles; the influence lasted throughout the whole experiments. The strong impact of the capillary forces means that liquid CO_2 was stored as free gas since the mass transfer and diffusivity of liquid CO_2 in water are negligible [15].

On the other hand, the differential pressure profile of the gaseous and supercritical CO_2 displacements showed a high degree of similarity. The differential pressure profiles of the lower and higher-fluid pressure displacements were almost equal (with the exception of the reduction in the maximum-differential pressure) during the whole supercritical CO_2 displacements and slightly differed during the whole gaseous CO_2 displacements, as shown in Figure 8-1 and Figure 8-3. This indicates a slight impact for the capillary forces on the differential pressures after a quasi-steady state was reached and until the end of the experiments. The slight impact of the capillary forces and the resemblance observed between the gaseous and supercritical pressure profiles might be associated: (a) mainly with the high mass transfer and diffusion of CO_2 in water [15], and (b) to a lesser extent with the similarity between the CO_2 distribution of gaseous and supercritical CO_2 within the pore space [20]. According to Plug and Bruining [15], the high mass transfer rate and diffusion of

CO_2 in water influence the water production and injection behaviour of gaseous CO_2 greatly. During these displacements, the injected water was not saturated with CO_2 (i.e. high impact of mass transfer and diffusion), thus it is expected that as water imbibition progressed, most of the gaseous and supercritical CO_2 dissolved in water or stored in the form of tiny bubbles in the porous media (i.e. residual saturation) [21]. As a result of the CO_2 dissolution in water, the water-CO_2 IFT diminished and; hence, the impact of the capillary forces disappeared. The disappearance of the impact of the capillary forces may cause the viscous forces, which are insignificant comparing to capillary forces, to govern the magnitude and the behaviour of the differential profiles after reaching a quasi-steady state until the end of the experiments.

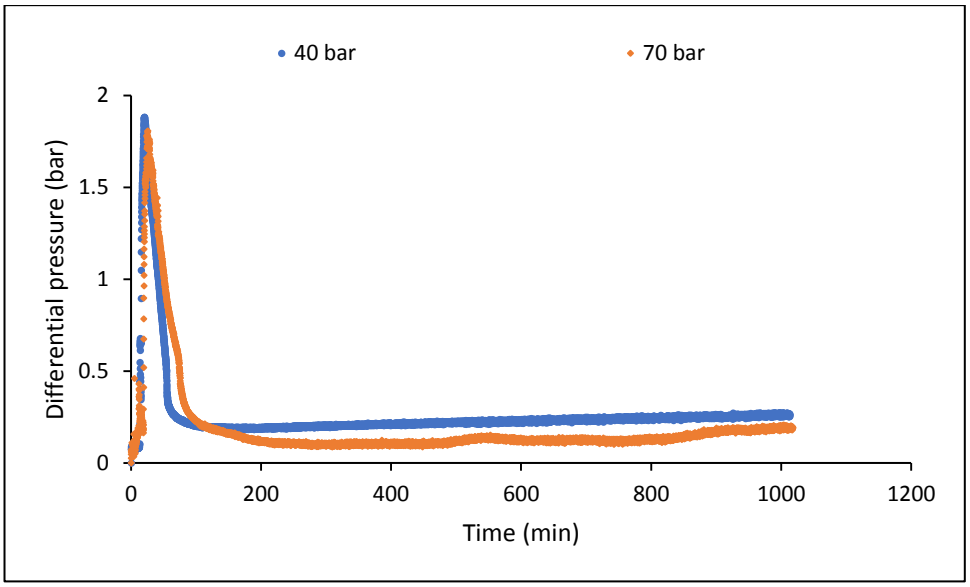

Figure 8-1: Effect of fluid pressure on the differential pressure profile of Water-GCO_2 imbibition displacements conducted at 0.1 ml/min and 33 °C

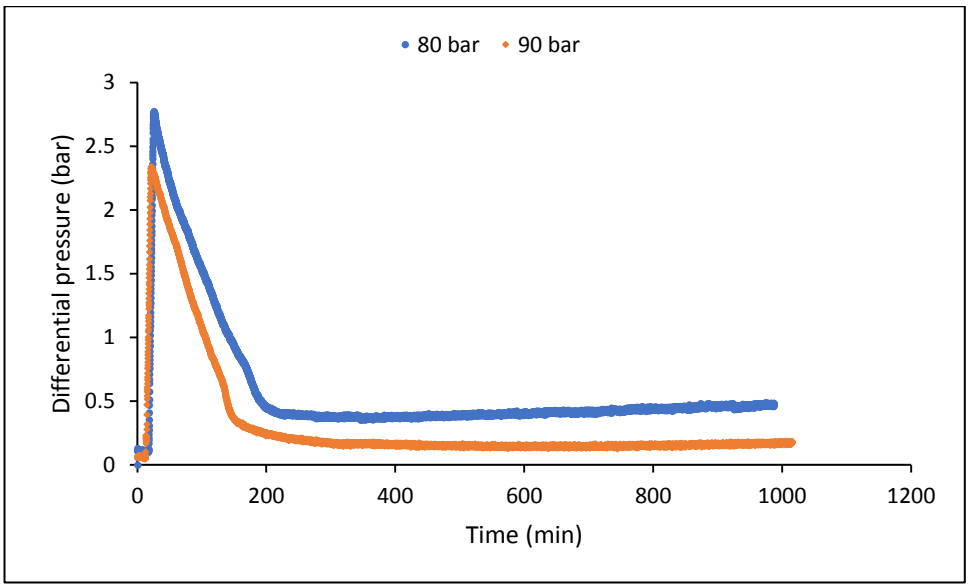

Figure 8-2: Effect of fluid pressure on the differential pressure profile of Water-LCO_2 imbibition displacements conducted at 0.1 ml/min and 29 °C

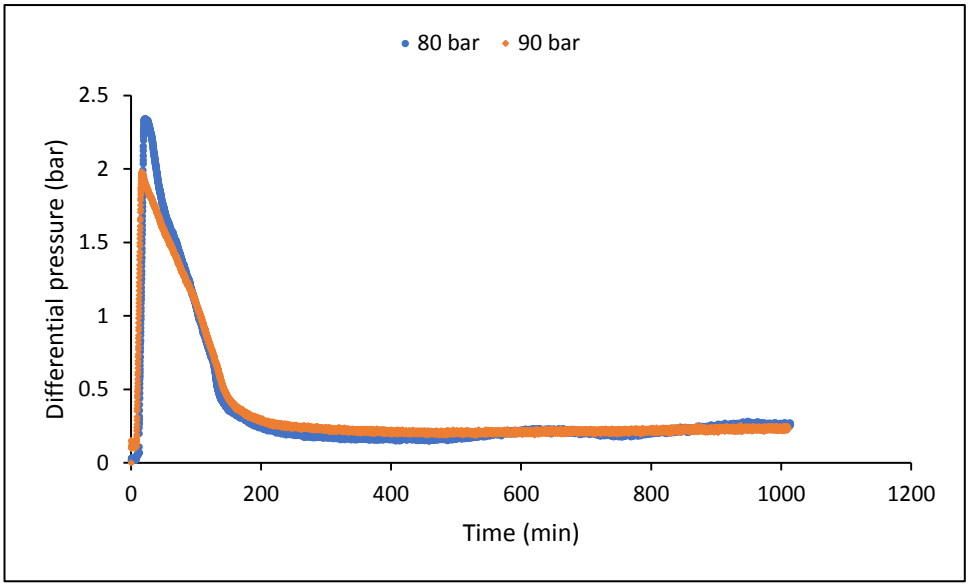

Figure 8-3: Effect of fluid pressure on the differential pressure profile of Water-$ScCO_2$ imbibition displacements conducted at 0.1 ml/min and 33 °C

8.2.2 Effect of Experimental Temperature on the Differential Pressure Profile of Water-CO_2 Displacements as a Function of the CO_2 Phase

The data presented in Figure 8-4, Figure 8-5, and Figure 8-6 exhibit the effect of the experimental temperature on the differential pressure profiles during dynamic water

imbibition into a gaseous, liquid, and supercritical CO_2 saturated-sandstone core sample. During all experiments, the fluid pressure and water influx rate were kept constant.

In general, the increase in the experimental temperature resulted in a considerable reduction in the maximum and quasi-steady differential pressures. The magnitude of the reduction is a function of the CO_2 phase. The highest reduction in the maximum-differential pressure was observed by far in the liquid CO_2 displacements, followed by low-fluid pressure gaseous CO_2, and finally by supercritical CO_2 displacements. For illustration, for the liquid CO_2 experiments, increasing the temperature by 9° (from 20 to 29 °C) at 90 bar led to the dropping of the maximum-differential pressure by around 36% (from 3.653 to 2.34 bar) and the quasi-steady differential pressure by about 61.7% (from 0.459 to 0.176 bar). For the gaseous CO_2 displacements, as the temperature increased by 12° (from 33 to 45 °C), the maximum-differential pressure reduced by 24.55% (from 1.882 to 1.42 bar) and the quasi-steady differential pressure decreased by 44.62% (from 0.26 to 0.144 bar). Nonetheless, for the supercritical CO_2 displacements, as the temperature raised by 12° (from 33 to 45 °C) at 90 bar, the maximum-differential pressure decreased by 8.53% (from 1.981 to 1.812 bar) and the quasi-steady differential pressure decreased by 8.47% (from 0.236 to 0.216 bar).

The reduction observed in the maximum and quasi-steady differential pressures with increasing temperature can be related to the reduction in the capillary number (*Ca*), (Eq. 2-7 Chapter 2 can be used to calculate *Ca*). The *Ca* is a function of the magnitude of the viscous forces to the magnitude of the capillary forces. The reduction in *Ca* with increasing temperature is due to the simultaneous effect of decreasing the viscous forces and increasing the capillary forces. This means that both capillary and viscous forces have helped in reducing the differential pressure. This is in agreement with Nutt's [22] observations. According to Nutt, if a wetting fluid (e.g. brine or water) is injected to displace a non-wetting fluid (e.g. CO_2), then the capillary forces would aid the applied viscous forces [22, 23]. The decrease in the viscous forces with increasing temperature is due to the reduction in the viscosity of water and CO_2 [16]. The increase in capillary forces with increasing temperature is because of the increase in the interfacial tension and the reduction in the contact angle caused by reducing CO_2 solubility [14, 15].

For the Water-GCO_2 core flooding, as the temperature increased from 33 to 45 °C at 40 bar, the IFT increased from 37.1 to 45.5 mN/m, the deionised water viscosity reduced from 7.488 to 5.966 $\times$ [10^{-4} (Pa·s)]; and thus, the *Ca* declined from 5.514 $\times$ 10^{-7} to 3.597 $\times$ 10^{-7}. The reduction in the maximum and quasi-steady differential pressures of the gaseous displacements with increasing temperature agrees well with the reduction in the *Ca*. This means that the reduction in the differential pressures can be associated with the large reduction in the viscous forces and the considerable increase in the capillary forces during these displacements.

For the Water-LCO_2 core flooding, as the temperature increased from 20 to 29 °C at 90 bar, the IFT increased from 28.1 to 31.75 mN/m, the water viscosity was constant at around 8.137 $\times$ [10^{-4} (Pa·s)], and the *Ca* declined from 7.88 $\times$ 10^{-7} to 6.9 $\times$ 10^{-7}. For the liquid CO_2 displacement, the reduction in the differential pressures can be attributed to the reduction in the *Ca* only because of the increase in the capillary forces. This is because the displacing fluid (water) viscosity was constant with increasing temperature and hence no change in viscous forces that can lead to a change in the *Ca* is expected to occur.

For the Water-$ScCO_2$ core flooding, as the temperature increased from 33 to 45 °C at 90 bar, the IFT increased from 25 to 28 mN/m, the water viscosity reduced from 7.488 to 5.97 $\times$ [10^{-4} (Pa·s)], and the *Ca* declined from 8.182 $\times$ 10^{-7} to 5.85 $\times$ 10^{-7}. For the supercritical CO_2 displacements, the reduction in the differential pressure can be attributed to the reduction in the *Ca* because of the rise in the capillary forces due to increasing interfacial tension and the reduction in viscous forces due to the reduction in water viscosity.

In summary, the high reduction in the differential pressure with increasing temperature might be related mainly to the increase in capillary forces. This is because (a) the capillary forces are greater than the viscous forces by an order of magnitude and (b) the viscous forces experienced only a slight reduction due to the slight decline in water and CO_2 viscosity.

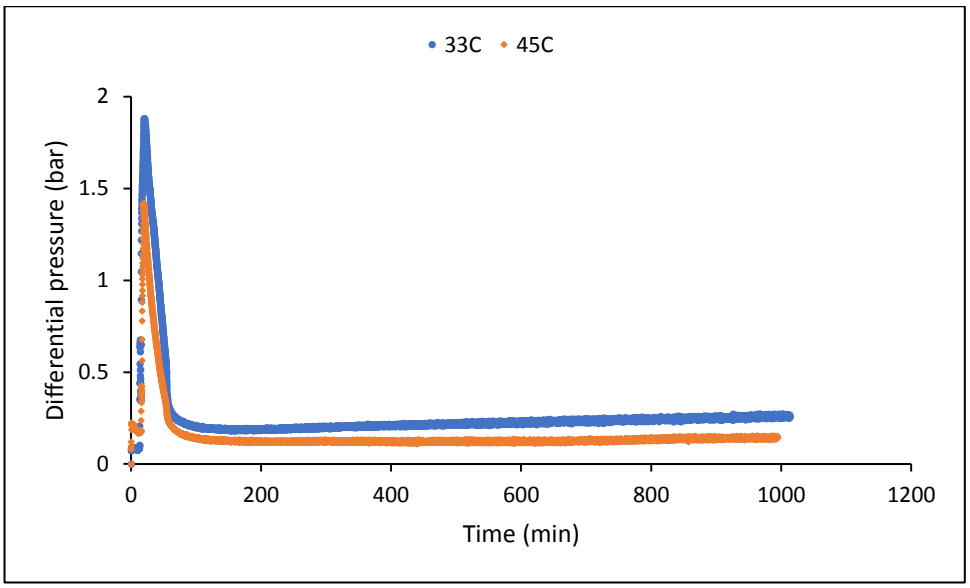

Figure 8-4: Effect of experimental temperature on the differential pressure profile of Water-GCO_2 imbibition displacements conducted at 40 bar and 0.1 ml/min

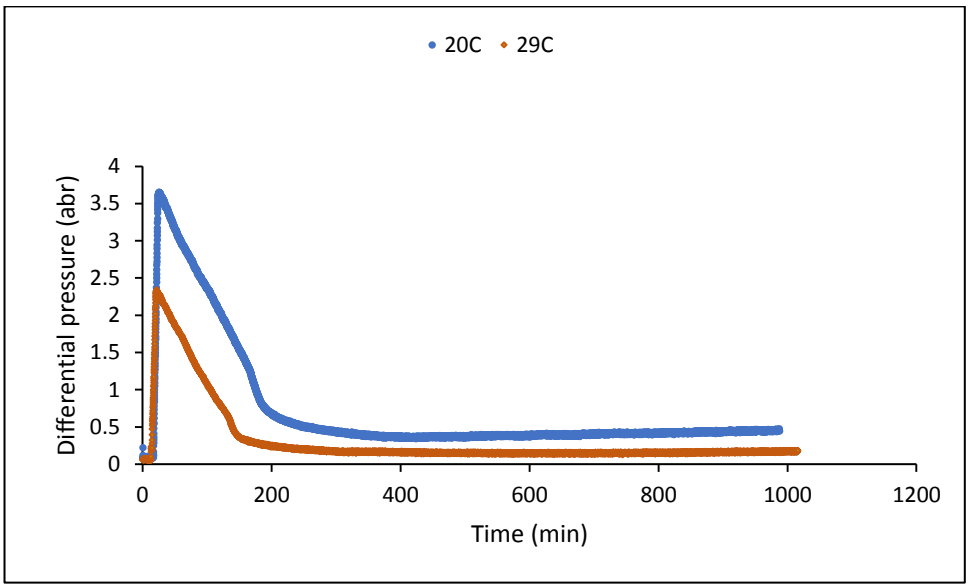

Figure 8-5: Effect of experimental temperature on the differential pressure profile of Water-LCO_2 imbibition displacements conducted at 90 bar and 0.1 ml/min

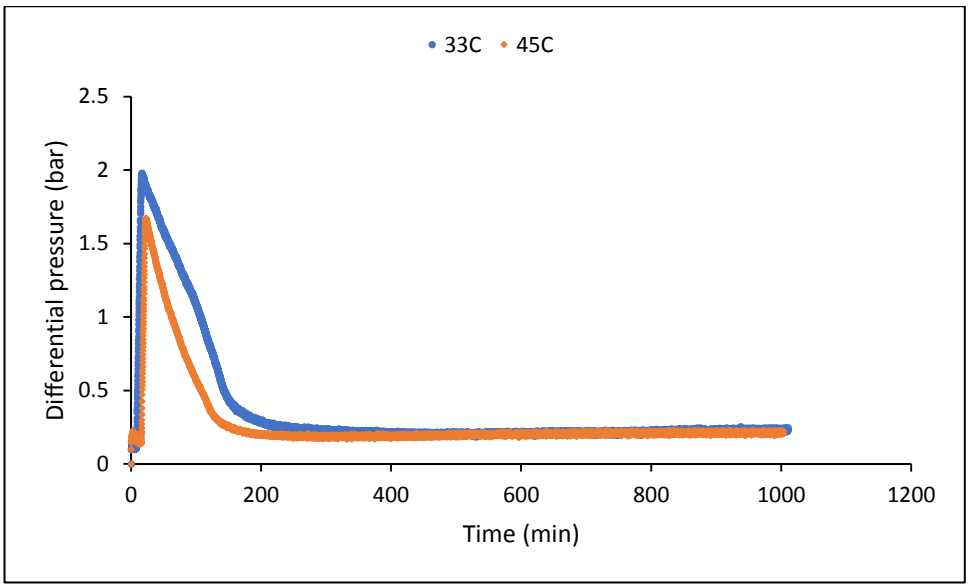

Figure 8-6: Effect of experimental temperature on differential pressure profile of Water-ScCO_2 imbibition displacements conducted at 90 bar and 0.1 ml/min

8.2.3 Salinity Effect on the Differential Pressure Profile of Water-CO_2 Displacements as a Function of the CO_2 Phase

The data in Figure 8-7, Figure 8-8, and Figure 8-9 show the effect of using brine (1 wt. % $CaCl_2$) solution instead of deionised water on the differential pressure profile during gaseous, liquid, and supercritical CO_2 dynamic imbibition displacements. During these experiments, the fluid pressure, temperature, and brine (water) injection rate were kept unchanged. The data show two main observations (A and B) as follows:

A) Overall, the results show that the differential pressure profiles for both brine and water-CO_2 displacements are in good agreement. However, using saline water (1 wt. % $CaCl_2$) instead of deionised water led to a marked reduction in the maximum-differential pressure. The magnitude of the reduction is a function of the CO_2 phase. The highest reduction in the maximum-differential pressure occurred during the liquid CO_2 displacements, followed by low-fluid pressure gaseous CO_2 displacements, and finally by supercritical CO_2 imbibition displacements. The order of the differential pressure with brine usage agrees with the order of the differential pressure observed with increasing temperature, as discussed in Section 8.2.2. For the liquid CO_2 imbibition displacements, when brine instead of water was injected to displace the liquid CO_2, the maximum-differential pressure reduced by around 19% (from 3.653 to 2.964 bar) and the quasi-steady differential pressure decreased by around 17%

(from 0.459 to 0.381 bar). It is worth stating here that due to some technical difficulties, the comparison between water and brine (1 wt. % $CaCl_2$) imbibition displacements was conducted at different pressures, 90 and 70 bar, respectively. Providing that the 1 wt. % $CaCl_2$ displacement was also run at 90 bar instead of 70 bar, the actual reduction in the maximum-differential pressure with salinity would be higher than 19%. This is based on the aforementioned observation in Section 8.2.1, which showed a reduction in the maximum-differential pressure value with increasing fluid pressure. Regarding the gaseous and supercritical CO_2 imbibition displacements, the brine usage caused the maximum-differential pressure to decrease by around 15.6% (from 1.882 to 1.589 bar) for the gaseous CO_2 displacements and by 5.63% (from 1.812 to 1.71 bar) for the supercritical CO_2 displacements.

According to Eq.4-1-Chapter 4, the reduction in the differential pressure with increasing salinity can be associated entirely with the changes in capillary forces as no practical change is expected to occur in the viscous forces with adding slight amounts of salt. Using a brine solution caused the capillary forces either to increase due to the increase in the interfacial tension [24] or to decrease due to the increase in contact angle [25], more information can be found in Appendix A. Hence, the magnitude of the capillary forces depends on whether the change in interfacial tension or the change in contact angle is dominant.

B) The results shows that for the gaseous and supercritical CO_2 phases' imbibition displacements, the increase in salinity produced a gradual increase in the differential pressure after reaching a quasi-steady state until the end of the displacement, as shown in Figure 8-7 and Figure 8-9. This gradual increase in the differential pressure was more obvious in the supercritical CO_2 displacements than the gaseous CO_2 imbibition displacements. For illustration, the brine usage caused the quasi-steady differential pressure to increase by around 24.6% (from 0.26 to 0.324 bar) for the gaseous CO_2 imbibition displacement and to increase by around 159.3% (from 0.216 to 0.56 bar) for the supercritical CO_2 imbibition displacements.

This increase in the differential pressure can be related to two likely reasons. The first possible reason is that the gradual increase in the differential pressure can be related to a possible gradual reduction in the capillary forces due to a possible gradual increase in contact angle. As a result, this reduction in the capillary forces might have resulted in increasing the

differential pressure since the capillary forces complement the viscous forces [22], as stated above. The gradual increase in the contact angle might be associated with CO_2 dissolution in brine. This is because, as stated before, the effects of mass transfer and diffusivity of CO_2 in water are negligible in case of liquid CO_2 but can have a strong influence on the water production and injection behaviour of gaseous CO_2 [15] and supercritical CO_2.

The second likely reason for the increase in the differential pressure is due to the formation of the calcium carbonates. This scenario is possible due to a potential reaction of the calcium chloride with the carbon dioxide and water as follows:

$10CaCl_2 + H2O + 15\ CO_2 = 10\ CaCO_3 + 20\ HCl$ (1)

Because of the small brine injection rate (0.1 ml/min), the calcium carbonates might have precipitated [26] and led to a gradual pore blocking, which led to a gradual increase in the differential pressure. However, the second reason might be less likely since the increase in the differential pressure was not observed in the liquid CO_2 displacements and was only minor in the case of the gaseous CO_2.

In summary, the second observation (B) confirms that the capillary forces have worked to (a) reduce the maximum differential pressure for the three CO_2 phases and (b) increase the quasi-differential pressure of gaseous and supercritical CO_2 displacements. The results indicate a less impact for contact angles on the maximum differential pressure but a high impact for them on the quasi-differential pressure profile. This indicates that the impact of contact angle increased as core flooding continued.

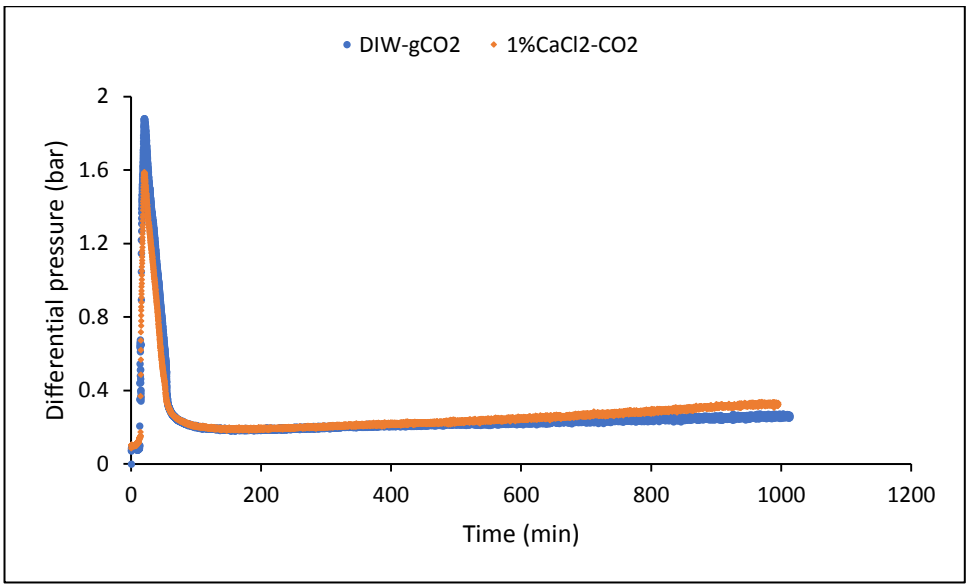

Figure 8-7: Effect of salinity on the differential pressure profile during gaseous CO_2 dynamic imbibition displacements conducted at 40 bar, 0.1 ml/min, and 33 °C

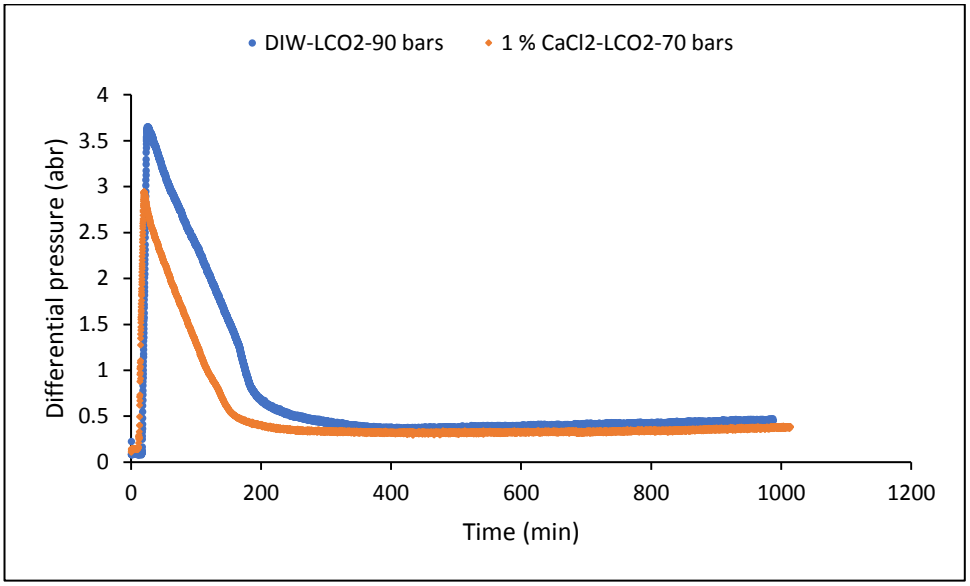

Figure 8-8: Effect of salinity on the differential pressure profile during liquid CO_2 dynamic imbibition displacements conducted at 90/70 bar, 0.1 ml/min, and 20 °C

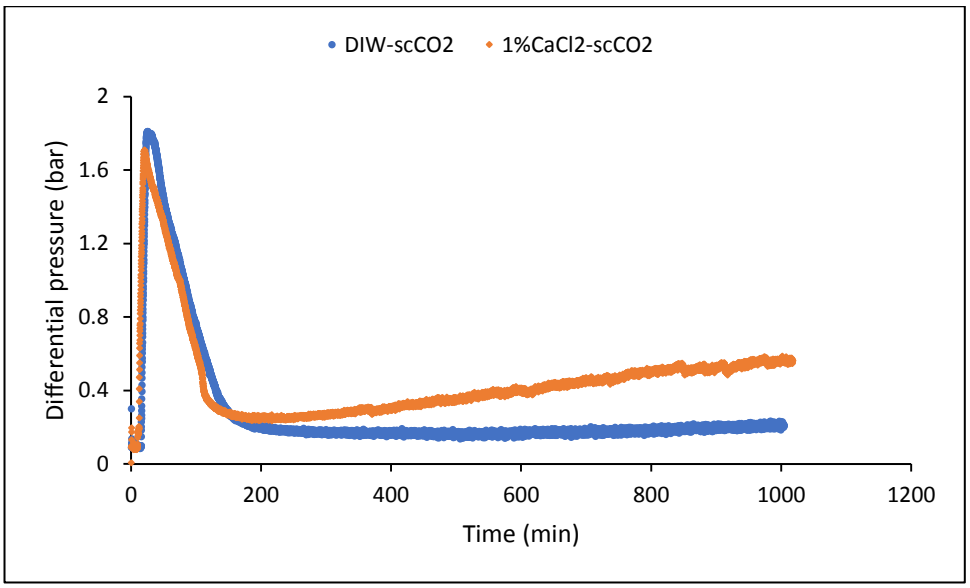

Figure 8-9: Effect of salinity on the differential pressure profile during supercritical CO_2 dynamic imbibition displacements conducted at 90 bar, 0.1 ml/min, and 45 °C

8.2.4 Endpoint Water (brine) Saturation and Endpoint Effective and Relative Permeabilities of Water (brine) as a Function of the CO_2 Phase

In this section, the same procedures that were presented in Chapter 4-Section 4.2.3 for calculating and measuring the endpoint water (brine) effective and relative permeabilities and endpoint water (brine) saturation are followed here.

The data from Table 8-1 shows that for the three CO_2 phases the increase in fluid pressure led to an increase in the endpoint water saturation (S_{ew}) while the increase in experimental temperature caused a reduction in the S_{ew}. On the other hand, the increase in the fluid pressure caused an increase in the endpoint water relative permeability (K_{rew}) for the three CO_2 phases; the highest increase in the K_{rew} occurred in the liquid CO_2 displacements whilst the slowest occurred in the supercritical CO_2 displacements. Nevertheless, the increase in the experimental temperature caused an increase in the K_{rew} for subcritical CO_2 phases but a reduction for supercritical CO_2 phase. The fluid pressure and temperature data will be discussed for each phase but the impact of using brine will be discussed for the three CO_2 phases altogether later.

For the liquid CO_2 displacements, the increase in the fluid pressure and temperature caused a considerable increase in the K_{rew} by 47.1% and 46.3%, respectively. On the other hand, the increase in the fluid pressure caused an increase in the S_{ew} (4%) but the increase in the temperature caused a slight reduction in the S_{ew} (1%). The results indicate that if the aim of the CO_2 injection project is to increase recovery and reduce CO_2 consumption, then increasing fluid pressure would be preferable.

For the supercritical CO_2 displacements, the increase in fluid pressure resulted in an increase in both K_{rew} (5.4%) and S_{ew} (2%). On the other hand, increasing temperature caused a strong reduction in the K_{rew} (6.4%) and a substantial reduction in the S_{ew} (23%). The substantial reduction in the S_{ew} (23%) with increasing temperature, despite the large quantities of water injected (about 20 PVs), suggests a large retention of CO_2 can occur in high-temperature environments.

For the gaseous CO_2-imbibition displacements, the increase in the fluid pressure caused an increase in both K_{rew} (18.3%) and S_{ew} (1%). However, increasing temperature caused an increase in the K_{rew} (20.8%) but a reduction in the S_{ew} (5%).

Overall, the increase and decrease in the S_{ew} can be related to the increase and decrease in the *Ca*, as shown in Table 8-1. In general, the higher the change in the *Ca*, the higher the corresponding change in the S_{ew} (i.e. residual CO_2 saturation) is. On the other hand, according to Darcy's law, the change observed in the relative permeability can be related only to the change in the average quasi-differential pressure at the end of the core flooding experiment and the water viscosity. This is because the displacements were conducted in the same core sample (i.e. the sample's length, frontal face area, and absolute permeability are constant) and at a constant injection rate. The increase in the K_{rew} with increasing fluid pressure for the three CO_2 phases can be attributed to the reasons behind the reduction in the quasi-differential pressure and the increase in water viscosity. The reduction in the differential pressure with increasing fluid pressure can be linked to the reduction in capillary forces because of the reduction in the interfacial tension and the increase in contact angle when fluid pressure increases; more information can be found in Section 8.2.1.

On the other hand, the increase in the K_{rew} of the gaseous and liquid CO_2 imbibition displacements with increasing experimental temperature can be attributed to the reasons behind the reduction in the quasi-differential pressure only. On the other hand, the slight reduction in the K_{rew} of the supercritical CO_2 displacements can be related mainly to the high reduction in the water viscosity; the magnitude of reduction might be slightly offset by the very slight reduction in the quasi-differential pressure of supercritical CO_2 displacements; more information about the reason behind the reduction in the differential pressure with temperature can be found in Section 8.2.2.

Using brine (1 wt. % $CaCl_2$) solution instead of deionised water increased the endpoint brine saturation (S_{eb}) and reduced the endpoint brine relative permeability (K_{reb}) for gaseous and supercritical CO_2 displacements but caused a high reduction in the S_{eb} and a significant increase in K_{reb} for liquid CO_2 displacements. Rathnaweera and Ranjith [27] observed a reduction in the effective permeability of supercritical CO_2 as salinity increased. The S_{eb} increased by 1% for the gaseous displacements and increased by 35% for the supercritical displacements but decreased by about 25% for the liquid displacements. The K_{reb} decreased by 9.3% for the gaseous CO_2 and decreased by 27.7% for the supercritical CO_2 but increased by 13.7% for the liquid CO_2.

The reduction in the K_{reb} for the gaseous and supercritical CO_2 displacements can be related to the reasons behind the increase in the quasi-differential pressure; more information can be seen in Section 8.2.3. However, the increase in the K_{reb} for the liquid CO_2 phase can be attributed to the reasons behind the reduction in the quasi-differential pressure as well as the slight increase in viscosity; more information can be found in Section 8.2.3.

On the other hand, the increase and reduction in the S_{eb} cannot be explained by the calculated *Ca* for the brine displacements. This indicates that the calculated *Ca* of the brine displacements is different from the real *Ca*. The main reason for the difference is the contact angle value. The *Ca* of the brine displacements is calculated on the assumption that the brine-CO_2 contact angle is 40° [28]; the $CaCl_2$-CO_2 interfacial data are extrapolated from Figure 8-10. However, the data, from Figure 8-7 and Figure 8-9, suggest a gradual increase in the contact angle of the gaseous and supercritical CO_2 imbibition displacements; as discussed in Section 8.2.3. Therefore, the real contact angle might be higher than 40°. Assuming a contact angle

higher than 40° for the gaseous and supercritical CO_2 imbibition displacements would result in having a higher *Ca* for the brine displacements than that for the water displacements, which could explain the higher brine saturation obtained. Thus, the high increase in the S_{eb} for the brine-supercritical CO_2 displacements means a significant increase in the *Ca* should occur. This increase in the *Ca* can be attributed to the increase in the contact angle.

The strong reduction in the S_{eb} for the liquid CO_2 imbibition displacement means a high reduction in the *Ca* occurred. The reduction in the *Ca* with increasing salinity can be related mainly to the high increase in the capillary forces owing to the increase in the interfacial tension (because of increasing salinity and reducing fluid pressure) and the reduction in the contact angle [14] because of reducing the fluid pressure; the brine displacements conducted at lower fluid pressure (70 bar) than the water displacement (90 bar), as discussed in Section 8.2.3. Thus, the reduction in contact angle might have occurred in case of liquid CO displacements due to decreasing fluid pressure despite the possible slight increase in contact angle due to increasing salinity.

Table 8-1: Effect of fluid pressure, temperature, and salinity on endpoint water (brine) effective and relative permeabilities and endpoint water (brine) saturation

Status	Experiment	S_{ew}/ S_{eb}	K_{few}/ K_{feb}	K_{rew}/ K_{reb}	*Ca* ($\times 10^{-7}$)
DIW-GCO_2	40 bar-0.1 ml/min-33 °C	0.93	7.337	0.468	5.514
	40 bar-0.1 ml/min-45 °C	0.88	10.601	0.676	3.597
	70 bar-0.1 ml/min-33 °C	0.94	10.201	0.651	7.070
DIW-LCO_2	90 bar-0.1 ml/min-20 °C	0.80	4.500	0.287	7.880
	80 bar-0.1 ml/min-29 °C	0.75	4.377	0.279	6.697
	90 bar-0.1 ml/min-29 °C	0.79	11.762	0.750	6.990
DIW-$ScCO_2$	80 bar-0.1 ml/min-33 °C	0.80	7.225	0.461	7.520
	90 bar-0.1 ml/min-33 °C	0.82	8.083	0.515	8.182
	90 bar-0.1 ml/min-45 °C	0.59	7.077	0.451	5.850
1%$CaCl_2$-GCO_2/LCO_2/$ScCO_2$	40 bar-0.1 ml/min-33 °C	0.94	5.887	0.375	5.160
	70 bar-0.1 ml/min-20 °C	0.55	0.654	0.424	10.00
	90 bar-0.1 ml/min-45 °C	0.94	2.73	0.174	5.630

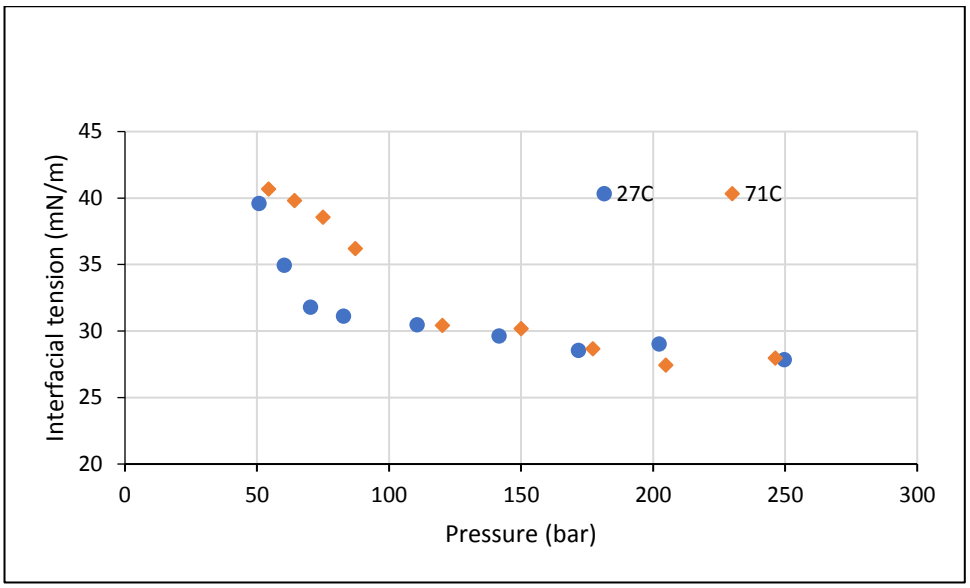

Figure 8-10: Interfacial tension for a CO_2/$CaCl_2$ solution as a function of pressure for different temperatures and aqueous phase salinities (a) 0.045m (5 g/L) [24]

8.3 Summary

In this study, Water-gaseous/liquid/supercritical CO_2 imbibition displacements were conducted in a sandstone core sample to study the effect of fluid pressure, experimental temperature, and salinity on the dynamic pressure evolution, displacement efficiency, and endpoint effective and relative permeabilities as a function of the CO_2 phase. The results indicate a considerable influence of the fluid pressure, experimental temperature, and salinity on the differential pressure profile, endpoint water effective and relative permeabilities, and endpoint water saturation; CO_2 phase affects the magnitude of the change significantly. The K_{rew} was in ranges of 0.174 to 0.711 while the S_{ew} was in ranges of 0.55 to 94.

The increase in the fluid pressure and experimental temperature as well as using brine solution (1 wt. % $CaCl_2$) instead of deionised water caused a considerable reduction in the differential pressure profile of the gaseous, liquid, and supercritical CO_2 displacements, from 4 to 36%. The magnitude of the reduction depends on the CO_2 phase considerably. However, using brine produced a gradual increase in the differential pressure of gaseous and supercritical CO_2 phases after reaching a quasi-steady state until the end of the displacement. The gradual increase in the differential pressure is more obvious in the supercritical CO_2 than in the gaseous CO_2 displacements.

The increase in fluid pressure led to an increase in both endpoint water relative permeability and endpoint water saturation for the gaseous, liquid, and supercritical CO_2 displacements; the magnitude of the increase depends on the CO_2 phase. The increase in the experimental temperature caused a reduction in the endpoint water saturation (from 1 to 23%) for the three CO_2 displacements; the highest reduction occurred in the supercritical CO_2 displacements. On the other hand, increasing temperature caused a considerable reduction in the endpoint relative permeability of the subcritical CO_2 displacements but caused an increase in the relative permeability of the supercritical CO_2 displacements.

Using brine (1% $CaCl_2$) instead of deionised water produced a reduction in the endpoint brine relative permeability and an increase in endpoint brine saturation for gaseous and supercritical CO_2 displacements but caused a significant increase in the endpoint relative permeability and a high reduction in endpoint brine saturation for liquid CO_2 displacements.

8.4 References

1. Zhang C, Oostrom M, Wietsma TW, Grate JW, Warner MG. Influence of viscous and capillary forces on immiscible fluid displacement: Pore-scale experimental study in a water-wet micromodel demonstrating viscous and capillary fingering. Energy & Fuels. 2011;25(8):3493-505.

2. Singhal A, Dranchuk P. Wettability control of glass beads. The Canadian Journal of Chemical Engineering. 1975;53(1):3-8.

3. Burnside N, Naylor M. Review and implications of relative permeability of CO_2/brine systems and residual trapping of CO_2. IJGGC. 2014;23:1-11.

4. Price J, Smith B. Geologic Storage of carbon dioxide–staying safely underground. International Energy Agency (IEA) Greenhouse Gas R & D Programme. 2008.

5. Zhang D, Song J. Mechanisms for geological carbon sequestration. Procedia IUTAM. 2014;10:319-27.

6. Delshad M, Wheeler MF, Kong X, editors. A critical assessment of CO_2 injection strategies in saline aquifers. SPE Western Regional Meeting; 2010.

7. Wang D, Dong B, Breen S, Zhao M, Qiao J, Liu Y, et al. Review: Approaches to research on CO_2/brine two-phase migration in saline aquifers. Hydrogeology Journal. 2015;23(1):1-18.

8. Chalbaud C, Robin M, Lombard J, Martin F, Egermann P, Bertin H. Interfacial tension measurements and wettability evaluation for geological CO_2 storage. Advances in Water Resources. 2009;32(1):98-109.

9. Berg S, Oedai S, Ott H. Displacement and mass transfer between saturated and unsaturated CO_2–brine systems in sandstone. IJGGC. 2013;12:478-92.

10. Chang C, Zhou Q, Xia L, Li X, Yu Q. Dynamic displacement and non-equilibrium dissolution of supercritical CO_2 in low-permeability sandstone: An experimental study. IJGGC. 2013;14:1-14.

11. Saeedi A, Rezaee R, Evans B, Clennell B. Multiphase flow behaviour during CO_2 geo-sequestration: Emphasis on the effect of cyclic CO_2–brine flooding. JPSE. 2011;79(3):65-85.

12. Alemu BL, Aker E, Soldal M, Johnsen Ø, Aagaard P. Influence of CO_2 on rock physics properties in typical reservoir rock: A CO_2 flooding experiment of brine-saturated sandstone in a CT-scanner. Energy Procedia. 2011;4:4379-86.

13. Shi J-Q, Xue Z, Durucan S. Supercritical CO_2 core flooding and imbibition in Tako sandstone—Influence of sub-core scale heterogeneity. IJGGC. 2011;5(1):75-87.

14. Yang D, Gu Y, Tontiwachwuthikul P. Wettability determination of the reservoir brine− reservoir rock system with dissolution of CO_2 at high pressures and elevated temperatures. Energy & Fuels. 2007;22(1):504-9.

15. Plug W-J, Bruining J. Capillary pressure for the sand–CO_2–water system under various pressure conditions. Application to CO_2 sequestration. Advances in Water Resources. 2007;30(11):2339-53.

16. Peace software. 2017 [http://www.peacesoftware.de/einigewerte/co2_e.html].

17. Bachu S, Bennion DB. Interfacial tension between CO_2, freshwater, and brine in the range of pressure from (2 to 27) MPa, temperature from (20 to 125) °C, and water salinity from (0 to 334 000) mg· L− 1. Journal of Chemical & Engineering Data. 2008;54(3):765-75.

18. Liu N, Ghorpade SV, Harris L, Li L, Grigg RB, Lee RL, editors. The effect of pressure and temperature on brine-CO_2 relative permeability and IFT at reservoir conditions. In Proceedings of the SPE Eastern Regional Meeting; Morgantown, WV, USA, 13–15 October 2010: SPE: Houston, TX, USA, 2010.

19. Yang D, Tontiwachwuthikul P, Gu Y. Interfacial interactions between reservoir brine and CO_2 at high pressures and elevated temperatures. Energy & Fuels. 2005;19(1):216-23.

20. Jiang L, Yu M, Liu Y, Yang M, Zhang Y, Xue Z, et al. Behavior of CO_2/water flow in porous media for CO_2 geological storage. Magnetic Resonance Imaging. 2017;37:100-6.

21. Ding M, Kantzas A. Capillary number correlations for gas-liquid systems. Journal of Canadian Petroleum Technology. 2007;46(02).

22. Nutt C, editor. The physical basis of the displacement of oil from porous media by other fluids: a capillary bundle model. Proceedings of the Royal Society of London A: Mathematical, Physical and Engineering Sciences; 1982.

23. Gupta R, Mohanty KK, editors. Wettability alteration of fractured carbonate reservoirs. SPE Symposium on Improved Oil Recovery; 2008.

24. Aggelopoulos C, Robin M, Perfetti E, Vizika O. CO_2/$CaCl_2$ solution interfacial tensions under CO_2 geological storage conditions: Influence of cation valence on interfacial tension. Advances in Water Resources. 2010;33(6):691-7.

25. Leelamanie D, Karube J. Soil-water contact angle as affected by the aqueous electrolyte concentration. Soil Science and Plant Nutrition. 2013;59(4):501-8.

26. Wang X, Gu Y. Oil Recovery and permeability reduction of a tight sandstone reservoir in immiscible and miscible CO_2 flooding processes. Industrial & Engineering Chemistry Research. 2011;50(4):2388-99.

27. Rathnaweera T, Ranjith P, Perera M. Effect of salinity on effective CO_2 permeability in reservoir rock determined by pressure transient methods: An experimental study on Hawkesbury sandstone. Rock Mechanics and Rock Engineering. 2015;48(5):2093-110.

28. Li X. Experimental studies on pore wetting and displacement of fluid by CO_2 in porous media [PhD thesis]: University of Edinburgh, Edinburgh, UK; 2015.

9 Chapter 9: Conclusions and Recommendations

9.1 Introduction

Multiphase flow characteristics, during CO_2 geological sequestration and CO_2 enhanced oil recovery projects, are expected to be affected by a range of variable factors; the extent of the effect of each factor can range from a moderate to substantial. In this study, CO_2-water and oil drainage displacements as well as water-CO_2 imbibition displacements were conducted under gaseous, liquid, and supercritical CO_2 conditions to evaluate the impact of the CO_2 phase as well as fluid pressure, temperature, injection rate, and salinity on multiphase flow characteristics. The main conclusions arising from the experiments and subsequent analyses and discussions are summarised as follows:

9.1.1 Gaseous (G)/Liquid (L)/Supercritical (Sc) CO_2-Water Drainage Displacements

During Chapter 4 to 6, GCO_2-water, LCO_2-water, and $ScCO_2$-water drainage displacements were carried out to investigate the effect of fluid pressure, temperature, and CO_2 injection rate on multiphase flow characteristics when CO_2 is injected as a gaseous, liquid, or supercritical state into a water-saturated sandstone core sample, respectively. During the LCO_2-water displacements, the impact of salinity (brine concentration and valency) is also investigated by injecting LCO_2 into a brine (1% wt. NaCl, 5% wt. NaCl, 1% wt. $CaCl_2$) saturated sandstone core sample. The results indicate that the factors investigated can have a moderate to a significant influence on multiphase flow characteristics, namely, the differential pressure profile, production profile (e.g. cumulative produced volumes), endpoint CO_2 effective (relative) permeability, and displacement efficiency (i.e. residual water saturation). The magnitude and the trend of the impact of these factors differ significantly depending on the state of the injected CO_2.

The data indicate that both capillary and viscous forces can moderately to considerably affect multiphase flow characteristics. The impact of these forces is substantially influenced by the state of the injected CO_2. The order of the impact of capillary forces on differential pressure profiles (i.e. multiphase flow characteristics) was as follows: GCO_2-water, $ScCO_2$-water and LCO_2-water displacements. This order indicates an increase in capillary forces impact as CO_2

transforms to a gaseous state. For GCO_2-water displacements, the capillary forces produced cyclic oscillations within the differential pressure and production profiles. Increasing viscous forces impeded the appearance of these oscillations, which indicates that capillary forces worked in an opposite direction to the viscous forces. For $ScCO_2$-water displacements, the results suggest that capillary forces had more impact on differential pressure profiles than viscous forces when fluid pressure and temperature increased. As CO_2 injection rate increased significantly, the impact of the viscous forces become more influential on differential pressure profiles than that of capillary forces. For LCO_2-water displacements, the impact of capillary forces on differential pressure profiles was less than that of viscous forces when fluid pressure, temperature, and CO_2 injection rate increased; however, as salinity (brine concentration and valency) increased the impact of capillary forces became more influential on differential pressure profiles than that of viscous forces. These findings show the conditions when capillary or viscous forces dominate multiphase flow. The increase observed in capillary forces as CO_2 transforms from a supercritical or a liquid state to a gaseous state might cause an increase in the entry pressure according to Young-Laplace equation, thereby increasing storage capacity and security of CO_2 by preventing its upward migration. Nevertheless, this phase transformation to a gaseous state causes a reduction in density, thereby enhancing buoyancy forces which can result in a reduction in storage capacity and security of CO_2 by increasing CO_2 upward migration. In summary, in order to determine the extent of the impact of the CO_2 phase transformation on storage capacity and security of CO_2, the size of the change in both capillary and buoyancy forces is needed to be determined.

The data showed that for all fluid pressures, temperatures, and CO_2 injection rates, the differential pressure profiles of the GCO_2-water displacements are characterized by a sharp increase followed immediately by a sharp reduction, and, finally by a gradual pressure reduction. On the other hand, the differential pressure profiles of the LCO_2-water displacements experienced a sharp increase which was followed by a rather stable pressure reduction for a while; and, then they experienced a high-pressure reduction that was followed by a gradual pressure reduction. Depending on the operational conditions of pressure, temperature, and injection rate, the differential pressure profiles of the $ScCO_2$-water displacements can be either similar to that of GCO_2-water displacements or to that of LCO_2-water displacements.

Gaseous CO_2 experiments experienced the highest differential pressure followed by supercritical and then by liquid displacements. This means that as CO_2 transforms from a supercritical or liquid state to a gaseous state, the energy required for the upward migration of CO_2 becomes higher, which can enhance the security and capacity of CO_2 sequestration.

The data showed oscillations in the differential pressure profiles of both gaseous and supercritical CO_2-displacements but not in that of liquid CO_2-displacements. The appearance and frequency of the oscillations depend on CO_2 state, fluid pressure, temperature, and CO_2 injection rate. For GCO_2-water displacements, the oscillations appeared at low and high fluid pressures. However, for SCO_2-water displacements, the oscillations appeared only at a relatively low fluid pressure (75 bar) as temperature increased. For SCO_2-water displacements, increasing fluid pressure led to the disappearance of the oscillations. For GCO_2-water displacements, increasing both fluid pressure and temperature caused an increase in the frequency of the oscillations. Nevertheless, increasing injection rate (from 0.4 to 1 ml/min) caused the disappearance of the oscillations for GCO_2-water displacement conducted at low pressures (40 bar) but not for those conducted at high pressures (70 bar). The appearance of the oscillations can increase CO_2 residual saturation (due to the re-imbibition process accompanied with these oscillations), thereby increasing the storage capacity and integrity of CO_2. The differential pressure required to open the blocked flow channels during these oscillations can be useful in calculating the largest effective pore diameters and hence the sealing efficiency of the rock. Since these oscillations occurred mainly at gaseous state, thus CO_2 transformation from a supercritical or a liquid state to a gaseous state might result in an increase in residual trapping.

The results showed that the response of the differential pressure profile to the change in the operational conditions is significantly dependent on the state of CO_2 as well as the associated operational conditions. The increase in fluid pressure, temperature, and CO_2 injection rate led to: (I) an increase in the maximum and quasi-differential pressures (the magnitude of the increase is dependent on the concomitant operational conditions) of the GCO_2-water displacements, and (II) an increase in the differential pressures of the LCO_2-water displacements with increasing pressure, salinity, and CO_2 injection rate but caused a slight reduction in the differential pressure during the mixed period with increasing temperature, which followed by an increase during the last period. For $ScCO_2$-water, the increase in fluid

pressure caused a substantial drop in the maximum and quasi-differential pressures while the increase in temperature and CO_2 injection rate caused a considerable increase in them. The decrease in the differential pressure means less energy is required for the displacement or migration of CO_2. Thus, for supercritical displacements increasing pressure can reduce the amount of energy required for CO_2 displacement or migration while increasing temperature can increase the energy required. Thus, the potential reduction in reservoir temperature due to the injection of large quantities of CO_2 might have a preferable impact on energy loss. However, the increase in differential pressure profile observed during gaseous and liquid displacements means that viscous forces dominate multiphase flow in comparison to capillary forces which might lead to better displacement efficiency.

For $ScCO_2$-water, the data show that as fluid pressure increased the differential pressure profiles of the $ScCO_2$-water displacements became similar to those of LCO_2-water displacements. On contrary, increasing temperature caused them to be similar to those of GCO_2-water displacements. Increasing CO_2 injection rate caused the transition of supercritical CO_2 behaviour to gaseous or liquid CO_2 behaviour to occur at lower pressures. The potential increase in the viscous forces and the reduction in the capillary forces with transforming supercritical CO_2 behaviour to a liquid CO_2 behaviour might result in an increase in the storage capacity and displacement efficiency of CO_2 but a reduction in the sealing efficiency of CO_2. The displacement efficiency can increase due to increasing the capillary number and reducing the mobility ratio. The reduction observed in the differential pressure as CO_2 transformed to a liquid CO_2 behaviour means less energy is required for the displacement of fluids in host formations, which can reduce the cost of production significantly.

The data showed that the change in the cumulative produced volumes with the operational conditions is largely dependent on the state of CO_2. For GCO_2-water displacements, increasing fluid pressure, temperature, and CO_2 injection rate caused an increase in the cumulative produced volumes. For LCO_2-water displacements, the cumulative produced volumes: (I) decreased slightly with increasing fluid pressure and salinity, (II) but showed no noticeable change with increasing temperature and injection rate. For $ScCO_2$-water displacements, the increase in fluid pressure led to a reduction in the cumulative produced

volumes while increasing temperature and CO_2 injection rate caused an increase in the cumulative produced volumes.

The results showed a significant impact of the CO_2 phase and the operational conditions on the water displacement efficiency (residual water saturation (S_{wr})) and the endpoint CO_2 relative permeability (K_{rCO2}). The data showed that the water displacement efficiency was in the order of LCO_2>$ScCO_2$> GCO_2 displacement, respectively. Depending on the operational conditions, S_{wr} was in ranges of 0.38-0.42 for GCO_2-water displacements, in ranges of 0.3062-0.384 for LCO_2-water displacements, and in ranges of 0.34-0.41 for $ScCO_2$-water displacements. However, K_{rCO2} was less than 0.25 for GCO_2-water displacements, in ranges of 0.112-0.203 for LCO_2-water displacements, and was less than 0.37 for $ScCO_2$-water displacements. The increase in fluid pressure, temperature, and CO_2 injection rate led to a decline in the S_{wr} of the GCO_2-water displacements. For both LCO_2 and $ScCO_2$-water displacements, increasing fluid pressure and CO_2 injection rate caused a reduction in the S_{wr} while increasing temperature caused an increase in the S_{wr}. For LCO_2-water displacement, increasing salinity caused an increase in the S_{wr}, too. On the other hand, the increase in fluid pressure, temperature, and CO_2 injection rate led to an increase in the K_{rCO2} of the GCO_2-water displacements but a reduction in that of LCO_2-water displacements. For SCO_2-water displacements, increasing fluid pressure and CO_2 injection rate caused an increase in the K_{rCO2}. With increasing temperature, the K_{rCO2} showed a declining trend at high fluid pressures (90 bar) but an increasing trend at low fluid pressures (75 bar).

9.1.2 CO_2-Oil Drainage Displacements

In this chapter, the effect of the CO_2 phase, fluid pressure, experimental temperature and CO_2 injection rate on multiphase flow characteristics were investigated when CO_2 in its gaseous, liquid, or supercritical state is flooded an oil-saturated Berea sandstone core sample. The results showed a moderate to a significant impact for the factors investigated on the differential pressure profile, cumulative produced volumes, endpoint CO_2 effective and relative permeabilities, and oil recovery. The trend (i.e. increase or decrease) and the size of the change are dependent significantly on the phase of CO_2 as well the fluid pressure range for GCO_2-displacements. The data indicate that with increasing fluid pressure, the capillary forces had a stronger impact on the differential pressure profiles of supercritical

CO_2-oil displacements than on that of subcritical CO_2-oil displacements. With increasing temperature and injection rates, the viscous forces became more dominant than capillary forces.

For all fluid pressures, temperature, and CO_2 injection rates, the differential pressure profile is characterized by a strong increase, followed by a high reduction to the value of quasi-differential pressure. The rate of the increase and reduction in the differential pressure depends on the CO_2 phase and the fluid pressure range for the GCO_2-displacements. In general, liquid CO_2-displacements gave the highest differential pressure magnitude, which indicates a higher energy is required for the displacement of oils in cold environments where CO_2 exists in a liquid state, e.g. West Sak reservoir.

Increasing fluid pressure caused an increase in the differential pressure profile of the subcritical CO_2 displacements but a reduction in that of the supercritical CO_2 displacements. In addition, increasing fluid pressure for low-fluid pressure GCO_2 displacements increased the frequency of the oscillations in the differential pressure and reduced the entry pressure and its associated time. This implies that for reservoirs with supercritical CO_2 conditions, the reduction in the differential with increasing pressure means that maintaining the reservoir pressure at its highest possible level would result in reducing the energy loss, for the displacement of oil to producing wells, to its lowest level.

On the other hand, increasing temperature caused a reduction in the differential pressure profile of gaseous, liquid, and supercritical CO_2 displacements but caused the appearance of the pressure oscillations only in the gaseous and supercritical CO_2 displacements. The appearance of oscillations with increasing temperature means that as temperature increases the residual trapping due to capillary forces increases; consequently, a possible reduction in the reservoir temperature due to CO_2 injection would result in reducing the impact of capillary forces, thereby increasing displacement efficiency.

Nonetheless, increasing CO_2 injection rate caused a substantial increase in the differential pressure of gaseous, liquid, and supercritical CO_2 displacements. This shows a considerable reduction can occur in the formation energy as the injection rate increases during multiphase flow flooding. Thus, an optimization evaluation is required to determine the optimum

injection rate that leads to the highest displacement efficiency and the least reduction in the reservoir energy.

The increase in fluid pressure caused an increase in the cumulative produced volumes of low-fluid pressure GCO_2 displacements but a reduction in that of high-fluid pressure GCO_2, LCO_2, and SCO_2 displacements. Increasing fluid pressure reduced the time required to achieve the majority of the oil production; this is useful in terms of achieving economical revenues during less time period. However, increasing temperature caused an increase in the cumulative produced volumes; the lowest increase occurred in LCO_2-oil displacements.

Residual oil saturation (S_{or}) was in ranges of around 0.44 to 0.7; liquid CO_2 gave the lowest and low-fluid pressure gaseous CO_2 gave the highest. Endpoint CO_2 relative permeability (K_{rCO2}) was in ranges of about 0.015 to 0.657; supercritical CO_2 gave the highest and low-pressure gaseous CO_2 gave the lowest. Increasing fluid pressure caused the K_{rCO2} of liquid CO_2 to decrease but that of gaseous and supercritical CO_2 to increase. However, increasing fluid pressure caused the S_{or} to decrease for the subcritical CO_2 displacements but to increase for the supercritical CO_2 displacements. On the other hand, increasing the experimental temperature caused the K_{rCO2} of the gaseous, liquid, supercritical CO_2-displacements to increase. However, it caused the S_{or} to increase for liquid CO_2 displacements but to decrease for gaseous and supercritical CO_2 displacements. Increasing the CO_2 injection rate caused the K_{rCO2} of the gaseous, liquid, and supercritical CO_2-displacements to increase and the S_{or} to decrease.

9.1.3 Water- CO_2 Imbibition Displacements

In this chapter, the effect of the CO_2 phase, fluid pressure, experimental temperature, and salinity on multiphase flow characteristics of water-CO_2 imbibition displacements were investigated. These imbibition displacements were performed by injecting deionised water or brine solution (1 wt. % $CaCl_2$) to displace CO_2 (as a gaseous, liquid, or supercritical CO_2 state) from a sandstone core sample. The results indicated a slight to considerable influence of the factors investigated on the differential pressure profile, endpoint water effective (relative) permeability, and endpoint water saturation (i.e. residual CO_2 saturation). The magnitude of the change depends significantly on the state of CO_2. Endpoint water relative

permeability (K_{ew}) was in ranges of 0.174 to 0.711 while endpoint water saturation (S_{ew}) was in ranges of 0.55 to 0.94.

For gaseous, liquid, and supercritical CO_2 imbibition displacements, increasing fluid pressure and temperature as well as using brine solution instead of deionised water resulted in a considerable reduction in the differential pressure profile (from 4 to 36%). The magnitude of the reduction depends largely on the CO_2 state; the highest change occurred in liquid CO_2 imbibition displacements. The reduction in the differential pressure with increasing pressure and temperature means that as CO_2 travels upward formation and hence pressure and temperature decrease, then more and more energy will be required to displace CO_2 out of the system, which can increase the security of CO_2 storage. Similarly, reducing the salinity of formation fluids would increase CO_2 storage security. A potential reduction in formation fluids salinity might occur upon the injection of large quantities of low salinity brine.

Increasing fluid pressure led to an increase in both K_{ew} and S_{ew} for gaseous, liquid, and supercritical CO_2 imbibition displacements; the magnitude of the increase in K_{ew} and S_{ew} is dependent on the CO_2 phase. For all CO_2 imbibition displacements, increasing temperature caused a reduction in the S_{ew} from 1 to 23%; on the other hand, increasing temperature caused a considerable reduction in the K_{ew} of the subcritical CO_2 displacements but caused an increase in the K_{ew} of the supercritical CO_2 displacements. For gaseous and supercritical CO_2 core flooding, using brine (1wt.% $CaCl_2$) instead of deionised water produced a reduction in the endpoint brine relative permeability and an increase in the endpoint brine saturation; however, for liquid CO_2 displacements, using brine (1wt.% $CaCl_2$) caused a significant increase in the endpoint brine relative permeability and a high reduction in the endpoint brine saturation.

9.2 Recommendations

For all drainage and imbibition displacements, having accurate measurements of the interfacial tensions and contact angle data at the experimental conditions will provide a more accurate insight into the impact of capillary forces on multiphase flow characteristics investigated. Performing the displacements at very low injection rates (less than 0.1 ml/min) can reduce the impact of viscous forces; hence, more light can be shed on the impact of the capillary forces on the differential pressure profiles as a function of the CO_2 state.

The effect of the CO_2 phase can be investigated in more depth by conducting experiments under higher pressure and temperature conditions as well as using different sandstone and carbonate samples with a wide range of permeabilities, different wetting conditions, and different brines and concentrations. It would be more useful if the impact of the CO_2 phase on relative permeability and capillary pressure-saturations curves is explored under steady state and unsteady state conditions.

In the water-CO_2 imbibition displacements, only one brine solution with low concentration (1% wt. $CaCl_2$) was investigated. Thus, it would be more useful if a wide range of single brine solutions, formations waters, and sea waters are explored.

The differential pressure profile of the supercritical CO_2 displacements showed a transition towards the behaviour of gaseous CO_2 displacements with increasing temperature and a transition towards the behaviour of liquid CO_2 displacements with increasing fluid pressure. This phenomenon might need further investigation under a wider range of pressure and temperature conditions.

A. Appendix A: Contact Angle on Flat Glass Surfaces and Inside Glass Capillaries

A.1 Introduction

Characterisation of multiphase flow is of a high practical importance in many engineering fields such as CO_2 sequestration and CO_2 enhanced oil recovery projects. The multiphase flow is considerably influenced by the capillary forces that depend on the liquid-liquid and gas-liquid interfacial tensions, system wettability (i.e. contact angle) and pore diameter. The system wettability depends on the chemical and physical properties of the fluids and the surfaces involved [1], including brine concentration, valency, pH level and geometry of the surface [2-6].

Despite its significant impact on the system wettability, the influence of electrolyte concentrations on the equilibrium contact angle is very rarely studied [7, 8], more information can be found in Appendix B- Section B.2.3. Moreover, to the best of our knowledge, no study has been reported for the effect of electrolyte concentrations on the equilibrium static contact angle inside glass capillary tubes. This is important because the contact angle inside capillary porous media has been proposed in many simulations and model studies as an equivalent to the contact angle on flat surfaces [9]. However, a recent study by Li and co-workers found that the contact angles inside capillary tubes for deionised water, 1-propanol, n-decane and crude oil are different from their contact angles measured on flat surfaces [9]. The aim of this study is to extend these investigations to the salts that commonly exist in saline and formation waters.

In this study, the static contact angles on flat glass surfaces have been explored as a function of brine concentrations, while the static contact angles inside glass micro-tubes have been studied as a function of pore diameter and brine concentrations of these monovalent (NaCl, KCl) and divalent brine ($CaCl_2$ and $MgCl_2$) solutions. The concentrations ranged from 0.001 to 6 molarity (M) under ambient conditions, depending on the salt investigated, while the capillary tubes' inner diameters ranged from 100-1000 µm.

A.2 Results and Discussion

This study consists of two sections. The first section deals with the impact of the electrolyte concentration of sodium chloride (NaCl), potassium chloride (KCl), and calcium chloride

dihydrate ($CaCl_2 \cdot 2H_2O$) on contact angles on flat glass surface. The second section deals with the impact of the electrolyte concentration and pore diameter on contact angles insides micro-glass tubes. For glass capillary tubes, all three salts, in addition to magnesium chloride hexahydrate ($MgCl_2 \cdot 6H_2O$), were used.

A.2.1 Effect of Electrolyte Concentration on Contact Angle on Flat Glass Surfaces

Figure A-1 shows the effect of electrolyte concentration of NaCl, KCl, and $CaCl_2 \cdot 2H_2O$ on the static contact angle on flat glass surfaces.

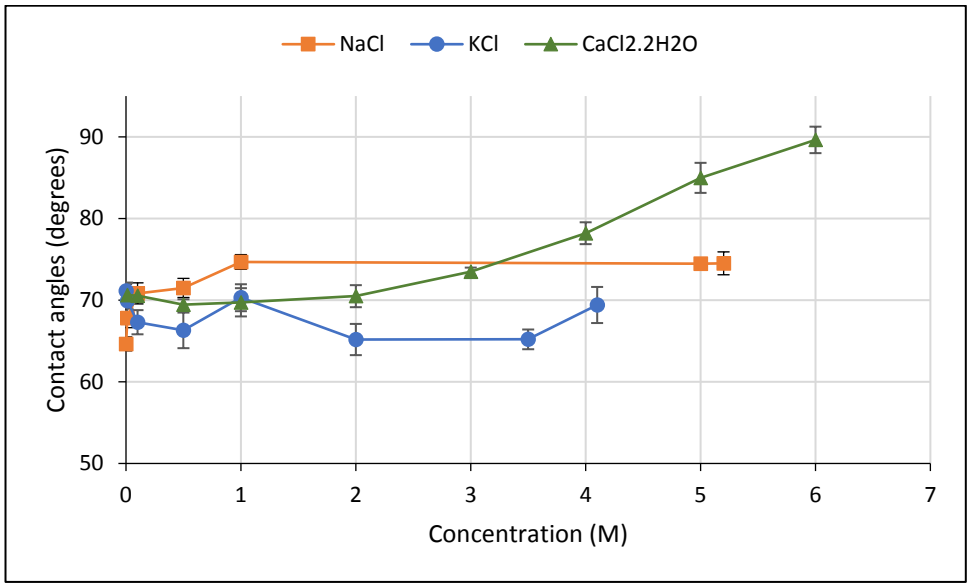

Figure A-1: Contact angles on flat surfaces as a function of concentration for NaCl, KCl, and $CaCl_2 \cdot 2H_2O$ brine solutions

The contact angle of NaCl and $CaCl_2 \cdot 2H_2O$ increased as the electrolyte concentrations increased but the relationship was not linear. The overall increase in the contact angle was about 10° for the NaCl brine solutions and around 20° for the $CaCl_2$ brine solutions. The greatest increase in the contact angles was observed with concentrations less than 1 M for the NaCl solutions but higher than 2 M for the $CaCl_2$ solutions. Qualitatively, the trend of our NaCl data agrees very well with the trend of the NaCl data obtained by Leelamanie and Karube [8]. On the other hand, increasing the concentration of KCl solutions was not accompanied by observable changes in the contact angles. The contact angles had almost a constant value, around 67 °, as shown in Figure A-1, independently of the brine concentration. A likely reason is that the impact of K^+ cations on surface tension is not as

great as that of Na^+ and Ca^{2+} cations [10]. In summary, the general trend for the contact angles on flat glass surfaces is in the order of $CaCl_2$> NaCl> KCl solutions, as shown in Figure A-1. This trend agrees well with the arrangement of cations according to their impact on the surface tension [10].

The addition of inorganic salts to pure water leads to an increase in the surface tension of a water-air system [7, 8, 10-12]. This increase in the surface tension can be related to the preferred position of the cations in the aqueous phases as well as the force balance at the three-phase contact line of an electrolyte drop placed on a glass surface [8, 10]. The cations have the inclination to stay and accumulate in the bulk phase rather than in the vapour-liquid interface. Hence, the solvation of cations attracts the water molecules to the bulk phase. The attraction of cations increases when the cation concentration and the ratio of cation charge z^+ to cation surface area r^2 increase [10]. The cations below are arranged in order of their impact on the increase in surface tension: Cs^+<Rb^+<NH_4^+<K^+<Na^+<Li^+<Ca^{2+} Mg^{2+} [10].

According to the well-known Young's equation (1805), the equilibrium contact angle depends on the free energies of the solid-vapour, liquid-vapour, and solid-liquid interfaces. The force balance at the mechanical equilibrium is:

$$\gamma_{LV}\cos\theta = \gamma_{SV}\text{-}\gamma_{SL} \quad \text{(A-1)}$$

where Θ is Young's contact angle and γ_{LV}, γ_{SV}, γ_{SL} are the free energies of the liquid-vapour, solid-vapour, and solid-liquid interfaces. Based on Eq. A-1, the increase in the solid surface free energy (γ_{SV}) will act in favour of the spreading of the electrolyte drop on the glass substrates, while the increase in the liquid free energy (γ_{LV}) and the interfacial free energy of the solid-liquid (γ_{SL}) will oppose it. In a situation where the solid surface energy is constant, the increase in the liquid free energy would result in increasing the contact angle. Subsequently, the increase observed in the contact angle, as shown in Figure A-1, was related to the increase in the surface tension with increasing electrolyte concentration.

The surface tension of electrolyte solutions increases with increasing concentration up to high salinities [13, 14], as shown in Figure A-2. Ozdemir et al. noticed that the surface tension of NaCl was higher than that of KCl, with increasing concentration up to saturation [13]. Since the contact angle is positively related to the increase in surface tension, the contact angle is also expected to increase as the concentration increases up to high salinities. However, in

this study, the response of the contact angle was not only dependent on the electrolyte concentration but also on the type of the salt investigated, as illustrated above. This result suggests that in addition to the impact of increasing surface tension with increasing electrolyte concentration, another factor (the adsorption of ions) might have influenced the trend of contact angles.

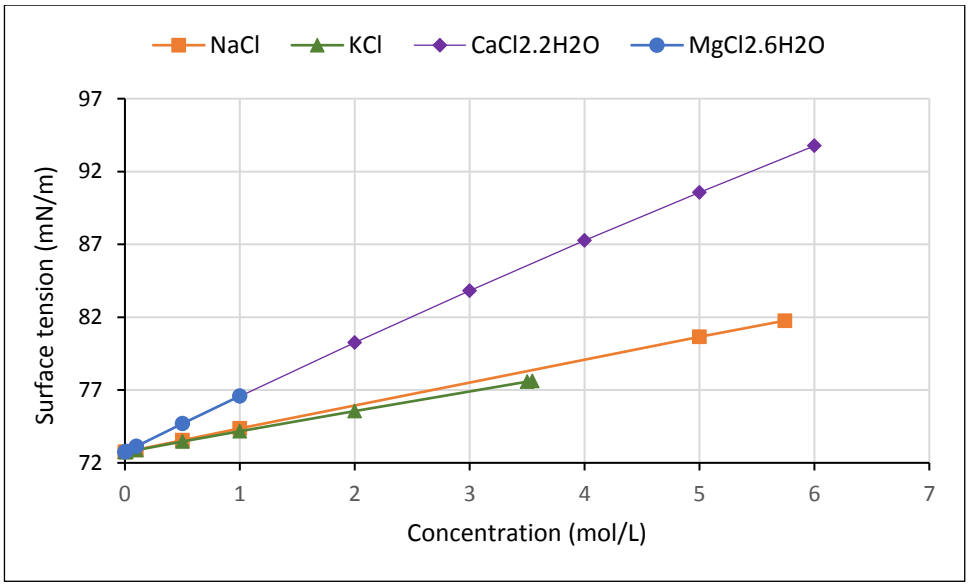

Figure A-2: Surface tension dependence on concentration of (a) NaCl, (b) KCl, (c) $CaCl_2 \cdot 2H_2O$ and $MgCl_2 \cdot 6H_2O$ calculated at 20 °C from Clegg et al. [14]

The adsorption of ions depends on the surface charge, which, in turn, depends on the ionic strength and pH level of the solution [15]. The adsorption of ions on the interface will result in decreasing the interfacial free energy of the solid-liquid interface [8], and, therefore, decreasing the contact angle (Eq. A-1). Table A-1 shows the pH levels of the brines investigated as a function of salt concentrations; a SveenCompat pH meter s210 was used to measure the pH level. With increasing the salt concentration, the pH showed an increasing trend for NaCl, an almost constant trend for KCl, and a declining trend for both $CaCl_2$ solutions. For the NaCl solutions, the highest increase in the pH level occurred as the electrolyte concentration increased from 0.5 to 1 M. In general, the pH of the NaCl solutions was around 6.6 for concentrations less than or equal to 0.5 M and around 8.6 for concentrations higher than or equal to 1 M. Shu et al. also observed an increasing trend for pH level as NaCl concentration increases and a decreasing trend as $CaCl_2$ concentration increases [16]. Thus, based on the measured pH data, the glass surface charge is negative for

all solutions investigated, but the density of the surface charge is dependent on the pH level and the electrolyte solution concentration.

Table A-1: PH readings

NaCl		***KCl***		***$CaCl_2 \cdot 2H_2O$***	
Concentration (M)	***pH***	***Concentration (M)***	***pH***	***Concentration (M)***	***pH***
0.001	6.38	0.001	9.94	0.001	8.31
0.01	6.57	0.01	8.95	0.01	8.51
0.1	6.8	0.1	10.1	0.1	6.71
0.5	6.55	0.5	10.08	0.5	6.1
1	8.14	1	9.85	1	6.05
5	8.55	2	10.09	2	6.22
5.2	9.06	3.5	9.72	3	5.6
		4.1	9.49	4	5.53
				5	4.9
				6	4.48

The surface charge density of silica particles increases with increasing pH level or the bulk salt concentration [17-19]. The surface charge of a glass and silica surface is acquired mainly by the dissociation of silanol group [15] as follows:

$$SiOH \rightleftharpoons SiO^- + H^+ \quad \text{(A-2)}$$

The increase in pH level causes a reduction in the bulk concentration of hydrogen ions (H^+), which leads to a lower concentration of H^+ ions on the solid surface. As the concentration of H^+ decreases with increasing concentration, more negatively charged SiO^- ions are dissociated from the functional group SiOH, leading to a higher negative surface charge density [17].

The degree of dissociation and the surface charge density depend on the equilibrium between the electrolyte concentrations at the glass surface and the free ions in the bulk electrolyte [15]. For instance, generally, the increase in electrolyte concentration of NaCl brine results in increasing the number of Na^+ ions and decreasing the number of H^+ ions. Hence, with increasing electrolyte concentration, more Na^+ ions are attracted to the negatively charged glass substrates. The increased number of Na^+ ions excludes H^+ ions,

leading to a lower concentration of H^+ ions on the glass surface and, therefore, a higher negative surface charge density [17].

For NaCl solutions, the pH increased as the electrolyte concentration increased, and, therefore, the negative charge density of the glass surface is expected to increase, as shown in Figure A-3 for KCl solutions. Increasing the negative surface charge density leads to an increase in the adsorption of the ions on the solid-liquid interface and hence reducing the solid-liquid interfacial energy, which will result in decreasing the contact angle, according to Eq. A-1. The smallest increase in the contact angle of NaCl solutions occurred when the concentration exceeded 1 M. This is because the increase in the contact angle is the net result of the increase in surface tension and the large reduction in the solid-liquid interfacial energy, which occurred because of the large increase in the glass surface charge density due to the large rise in the pH level after 1 M.

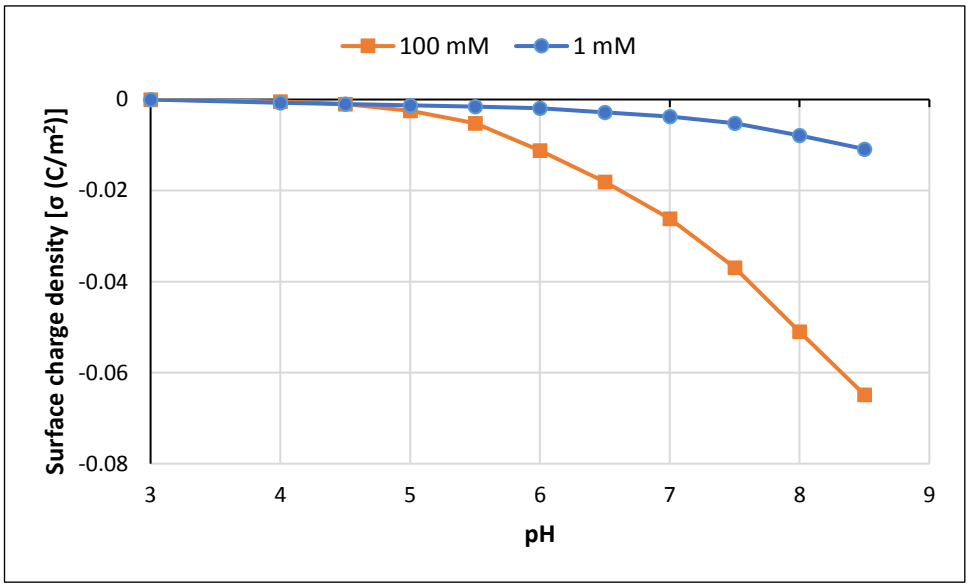

Figure A-3: Surface charge density of a flat silica surface as a function of pH in 1 and 100 mM KCl solutions from [17]

For the $CaCl_2$ solutions, the pH decreased as the concentration increased, and, hence, the negative surface charge density is expected to be reduced. The largest increase in contact angle occurred as the concentration exceeded 2 M, which can be associated with the largest reduction in the pH level after 2 M. This suggests that the sharp increase in the contact angle was due to the simultaneous effect of increasing the electrolyte surface tension and reducing the strength of the negative surface charge density due to the pH reduction. On the other

hand, the pH level was the highest for KCl solutions. This high pH level would indicate a strong negative charge density of the solid surface, as shown in Figure A-3. Thus, as the KCl concentration increased, the negative surface density of the glass substrate might have increased [17]. Consequently, since the surface tension of the KCl is the lowest and its negative surface charge density is the highest, it is expected that the increase in contact angle due to increasing concentration might have been opposed by the reduction in the solid-liquid interfacial energy. Thus, the result was an almost constant trend for KCl contact angles.

A.2.2 Effect of Pore Size and Electrolyte Concentration on Static Pore Contact Angles

According to the Young-Laplace equation, the capillary pressure depends on the surface tension, contact angle and pore diameter. Hence, it would be of utmost importance to investigate the relationship between the contact angle and the pore diameter for a range of surface tensions.

Figure A-4 to Figure A-7 show the effect of electrolyte concentration of NaCl, KCl, $CaCl_2$, and $MgCl_2$ solutions on the static contact angle inside glass pores. The data are only presented for concentrations less than 1M. At higher concentrations; no clear relationship between contact angles and capillary inner diameters were observed. Overall, the increases in brine concentration caused no observable change in the static contact angle inside the capillaries for the investigated inner diameters ranging from 100 to 1000 µm. When the concentrations increased from 0.001 to 1 M, all the brines investigated showed similar trends, as shown in Figure A-4 to Figure A-7. Nonetheless, increasing the KCl concentration to 1 M results in increasing the contact angle by about 5° and causes the emergence of a fairly constant trend, despite the change in the size of the capillaries' inner diameter.

The results also showed that decreasing the inner diameters of the capillaries led to a small increase in the contact angles. Similarly, Li et al. observed an increase in contact angle as the pore diameter decreased from 1000 to 300 µm [9]. In this study, as the pore diameters decreased from 1000 to 100 µm, the pore contact angle increased by around 5°. The most obvious increase in the contact angles can be seen with capillaries having an inner diameter of less than 400 µm. For inner diameters ranging from 400 to 600 µm, the contact angle

decreased slightly. After 600 µm, the contact angle approached almost 25°, independently of the capillary inner diameter size.

Since almost all the brine solutions investigated experienced a nearly similar trend for a wide range of concentrations (≤ 1 M), this might suggest that surface tension is not the main factor that governs contact angle inside capillary tubes and another factor might have influenced the trend of contact angles. This assumption is because the wetting of the surface depends not only on its chemical properties but also on its physical properties (surface roughness, shape, and particle size) [6].

Wenzel observed that the geometry of the surface had a more influence on the static contact angle than the chemistry [6]. Many investigators have reported that the contact depends on the curvature of the three-phase line [9, 20-23]. Good and Koo reported a good agreement between their theoretical and experimental work when they included the effect of the curvature of the three-phase line on contact angle [21]. However, the mechanism of contact angle dependence on the curvature of the three-phase line is not clear [20, 24], as many investigators attribute the curvature effect to the line tension [25-27], while others attribute it to the adsorption at the solid-liquid interface [20, 22, 23]. Neumann observed that the contact angle decreased by 3° to 5° as the radius of the of the three-phase contact line increased from 1 to 5 mm [26]. Duncan, Li et al observed a reduction in the contact angle with increasing the radius of the three-phase contact line [27]; this was interpreted in terms of the line tension. Duncan's observation might explain the observed reduction of our contact angle data with increasing pore diameter.

The data showed also a linear correlation of the meniscus height with the pore inner diameter for the brines and concentrations investigated, as shown in Figure A-8. Extrand and Moon noticed that the critical meniscus height around PTFE and PC rods increased with the rod diameter [28]. The linear correlation obtained is as follows:

$$\mathrm{h} = 0.3249 \times \mathrm{d}\text{-}4.6203 \qquad \text{(A-3)}$$

where *h* is the meniscus height and *d* is the capillary tube's inner diameter. By substituting Eq. A-3 into Cheong et al.'s equation, Eq. 3-1 in Chapter 3, the contact angle of the brines investigated can be calculated when only the glass tube inner diameter is known. The constants in Eq. A-3 might not depend only on the properties of the fluids and solid surface investigated, but also on the wetting status of the porous material. This correlation is of

utmost importance as it would enable the calculation of a porous material's wettability once its pore size distributions are known. However, this correlation needs to be further studied with other fluids.

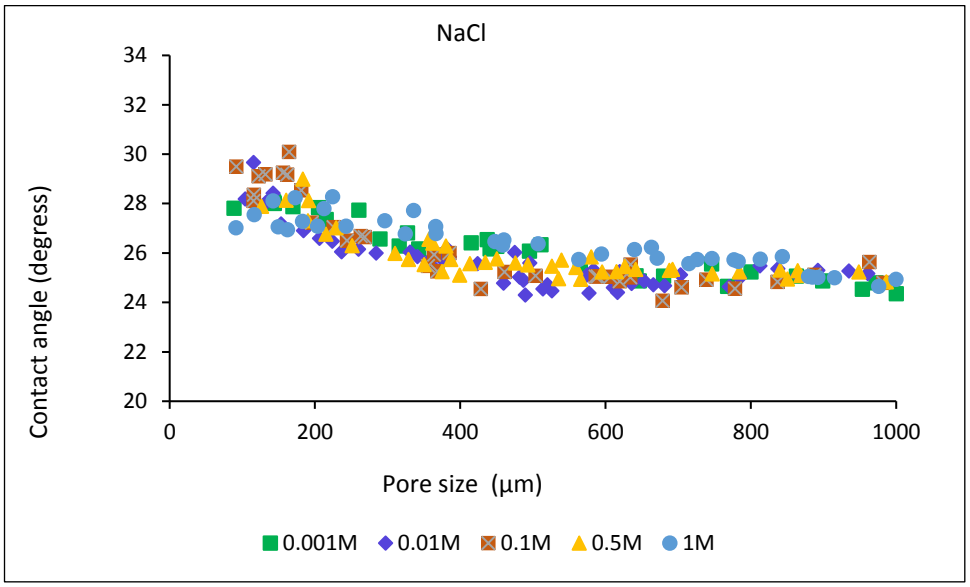

Figure A-4: Effect of capillary inner diameters on NaCl contact angles

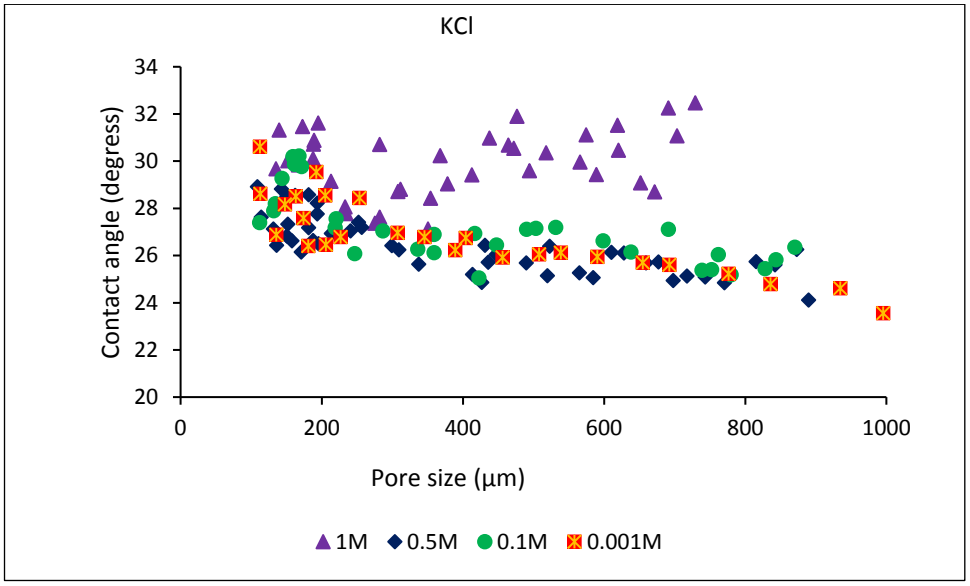

Figure A-5: Effect of capillary inner diameters on KCl contact angles

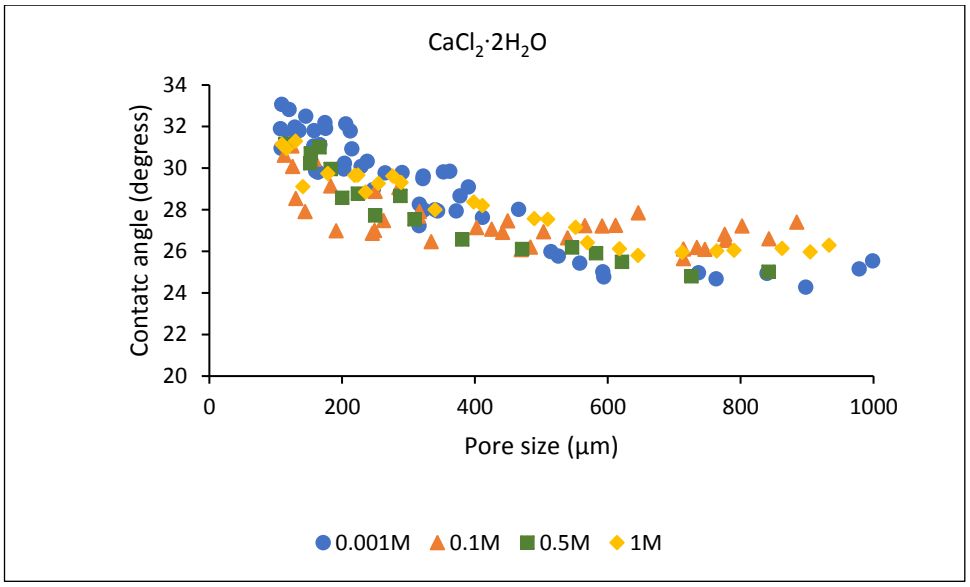

Figure A-6: Effect of capillary inner diameters on $CaCl_2 \cdot 2H_2O$ contact angles

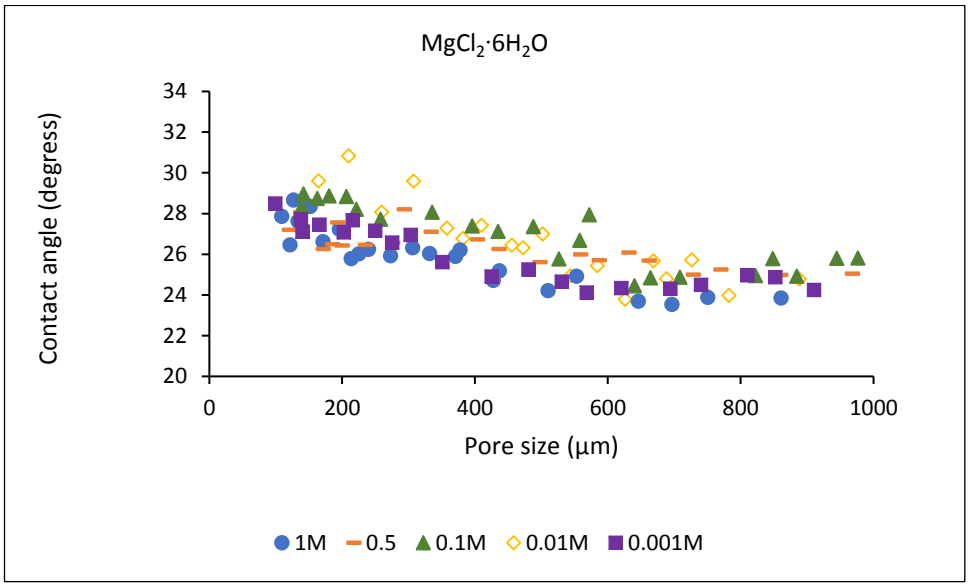

Figure A-7: Effect of capillary inner diameters on $MgCl_2 \cdot 6H_2O$ contact angles

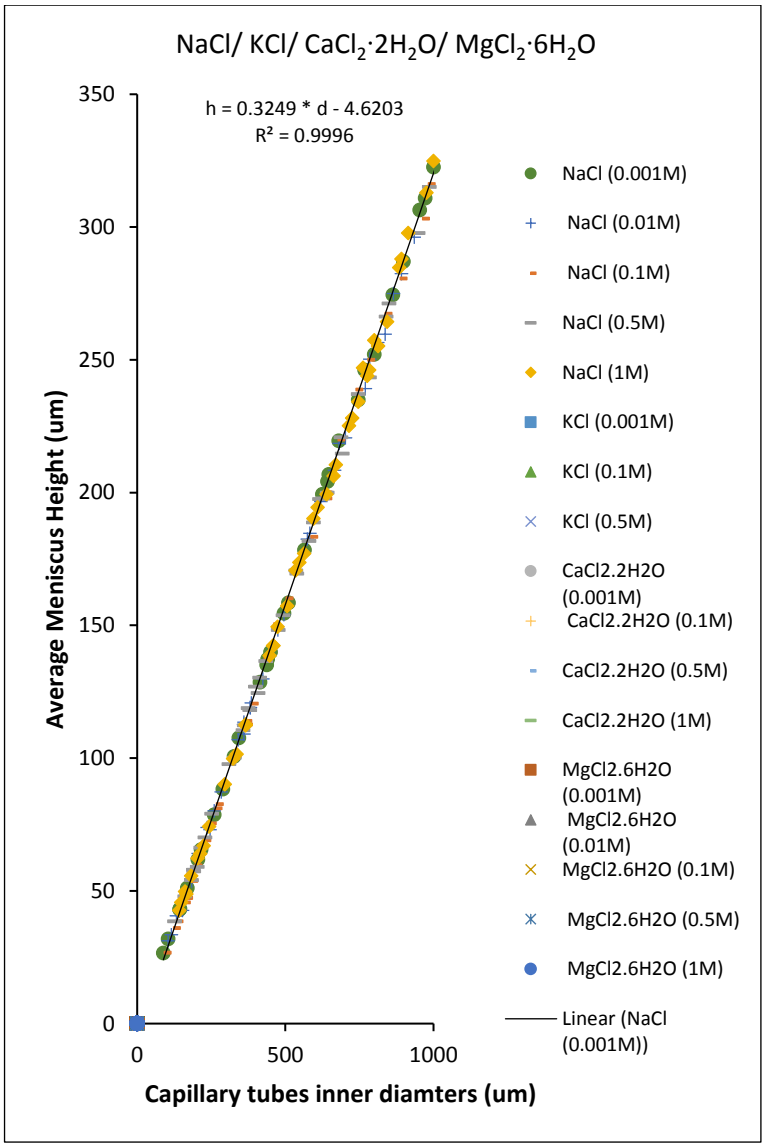

Figure A-8: Average meniscus height against capillary inner diameters of NaCl/ KCl/ $CaCl_2 \cdot 2H_2O$ /$MgCl_2 \cdot 6H_2O$

A.3 Summary

In this study, the static contact angles on flat glass surfaces have been explored as a function of brines concentrations, while the static contact angles inside micro-glass tubes have been studied as a function of the pore diameter and brines concentrations for monovalent (NaCl and KCl) and divalent brine ($CaCl_2$ and $MgCl_2$) solutions. The concentrations ranged from 0.001 to 6 M under ambient conditions, depending on the salt investigated; while the capillary tubes' inner diameters ranged from 100-1000 µm.

- A linear correlation (*h= 0.3249×d – 4.6203*) between the micro-glass tube inner diameter and the meniscus height was obtained for the above solutions for concentration of less than or equal to 1 M. This correlation can be used with the Cheong's equation to calculate the contact angle of the solutions investigated when only the micro-glass pore diameter is known.

- The contact angles on flat glass surfaces (≈ 63-90°) are much higher than contact angles inside glass capillaries (≈24-33°).

- With increasing salt concentration, the overall increase in the contact angle on flat surfaces was about 10° for NaCl and 20° for $CaCl_2$ solutions. However, the increase in KCl concentration was not accompanied by any change in the contact angles. The general trend for the contact angle on flat glass surfaces is in the order of $CaCl_2$> NaCl> KCl solutions.

- Increasing salt concentrations had no influence on contact angles inside capillaries for the investigated inner diameters ranging from 100 to 1000 µm.

- Decreasing the inner diameters of the capillaries led to a small increase in the contact angles. The most obvious increase in the contact angles could be seen with capillaries having an inner diameter of less than 400 µm. For inner diameters ranging from 400 µm to 600 µm, the contact angle decreased slightly. After 600 µm, the contact angle approached almost 25°, independently of the capillary inner diameter size.

- The measured pH data showed that the increase in NaCl concentration led to an increase in the pH, while the increase in $CaCl_2 \cdot 2H_2O$ concentration led to a decrease in the pH. The increase in KCl concentration caused no change in the pH.

- It was concluded that both pH and surface tension have an impact on the contact angle data on a flat glass surface.

Some of these conclusions are based on equilibrium contact angles measured inside capillary tubes diameters ranging from 100 to 1000 µm. Thus, it is important for further studies to

investigate the impact of capillary diameters on contact angle for diameters less than 100 µm and under reservoir conditions.

A.4 References

1. Chaudhuri RG, Paria S. Dynamic contact angles on PTFE surface by aqueous surfactant solution in the absence and presence of electrolytes. Journal of colloid and interface science. 2009;337(2):555-62.

2. Wu S, Firoozabadi A. Effect of salinity on wettability alteration to intermediate gas-wetting. SPE Reservoir Evaluation & Engineering. 2010;13(02):228-45.

3. Zhang P, Tweheyo MT, Austad T. Wettability alteration and improved oil recovery in chalk: The effect of calcium in the presence of sulfate. Energy & Fuels. 2006;20(5):2056-62.

4. Zhang P, Austad T. Wettability and oil recovery from carbonates: Effects of temperature and potential determining ions. Colloids and Surfaces A: Physicochemical and Engineering Aspects. 2006;279(1):179-87.

5. Tweheyo MT, Zhang P, Austad T, editors. The effects of temperature and potential determining ions present in seawater on oil recovery from fractured carbonates. SPE/DOE Symposium on Improved Oil Recovery; 2006: Society of Petroleum Engineers.

6. Chau T, Bruckard W, Koh P, Nguyen A. A review of factors that affect contact angle and implications for flotation practice. Advances in Colloid and Interface Science. 2009;150(2):106-15.

7. Sghaier N, Prat M, Nasrallah SB. On the influence of sodium chloride concentration on equilibrium contact angle. Chemical Engineering Journal. 2006;122(1):47-53.

8. Leelamanie D, Karube J. Soil-water contact angle as affected by the aqueous electrolyte concentration. Soil Science and Plant Nutrition. 2013;59(4):501-8.

9. Li X, Fan X, Brandani S. Difference in pore contact angle and the contact angle measured on a flat surface and in an open space. Chemical Engineering Science. 2014;117:137-45.

10. Chalbaud C, Robin M, Lombard JM, Martin F, Egermann P, Bertin H. Interfacial tension measurements and wettability evaluation for geological CO_2 storage. Advances in Water Resources. 2009;32(1):98-109.

11. Cutts RE. Experimental investigation of the influence of surface energy and pore fluid characteristics on the behavior of partially saturated coarse-grained soils. 2009.

12. Ali K, Shah A-u-HA, Bilal S, Shah A-u-HA. Surface tensions and thermodynamic parameters of surface formation of aqueous salt solutions: III. Aqueous solution of KCl, KBr and KI. Colloids and Surfaces A: Physicochemical and Engineering Aspects. 2009;337(1-3):194-9.

13. Ozdemir O, Karakashev SI, Nguyen AV, Miller JD. Adsorption and surface tension analysis of concentrated alkali halide brine solutions. Minerals engineering. 2009;22(3):263-71.

14. Clegg SL, Brimblecombe P, Anthony S. Wexler. Surface tensions of inorganic multicomponent aqueous electrolyte solutions and melts 2010 [Available from: http://www.aim.env.uea.ac.uk/aim/aim.php.

15. Behrens SH, Grier DG. The charge of glass and silica surfaces. The Journal of Chemical Physics. 2001;115(14):6716-21.

16. Shu L, Obagbemi IJ, Liyanaarachchi S, Navaratna D, Parthasarathy R, Aim RB, et al. Why does pH increase with $CaCl_2$ as draw solution during forward osmosis filtration. Process Safety and Environmental Protection. 2016;104:465-71.

17. Barisik M, Atalay S, Beskok A, Qian S. Size dependent surface charge properties of silica nanoparticles. 2014.

18. Dunér G, Iruthayaraj J, Daasbjerg K, Pedersen SU, Thormann E, Dėdinaitė A. Attractive double-layer forces and charge regulation upon interaction between electrografted amine layers and silica. Journal of colloid and interface science. 2012;385(1):225-34.

19. Kobayashi M, Juillerat F, Galletto P, Bowen P, Borkovec M. Aggregation and charging of colloidal silica particles: Effect of particle size. Langmuir: the ACS journal of surfaces and colloids. 2005;21(13):5761-9.

20. Ward C, Wu J. Effect of contact line curvature on solid-fluid surface tensions without line tension. Physical review letters. 2008;100(25):256103.

21. Good RJ, Koo M. The effect of drop size on contact angle. Journal of Colloid and Interface Science. 1979;71(2):283-92.

22. Wu J, Farouk T, Ward C. Pressure dependence of the contact angle. The journal of physical chemistry B. 2007;111(22):6189-97.

23. Ward C, Sefiane K. Adsorption at the solid-liquid interface as the source of contact angle dependence on the curvature of the three-phase line. Advances in colloid and interface science. 2010;161(1):171-80.

24. Vafaei S, Podowski M. Theoretical analysis on the effect of liquid droplet geometry on contact angle. Nuclear engineering and design. 2005;235(10):1293-301.

25. Gaydos J, Neumann A. The dependence of contact angles on drop size and line tension. Journal of colloid and interface science. 1987;120(1):76-86.

26. Li D, Neumann A. Determination of line tension from the drop size dependence of contact angles. Colloids and Surfaces. 1990;43(2):195-206.

27. Duncan D, Li D, Gaydos J, Neumann A. Correlation of line tension and solid-liquid interfacial tension from the measurement of drop size dependence of contact angles. Journal of Colloid and Interface Science. 1995;169(2):256-61.

28. Extrand C, Moon SI. Critical meniscus height of liquids at the circular edge of cylindrical rods and disks. Langmuir: the ACS journal of surfaces and colloids. 2008;25(2):992-6.

B. Background Information

B.1 Contact Angle Formulas

In literature, there are a wide range of formulations that are proposed for contact angle calculations such as Young's equation, Wenzel's equation, Cassie- Baxter's equation and Drelich et al.'s theoretical correlation. However, Young's equation is the most widely used formula [1, 2]. This equation relates the contact angle to the interfacial tension energies of the three phases (solid-liquid-vapour), as shown in Figure B-1.

$$\cos\theta = \frac{\gamma_{SV}-\gamma_{SL}}{\gamma_{LV}} \quad \text{(B-1)}$$

where Θ is Young's contact angle, γ_{SV} the solid-vapour surface tension, γ_{SL} the solid-liquid surface tension, and γ_{LV} the liquid-vapour surface tension. γ_{SL} and γ_{LV} will act in favour of shrinking the liquid droplet on the solid surface while γ_{SV} will act in favour of spreading it [3].

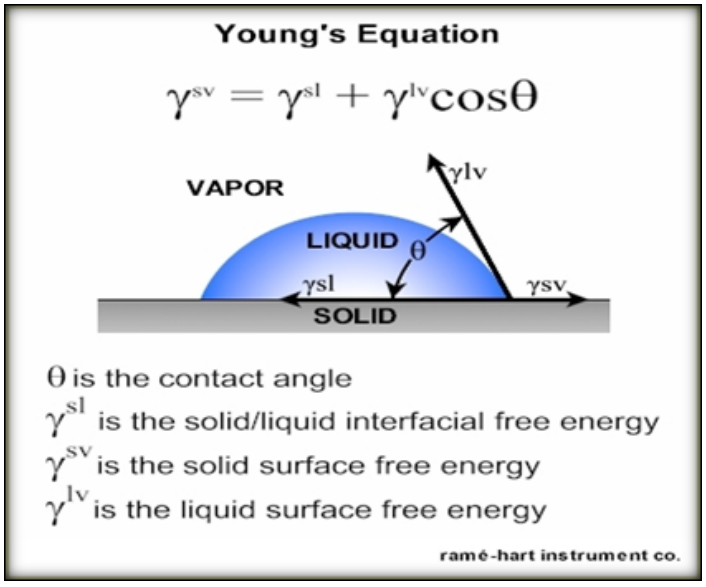

Figure B-1: A liquid drop schematic showing the quantities in Young's equation [4]

Young's equation is applicable only to an ideal surface [3], which refers to a smooth, homogeneous, isotropic, rigid, and inert to fluids solid surface [1, 2]. Young's equation assumes a unique contact angle in equilibrium [3, 5]. However, in reality, a fluid droplet/bubble can adopt many metastable states on the solid surface, leading to the difference between the measured contact angle and Young's contact angle. This difference is called the contact angle hysteresis and arises when the receding contact angle differs from

the advancing one due to the impact of many factors such as surface roughness and heterogeneity [5].

Wenzel's equation, Eq.2, becomes applicable [1, 3] when a fluid droplet/bubble is deposited on a rough solid surface and completely wets the surface, as shown in Figure B-2a. In 1936, Wenzel related the contact angle measured on a rough surface (θ_w) with the roughness factor(r), and the contact angle measured on an ideal surface, i.e. Young's angle (θ_Y), as follows:

$$\cos\theta_w = r\left(\frac{\gamma_{SL}-\gamma_{SV}}{\gamma_{LV}}\right) = r\cos\theta_Y \quad \text{(B-2)}$$

The roughness factor refers to the ratio of the actual to the apparent surface area of a rough surface and is always greater than one. Wenzel's contact angle is smaller than Young's contact angle on a water-wet surface ($\Theta \leq 90°$) but larger than Young 's angle on an oil-wet surface ($\Theta \geq 90°$) [1, 3].

On the other hand, Cassie-Baxter's equation, Eq.3, becomes applicable in case of partial wetting, as shown in Figure B-2b. In 1946, Cassie-Baxter introduced Eq.3 for the partially wetted surfaces, which contain air pockets between the droplet and the solid surface, [1]:

$$\cos\theta_{CB} = f\cos\theta_Y + (1-f)\cos\theta_{air} \quad \text{(B-11)}$$

When the contact angle between the water droplet and the air reaches 180°, Cassie-Baxter's equation becomes as follows:

$$\cos\theta_{CB} = f\cos_{\theta Y} + (f-1) \quad \text{(B-12)}$$

Θ_{CB} is the Cassie-Baxter's contact angle, f the fraction of the droplet that is in actual contact with the surface. According to the Cassie-Baxter's equation, a range of hydrophobic contact angles can be obtained from the originally hydrophilic surfaces [1].

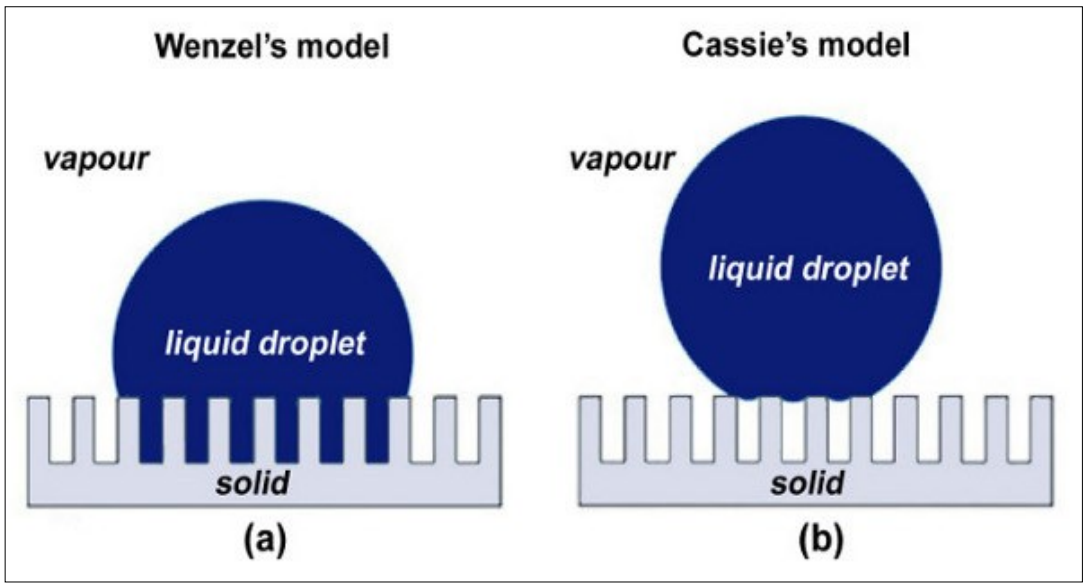

Figure B-2: A schematic showing a liquid drop completely and partially wetting the surface [6]

Since the aforementioned equations have many practical limitations when they applied to rough and heterogeneous surfaces, many researchers have been trying to develop more robust formulations. Drelich et al. developed the following theoretical relation to predict the contact angle on heterogonous and porous surfaces, where distortion of the triple line occurs [2, 7].

$$\cos\theta_r = fx_1\cos\theta_{s1} + (1\text{-}f)x_2\cos\theta_{s2}\text{-}\left(\frac{1}{\gamma_{Lv}}\right)(y_1\gamma_{SLV_1}k_{gs1}\text{-}y_2\gamma_{SLV_2}k_{gs2}) \quad \text{(B-5)}$$

$$x = \frac{a}{A} \geq 1, y = \frac{l}{L} \geq 1\ k_{gs} = \frac{1}{\rho}$$

Where *a* and *A* are the actual and "apparent" interfacial areas, respectively; *l* and *L* are the actual and "apparent" lengths of the three-phase contact line, respectively. The subscripts *1* and *2* refer to two kinds of surface area varying in energetic features. Sub-fixes *s* and *r* stands for smooth and rough surfaces, respectively. The nomenclatures γ_{SLV} and k_{gs} corresponds to the line tension and geodesic curvatures of the triple line, respectively. ρ represents the curvature radius of the triple line.

B.2 Contact angle measuring techniques

In literature, there are several techniques that have been introduced to measure contact angle on flat surfaces, directly or indirectly. However, the success of these measurements

depends greatly on the surface characteristics and its cleanliness [8]. Below is a short description of some of the main techniques, which are: the sessile drop (goniometer), captive-bubble, axisymmetric drop shape analysis-profile (ADSA-P), tilting plate, and Wilhelmy balance method [9].

B.2.1 Sessile Drop (Goniometer) Method

This technique is the most widely used direct method for measuring the contact angle of a liquid drop on a solid surface with an accuracy range of ± 2°. In this method, a drop of liquid is rested on a solid surface and the contact angle is measured using a goniometer or a semi-automatic computer recognition programme [10].

The apparatus of this technique was invented by Bigelow and his colleagues. Lately, W.A. Zisman designed the first commercially version of this setup, which then produced on a wide scale by the ramé-hart instrument company in the early 1960s. The first version of the apparatus was composed of four parts: a horizontal stage to mount a solid or a liquid sample on it, a micropipette to make a liquid drop, an illumination source, and finally, a telescope combined with protractor eyepiece [11]. Over the years, many modifications have been added to make the equipment more convenient and more accurate. For instance, a camera has been integrated to capture photographs of the drop profile and then determine the contact angle later. A motor drive syringe was also added that can be used for adding or removing liquid to the drop so both advancing and receding contact angles can be measured.

The main advantages of this method are its simplicity, and the limited amount of liquid and solid surface required, which is only a few square millimetres [7]. Yet, the small volume of solid and liquid can be one of its drawbacks because of the high chance of contaminations in the liquid and solid substrate [11]. Moreover, this method is not suitable when the contact angle is less than 20° [11, 12]. This is because when the droplet profile is approximately flat, the uncertainty of assigning a tangential line can increase [11].

B.2.1.1 Captive Bubble Method

This technique was first introduced by Taggart et al. to measure the contact angle between gas, liquid and solid surface [13]. In this technique, a small amount of gas (e.g. CO_2) is injected to form a bubble under the solid surface which is saturated with liquid (e.g. water). The main advantages of the technique are: the direct contact between the solid surface and the

saturated atmosphere, the less exposure of the solid-vapour interface to contaminations such as the airborne oil droplets, and the easiness of monitoring liquid temperature compared to the sessile drop technique, which can help in exploring the temperature effect on contact angle [11]. However, the main disadvantages of the techniques are: the large volume of the liquid required for the measurements compared with the sessile drop, the swelling of the solid surface after its immersion into the liquid, and the dissolving of the film on the solid by the liquid [11].

B.2.1.2 Axisymmetric Drop Shape Analysis- Profile (ADSA-P) Method

This technique has been developed to determine the liquid-fluid interfacial tension and the contact angles (of the pendant drops, sessile drops, and bubbles) by best fitting the theoretical Laplacian curves with the experimental profile. The main problem with this technique is its difficulty in obtaining accurate coordinate points along the edge of the drop profile [14]. To tackle this problem, Skinner et al. 1989 introduced the axisymmetric drop shape analysis-contact diameter (ADSA-CD) technique. In this new technique, the drop is viewed from above and thus the contact diameter can be determined. Then, the contact angle is determined by numerically solving the Laplace capillarity equation. The inputs parameters for this technique are: the drop volume, contact diameter of the drop, and liquid surface tension. This technique is accurate for contact angles less than 90°, and especially useful for the very hydrophilic biological specimens [14, 15].

B.2.1.3 Tilting Plate Method

The tilting plate method was introduced by Adam and Jessop in 1925 as an alternative to the direct optical methods of contact angle measurements. In this method, a solid plate with few centimetres width is immersed gradually into the liquid existed in the bath. As a result, the free surface of the liquid will form either a convex or concave shape, as shown in Figure B-3. Later, the plate is tilted until the liquid meniscus becomes completely flat. To check this flattens, a side view imaging or a light reflection is used [16]. With this method, both the advancing and receding contact angles can be measured simultaneously [17]. The main drawback is that the curvature of the meniscus depends on the subjectivity of the operator [16, 18].

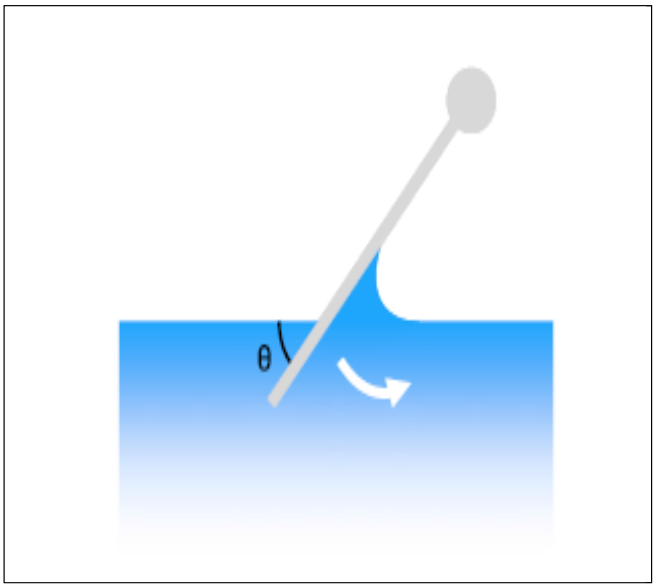

Figure B-3: Tilting plate method illustration [11]

B.2.1.4 Wilhelmy Balance Method

This method measures the forces along the perimeter of a thin, smooth and vertical regular shape (e.g. plate/cylinder). The advancing and receding angles can be calculated by moving the regular shape in or out of the liquid [8, 19], as illustrated in Figure B-4. If the contact angle is smaller than 90°, a downward force is exerted on the plate/cylinder when it is brought into contact with a liquid. The measured force change on the balance is a combination of the buoyancy and the force of wetting (the force of gravity remains constant). The wetting force is defined as follows [11]:

$$f = \gamma_{lv}\, p \cos\theta \tag{B-6}$$

where γ_{lv} is the liquid surface tension; p is the perimeter of the contact line, which is equal to the cross-sectional diameter of the solid surface; and Θ is the contact angle.

The total measured force F on the balance is:

$$F = \gamma_{lv} p \cos\theta - V\Delta\rho g \tag{B-7}$$

where V is the liquid volume; $\Delta\rho$ is the density difference between the liquid and the fluid; and g is the gravity constant.

It can be concluded from Eq. 9 and 10 that when the liquid surface tension and the perimeter of the contact line are known, the contact angle is readily computed [11]. However, if the

contact angle is assumed to be zero, then the measured force corresponds directly to the liquid surface tension.

The main problem of this technique is that the liquid surface tension must be known (which is very difficult to be determined when, in some cases, the solution has active agents) if not it leads to serious uncertainty [8]. Moreover, the solution must not swell and its vapour should not adsorb onto the plate. The plate must have sharp edges to minimize the edge/corner effect, have a constant perimeter, have the same composition and morphology at all surfaces(i.e. front, back and both edges) [8]. These conditions probably making it difficult to be applied to real solid surfaces [8].

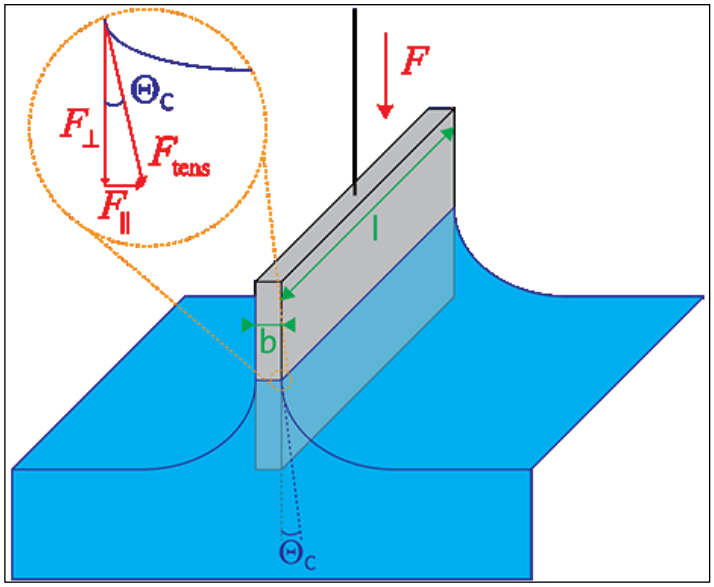

Figure B-4: Wilhelmy method illustration [20]

B.2.2 Spreading

Wetting and spreading have been in practice for thousands of years. An example is the use of lubricated stones by the ancient Egyptian people in the processes of building pyramids. These phenomena imply a flow of fluid on a solid substrate. The fluid flow depends on many physical and chemicals factors that include: the dynamic, non–ideality, surface energy, roughness, and heterogeneity of the solid surface, the shape and size of the drop, the viscosity and temperature of the fluid and solid surfaces, and the interaction between fluids and solid [7, 8, 21] as well as capillary forces, hydrostatic pressure, and adhesion forces [12, 22]. The capillary forces tend to sphere the bubble while the hydrostatic pressure and adhesion forces tend to spread and flatten the bubble [12, 22].

The spreading phenomenon has an impact on the capillary pressure curve, gas and oil relative permeability curves, residual oil saturation, and wettability of the solid surface [23, 24]. The spreading coefficient, *S*, refers to the difference between the surface energy of a dry substrate and the surface energy of a wet substrate as follows [24]:

$$S = (E_{substrate})_{dry} - (E_{usbstrate})_{wet} \quad \text{(B-8)}$$

Complete wetting, or $S > 0$, occurs when the surface energy of the wet substrate is smaller than that of the dry surface [24].

The following equation is used to describe the spreading coefficient during the replacements of a solid-CO_2 interface by solid-water and water-CO_2 interfaces.

$$S = \gamma_{sc} - (\gamma_{sw} - \gamma_{wc}) \quad \text{(B-9)}$$

By rearranging Eq.7 and Eq.1, *S* can also be expressed as follows:

$$S = \gamma_{wc}[\cos(\theta) - 1] \quad \text{(B-10)}$$

where γ is the interfacial tension. The subscripts *s*, *w* and *c* refer to solid, water and CO_2, respectively [24]. The complete spreading, $S = 0$, occurs when θ is zero. The partial spreading, $S < 0$, occurs when the equilibrium contact angle is not zero [25].

Nevertheless, the spreading coefficient of a three-phase system (oil – gas –water) is defined as the balance between the interfacial tensions of the present fluids.

$$S = \gamma_{wg} - \gamma_{og} - \gamma_{ow} \quad \text{(B-11)}$$

The subscripts *w*, *o*, and *g* to water, oil and gas, respectively. For the three-phase system (oil – gas –water), the spreading coefficient plays a major factor in modifying the oil ability to formulate a thin film that spreads on water in the presence of gas [26]. If the spreading coefficient is positive, $S \geq 0$, oil tends to form continuous thin structures of the oil films on water in the presence of gas, i.e. oleic phase films. These oleic phase films are hydraulically continuous and help in reaching low oil saturation, as shown in Figure B-5a. On the other hand, if the spreading coefficient is negative, $S < 0$, oil tends to form disconnected droplets and globules, as shown in Figure B-5b. The discontinuity in these films can result in an early disconnection of the oil phase, oil phase trapping, and less production rate [26].

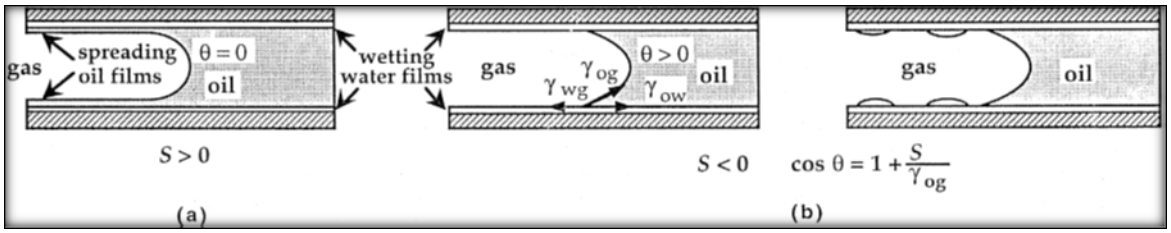

Figure B-5: Schematic representation of the distribution of water, oil and gas in a water-wet capillary tube: (a) positive spreading coefficient, (b) negative spreading coefficient [26].

B.3 Previous work on Salinity Impact on Wettability

The wettability of liquid on solid surface is generally dependent on the physical and chemical properties of the solid surface and fluid. That is, the system wettability can be affected by the adsorption and desorption of the polar compounds and/or organic materials [27], salinity, pH level, temperature and duration of ageing in oil, initial water saturation, and mineralogy, surface roughness, and heterogeneity [5, 28, 29].

Salinity (Brine composition, concentration, and valency) and pH level have a direct impact on the system's wettability since they govern the charge of the solid surface, which, in turn, determines the kind of materials adsorbed. The silica surface charge in water is negative at high pH levels and positive at low pH levels but turns to negative when the pH level increases above 2 to 3.7. At neutral pH, the silica surface charge is normally negative and has a weak acidic surface and, therefore, the adsorption of organic bases is favoured [30]. The presence of divalent ions such as Ca^{2+}, Mg^{2+} and $SO4^{2-}$ has an important role in changing the surface charge and modifying wettability [31-33].

Literature shows extensive investigations have been conducted about the impact of salinity on different topics such as wettability alteration, oil recovery, zeta potential, interfacial tension, and effective CO_2 permeability [29, 30, 34-39]. For instance, Alotaibi et al. evaluated the impact of the ionic strength of the injected water on wettability alterations under high-pressure conditions using a HTHP (high temperature, high pressure) contact angle method and zeta potential technique. The brines investigated were synthetic formation brines, aquifer water, and seawater. They used outcrop rocks and stock-tank crude oil sample in all experiments. The results showed a direct relationship between the ionic strength and the zeta potential of the sandstone rocks and the selected clays minerals. The ionic strength of

the injected water showed a considerable impact on the wettability due to its direct impact on the surface charges of clays and sandstone particles. The wettability revealed a dependency on rock mineralogy, brine salinity and temperature. The use of aquifer water decreased the Berea sandstone wettability toward strong water-wet condition but enhanced the wettability to a neutral state in Scioto sandstone; the optimum salinity for this rock was seawater [29].

Wu and Firoozabadi studied the impact of salinity on wettability alteration from a water-wetting to intermediate gas-wetting status. They used fresh water and 1 wt. % NaCl (aq.) with a Berea sandstone core sample. They noticed an adverse impact for the NaCl, KCl, and $CaCl_2$ brines on wettability alteration. The increase in NaCl salinity led to an increase in water wetness. Increasing NaCl salinity reduced the gas absolute permeability while increasing $CaCl_2$ salinity caused a minor impact on permeability [30].

Tang and Morrow investigated, among many factors, the impact of salinity of connate and invading brines on the wettability and recovery of crude oil at reservoir conditions. They observed that with decreasing salinity of both the initial (connate) and invading brine or either, the water wetness and oil recovery by waterflooding increase [34]. Saraji et al. investigated, among many factors, the impact of brine salinity (0.2–5 M) on the interfacial tension and contact angle hysteresis under high pressures (137.9–275.8 bar) and temperatures (50–100 °C) conditions using Axisymmetric Drop Shape Analysis with no-Apex (ADSA-NA) method. They observed that increasing brine salinity caused an increase in the interfacial tension, contact angle, and contact angle hysteresis [35].

Ali et al. investigated the impact of salt concentration on the surface tension of aqueous solutions of four different salts, i.e. the chloride salts of lithium, sodium, potassium and ammonium. The concentration investigated ranged from 0.1 to 2.0 M. In general, they observed a linear increase in the surface tension with concentration [36].

Al-Aulaqi et al. studied, among other factors, the impact of brine salinity on wettability alteration of three core samples: Berea, reservoir sandstone and reservoir carbonate. The change in salinity led to an impact on both oil recovery and water injectivity. As salinity of the monovalent cations decreased, the oil recovery increased, which was attributed to wettability shifting towards a more wetting status. Moreover, as the salinity range reduced

from 0.1-0.5 M to 0.01-0.1 M, the water injectivity reduced, which was attributed to the detachment of clay minerals that coats the grains, thereby blocking pore throats [37].

Nasralla et al. studied, among other factors, the influence of water salinity on wettability alteration by conducting contact angle and zeta potential measurements. Using mica sheets and two crude oils, the displacements were performed under a range of pressures and temperatures (34.5-69 bar, and 60-121.1 °C), and a range of salinities (0-174, 000 mg/l) conditions. They observed that the increase in salinity led to a significant increase in the contact angles for both oils. The zeta potential measurements showed highly negative electrokinetic charges at the oil-brine interface with low salinity water. The change in electrokinetic resulted in forming repulsive forces between oil/brine and brine/rock and altering the wettability towards water-wet [38].

Arif et al. studied, among other factors, the impact of salinity (0 to 5 wt. % NaCl), and salt type (NaCl, $CaCl_2$, $MgCl_2$) on the zeta potential of the brine/mica interface and the contact angle under ambient and high-pressure conditions. The divalent cations (Mg^{2+} and Ca^{2+}) produced an increase in the zeta potential and a concomitant increase in the contact angle. The trend of both interfacial tension and contact angle were in the order of CO_2-$MgCl_2$ > CO_2-$CaCl_2$ > CO_2-NaCl brines. They observed that using brine instead of deionised water leads to a decrease in the storage capacity which was attributed to surface de-wetting. The storage capacity with NaCl brine is higher than that with $MgCl_2$ and $CaCl_2$ brines due to better wetting performance [39].

Rathnaweera et al. investigated the impact of salinity on the effective CO_2 permeability of a Hawkesbury sandstone core sample at a constant temperature of 35 °C. The tests were conducted for a range of pressures (20-120 bar), and a range of NaCl concentrations (0-30 wt. %). They observed: (I) a reduction in the effective permeability as the salinity increases, and (II) a sudden drop in the effective permeability as CO_2 phase transforms from a gaseous to a supercritical state. The former reduction was linked to the presence of the NaCl crystals in the pore structure that obstructs the flow paths, thereby reducing effective permeability. The latter was attributed to the slip flow impact due to phase change [40].

On the other hand, the literature shows that studies on the influence of electrolyte concentrations on the equilibrium contact angle [41, 42] are rare. Only two studies were found. For instance, Sghaier et al. measured equilibrium contact angles as a function of NaCl

concentrations on both hydrophilic and hydrophobic glass surfaces. With increasing salt concentration, the hydrophilic surfaces showed a greater increase in contact angle than the hydrophobic surfaces [41]. Leelamanie and Karube examined the impact of aqueous electrolyte concentration on the contact angle of soil samples (Andisol and silica sand) with different hydrophobicities, using NaCl and $CaCl_2$ brines. They noticed that the increase in concentration leads to an increase in the contact angle, due to increasing surface tension, and that the relation between the concentration and contact angle is not linear. In addition, the contact angle showed an almost negligible response to increasing concentration when the concentrations of NaCl and $CaCl_2$ exceeded 0.06 and 0.1 mol/l, respectively [42].

B.3.1.1 Trapping Seals

According to Watt, the trapping seals can be divided generically into membrane seals or hydraulic seals [43]. These seals would not allow the passage of fluid to occur across them as long as their integrity is not distributed, which depends on the capillary forces and permeability.

The membrane seals can fail through capillary leakage while the hydraulic seals can fail through fracturing or wedging open of the faults [43]. The membrane seal will leak once the differential pressure across the seal rock (due to the buoyancy forces and injection-related overpressure) exceeds the threshold displacement pore pressure, allowing fluid to transfer through the seal [44, 45]. However, the membrane seal will reseal when the differential pressure across the seal reduces just below the threshold displacement pressure [45]. On the other hand, the hydraulic seal occurs when the threshold displacement pressure of some extremely tight shales, and various evaporites, is so high such that exceeds the pressure required for fracturing or wedging, and vertical migration along, of faults. These tight formations would fracture once pore fluid pressure at the caprock reservoir interface exceeds both minimum stress and tensile strength of the rock; however, once the differential pressure drops below the pore fluid pressure, the rock fracture will reseal again [43].

The capacity of the trapping seals can be determined based on the capillary pressure (column height) at which the trapped fluids begin leaking through adjacent sealing layers; the leakage occurs as the wetting pore fluid (water) displaces the nonwetting fluid (e.g. CO_2) in the largest pore-throats of the interconnected pore system [44, 46]. The trapped fluid (e.g. CO_2) can escape sealing formations upon the occurrence of a mechanical failure of the caprock,

damage of the wells casing because of corrosions of pipes and cement, capillary breakthrough, and/or diffusion along the open fault systems and fracture network [44, 47]; once it happens, the mechanical failure can lead to a rapid or catastrophic leakage [44].

B.4 Surface Tension

Surface tension is a ubiquitous phenomenon that exists everywhere in nature. It leads to the presence of many phenomena such as capillarity in tubes, spherical shape of a liquid drop, concavity or convexity of the liquid surface in different tubes of different materials, walking of water strider on water, and floating of small needle on the surface of the water.

Surface tension is defined as the force required to break a unit length of a liquid surface or the work required to create an additional unit surface of the liquid. The surface tension can be considered as the property of the liquid surface that resists the externally applied force due to the cohesive forces that hold liquid molecules together; the cohesive forces are shared with all adjacent molecules. Owing to the cohesive action, the liquid molecules inside the bulk phase are equally attracted in all direction by their neighbouring molecules and thus the net force is zero. However, the liquid molecules acting on the surface do not have neighbouring molecules on all sides of them. The result is unbalanced intermolecular forces acting on the surface molecules of the liquid, as shown in Figure B-6. The net downward attractive force causes a stronger attraction between the molecules on and below the surface. As a direct consequence, the liquid droplets adopt a spherical shape because: (a) the molecules on the surface try to shrink together due to the net downward force, and (b) the spherical shape is the only configuration possible with the least surface area.

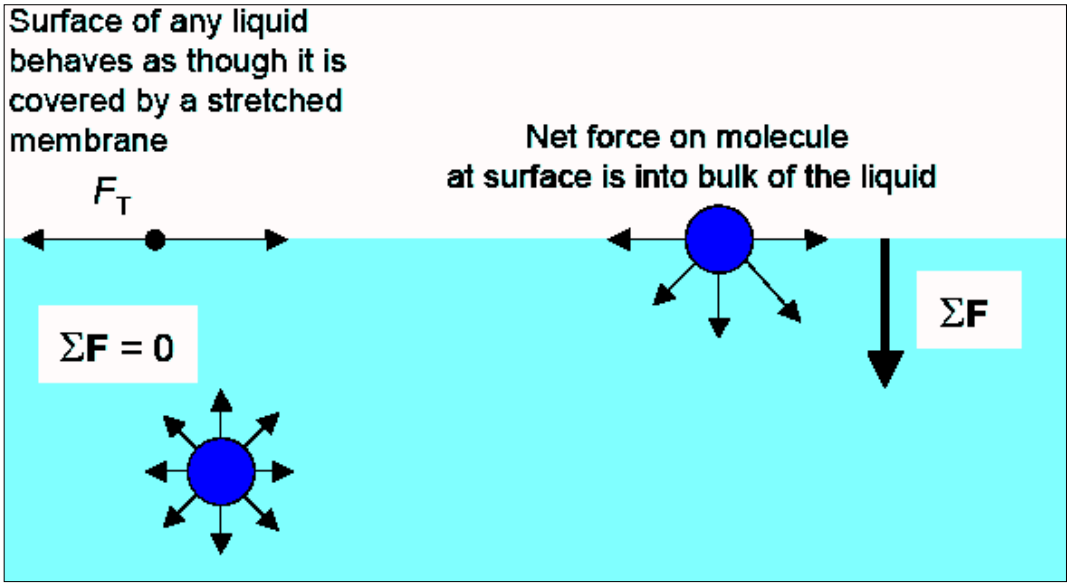

Figure B-6: Surface tension of liquid [48]

B.5 Conventional EOR Techniques

Traditionally, conventional EOR techniques consist of waterflooding, thermal flooding (e.g. steam and combustion), electric flooding, gas flooding (miscible and immiscible flooding), and chemical flooding (surfactant and polymer flooding) [49]. The most used methods for the enhancement of oil production are: water flooding, thermal flooding, and chemical flooding processes. Below is a summary of these methods.

B.5.1 Water Recovery Flooding

During waterflooding methods, water is injected to raise the reservoir pressure higher than the bubble point pressure and displace oil towards producing oil wells [50]. The injected water will form a bank that displaces oil ahead of it. The performance of this process is governed by the sweep efficiency and mobility ratio, which is largely controlled by the ratio of oil and water viscosities [51]. The sweep efficiency is a measure of the contact efficiency between the injected water and oil in pore space. The sweep efficiency is enhanced by the presence of homogenous formation but reduced significantly by the presence of heterogeneous formations, such as high permeability streaks, fractures and faults [51].

B.5.2 Thermal Recovery Flooding

Thermal methods have been tested since the 1950's [52]. They are designed for the extraction of heavy oils (10-20 API°) and tar sands (≤ 10 API°) [52, 53]. However, they are not

suitable for heavy oil reservoirs if: (I) the formations are thin (<10 m), or too deep (> 1000 m) due to heat loss to surrounding formations [54], and (II) the formations have low permeability and low oil saturation [55]. These are the reasons why many of the heavy oil reservoirs in Saskatchewan and Alberta in Canada and in other areas of the world are not suitable for the use of thermal recovery techniques [55].

According to Prats, the thermal recovery is "any process in which heat is introduced intentionally into a subsurface accumulation of organic compounds for the purpose of recovering fuels through wells" [56]. The purpose of introducing heat is to reduce oil viscosity to the point when oil becomes mobile. The oil viscosity is very sensitive to temperature. For instance, the viscosity of a dead oil (a sample from the north sea) was reduced from hundreds to 10 cp upon increasing temperature from 100 to 300 °F (from around 38-149 °C) [57].

Introducing heat to an oil reservoir can be achieved through steam injection or in situ combustions. The steam injection, in turn, is composed of many methods such as cyclic steam injection "huff- and puff", steam flooding and steam assisted-gravity drainage (SAGD). The huff and puff method is implemented in a single well and consists of three stages: steam injection, soak, and production. At first, the steam is injected at a high rate for a period that can last for 2-3 weeks. Then, after the steam is soaked for 2-3 days to allow heat transfer to the in-situ oil and hence reducing the oil viscosity, the well is put on production [52, 58].

The steam flooding processes involve the continuous injection of steam into the target oil reservoir. The result is that light oil can be moved easily to the production wells due to differential pressure influence. The steam flooding depends largely on the geology of the target formation and the pattern size of the wells. On the other hand, the steam assisted-gravity drainage (SAGD) processes target the bitumen production and depend mainly on gravity segregation; the severity of the segregation and its impact on oil recovery is controlled by reservoir properties, vertical permeability, and distribution of horizontal permeabilities [59]. The SAGD method is more effective than the steam flooding process, which does not permit the bitumen to be exposed long enough to steam. In this method, the injection and extraction wells are in close proximity to one other and are located at the bottom of the reservoir [52, 53].

In-situ combustion method, also known as fire flooding, includes the introduction of air or oxygen to burn a portion of oil in place (about 10%) to generate heat [52]. Consequently, a

very high temperature (450-600 °C) is generated in a narrow zone, which leads to a very high reduction in oil viscosity. Nevertheless, the most common problems with this method are severe corrosion, toxic gas production and gravity override [52].

B.5.3 Chemical Flooding

Chemical flooding refers to the processes of using chemical substances to improve oil recovery. These processes are categorized based on the chemicals involved such as surfactants, polymers (e.g. partially-hydrolysed polyacrylamide HPAM), and alkalis as well as a combination of these chemicals [60].

Chemical flooding processes improve oil recovery by: (I) increasing the capillary number to displace trapped oil, (II) decreasing mobility ratio to obtain better sweep efficiency, and (III) controlling performance in heterogeneous formations, e.g. layered and channelled structures, to have better sweep efficiency [50]. Surfactants enhance microscopic sweep efficiency via the extreme reduction of the interfacial tension, thereby increasing the capillary number and reducing the pressure required to displace oil on a pore scale. Polymers, on the other hand, enhance macroscopic sweep efficiency by increasing viscosity. The increase in viscosity will result in increasing the capillary number and decreasing mobility ratio. The reduction in mobility ratio will improve water floods efficiency by suppressing viscous fingering, especially in heterogeneous formations [50, 61].

B.6 CO_2-EOR Recovery Techniques

To enhance oil recovery, several CO_2-EOR recovery techniques have been employed worldwide, such as continuous CO_2 injection, CO_2 slug (small slug size) injection, continuous CO_2 injection followed with water, conventional water-alternating-gas (WAG) followed with water, WAG followed with gas, tapered WAG (a gradual reduction in the injected CO_2 volume proportional to the water volume) [55, 62], and carbonated water injection (CWI) method.

B.6.1 Water Alternative CO_2 Process (WAG)

WAG refer to the processes of consecutive injection of water and CO_2 in the target oil reservoir. These processes enhance oil recovery by improving sweep efficiency via reduction the amount of the injected CO_2, thereby alleviating CO_2 fingering and decreasing CO_2 mobility [63-65]. The injected water slugs act as barriers and hence preventing the preferential flow

of CO_2 through high permeability layers, thereby alleviating CO_2 fingering that leads some of the oil in place without contact [65-67]. Moreover, the injected water will result in increasing the water saturation in the oil reservoir, thereby decreasing the CO_2 saturation, consequently reducing CO_2 relative permeability. This, in turn, will lower the mobility ratio and alleviate CO_2 fingering [65, 67]. Contrariwise, the increase in water saturation can decrease hydrocarbon extraction by isolating oil droplets, thereby preventing a direct contact between oil and the injected CO_2 [65].

It is worth mentioning that sometimes the WAG techniques are economically un-favourable because of: (a) the late production compared to the single-slug CO_2 flooding, and (b) the high CO_2 consumption because of increasing CO_2 solubility in water [64, 68, 69]. Moreover, the WAG techniques are less preferable for tight reservoirs or water-sensitive reservoirs compared to CO_2 continuous injection processes [65].

B.6.2 Carbonated Water Injection (CWI) Techniques

CWI processes include the injection of CO_2 as a dissolved phase not as a free phase as in the case of the WAG processes. As a result, the CWI processes can: (I) overcome the gravity segregation issue encountered in the WAG techniques due to the density contrast between CO_2 and reservoir fluids, (II) safely secure CO_2 in sealed geological sites, and (III) enhance oil recovery [70] through sweep efficiency improvement, oil swelling, and reconnecting and redistributing of residual oil saturation [71].

CWI can enhance oil recovery through many mechanisms, namely interfacial tension reduction, fines (small solid materials) migration, wettability alteration, increasing CO_2 solubility due to salinity reduction, multi-component ionic exchange (MIE), emulsion formation, desorption, electrical double layer expansion effects, and in-situ saponification due to change in pH (increase) [61, 68, 72, 73]. The in-situ saponification mechanism has been associated with the increase in the production of natural surfactants, which reduce interfacial tension and increases oil recovery [74]. It is worth mentioning that the interfacial tension should be tailored for each reservoir depending on the geological characteristics, properties of oil and formation water, and source of CO_2 [68].

B.7 Parameters Controlling CO_2 Flood Performance

According to Klins 1984, the displacement of CO_2 can be categorized into five regions based on the dominant mechanism, Figure B-7:

Region I: Low-pressure formations (generally immiscible).

Region II: Intermediate pressure, high-temperature formations (immiscible).

Region III: Intermediate pressure, low-temperature formations (immiscible).

Region IV: High-pressure formations (miscible).

Region V: High pressure, low-temperature liquid formations (immiscible).

For Region I (< 6.89 MPa), the main mechanism that controls the displacements efficiency in this region is the solubility of CO_2 into crude oil [54, 75]. The CO_2 solubility contributes to displacement through oil swelling, oil viscosity reduction, and internal solution gas drive mechanism. Increasing pressure until reaching Region II (> 6.89 MPa), results in a significant increase in crude oil extraction due to CO_2 dissolution [75]. During Region II, the oil extraction by CO_2 which increases with increasing pressure is added to the mechanisms in Region I if the conditions are favourable. As the pressure reaches Region III by exceeding the minimum miscibility pressure (MMP), miscibility occurs through first or multiple-contact processes. Once miscibility is achieved, the displacement efficiency increases significantly owing to the alleviating of the trapping forces.

On the other hand, Region IV is characterized by the evolution of a third phase, which is rich in CO_2 and contains light and intermediate hydrocarbon components. The CO_2 injection into reservoirs with characteristics like that presented in Region IV may, instead of vaporizing oil, condense into the crude oil leading to the formation of CO_2-rich liquid mixtures. Nevertheless, if a reservoir temperature is below the critical degree (e.g. heavy oil reservoirs in Alaska), then CO_2 can exist in a liquid state (Region V). As liquid CO_2 is immiscible with oil in most cases, its enhancement of oil recovery can be achieved by mechanisms similar to those mentioned in Region II [54]. Liquid CO_2, which is similar to solvent action, will extract light hydrocarbons from crude oil during its displacement [75]. Moreover, the liquid CO_2 will result in avoiding the gravity segregation problem due to its high density, which is close to crude oil and brine density.

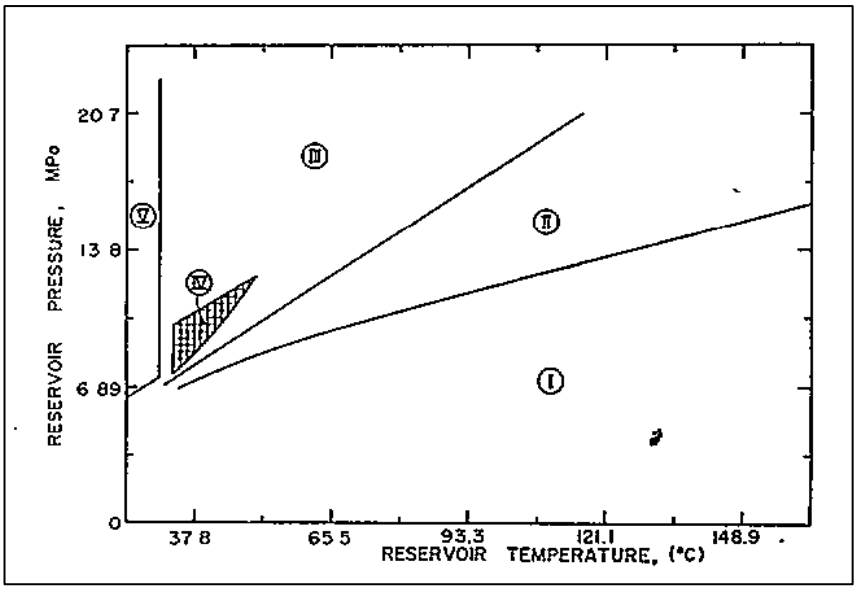

Figure B-7: The effect of reservoir temperature and pressure on CO_2 displacement mechanisms [75]

B.8 Fundamentals of Displacement Efficiency

Typically, the efficiency of CO_2 displacement is divided into microscopic and macroscopic efficiencies.

B.8.1 Microscopic Sweep Efficiency

Microscopic efficiency (E_{mi}) is a measure of the efficiency of oil mobilization or displacement at a pore-scale level after the contact between the displacing and displaced fluids is achieved. It denotes the difference between the initial oil saturation and the ratio of the residual to the initial oil saturation [51, 76] as follows:

$$\mathrm{E_{mi}} = \mathrm{S_{oi}}\text{-}\mathrm{S_{or}}/\mathrm{S_{oi}} \quad \text{(B-12)}$$

where S_{oi} and S_{or} is the initial and residual oil saturation, respectively. The microscopic efficiency of CO_2-water flooding displacements depends on the interfacial tension, wettability, relative permeability [51] as well as rock pore geometry and pore structure [76].

B.8.2 Macroscopic Sweep Efficiency

Macroscopic sweep efficiency is a measure of oil displacement efficiency (i.e. the effectiveness of the contact between the displacing fluid and the fluid in place) on a

macroscopic scale [51, 77]. The macroscopic sweep efficiency consists of the areal (*Ea*) and vertical sweep (E_v) efficiencies:

$$\mathrm{E_{ma}} = \mathrm{E_A} \times \mathrm{E_V} = \left(\frac{\mathrm{A_d}}{\mathrm{A_R}}\right) \times \mathrm{h} \times \theta \times \mathrm{S} \qquad \text{(B-13)}$$

where E_A is the areal sweep efficiency, E_V the vertical sweep efficiency, A_d area of displacement, A_R area of the reservoir, h the thickness of production layers, Θ the porosity, and S the gas or oil saturation [51]. E_A refers to the fraction of the total reservoir area that is swept by the displacing fluid at the time of breakthrough, as shown in Figure B-8a. E_V refers to the cross-sectional area that is contacted by the injected fluid in all layers, as shown in Figure B-8b.

The macroscopic sweep efficiency depends on many factors that involve: the patterns of the injection and producing wells, heterogeneities and anisotropy of oil reservoirs, type of oil-bearing rock matrix, and difference in properties between the displacing and displaced fluids [51, 59, 76, 78]. The configuration of the injection and producing well depends mainly on the characteristics of the oil reservoir, i.e. geological properties and size of the reservoir. The heterogeneities and anisotropy of the oil reservoirs are strongly influenced the macroscopic sweep efficiency. The variations in porosity, permeability, and clay content can result in non-uniform fluid movements within the oil-bearing formations layers [51]. Moreover, the presence of microfractures and macrofractures in many formations provides a preferential flow path for the displacing fluids. This will result in the bypassing of substantial portions of oils, thereby increasing residual oil saturation. There is not much can be done about reservoirs heterogeneities apart from drilling new wells and/or producing through different types of wells.

The difference in properties between the displacing and displaced fluids can have a direct impact on both areal and vertical sweep efficiencies [76] by affecting the mobility ratio. The mobility ratio shows how easily a fluid can move through a porous media. The apparent mobility ratio represents the ratio of the effective permeability to fluid saturation [51]. Since the effective permeability is a dynamic property, thus a dynamic change in the mobility of displacing and displaced fluids can occur along the course of displacement process. If the mobility ratio (M_R) is close to unity, then a stable displacement front will evolve. However, if the mobility ratio is much higher than unity, then viscous fingering will occur.

$$M_R = \frac{\text{mobility of the displacing fluid}}{\text{mobility of the displaced fluid}} \quad \text{(B-14)}$$

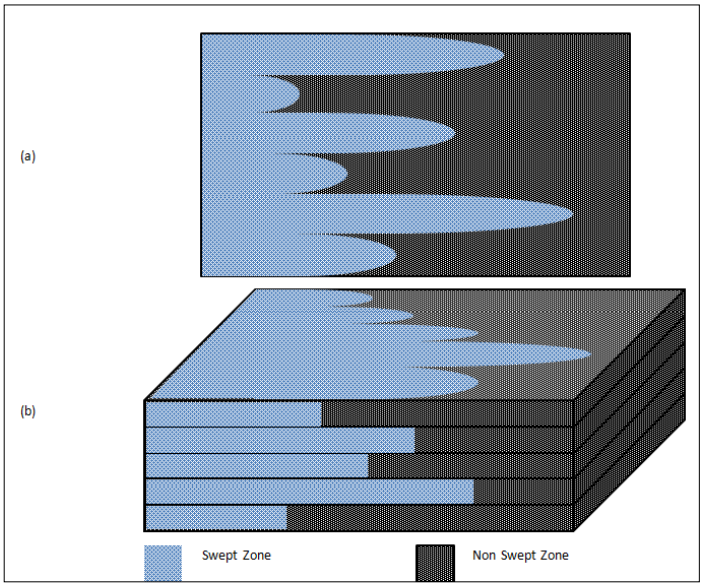

Figure B-8: Schematic representation of the two components of the macroscopic Sweep: (a) Areal sweep and (b) Vertical Sweep [77]

B.8.3 Overall Recovery Efficiency

The overall displacement efficiency, *E*, refers to the product of the macroscopic displacement efficiency (E_{ma}) and the microscopic sweep efficiency (E_{mi}):

$$E = E_{ma} \times E_{mi} = \left(\frac{A_d}{A_R}\right) \quad \text{(B-15)}$$

B.9 References

1. Ryan BJ, Poduska KM. Roughness effects on contact angle measurements. American Journal of Physics. 2008;76(11):1074-7.

2. Drelich J, Miller JD, Good RJ. The effect of drop (bubble) size on advancing and receding contact angles for heterogeneous and rough solid surfaces as observed with sessile-drop and captive-bubble techniques. Journal of Colloid and Interface Science. 1996;179(1):37-50.

3. Qu M, He J, Zhang J. Superhydrophobicity, learn from the lotus leaf: INTECH Open Access Publisher; 2010.

4. ramé-hart. Information on contact angle 2017 [Available from: http://www.ramehart.com/contactangle.htm.

5. Kaveh NS, Rudolph ESJ, van Hemert P, Rossen WR, Wolf KH. Wettability evaluation of a CO_2/water/Bentheimer sandstone system: Contact angle, dissolution, and bubble size. Energy & Fuels. 2014;28(6):4002-20.

6. INTECH open science. SuperhydrophobiCity, Learn from the Lotus Leaf 2017 [Available from: https://www.intechopen.com/books/biomimetics-learning-from-nature/superhydrophobicity-learn-from-the-lotus-leaf.

7. Drelich J, Miller JD. The effect of solid surface heterogeneity and roughness on the contact angle/drop (bubble) size relationship. Journal of Colloid and Interface Science. 1994;164(1):252-9.

8. Chau T, Bruckard W, Koh P, Nguyen A. A review of factors that affect contact angle and implications for flotation practice. Advances in Colloid and Interface Science. 2009;150(2):106-15.

9. Yang D, Gu Y, Tontiwachwuthikul P. Wettability determination of the crude oil–reservoir brine– reservoir rock system with dissolution of CO_2 at high pressures and elevated temperatures. Energy & Fuels. 2008;22(4):2362-71.

10. Korhonen JT, Huhtamäki T, Ikkala O, Ras RH. Reliable measurement of the receding contact angle. Langmuir : the ACS journal of surfaces and colloids. 2013;29(12):3858-63.

11. Yuan Y, Lee TR. Contact angle and wetting properties. Surface science techniques: Springer; 2013. p. 3-34.

12. Nikolov A, Wasan D. Wetting–dewetting films: The role of structural forces. Advances in colloid and interface science. 2014;206:207-21.

13. Taggart AF, Taylor TC, Knoll A. Chemical reactions in flotation: American Institute of Mining and Metallurgical Engineers, Incorporated; 1930.

14. Cheng P, Li D, Boruvka L, Rotenberg Y, Neumann A. Automation of axisymmetric drop shape analysis for measurements of interfacial tensions and contact angles. Colloids and Surfaces. 1990;43(2):151-67.

15. Skinner F, Rotenberg Y, Neumann A. Contact angle measurements from the contact diameter of sessile drops by means of a modified axisymmetric drop shape analysis. Journal of Colloid and Interface Science. 1989;130(1):25-34.

16. Eibach TF, Fell D, Nguyen H, Butt H-J, Auernhammer GK. Measuring contact angle and meniscus shape with a reflected laser beam. Review of Scientific Instruments. 2014;85(1):013703.

17. Al-Yaseri AZ, Lebedev M, Barifcani A, Iglauer S. Receding and advancing (CO_2+ brine+ quartz) contact angles as a function of pressure, temperature, surface roughness, salt type and salinity. The Journal of Chemical Thermodynamics. 2015.

18. Bezuglyi B, Tarasov O, Fedorets A. Modified tilting-plate method for measuring contact angles. Colloid Journal. 2001;63(6):668-74.

19. Krishnan A, Liu Y-H, Cha P, Woodward R, Allara D, Vogler EA. An evaluation of methods for contact angle measurement. Colloids and Surfaces B: Biointerfaces. 2005;43(2):95-8.

20. DataPhysics - Wilhelmy plate method 2017 [Available from: http://www.dataphysics.de/2/start/understanding-interfaces/tensiometry/wilhelmy-plate-method/.

21. Sefiane K, Shanahan ME, Antoni M. Wetting and phase change: Opportunities and challenges. Current opinion in colloid & interface science. 2011;16(4):317-25.

22. Kaplan WD, Chatain D, Wynblatt P, Carter WC. A review of wetting versus adsorption, complexions, and related phenomena: the rosetta stone of wetting. Journal of Materials Science. 2013;48(17):5681-717.

23. Vizika O, Lombard J. Wettability and spreading: Two key parameters in oil recovery with three-phase gravity drainage. SPE Reservoir Engineering. 1996;11(01):54-60.

24. Dickson JL, Gupta G, Horozov TS, Binks BP, Johnston KP. Wetting phenomena at the CO_2/water/glass interface. Langmuir: the ACS journal of surfaces and colloids. 2006;22(5):2161-70.

25. Wasan D, Nikolov A, Kondiparty K. The wetting and spreading of nanofluids on solids: Role of the structural disjoining pressure. Current Opinion in Colloid & Interface Science. 2011;16(4):344-9.

26. Vizika O, Rosenberg E, Kalaydjian F. Study of wettability and spreading impact in three-phase gas injection by cryo-scanning electron microscopy. JPSE. 1998;20(3):189-202.

27. Anderson W. Wettability literature survey-part 2: Wettability measurement. JPT. 1986;38(11):1,246-1,62.

28. Buckley JS, Bousseau C, Liu Y. Wetting alteration by brine and crude oil: from contact angles to cores. SPE Journal. 1996;1(03):341-50.

29. Alotaibi MB, Nasralla RA, Nasr-El-Din HA. Wettability studies using low-salinity water in sandstone reservoirs. SPE Reservoir Evaluation & Engineering. 2011;14(06):713-25.

30. Wu S, Firoozabadi A. Effect of salinity on wettability alteration to intermediate gas-wetting. SPE Reservoir Evaluation & Engineering. 2010;13(02):228-45.

31. Zhang P, Tweheyo MT, Austad T. Wettability alteration and improved oil recovery in chalk: The effect of calcium in the presence of sulfate. Energy & Fuels. 2006;20(5):2056-62.

32. Zhang P, Austad T. Wettability and oil recovery from carbonates: Effects of temperature and potential determining ions. Colloids and Surfaces A: Physicochemical and Engineering Aspects. 2006;279(1):179-87.

33. Tweheyo MT, Zhang P, Austad T, editors. The effects of temperature and potential determining ions present in seawater on oil recovery from fractured carbonates. SPE/DOE Symposium on Improved Oil Recovery; 2006.

34. Tang G, Morrow NR. Salinity, temperature, oil composition, and oil recovery by waterflooding. SPE Reservoir Engineering. 1997;12(04):269-76.

35. Saraji S, Piri M, Goual L. The effects of SO_2 contamination, brine salinity, pressure, and temperature on dynamic contact angles and interfacial tension of supercritical CO_2/brine/quartz systems. IJGGC. 2014;28:147-55.

36. Ali K, Anwar ul H, Bilal S, Siddiqi S. Concentration and temperature dependence of surface parameters of some aqueous salt solutions. Colloids and Surfaces A: Physicochemical and Engineering Aspects. 2006;272(1-2):105-10.

37. Al-Aulaqi T, Fisher Q, Grattoni C, Al-Hinai SM, editors. Wettability alteration by brine salinity and temperature in reservoir cores. SPE Saudi Arabia Section Technical Symposium and Exhibition; 2013.

38. Nasralla RA, Bataweel MA, Nasr-El-Din HA, editors. Investigation of wettability alteration by low salinity water. Offshore Europe; 2011: SPE.

39. Arif M, Jones F, Barifcani A, Iglauer S. Electrochemical investigation of the effect of temperature, salinity and salt type on brine/mineral interfacial properties. IJGGC. 2017;59:136-47.

40. Rathnaweera T, Ranjith P, Perera M. Effect of salinity on effective CO_2 permeability in reservoir rock determined by pressure transient methods: An experimental study on Hawkesbury sandstone. Rock Mechanics and Rock Engineering. 2015;48(5):2093-110.

41. Sghaier N, Prat M, Nasrallah SB. On the influence of sodium chloride concentration on equilibrium contact angle. Chemical Engineering Journal. 2006;122(1):47-53.

42. Leelamanie D, Karube J. Soil-water contact angle as affected by the aqueous electrolyte concentration. Soil Science and Plant Nutrition. 2013;59(4):501-8.

43. Watts NL. Theoretical aspects of cap-rock and fault seals for single- and two-phase hydrocarbon columns. Marine and Petroleum Geology. 1987;4(4):274-307.

44. Wollenweber J, Alles S, Busch A, Krooss B, Stanjek H, Littke R. Experimental investigation of the CO_2 sealing efficiency of caprocks. IJGGC. 2010;4(2):231-41.

45. Li S, Dong M, Li Z, Huang S, Qing H, Nickel E. Gas breakthrough pressure for hydrocarbon reservoir seal rocks: Implications for the security of long-term CO_2 storage in the Weyburn field. Geofluids. 2005;5(4):326-34.

46. Busch A, Müller N. Determining CO_2/brine relative permeability and capillary threshold pressures for reservoir rocks and caprocks: Recommendations for development of standard laboratory protocols. Energy Procedia. 2011;4:6053-60.

47. Aggelopoulos C, Robin M, Perfetti E, Vizika O. CO_2/$CaCl_2$ solution interfacial tensions under CO_2 geological storage conditions: Influence of cation valence on interfacial tension. Advances in Water Resources. 2010;33(6):691-7.

48. Labman physics. Surface tension 2017 [Available from: http://labman.phys.utk.edu/phys221core/modules/m7/surface_tension.html.

49. Voormeij DA, Simandl GJ. Geological, ocean, and mineral CO_2 sequestration options: a technical review. Geoscience Canada. 2004;31(1).

50. Fletcher A, Davis J, editors. How EOR can be transformed by nanotechnology. SPE Improved Oil Recovery Symposium; 2010.

51. Terry RE. Enhanced oil recovery. Encyclopedia of physical science and technology. 2001;18:503-18.

52. Thomas S. Enhanced oil recovery-an overview. Oil & Gas Science and Technology-Revue de l'IFP. 2008;63(1):9-19.

53. Thermal enhanced oil recovery techniques | Control Engineering 2017 [Available from: https://www.controleng.com/single-article/thermal-enhanced-oil-recovery-techniques/f2afa85b34b1c57c875d0ae86709c344.html?OCVALIDATE.

54. Emadi A, Sohrabi M, Farzaneh SA, Ireland S, editors. Experimental Investigation of Liquid-CO_2 and CO_2-Emulsion Application for Enhanced Heavy Oil Recovery. EAGE Annual Conference & Exhibition incorporating SPE Europec; London, UK, 10–13 June 2013: SPE: Houston, TX, USA, 2013.

55. Srivastava R, Huang S, Dyer S, Mourits F, editors. Heavy oil recovery by subcritical carbon dioxide flooding. SPE Latin America/Caribbean Petroleum Engineering Conference; Buenos Aires, Argentina, 27–29 April 1994: SPE: Houston, TX, USA, 1994.

56. Levine JS, Matter JM, Goldberg DS, Lackner KS, Supp MG, Ramakrishnan T. Two phase brine-CO_2 flow experiments in synthetic and natural media. Energy Procedia. 2011;4:4347-53.

57. Bennison T, editor. Prediction of heavy oil viscosity. Presented at the IBC Heavy Oil Field Development Conference; 1998.

58. Satter A, M. Iqbal G. Enhanced oil recovery processes: Thermal, chemical, and miscible floods2016. 313-37 p.

59. Stalkup F. Carbon dioxide miscible flooding: Past, present, and outlook for the future. JPT. 1978;30(08):1,102-1,12.

60. Kokal S, Al-Kaabi A. Enhanced oil recovery: Challenges & opportunities. World Petroleum Council: Official Publication. 2010;64.

61. Dang CT, Nghiem LX, Chen Z, Nguyen QP, Nguyen NT, editors. State-of-the-art low salinity waterflooding for enhanced oil recovery. SPE Asia Pacific Oil and Gas Conference and Exhibition; 2013.

62. Verma MK. Fundamentals of carbon dioxide-enhanced oil recovery (CO_2-EOR): A supporting document of the assessment methodology for hydrocarbon recovery using CO_2-EOR associated with carbon sequestration. US Geological Survey; 2015. Report No.: 2331-1258.

63. Grigg RB, Svec RK, editors. CO_2 transport mechanisms in CO_2/brine coreflooding. SPE Annual Technical Conference and Exhibition; 2006.

64. Khalil F, Asghari K. Application of CO_2-Foam as a Means of Reducing Carbon Dioxide Mobility. Journal of Canadian petroleum technology. 2006;45(05).

65. Enick RM, Olsen DK, Ammer JR, Schuller W, editors. Mobility and conformance control for CO_2 EOR via thickeners, foams, and gels-A Literature review of 40 years of research and pilot tests. SPE Improved Oil Recovery Symposium; 2012.

66. Bondor P. Applications of carbon dioxide in enhanced oil recovery. Energy Conversion and Management. 1992;33(5):579-86.

67. Ross GD, Todd AC, Tweedie JA, Will AG, editors. The dissolution effects of CO_2-brine systems on the permeability of UK and North Sea calcareous sandstones. SPE Enhanced Oil Recovery Symposium; 1982.

68. Dang CT, Nghiem LX, Chen Z, Nguyen NT, Nguyen QP, editors. CO_2 low salinity water alternating gas: A new promising approach for enhanced oil recovery. SPE Improved Oil Recovery Symposium; 2014.

69. Zolfaghari H, Zebarjadi A, Shahrokhi O, Ghazanfari MH. An experimental study of co_2-low salinity water alternating gas injection in sandstone heavy oil reservoirs. Iranian Journal of Oil & Gas Science and Technology. 2013;2(3):37-47.

70. Mosavat N, Torabi F. Experimental evaluation of the performance of carbonated water injection (CWI) under various operating conditions in light oil systems. Fuel. 2014;123:274-84.

71. Ayirala S, Yousef A. A state-of-the-art review to develop injection-water-chemistry requirement guidelines for IOR/EOR projects. SPE Production & Operations. 2015;30(01):26-42.

72. Zekri AY, Nasr M, Al-Arabai Z, editors. Effect of EOR technology on wettability and oil recovery of carbonate and sandstone formation. IPTC 2012: International Petroleum Technology Conference; 2012.

73. Bahramian A, Danesh A. Prediction of solid–fluid interfacial tension and contact angle. Journal of colloid and interface science. 2004;279(1):206-12.

74. Zhang Y, Xie X, Morrow NR, editors. Waterflood performance by injection of brine with different salinity for reservoir cores. SPE Annual Technical Conference and Exhibition; 2007.

75. Klins MA, Ali SMF. Heavy oil production by carbon dioxide injection. PETSOC-82-05-06. 1982.

76. Sehbi BS, Frailey SM, Lawal AS, editors. Analysis of factors affecting microscopic displacement efficiency in CO_2 floods. SPE Permian Basin Oil and Gas Recovery Conference; 2001.

77. PERMInc. Fundamentals of Fluid Flow in Porous Media 2017 [Available from: http://perminc.com/resources/fundamentals-of-fluid-flow-in-porous-media/chapter-4-immiscible-displacement/vertical-volumetric-sweep-efficiencies/.

78. Schlumberger. Oilfield Glossary 2017 [Available from: http://www.glossary.oilfield.slb.com/en/Terms/v/vertical_displacement_efficiency.aspx.

C. Appendix C: Core Sample Description

As shown under an optical microscope (Figure C-1), the North Sea sandstone core sample used during CO_2-water drainage displacements and Water-CO_2 imbibition displacements is made up of fine-grained, well-sorted sub-angular sand grains. The composition of the sandstone core was determined by the point count method under the microscope [8] (600 counts, Table C-1) and by the X-ray diffraction method (Table C-2). Under an optical light microscope, the predominant component of the sandstone sample can be identified as quartz; followed by a clay mineral, which is generally brown and distributed as rims around detrital quartz grains (Figure C-1). The X-ray diffraction result shows that the clay mineral is mostly illite with a trace amount of chlorite (Table C-2, Figure C-2). Feldspar, dolomite, mica and carbonate minerals are rare in the sample.

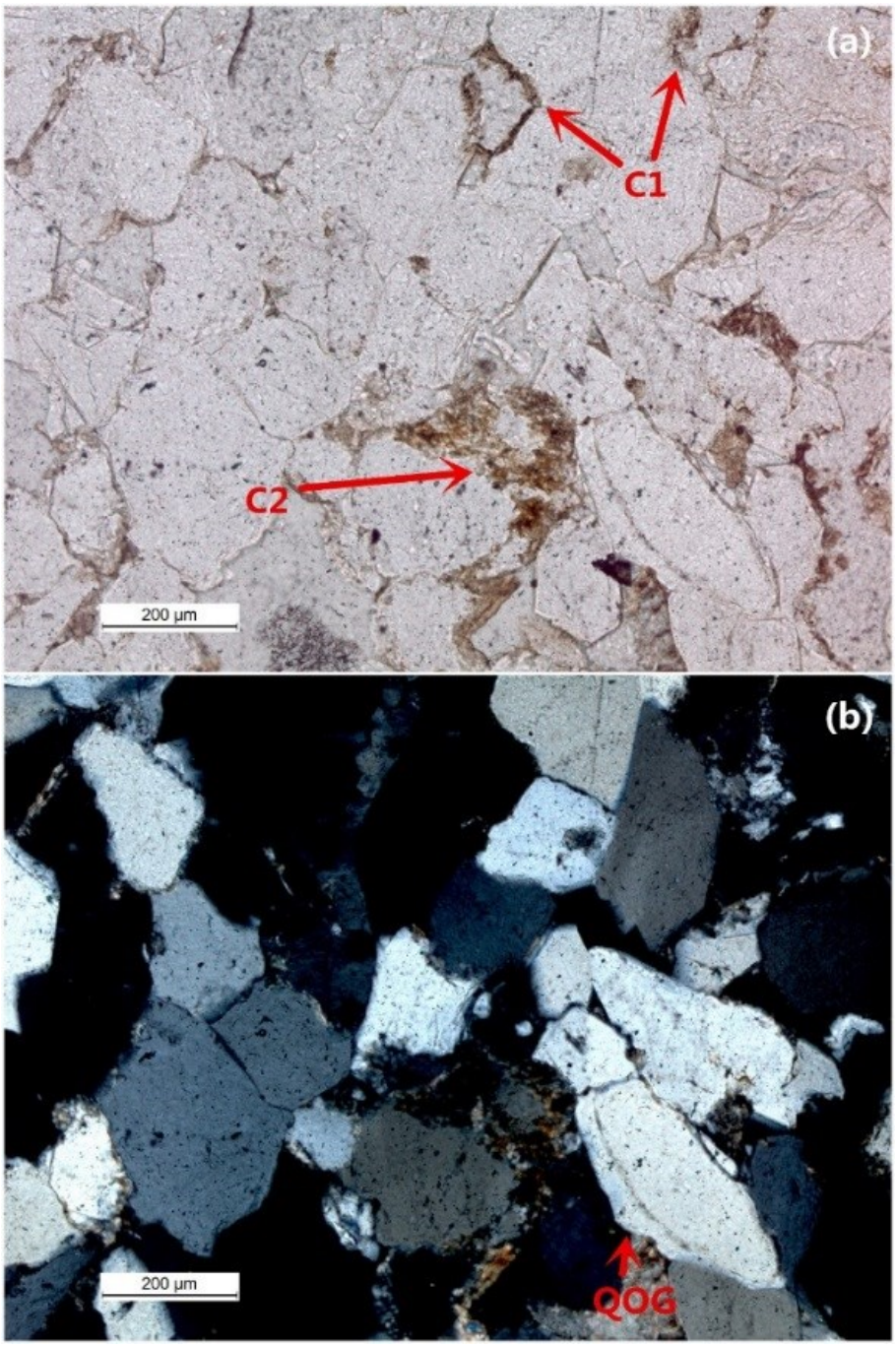

Figure C-1: The North Sea sandstone core under the microscope. The two images of the same section are taken under (a) microscopic plane polarised light and (b) cross polarised light. Most of the grains are quartz, which are white in the first image (a), grey or black in the second image (b). C1 = brown clay rims around quartz grains, C2 = a clay grain, QOG = quartz overgrowth.

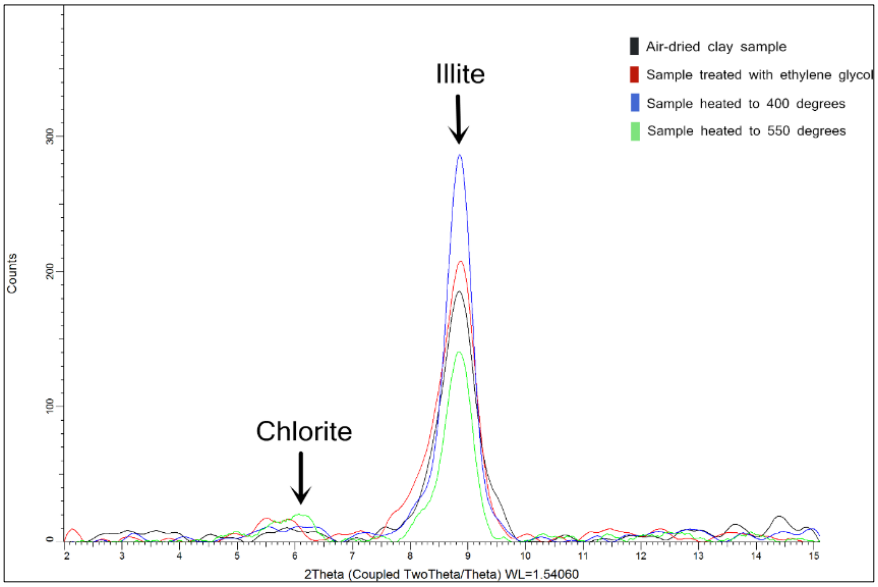

Figure C-2: X-ray diffraction spectrum for clay mineral analysis of the North Sea sandstone core. It shows that there are only two types of clay minerals, illite and chlorite, in the sandstone

Table C-1: Composition of the North Sea sandstone core sample determined by the point count method

Minerals	Number of points	Percentage	Errors (90% confidence)
Quartz	486	81.0%	3.2%
K-feldspar	1	0.2%	0.3%
Lithics	6	1.0%	0.8%
Quartz overgrowth	51	8.5%	2.3%
Dolomite	1	0.2%	0.3%
Mica	0	0.0%	0
Clay	38	6.3%	2.0%
***Primary porosity**	1	0.2%	0.3%
***Secondary porosity**	15	2.7%	1.3%
Opaque	1	0.2%	0.3%
Total	600		

** **Primary porosity** is the initial pore space between detrital grains formed upon the deposition of a sandstone; ***Secondary porosity** is the pore space that is created by mineral dissolution during the subsequent burial process.*

Table C-2: Composition of the North Sea sandstone core measured by X-ray diffraction

Minerals	Percentages
Quartz	92.8%
K-feldspar	0.9%
Plagioclase	2.2%
Dolomite	0.5%
Illite	1.6%
Chlorite	0.5%
Muscovite (Mica)	1.0%